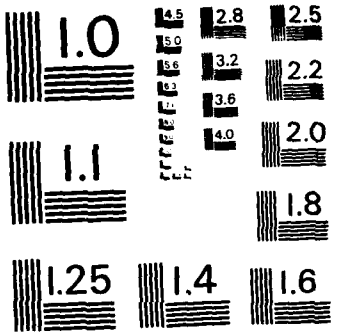
1.0
1.1
1.25
1.4
1.6
1.8
2.0
2.2
2.5
2.8
3.2
3.6
4.0
4.5
5.0
5.6

DISCLAIMER NOTICE

THIS DOCUMENT IS BEST QUALITY PRACTICABLE. THE COPY FURNISHED TO DTIC CONTAINED A SIGNIFICANT NUMBER OF PAGES WHICH DO NOT REPRODUCE LEGIBLY.

OR are
Blank pgs
that have
Been Removed

BEST AVAILABLE COPY

DTIC FILE COPY

UNITED STATES AIR FORCE

AD-A204 244

GRADUATE STUDENT RESEARCH PROGRAM

1988

PROGRAM TECHNICAL REPORT

UNIVERSAL ENERGY SYSTEMS, INC.

VOLUME 2 OF 3

PROGRAM DIRECTOR, U.E.S.
RODNEY C. DARRAH
PROGRAM ADMINISTRATOR, U.E.S.
SUSAN K. ESPY

PROGRAM MANAGER, A.F.O.S.R.
LT. COL. CLAUDE CAVENDER

DISTRIBUTION STATEMENT A
Approved for public release;
Distribution Unlimited

SUBMITTED TO
AIR FORCE OFFICE OF SCIENTIFIC RESEARCH
BOLLING AIR FORCE BASE
WASHINGTON, D.C.

DECEMBER 1988

DTIC
ELECTE
FEB 0 8 1989
D

89 2 8 054

ECURITY CLASSIFICATION OF THIS PAGE

REPORT DOCUMENTATION PAGE

EPORT SECURITY CLASSIFICATION: UNCLASSIFIED	1b. RESTRICTIVE MARKINGS
2a. SECURITY CLASSIFICATION AUTHORITY	3. DISTRIBUTION/AVAILABILITY OF REPORT: APPROVED FOR PUBLIC RELEASE; Distribution Unlimited
2b. DECLASSIFICATION/DOWNGRADING SCHEDULE	
4. PERFORMING ORGANIZATION REPORT NUMBER(S)	5. MONITORING ORGANIZATION REPORT NUMBER(S): AFOSR-TR-89-0042
6a. NAME OF PERFORMING ORGANIZATION: Universal Energy Systems Inc. / 6b. OFFICE SYMBOL (If applicable)	7a. NAME OF MONITORING ORGANIZATION: AFOSR/XOT
6c. ADDRESS (City, State and ZIP Code): 4401 Dayton-Xenia Road, Dayton, OH 45432	7b. ADDRESS (City, State and ZIP Code): Building 410, Bolling AFB, DC 20332-6448
8a. NAME OF FUNDING/SPONSORING ORGANIZATION: Same as #7 / 8b. OFFICE SYMBOL (If applicable)	9. PROCUREMENT INSTRUMENT IDENTIFICATION NUMBER: F49620-85-C-0013
8c. ADDRESS (City, State and ZIP Code): Same as 7b	10. SOURCE OF FUNDING NOS.

PROGRAM ELEMENT NO.	PROJECT NO.	TASK NO.	WORK UNIT NO.
61102F	3396	D5	

11. TITLE (Include Security Classification): USAF Graduate Student Summer Support Program - Program Management Report-1988 Vol 2 of 3

12. PERSONAL AUTHOR(S): dney C. Darrah, Susan K. Espy

13a. TYPE OF REPORT	13b. TIME COVERED	14. DATE OF REPORT (Yr., Mo., Day)	15. PAGE COUNT
Annual	FROM ____ TO ____	December 1988	

16. SUPPLEMENTARY NOTATION

17. COSATI CODES			18. SUBJECT TERMS (Continue on reverse if necessary and identify by block number)
FIELD	GROUP	SUB. GR.	

19. ABSTRACT (Continue on reverse if necessary and identify by block number)

See Attached

20. DISTRIBUTION/AVAILABILITY OF ABSTRACT	21. ABSTRACT SECURITY CLASSIFICATION
ASSIFIED/UNLIMITED ☑ SAME AS RPT. ☐ DTIC USERS ☐	IMC:ASSOFOED

22a. NAME OF RESPONSIBLE INDIVIDUAL	22b. TELEPHONE NUMBER (Include Area Code)	22c. OFFICE SYMBOL
Lt Col Claude Cavender	202-767-4970	XOT

DD FORM 1473, 83 APR — EDITION OF 1 JAN 73 IS OBSOLETE.

AFOSR-TR- 89 0042

PREFACE

The United States Air Force Graduate Student Research Program (USAF-GSRP) is conducted under the United States Air Force Summer Faculty Research Program. The program provides funds for selected graduate students to work at an appropriate Air Force Facility with a supervising professor who holds a concurrent Summer Faculty Research Program appointment or with a supervising Air Force Engineer/Scientist. This is accomplished by the students being selected on a nationally advertised competitive basis for a ten-week assignment during the summer intersession period to perform research at Air Force laboratories/centers. Each assignment is in a subject area and at an Air Force facility mutually agreed upon by the students and the Air Force. In addition to compensation, travel and cost of living allowances are also paid. The USAF-GSRP is sponsored by the Air Force Office of Scientific Research, Air Force Systems Command, United States Air Force, and is conducted by Universal Energy Systems, Inc.

The specific objectives of the 1988 USAF-GSRP are:

(1) To provide a productive means for the graduate students to participate in research at the Air Force Laboratories/Centers;

(2) To stimulate continuing professional association among the Graduate Students and their professional peers in the Air Force;

(3) To further the research objectives of the United States Air Force;

(4) To enhance the research productivity and capabilities of the graduate students especially as these relate to Air Force technical interests.

During the summer of 1988, 107 graduate students participated. These researchers were assigned to 23 USAF laboratories/centers across the country. This three volume document is a compilation of the final reports written by the assigned students members about their summer research efforts.

UNITED STATES AIR FORCE

GRADUATE STUDENT RESEARCH PROGRAM

1988

PROGRAM TECHNICAL REPORT

UNIVERSAL ENERGY SYSTEMS, INC.

VOLUME II OF III

Program Director, UES
Rodney C. Darrah

Program Manager, AFOSR
Lt. Col. Claude Cavender

Program Administrator, UES
Susan K. Espy

Submitted to

Air Force Office of Scientific Research

Bolling Air Force Base

Washington, DC

December 1988

DTIC COPY INSPECTED

A-1

TABLE OF CONTENTS

SECTION	PAGE
Preface	i
List Of Participants	ii
Participant Laboratory Assignment	xviii
Research Reports	xxii

PREFACE

The United States Air Force Graduate Student Research Program (USAF-GSRP) is conducted under the United States Air Force Summer Faculty Research Program. The program provides funds for selected graduate students to work at an appropriate Air Force Facility with a supervising professor who holds a concurrent Summer Faculty Research Program appointment or with a supervising Air Force Engineer/Scientist. This is accomplished by the students being selected on a nationally advertised competitive basis for a ten-week assignment during the summer intersession period to perform research at Air Force laboratories/centers. Each assignment is in a subject area and at an Air Force facility mutually agreed upon by the students and the Air Force. In addition to compensation, travel and cost of living allowances are also paid. The USAF-GSRP is sponsored by the Air Force Office of Scientific Research, Air Force Systems Command, United States Air Force, and is conducted by Universal Energy Systems, Inc.

The specific objectives of the 1988 USAF-GSRP are:

(1) To provide a productive means for the graduate students to participate in research at the Air Force Laboratories/Centers;

(2) To stimulate continuing professional association among the Graduate Students and their professional peers in the Air Force;

(3) To further the research objectives of the United States Air Force;

(4) To enhance the research productivity and capabilities of the graduate students especially as these relate to Air Force technical interests.

During the summer of 1988, 107 graduate students participated. These researchers were assigned to 23 USAF laboratories/centers across the country. This three volume document is a compilation of the final reports written by the assigned students members about their summer research efforts.

LIST OF 1988 PARTICIPANTS

NAME/ADDRESS	DEGREE, SPECIALTY, LABORATORY ASSIGNED
Ben A. Abbott Electrical Engineering Dept. Vanderbilt University Nashville, TN 37240 (615) 332-2723	Degree: B.S., Computer Science, 1983 Specialty: Electrical Engineering Assigned: Arnold Engineering Development Center
Antoinne C. Able Meharry Medical College 1005 D.B. Todd Blvd. P O Box 882 Nashville, TN 37208 (615) 361-5303	Degree: M.S., Biology, 1982 Specialty: Biology Assigned: Wilford Hall Medical Center
Stanley D. Adams College of Medicine Meharry Medical College 1005 D.B. Todd Blvd. Nashville, TN 37208 (615) 327-6204	Degree: B.S., Cellular & Molecular Biology, 1987 Specialty: Physiology Assigned: Wilford Hall Medical Center
John D. Allison Dept. of Psychology Univ. of Texas at Austin Mezes Hall 330 Austin, TX 78712 (512) 471-5857	Degree: M.A., Psychology, 1987 Specialty: Comparative Neurobiology Assigned: Human Resources Laboratory: Manpower and Personnel Div.
James E. Angelo Dept. of Physics Univ. of Minnesota - Duluth Duluth, MN 55812 (218) 726-7124	Degree: B.S., Math/Physics, 1986 Specialty: Applied Physics Assigned: Materials Laboratory
John E. Bambery Dept. of Physics University of Pennsylvania Indiana, PA 15701 (412) 357-2611	Degree: B.S. Physics, 1987 Specialty: Computer Analysis Assigned: Avionics Laboratory

Daniel W. Barineau
Dept. of Engineering Science
Virginia Tech.
1300-B Terrace View Apts.
Blacksburg, VA 24060
(703) 552-7867

Degree: B.S., Chemical Eng., 1987
Specialty: Engineering Mechanics
Assigned: Harry G. Armstrong Aerospace Medical Research Laboratory

John W.J. Barnaby
Dept. of Electrical Engineering
University of Alabama
Box 6169, 317 Houser Hall
Tuscaloosa, AL 35487-6169
(205) 348-6351

Degree: B.S., Electrical Eng., 1987
Specialty: Electrical Engineering
Assigned: School of Aerospace Medicine

Kathleen M. Bennett
Dept. of Engineering Mgmt.
University of Dayton
300 College Park
Dayton, OH 45469
(513) 229-2699

Degree: B.S., Mechanical Eng., 1984
Specialty: Engineering Management
Assigned: Flight Dynamics Laboratory

Mark N. Beorkrem
Dept. of Psychology
Washington University
One Brookings Drive
Campus Box 1125
St. Louis, MO 63130
(314) 889-6536

Degree: B.S., Psychology, 1987
Specialty: Organizational Behavior
Assigned: Human Resources Laboratory: Operations Training Div.

Joel L. Berg
Dept. of Eng. Science & Mech.
Virginia Polytechnic Inst.&S.U.
Blacksburg, VA 24061
(703) 961-6326

Degree: M.S., Engr. Mechanics, 1984
Specialty: Structural Vibrations
Assigned: Astronautics Laboratory

Darwin L. Boyd
Dept. of Physics
Kent State University
Smith Laboratory of Physics
Kent, OH 44242
(216) 672-2880

Degree: B.S. Physics, 1982
Specialty: Condensed Matter Physics
Assigned: Materials Laboratory

George C. Boynton
Dept. of Physics
University of Miami
P O Box 248046
Coral Gables, FL 33124
(305) 284-2323

Degree: M.S., Physics, 1983
Specialty: Physics
Assigned: Armament Laboratory

Mark L. Brusseau
Dept. of Soil Science
University of Florida
2169 McCarty Hall
Gainesville, FL 32611-0151
(904) 392-1951

Degree: M.S., Geology, 1984
Specialty: Contaminant Hydrology
Assigned: Engineering & Services Center

Bruce W. Bullard
Dept. of Electrical Eng.
University of Colorado
1420 Austin Bluffs Pkwy.
P O Box 7150
Colorado Springs, CO 80933-7150
(719) 593-3351

Degree: B.S., Electrical Eng., 1988
Specialty: Electrical Engineering
Assigned: Frank. J. Seiler Research Lab.

Franklin A. Bynum
Dept. of Physics
Miami University
Culler Hall
Oxford, OH 45056
(513) 529-5657

Degree: M.S., Physics, 1988
Specialty: Physics
Assigned: Weapons Laboratory

Kevin L. Carmichael
Dept. of Physics
Wright State University
Dayton, OH 45435
(513) 873-2954

Degree: B.S., Physics, 1987
Specialty: Solid State Physics
Assigned: Avionics Laboratory

Lance H. Carter
Dept. of Aerospace Eng.
Virginia Polytechnic Inst.&S.U.
817 Claytor Square
Blacksburg, VA 24060
(703) 953-2289

Degree: B.S., Aerospace Eng., 1987
Specialty: Engineering Mechanics
Assigned: Astronautics Laboratory

David B. Chenault
Dept. of Physics
University of Alabama
Center for Applied Optics
Huntsville, AL 35899
(205) 895-6102

Degree: B.S. Physics, 1986
Specialty: Physics
Assigned: Armament Laboratory

Daniel B. Cook
Dept. of Electro-Optics
University of Dayton
300 College Park
Dayton, OH 45469
(513) 228-4111

Degree: B.S., Physics, 1987
Specialty: Image Processing
Assigned: Avionics Laboratory

Patricia P. Cooper
Dept. of Applied Psychology
Francis Marion College
Florence, SC 29501
(803) 661-1378

Degree: M.A., Information Sci., 1974
Specialty: Psychology
Assigned: Human Resources Laboratory: Operations Training Div.

Otis Cosby, Jr.
School of Medicine
Meharry Medical College
1005 D.B. Todd Blvd.
Nashville, TN 37208
(615) 327-6223

Degree: B.S., Natural Science, 1983
Specialty: Natural Science
Assigned: School of Aerospace Medicine

Richard E. Courtney
Dept. of Computing Info. & Sci.
Kansas State University
234 Nichols Hall
Manhattan, KS 66506
(913) 532-6350

Degree: M.S., Computer Science, 1986
Specialty: Computer Science
Assigned: Rome Air Development Center

Jerry W. Dillon
School of Dentistry
Meharry Medical College
1005 D.B. Todd Blvd.
Nashville, TN 37208
(615) 327-6207

Degree: M.S., Microbiology, 1988
Specialty: Microbiology
Assigned: School of Aerospace Medicine

Charles C. Drake
Dept. of Computer Science
Jackson State University
1400 Lynch StreetTraining Systems
Jackson, MS 39203
(601) 968-2105

Degree: B.S., Computer Science, 1987
Specialty: Computer Science
Assigned: Human Resources Laboratory:

Susan M. Dumbacher
Dept. of Aerospace Eng.
University of Cincinnati
Cincinnati, OH 45225
(513) 475-6185

Degree: B.S., Aerospace Eng., 1986
Specialty: Controls
Assigned: Flight Dynamics Laboratory

Michael K. Ellis
Dept. of Computer Science/Eng.
University of Arkansas
1900 N. Garland
Fayetteville, AR 72703
(501) 575-0722

Degree: B.S., Computer Sci., 1988
Specialty: Neural Network
Assigned: Harry G. Armstrong Aerospace Medical Research Laboratory

Bryan C. Foos
Dept. of Civil Engineering
Ohio State University
2070 Neil Avenue
Columbus, OH 43210
(614) 292-2771

Degree: B.S., Civil Engineering, 1988
Specialty: Geotechnical and Materials
Assigned: Flight Dynamics Laboratory

Ernest J. Freeman
Dept. of Biological Sciences
Kent State University
Kent, OH 44240
(216) 672-2363

Degree: B.S., Zoology, 1985
Specialty: Neurochemistry
Assigned: School of Aerospace Medicine

Peter Gaddis, Jr.
Dept. of Sociology
Jackson State University
1400 J.R. Lynch Street
Jackson, MS 39217
(601) 968-2350

Degree: M.A., Sociology, 1988
Specialty: Alcohol and Drug Studies
Assigned: Human Resources Laboratory: Manpower and Personnel Div.

Douglas P. Gagne
Dept. of Mechanical Eng.
University of New Hampshire
Durham, NH 03824
(603) 868-6160

Degree: B.S., Mechanical Eng., 1988
Specialty: Systems Modeling & Dynamics
Assigned: Materials Laboratory

William L. Geisler
College of Polymer Science
University of Akron
Akron, OH 44325
(216) 375-7500

Degree: B.S., Chemical Eng., 1988
Specialty: Polymeric Materials
Assigned: Astronautics Laboratory

Robert L. Goetz
Dept. of Mechanical Eng.
Ohio University
Athens, OH 45701
(614) 594-3499

Degree: B.S., Mechanical Eng., 1987
Specialty: Mechanical Design
Assigned: Materials Laboratory

David L. Graham
Dept. of Mechanical Eng.
Northwestern University
Tech. 2524
Evanston, IL 60208
(312) 491-3589

Degree: B.S., Mechanical Eng., 1988
Specialty: Mechanical Engineering
Assigned: Astronautics Laboratory

Gary E. Griesheim
Dept. of Civil Engineering
Southern Illinois University
Carbondale, IL 62901
(618) 536-2368

Degree: B.S., Eng. Mechanics, 1987
Specialty: Composite Materials Design
Assigned: Astronautics Laboratory

Edward A. Grissom
Dept. of Electrical Eng.
Tennessee Tech. University
1217 Springdale
Cookeville, TN 38501
(615) 526-1036

Degree: B.S., Electrical Eng., 1983
Specialty: Digital Signal Processing
Assigned: Avionics Laboratory

Virginia A. Gunther
Dept. of Psychology
State Univ. of New York
at Binghamton
Binghamton, NY 13901
(607) 777-4610

Degree: M.A., Exp. Psychology, 1978
Specialty: Cognitive Psychology
Assigned: Harry G. Armstrong Aerospace Medical Research Laboratory

Douglas R. Hansen
Dept. of Civil Engineering
Colorado State University
Room B302
Ft. Collins, CO 80523
(303) 491-8353

Degree: B.S., Wildlife Biology, 1981
Specialty: Environmental Engineering
Assigned: Engineering & Service Center

Thomas K. Harkins
Dept. of Mechanical Eng.
Louisiana State University
1636 Applewood Road
Baton Rouge, LA 70808
(504) 766-3671

Degree: B.S., Mechanical Eng., 1986
Specialty: Flight Dynamics
Assigned: Armament Laboratory

Gary A. Hellenga
Dept. of Mathematical Sciences
Montana State University
1116 South Hedges
Bozeman, MT 59715
(406) 994-5360

Degree: B.S., Mathematics, 1983
Specialty: Applied Mathematics
Assigned: Rome Air Development Center

Andrew Hensley
Dept. of Mechanical Eng.
University of Detroit
Detroit, MI 48603
(313) 927-1242

Degree: B.S., Mechanical Eng., 1988
Specialty: Process Modeling
Assigned: Materials Laboratory

Norman C. Holmes
Dept. of Mechanical Engineering
University of New Hampshire
Durham, NH 03824-3541
(617) 662-6386

Degree: B.S., Mechanical Eng., 1984
Specialty: Mechanical Engineering
Assigned: Flight Dynamics Laboratory

Stephen R. Jenei
Dept. of Biology
University of Dayton
300 College Park Drive
Dayton, OH 45469-0001
(513) 229-2135

Degree: B.S., Biology, 1986
Specialty: Endocrine Physiology
Assigned: Harry G. Armstrong Aerospace Medical Research Laboratory

Alan C. Jewell
Dept. of Civil Engineering
Colorado State University
Fort Collins, CO 80521
(303) 491-5048

Degree: B.S., Geophysical Eng., 1984
Specialty: Geophysical Engineering
Assigned: Weapons Laboratory

Jennifer A. Joyce
Dept. of Chemistry
Texas A&M University
College Station, TX 77843-3255
(409) 845-5345

Degree: B.S., Chemistry, 1988
Specialty: Inorganic Chemistry
Assigned: Frank. J. Seiler Research Lab.

Steven P. Kahn
Dept. of Eng. Science & Mech.
Virginia Tech. University
Blacksburg, VA 24060
(703) 953-1966

Degree: B.S., Eng. Science and Mechanics, 1988
Specialty: Engineering Mechanics
Assigned: Astronautics Laboratory

Elizabeth J. Kavran
Dept. of Biology
University of Dayton
300 College Park Road
Dayton, OH 45429
(513) 229-7660

Degree: B.A., Biology, 1987
Specialty: Biology
Assigned: Harry G. Armstrong Aerospace Medical Research Laboratory

Phyllis Y. Keys
Dept. of General Engineering
University of Illinois
909 S. Fifth Street
Champaign, IL 61820
(217) 332-5010

Degree: B.E., General Eng., 1987
Specialty: Human Factors
Assigned: Occupational and Environment Health Laboratory

Thomas E. Kimble
Center for Space Sciences
Physics Program
Univ. of Texas at Dallas
2601 North Floyd Road
P O Box 830688, M.S. FO-22
Richardson, TX 75083-0688
(214) 690-2884

Degree: B.A., Economics, 1981
Specialty: Space Sciences
Assigned: Air Force Geophysics Lab.

Charles L. King
Dept. of Industrial Eng.
University of Arkansas
4207 Bell Engineering Ctr.
Fayetteville, AR 72701
(501) 575-3156

Degree: B.S., Industrial Eng., 1988
Specialty: Management
Assigned: Human Resources Laboratory:
Logistics & Human Factors Div.

Scharine Kirchoff
Geophysical Institute
Univ. of Alaska - Fairbanks
P O Box 83328
Fairbanks, AK 99708
(907) 479-5866

Degree: M.A., Geology, 1986
Specialty: Geophysics
Assigned: Air Force Geophysics Lab.

Christopher G. Kocher
Dept. of Civil Engineering
Southern Illinois University
Carbondale, IL 62901
(618) 536-2368

Degree: B.S., Eng. Mechanics, 1986
Specialty: Engineering Mechanics
Assigned: Astronautics Laboratory

Michael J. Koharchik
Dept. of Engineering Mechanics
The Pennsylvania State Univ.
State College, PA 16802
(814) 237-6527

Degree: B.S., Aerospace Eng., 1987
Specialty: Aerospace Structures
Assigned: Astronautics Laboratory

Keith A. Krapels
Dept. of Electrical Eng.
Memphis State University
Memphis, TN 38152
(901) 454-3312

Degree: M.S., Electrical Eng., 1986
Specialty: Electrical Engineering
Assigned: Arnold Engineering
Development Center

Richard J. Kunze
Dept. of Psychology
University of Missouri-Columbia
210 McAlester Hall
UMC Campus
Columbia, MO 65211
(314) 882-4351

Degree: B.A., Psychology, 1986
Specialty: Experimental Psychology
Assigned: Harry G. Armstrong Aerospace
Medical Research Laboratory

Thomas E. Lane
Dept. of Chemistry
Ball State University
Muncie, IN 47306
(317) 285-8078

Degree: B.S., Biology, 1988
Specialty: Immunology & Microbiology
Assigned: School of Aerospace Medicine

Bobby L. Larry
Dental School
Meharry Medical College
1005 D.B. Todd Blvd.
Nashville, TN 37208
(615) 322-9819

Degree: B.S., Biology, 1978
Specialty: Dentistry
Assigned: Wilford Hall Medical Center

Aleshia C. Lewis
Dept. of Biology
Meharry Medical College
1005 D.B. Todd Blvd.
Nashville, TN 37208
(615) 327-6111

Degree: B.S., Microbiology, 1986
Specialty: Microbiology
Assigned: Wilford Hall Medical Center

Yuhong Y. Li
Dept. of Computer Science
University of Nebraska
Lincoln, NE 68588
(402) 472-7211

Degree: M.S., Chemical Eng., 1977
Specialty: Chemical Engineering
Assigned: Avionics Laboratory

Yolanda A. Malone
Dept. of Pharmacology
Meharry Medical College
1005 D.B. Todd Blvd.
Nashville, TN 37208
(615) 327-6111

Degree: M.S., Medicine, 1988
Specialty: Medicine
Assigned: School of Aerospace Medicine

Randal L. Mandock
School of Geophysical Science
Georgia Inst. of Technology
Atlanta, GA 30332
(404) 894-3890

Degree: M.S., Atmospheric Sci., 1986
Specialty: Atmospheric Science
Assigned: Avionics Laboratory

David L. Mayfield
Dept. of Ind./Org. Psychology
University of Georgia
Athens, GA 30602
(404) 542-3053

Degree: B.S., Psychology, 1987
Specialty: Industrial/Organ. Psychology
Assigned: Human Resources Laboratory:
Manpower and Personnel Div.

John E. McCord
Dept. of Chemistry
Murray State University
Murray, KY 42071
(502) 762-4490

Degree: B.S., Chemistry, 1987
Specialty: Physical Chemistry
Assigned: Weapons Laboratory

David B. McKenzie
Dept. of Civil Engineering
Michigan Technological Univ.
Houghton, MI 49931
(906) 482-4882

Degree: B.S., Civil Eng., 1988
Specialty: Environmental Engineering
Assigned: Engineering & Services Center

Salvatore P. Miceli
Dept. of Aerospace Eng. Sciences
Univ. of Colorado - Boulder
Campus Box 429
Boulder, CO 80309-0429
(303) 492-6417

Degree: B.S., Aerospace Eng., 1988
Specialty: Unsteady Aerodynamics
Assigned: Frank. J. Seiler Research Lab.

Hisook L. Min
Division of Basic Studies
Jarvis Christian College
Hawkins, TX 75765
(214) 769-2174

Degree: M.S., Computer Science, 1987
Specialty: Applied Physics
Assigned: Armament Laboratory

Deborah J. Mitchell
Dept. of Chemistry
Prairie View A&M University
Drawer C
Prairie View, TX 77446
(409) 857-3910

Degree: B.S., Chemistry, 1986
Specialty: Biochemistry
Assigned: Harry G. Armstrong Aerospace Medical Research Laboratory

William A. Moran
Dept. of Chemistry
Calif. State Univ. -Northridge
18111 Nordhoff Street
Northridge, CA 91330
(818) 885-3381

Degree: B.S., Chemistry, 1986
Specialty: Chemistry
Assigned: Astronautics Laboratory

William D. Morse
Dept. of Electrical Eng.
Ohio State University
205 Dresser Laboratory
2015 Neil Avenue
Columbus, OH 43210-1272
(614) 292-2572

Degree: B.S., Electrical Eng., 1987
Specialty: Electrical Engineering
Assigned: Flight Dynamics Laboratory

Lisa F. Weinstein
Dept. of Psychology
Univ. of Illinois
at Urbana-Champaign
Aviation Research Lab., Q5
#1 Airport Road
Savoy, IL 61874
(217) 244-8728

Degree: M.A., Experimental Psy., 1987
Specialty: Engineering Psychology
Assigned: Harry G. Armstrong Aerospace Medical Research Laboratory

Michael A. Zmuda
Dept. of Computer Science
Wright State University
Dayton, OH 45324
(513) 873-2491

Degree: B.S., Compt. Sci. & Math, 1987
Specialty: Pattern Recognition
Assigned: Avionics Laboratory

Robert G. Petroit
Dept. of Elect. & Compt. Eng.
Illinois Institute of Tech.
3300 So. Federal
Chicago, IL 60616
(312) 567-3400

Degree: B.S., Electrical Eng., 1987
Specialty: Communications Systems
Assigned: Rome Air Development Center

Peter E. Pidcoe
Dept. of Bioengineering
University of Illinois
Box 4348
Chicago, IL 60680
(312) 996-2331

Degree: B.S., Environ. Mgmt., 1988
Specialty: Signal Processing
Assigned: Human Resources Laboratory: Operations Training Div.

Steven J. Pierce
Dept. of Civil Engineering
Geotechnical Program
Colorado State University
Fort Collins, CO 80523
(303) 491-5048

Degree: B.S., Geology, 1985
Specialty: Geotechnical Engineering
Assigned: Engineering & Services Center

Julia Rennenkampff
Dept. of Mathematics
New York University
251 Mercer Street
New York, NY 10012
(212) 998-3140

Degree: M.S., Mathematics, 1987
Specialty: Waves in Random Media
Assigned: School of Aerospace Medicine

Robert J. Riley
Dept. of Mech. & Aero. Eng.
Cornell University
105 Upson Hall
Ithaca, NY 14853
(607) 255-3623

Degree: B.S., Mechanical Eng., 1987
Specialty: Combustion, Fluid Dynamics
Assigned: Aero Propulsion Laboratory

Mary C. Ritter
Dept. of Biology
Trinity University
715 Stadium Dr.
Box 937
San Antonio, TX 78284
(512) 737-4782

Degree: B.A., Biology, 1988
Specialty: Biological Oceanography
Assigned: School of Aerospace Medicine

Jacqueline Roberts
Dept. of Chemistry
Wright State University
229 Oelman Hall
Dayton, OH 45435
(513) 873-2855

Degree: B.S., Chemistry, 1986
Specialty: Toxicology
Assigned: Harry G. Armstrong Aerospace Medical Research Laboratory

James D. Roberts
Dept. of Engineering
Univ. of Texas-San Antonio
San Antonio, TX 78285
(512) 691-4490

Degree: B.S., Electrical Eng., 1988
Specialty: Order Statistic Filters
Assigned: School of Aerospace Medicine

Matthew S. Rubin
Dept. of Elect. & Compt. Eng.
Ohio University
West Green Drive
Stocker Center 329
Athens, OH 45701-2979
(614) 593-1568

Degree: B.S., Electrical Eng., 1987
Specialty: Microwave Network Theory
Assigned: Rome Air Development Center

John Y. Salinas
Dept. of Medicine
Meharry Medical College
1005 D.B. Todd Blvd.
Nashville, TN 37208
(615) 327-4537

Degree: M.S., Biochemistry, 1984
Specialty: Medicine
Assigned: Wilford Hall Medical Center

Eric O. Schmidt
Dept. of Geophysical Science
Georgia Inst. of Technology
Atlanta, GA 30332
(404) 894-3897

Degree: M.S., Physics, 1983
Specialty: Atmospheric Science
Assigned: Avionics Laboratory

Gregory A. Schoeppner
Dept. of Civil Engineering
Ohio State University
470 Hitchcock
2070 Neil Avenue
Columbus, OH 43210
(614) 292-7304

Degree: M.S., Civil Eng., 1987
Specialty: Civil Engineering
Assigned: Flight Dynamics Laboratory

Douglas J. Sego
Dept. of Organ./Behavior Mgmt.
Michigan State University
232 Eppley East
Lansing, MI 48824
(517) 353-5414

Degree: B.A., Business Info., 1987
Specialty: Organization/Behavior
Assigned: Human Resources Laboratory: Training Systems

Anne L. Siegman
Dept. of Mathematics
University of Miami
1107N 1239 Dickinson Dr.
Coral Gables, FL 33146
(305) 284-2925

Degree: B.A., Mathematics, 1986
Specialty: Mathematics
Assigned: Armament Laboratory

Jeff P. Simmons
Dept. of Engineering
Carnegie Mellon University
Pittsburgh, PA 15213
(412) 268-2684

Degree: M.S., Engineering, 1985
Specialty: Materials Science
Assigned: Materials Laboratory

Kimberly F. Smith
Dept. of Medicine
Meharry Medical College
P O Box 935
1005 D.B. Todd Blvd.
Nashville, TN 37208
(615) 327-6308

Degree: B.S., Microbiology, 1986
Specialty: Epidemiology
Assigned: Wilford Hall Medical Center

Brian K. Spielbusch
Dept. of Electrical Eng.
Univ. of Missouri-Columbia
Truman Campus
600 W. Mechanic
Independence, MO 64050
(816) 276-1250

Degree: B.S., Electrical Eng., 1985
Specialty: Electro Optics
Assigned: Weapons Laboratory

Daryl W. Sprehn
Dept. of Elect. Eng. Tech.
Oregon Inst. of Technology
3201 Campus Drive
Klamath Falls, OR 97601-8801
(503) 882-6890

Degree: B.S., Electrical Eng., 1988
Specialty: Electromagnetic Propagation
Assigned: Rome Air Development Center

Christopher Sullivan
Dept. of Psychology
Colorado State University
Fort Collins, CO 80523
(303) 491-7184

Degree: M.S., Psychology, 1986
Specialty: Experimental Psychology
Assigned: Harry G. Armstrong Aerospace Medical Research Laboratory

David A. Swick
Dept. of Mechanical Eng.
Ohio University
723 Carriage Hill
Athens, OH 45701
(614) 594-4818

Degree: B.S., Mechanical Eng., 1987
Specialty: Mechanical Design
Assigned: Materials Laboratory

Richard A. Swift
Dept. of Aero. & Mech. Eng.
University of Notre Dame
Notre Dame, IN 46556
(219) 239-5430

Degree: B.S., Aeronautical Eng., 1987
Specialty: Structural Mechanics
Assigned: Flight Dynamics Laboratory

Paul R. Tanner
Dept. of Physiology
Meharry Medical College
Nashville, TN 37212
(615) 269-0873

Degree: B.A., Psychology, 1986
Specialty: Sensory Neurophysiology
Assigned: Wilford Hall Medical Center

David F. Thompson
School of Mechanical Eng.
Purdue University
West Lafayette, IN 47906
(317) 494-4903

Degree: M.S., Engineering, 1985
Specialty: Computer Information
Assigned: Flight Dynamics Laboratory

Ronald C. Tomlinson
Dept. of Chemistry
Wright State University
Dayton, OH 45435
(513) 873-2855

Degree: B.S., Chemistry, 1987
Specialty: Polymer Synthesis
Assigned: Materials Laboratory

Robert W. Tramel
Dept. of Mathematics
Univ. of Tennessee Space Inst.
Tullahoma, TN 37388-8897
(615) 455-0631

Degree: B.S., Physics, 1986
Specialty: Computational Fluid Mechanics
Assigned: Arnold Engineering Development Center

Tien N. Tran
Dept. of Elect. & Comp. Eng.
University of Cincinnati
Cincinnati, OH 45221
(513) 475-4247

Degree: M.S., Electrical Eng., 1988
Specialty: Image Coding
Assigned: Avionics Laboratory

John P. VanTassel
Dept. of Computer Science
Wright State University
Dayton, OH 45435
(513) 873-2491

Degree: B.A., Computer Studies, 1987
Specialty: Formal Specifications
Assigned: Avionics Laboratory

Deborah L. Vezie
Dept. of Chemical, Bio.,
and Materials Engineering
Arizona State University
COB B210
Tempe, AZ 85287
(602) 965-3313

Degree: B.S., Biomedical Eng., 1987
Specialty: Materials Science & Eng.
Assigned: Materials Laboratory

Oden L. Warren
Dept. of Chemistry
Iowa State University
Ames, IA 50011
(515) 294-6342

Degree: B.S., Chemistry, 1988
Specialty: Physical Chemistry
Assigned: Materials Laboratory

Lisa F. Weinstein
Dept. of Psychology
Univ. of Illinois
at Urbana-Champaign
Aviation Research Lab., Q5
#1 Airport Road
Savoy, IL 61874
(217) 244-8728

Degree: M.A., Experimental Psy., 1987
Specialty: Engineering Psychology
Assigned: Harry G. Armstrong Aerospace Medical Research Laboratory

Michael A. Zmuda
Dept. of Computer Science
Wright State University
Dayton, OH 45324
(513) 873-2491

Degree: B.S., Compt. Sci. & Math, 1987
Specialty: Pattern Recognition
Assigned: Avionics Laboratory

PARTICIPANT LABORATORY ASSIGNMENT

C. PARTICIPANT LABORATORY ASSIGNMENT (Page 1)

1988 USAF/UES GRADUATE STUDENT RESEARCH PROGRAM

AERO PROPULSION LABORATORY (AFWAL/APL)
(Wright-Patterson Air Force Base)

1. Robert Riley

ARMAMENT LABORATORY (AD)
(Eglin Air Force Base)

1. George Boynton
2. David Chenault
3. Thomas Harkins
4. Hisook Min
5. Thomas Olsen
6. Anne Siegman

HARRY G. ARMSTRONG AEROSPACE MEDICAL RESEARCH LABORATORY (AAMRL)
(Wright-Patterson Air Force Base)

1. Daniel Barineau
2. Michael Ellis
3. Virginia Gunther
4. Stephen Jenei
5. Elizabeth Kavran
6. Richard Kunze
7. Deborah Mitchell
8. Jacqueline Roberts
9. Christopher Sullivan
10. Lisa Weinstein

ARNOLD ENGINEERING DEVELOPMENT CENTER (AEDC)
(Arnold Air Force Base)

1. Ben Abbott
2. Keith Krapels
3. Robert Tramel

ASTRONAUTICS LABORATORY (AL)
(Edwards Air Force Base)

1. Joel Berg
2. Lance Carter
3. William Geisler
4. David Graham
5. Gray Griesheim
6. Steven Kahn
7. Christopher Kocher
8. Michael Koharchik
9. William Moran

AVIONICS LABORATORY (AFWAL/AL)
(Wright-Patterson Air Force Base)

1. John Bambery
2. Kevin Carmichael
3. Daniel Cook
4. Edward Grissom
5. Yuhong Li
6. Randal Mandock
7. Phillip Pace
8. Eric Schmidt
9. Tien Tran
10. John VanTassel
11. Michael Zmuda

ENGINEERING AND SERVICES CENTER (ESC)
(Tyndall Air Force Base)

1. Mark Brusseau
2. Douglas Hansen
3. David McKenzie
4. James Normann
5. Steven Pierce

C. PARTICIPANT LABORATORY ASSIGNMENT (Page 2)

FLIGHT DYNAMICS LABORATORY (FDL)
(Wright-Patterson Air Force Base)

1. Kathleen Bennett
2. Susan Dumbacher
3. Bryan Foos
4. Norman Holmes
5. William Morse
6. Gregory Schoeppner
7. Richard Swift
8. David Thompson

FRANK J. SEILER RESEARCH LABORATORY (FJSRL)
(USAF Academy)

1. Bruce Bullard
2. Jennifer Joyce
3. Salvatore Miceli

GEOPHYSICS LABORATORY (AFGL)
(Hansom Air Force Base)

1. Thomas Kimble
2. Scharine Kirchoff
3. Thomas Pentecost

HUMAN RESOURCES LABORATORY
(Brooks, Williams and Wright-Patterson Air Force Bases)

1. John Allison
2. Mark Beorkrem
3. Patricia Cooper
4. Charles Drake
5. Peter Gaddis
6. Charles King
7. David Mayfield
8. Jerome Nadel
9. Peter Pidcoe
10. Douglas Sego

MATERIALS LABORATORY (ML)
(Wright-Patterson Air Force Base)

1. James Angelo
2. Darwin Boyd
3. Douglas Gagne
4. Robert Goetz
5. Andrew Hensley
6. Jeff Simmons
7. David Swick
8. Ronald Tomlinson
9. Deborah Vezie
10. Oden Warren

OCCUPATIONAL AND ENVIRONMENT HEALTH LABORATORY (OEHL)
(Brooks Air Force Base)

1. Phyllis Keys

C. PARTICIPANT LABORATORY ASSIGNMENT (Page 3)

ROME AIR DEVELOPMENT CENTER (RADC)
(Griffiss Air Force Base)

1. Richard Courtney
2. Gary Hellenga
3. Robert Petroit
4. Matthew Rubin
5. Daryl Sprehn

SCHOOL OF AEROSPACE MEDICINE (SAM)
(Brooks Air Force Base)

1. John Barnaby
2. Otis Cosby
3. Jerry Dillon
4. Ernest Freeman
5. Thomas Lane
6. Yolanda Malone
7. Conrad Murray
8. Christine Nelson
9. Julia Rennenkampff
10. Mary Ritter
11. James Roberts

WEAPONS LABORATORY (WL)
(Kirtland Air Force Base)

1. Franklin Bynum
2. Alan Jewell
3. John McCord
4. Brian Spielbusch

WILFORD HALL MEDICAL CENTER (WHMC)
(Lackland Air Force Base)

1. Antoinne Able
2. Stanley Adams
3. Bobby Larry
4. Aleshia Lewis
5. John Salinas
6. Kimberly Smith
7. Paul Tanner

RESEARCH REPORTS

RESEARCH REPORTS

1988 GRADUATE STUDENT RESEARCH PROGRAM

Technical Report Number	Title	Graduate Researcher
Volume I		
Armament Laboratory		
1	Two Dimensional Simulation of Railgun Plasma Armatures	George C. Boynton
2	Mueller Matrix Infrared Polarimetry	David Chenault
3	Determining the Aerodynamic Coefficients of High L/D Projectiles Using a Body-Fixed Coordinate System	Thomas Harkins
4	Filter Design and Signal Processing in the Development of Target-Aerosol Discrimination Techniques for Active Optical Proximity Sensors	Hisook Min
5	Viscous Grid Generation About a Two-Store Mutual Interference Problem	Thomas Olsen
6	Arima Modeling of Residuals in AD/KR TDOP Models *** Same Report as Dr. Shamma***	Anne Siegman
Arnold Engineering Development Center		
7	MULTIGRAPH Kernel for Transputer Based Systems	Ben Abbott
8	Performance Analyses of an IR Laser Scanner System Utilizing Bragg Cell Deflectors and Modulator for Writing Directly on FPAs Under Test	Keith Krapels
9	Test of a Locally Implicit Method for the Euler Equations and an Artificial Dissipation Scheme	Robert Tramel
Astronautics Laboratory		
10	Ground-Based Experimental Control Techniques for Space-Based Structures	Joel Berg
11	An Observer Design for the AFAL Grid	Lance Carter
12	Rheometrics Stress Rheometer Applications	William Geisler

13	Stability of Jets Under the Supercritical State	David Graham
14	In-Plane Fracture in 2-D Carbon-Carbon	Gary Griesheim
15	Experimental Verification of Identification Spillover for Distributed Structures	Steven Kahn
16	The Effects of Elevated Temperature Exposure on the Strength and Micro-structure of 2-D Carbon-Carbon	Christopher Kocher
17	Composite-Embedded Fiber-Optic Strain Sensors *** Same Report as Dr. David Jensen ***	Michael Koharchik
18	The Photochemistry of μ3-(η-Diethylacetylene)-Decacarbonyltriosmium in Solid Argon *** Same Report as Dr. Susan Collins ***	William Moran

Engineering and Services Center

19	Investigation of Sorption Kinetics	Mark Brusseau
20	Estimation of Jet Fuel Contamination in Soils *** Same Report as Prof. Durnford ***	Douglas Hansen
21	Soil Vapor Extraction of Volatile Organic Chemicals *** Same Report as Prof. Hutzler ***	David McKenzie
22	Evaluation of the Computer Program 'Structural Analysis for Severe Dynamic Environments'	James Normann
23	High Intensity Stress Wave Propagation in Partially Saturated Sand *** Same Report as Prof. Wayne Charlie ***	Steven Pierce

Frank J. Seiler Research Laboratory

24	Super Conducting Thin Films by Laser Evaporation of Bulk Material	Bruce Bullard
25	The Effects of Sodium Chloride on Room Temperature Molten Salts	Jennifer Joyce
26	Unsteady Multiple Body Studies for Two-Dimensional and Three-Dimensional Experiments	Salvatore Miceli

Geophysics Laboratory

27	No Report Submitted at this Time	Thomas Kimble
28	An Investigation of Economic Explosions in Littleton, Massachusetts and Healy, Alaska	Scharine Kirchoff
29	Gas Phase Ion-Molecule Reactions of Carbocations	Thomas Pentecost

Rome Air Development Center

30	Evaluation of Software Structured Designs Using Metrics	Richard Courtney
31	Free-Space Laser Communications Simulator Program	Gary Hellenga
32	The Effects of Nonlinearities of High Speed Analog-to-Digital Converters on Digital Beamforming Arrays ***Same Report as Dr. Donald Ucci***	Robert Petroit
33	Metal Semiconductor Field Effect Transistor Computer Modelling and Electron Transport Computation	Matthew Rubin
34	Noise Calculations in a RADAR Receiver *** Same Report as Dr. Beryl Barber ***	Daryl Sprehn

Weapons Laboratory

35	Chemical Kinetics Information Collected for IF Flow Tube, Report Period 1 June to 8 August 1988	Franklin Bynum
36	Stochastic Site Characterization and Modelling	Alan Jewell
37	Guide for the Diode Laser System to be Used in the Study of SO Radical	John McCord
38	The Experimental Validation of Imaging Correlography Through Atmospheric Intensity Scintillations	Brian Spielbusch

Volume II

Air Force Wright Aeronautical Laboratories

Aero Propulsion Laboratory

39	An Experimental Investigation of Fractal Surfaces in Turbulent Diffusion Flames	Robert Riley

Avionics Laboratory

40	Thermionic Emission vs. Drift-Diffusion and the Placement of the Spike Layer for the BICFET	John Bambery

41	Finite Elements Simulation of the Resonant Tunneling Diode	Kevin Carmichael
42	Software Tools Modeling Low Voltage Beam Steering Devices	Daniel Cook
43	Acquisition of Digital Radar Data for Use on the Improved TSPX Software	Edward Grissom
44	Model-based Target Recognition Using Laser Radar Imagery *** Same Report as Prof. Robert Li ***	Yuhong Li
45	A Proposed Turbulence Monitoring Facility For Wright-Patterson Air Force Base	Randal Mandock
46	Lightwave Systems and Device Database Development	Phillip Pace
47	A Study of Sky Backgrounds and Sub-Visual Cirrus	Eric Schmidt
48	Adaptive Array Architectures with Low-Sensitivity to Random Errors in the Steering Vector Elements	Tien Tran
49	Extraction of Circuit Definitions from VHDL Specifications	John VanTassel
50	Applications of Evolutionary Learning Strategies to Pattern Recognition Tasks *** Same Report as Prof. Mateen Rizki ***	Michael Zmuda

Flight Dynamics Laboratory

51	A Computer Model for Air-to-Air Combat (Force on Force) Assessment ***Same Report as Dr. P. Sweeney***	Kathleen Bennett
52	Evaluations of Suboptimal Filters as Applied to Large Flexible Space Structures	Susan Dumbacher
53	No Report Submitted at this Time	Bryan Foos
54	Development of an Aircraft Tire-Wheel Interface Model for Flange/Beadseat Contact Loads *** Same Report as Prof. James Sherwood ***	Norman Holmes
55	A Flight Control Reconfiguration Study Using Model Reference Adaptive Control	William Morse

56	Damage in Graphite/Epoxy Plates Subjected to Low Velocity Impact *** Same Report as Prof. William Wolfe ***	Gregory Schoeppner
57	Finite Element Analysis for Preliminary Structural Design/Optimization	Richard Swift
58	Optimal and Sub-Optimal Loop Shaping in Quantitative Feedback Theory	David Thompson
Materials Laboratory		
59	Photoreflectance as a Characterization Tool for Gallium Arsinide and Aluminum Gallium Arsinide Materials	James Angelo
60	Analytical and Numerical Solutions of the Nonlinear Diffusion Equation	Darwin Boyd
61	QPA Control of the End Milling Process ***Same Report as Prof. Barry Fussell ***	Douglas Gagne
62	Can Design for Extruded Powder Metallurgy Materials, and the Effects of Can Geometry and Can Material on the Powder Metallurgy Material Core	Robert Goetz
63	Interface Resistivity Modelling of the Hot Rolling of Ti-48Al-1V	Andrew Hensley
64	Phase Relationships in Al-Nb-X Ternary Alloy Systems	Jeff Simmons
65	Design of mechanical joints and their implications to the implementation of a comprehensive computer aided design package	David Swick
66	The Study of Trimethylsilylpolyphosphate (PPSE) as a Dehydrating Agent for Polymerizations and Model Compound Preperations of N-Phenylbenzimidazoles	Ronald Tomlinson
67	No Report Submitted at this Time	Deborah Vezie
68	Effect of Various Metals on the Thermal Degradation of a Chlorotrifluorethylene Based Fluid ***Same Report as Dr. Vijay Gupta***	Oden Warren

Volume III
Human Systems Divisions Laboratories
Harry G. Armstrong Aerospace Medical Research Laboratory

69	Improvements in the Control of Robotic Arm Simulations Using the Articulated Total Body (ATB) Model	Daniel Barineau
70	Auditory Modeling ***Same Report as Dr. David Covington***	Michael Ellis
71	Performance in a Visual Monitoring Task with Serial and Simultaneous Display Formats *** Same as Prof. David Payne ***	Virginia Gunther
72	Evaluation of the Toxic Effects of a 90-Day Continuous Exposure of Rats and to Shale Derived JP-4 Jet Fuel	Stephen Jenei
73	Ceramic Composite Materials for Establishing Ingrowth of Bone and Developing Bone Remodeling Models	Elizabeth Kavran
74	Visual-Spatial Localization with a Helmet-Mounted Display	Richard Kunze
75	Evaluation of an Extraction Procedure for the Analysis of Serum Steroids *** Same Report as Prof. Masingale ***	Deborah Mitchell
76	Nephrotoxicity of 2,5-DMH in Fischer 344 Rats	Jacqueline Robert
77	Physiological Measures of Workload During Actual Flight	Christopher Sulli
78	Ground-Texture Information for Aimpoint Estimation	Lisa Weinstein

Human Resources Laboratory

79	The Relationship Between Inspection Time and Intelligence *** Same Report as Dr. Robert Young ***	John Allison
80	Effectiveness of Contract Monitors in an Air Force Human Resources Laboratory: Prediction and Measurement *** Same Report as Dr. Alan Witt ***	Mark Beorkrem
81	No Report Submitted at this Time	Patricia Cooper

82	An Intelligent Tutor for the IBM System/360 Assembly Language: BIGBLUE *** Same Report as Dr. Sunita Rana ***	Charles Drake
83	Underlying Distributions of the New PACE Variables	Peter Gaddis
84	Development of a General Reliability Simulation Model	Charles King
85	Development of a Candidate Task Taxonomy for Air Force Enlisted Specialties	David Mayfield
86	Form Distortions in Computer Generated Moving Objects: An Assessment of Display Parameters	Jerome Nadel
87	Oculomotor Response to Sinusoidal Stimuli	Peter Pidcoe
88	Air Force Training Evaluation System: A Case Study	Douglas Sego
Occupational and Environmental Health Laboratory		
89	Evaluation of T-9 Noise Suppressor System at McConnell AFB, Kansas	Phyllis Keys
School of Aerospace Medicine		
90	No Report Submitted at this Time	John Barnaby
91	No Report Submitted at this Time	Otis Cosby
92	Standardization of DAIM Precipitate	Jerry Dillon
93	Membrane Alterations Involved in Evoked Release of L-Glutamic Acid from Mossy Fiber Synaptosomes	Ernest Freeman
94	Development of Improved Assays for Cholesterol and Major Lipoprotein Fractions *** Same Report as Dr. Eric Johnson ***	Thomas Lane
95	Glaucoma in U.S. Air Force Aviators - USAF School of Aerospace Medicine Study Group	Yolanda Malone
96	The Separation of HDL2 and HDL3 Using the Technique of Ultracentrifugation *** Same Report as Prof. Joe Ross ***	Conrad Murray
97	Light Beam Interaction Induced by a Transition Metal Complexed to a Tridentate Ligand	Christine Nelson

98	Electromagnetic Wave Propagation in a One-Dimensional Random Medium	Julia Rennenkampff
99	Synchronization of the Chlamydomonas reinhardtii cell cycle through light-dark cycling for subsequent testing with infra-red laser light in experiments concerning human night vision	Mary Ritter
100	Application of Nonlinear Filters to VEP Data *** Same Report as Prof. H. Longbotham ***	James Roberts
Wilford Hall Medical Center		
101	Three Selected Areas of Research in Endocrinology and Metabolism	Antoinne Able
102	Utility of Sensitive Immunoradiometric Assay (IRMA) to Predict Results of Thyroliberin Stimulation Test	Stanley Adams
103	Dental Materials	Bobby Larry
104	In Vitro Culture of Human Keratinocytes with Subsequent Induction of Stratification	Aleshia Lewis
105	Autologous Bone Marrow Transplant for Poor Prognosis Lymphomas - A Pilot Dose Escalation Study of a BACE Regimen and Follow-Up	John Salinas
106	Abdominal Abscess Formation in the Mouse Model	Kimberly Smith
107	I. Impact of Diabetes Mellitus on Overall Health and Functional Status: A Comparison of Two Instruments of Measurement. II. A Comparison of the Effects of Alprazolam, Amitriptyline, and Placebo on Reaction Time in Patients with Chronic Low Back Pain	Paul Tanner

1892s

1988 USAF-UES SUMMER FACULTY RESEARCH PROGRAM/

GRADUATE STUDENT RESEARCH PROGRAM

Sponsored by the

AIR FORCE OFFICE OF SCIENTIFIC RESEARCH

Conducted by the

Universal Energy Systems, Inc.

FINAL REPORT

AN EXPERIMENTAL INVESTIGATION OF FRACTAL SURFACES IN TURBULENT DIFFUSION FLAMES

Prepared by:	Jeff Riley
Academic Rank:	Graduate Student
Department and University:	Mechanical Engineering, Cornell University
Research Location:	AFWAL/POSF Wright Patterson AFB Dayton, OH 45433-6563
USAF Researcher:	W.M. Roquemore
Date:	Oct. 10, 1988
Contract No:	F49620-88-C-0053

An Experimental Investigation of Fractal Surfaces in Turbulent Combustion

by

Jeff Riley

ABSTRACT

Turbulent jet diffusion flames were seeded with $TiCl_4$ vapor which reacted with the water of combustion to form micron size TiO_2 particles near the reaction zone. The light scattering ability of the TiO_2 particles is known to decrease rapidly as the temperature of the particles nears 1,100 °K , thus the visual particle seed interface within the flame is expected to roughly follow the 1,100 °K isotherm. This particle seed interface was visualized by pulsing a thin ($\sim$1 mm) laser sheet of short time duration ($\sim$10 ns) through the jet flame, and recording the reflected light on photographic film. The image of the seed interface was then digitized, thus giving a set of (x,y) data points describing the interface. From this data a measure of the roughness or contortion of the surface was obtained by computing the fractal dimension of the surface using a line-segment length approximation algorithim. From the small sample of flame images analyzed (20), the preliminary results showed that the seed interface (approximate isotherm) was indeed fractal, with an average fractal dimension of approximately 2.4 for high Reynolds number turbulent jet diffusion flames.

I. INTRODUCTION

In most pratical combustion applications the burning of hydrocarbon fuels takes place in the turbulent regime, meaning that the combustion process is coupled with an intense fluctuating flow field. Very little is understood about the exact mechanisms that give rise to turbulence, much less how they distort the combustion process. Currently there is much research in the area of turbulent combustion aimed at assesing the effects of the turbulent flow field on the combustion process and vice versa.

One of the main research thrusts of the Aero Propulsion Labs at Wright-Patterson AFB is the experimental investigation of various turbulent combustion configurations. The facilities span the range from small tube burners up to near full-scale jet engine combustor simulations. One of the forms of data availible from the experiments is instantaneous 2-D flow visualization of the combusion region. This is accomplished by seeding the flow with various types of micron size particles and then illuminating the flow area with a thin laser sheet pulse. In this manner some of the flow features occuring within the combusing region can be deduced from the visual seed patterns.

My research deals with trying to model the distortion of the reaction zone in turbulent diffusion flames due to the turbulent velocity fluctuations from the flowfield. One method to view distorted surfaces within the combustion zone is to seed the flow with particles which are known to rapidly lose their light scattering properties at a given temperature, thus revealing an approximately isothermal surface. From the image of this seed interface the fractal dimension of the isothermal surface may be computed, thus giving an indication of how contorted the isotherms have become due to the turbulence. In the case of diffusion flames it is noted that high temperature isotherms may not be "near by" the actual reaction zone since hot product gases are constantly diffusing away from the reaction zone, thus broading the flame sturcture. However, it is still important to characterize the isotherms near the reaction zone as a first step toward understanding the total flame structure.

II. OBJECTIVES OF THE RESEARCH

In turbulent combustion it is recognized that the surface or zone where chemical reactions take place becomes contorted due to interaction with the turbulent flowfield. Just how contorted the surface becomes depends on a number of different parameters: Reynolds number, turbulent intensities, speed of the chemical reactions, combustor geometries, etc... One would like to be able to characterize the degree of contortion of the reaction zone by some quantitative means, rather than just describing it as " rough, squiggly, blob-like, etc...". The fractal dimension of a geometric surface is a quantitative measure of the topological complexity of rough surfaces. For "smooth" surfaces the fractal dimension is 2, as in euclidean geometry, and for "space filling" surfaces the fractal dimension approaches 3, the euclidean dimension for a volume (Mandelbrot, 1983).

My goal for this summer's work as a participant in the 1988 Summer Graduate Student Research Program was originally to experimentally determine the fractal dimension D, for the reaction surface in high Reynolds number turbulent jet diffusion flames under variations in Reynolds number and initial turbulence level (jet exit conditions). After seeing the images obtained from the laser sheet lighting technique using the reacting $TiCl_4$ scheme and discussing the results with researchers at Wright-Patterson, it was decided to try different types of seed particles in order to assess how well the seed interface represented the reaction surface. Although not originally intended, a substantial portion of my time this summer was devoted to the question of whether or not the seed interfaces actually represented anything remotely like the reaction surface. This is a tough question for diffusion flames since diffusion of products causes the flame structure to grow with downstream distance, and unfortunately a definite answer was not found. However, I feel that the time was well spent in that it raised many important questions and prompted ideas that may resolve the issue with future experiments.

III. FRACTAL DIMENSION

a. As previously mentioned, the main thurst of my work this summer was to determine the fractal dimension of the reaction surface occuring in turbulent diffusion flames. The fractal dimension gives a measure of the contortedness of a surface, but it does not to all types of surfaces. In general, fractal geometry is used to describe complex shapes which possess an underling pattern which holds over a large range of length scales. One can imaging viewing a fractal object which has some characteristic geometric pattern. Upon magnification of the object, the same general patterns appear, and after another magnification the patterns still appear, and so on and so on. Thus as one looks deeper and deeper into the structure of a fractal object, more and more detail is seen, yet similar patterns occur at every level of detail. Objects possessing this property are termed <u>self-similar</u>, meaning that they possess the same characteristics at all levels of detail. In the context of this work, the concepts of "fractal" and "geometrically self-similar" behavior will be taken as equivalent. The use of fractals however introduces a quantitative description of the geometry, the fractal dimension D.

As a more concrete example, consider a line in space which is contorted over a wide range of length scales. To cover the length of the line one could inscribe straight line segments of length ε over it (see fig. 1.). The approximate length of the line would be the number of line segments of length epsilon $N(\varepsilon)$, times the length epsilon. As the size of ε is made smaller, the number of segments required to cover the line increases as expected. However, for a fractal object the number of line segments increases as,

$$N(\varepsilon) = C\varepsilon^{-D} \qquad C = \text{constant} \qquad (1)$$

where D is <u>defined</u> as the fractal dimension. Thus the length of the contorted line increases as,

$$L(\varepsilon) = N(\varepsilon)\cdot\varepsilon = C\varepsilon^{1-D} \qquad (1 \le D \le 2) \qquad (2)$$

As seen from this definition, the fractal dimension D describes how <u>rapidly the effective length of the line increases</u> as one uses smaller measurement scales. Thus we now have a <u>quantitative</u> measure of the contortion of an object. That is, if an object is contorted over many length scales then it is intuitive that a

one views the object at smaller scales, previously unseen details appear; but the fractal dimension now gives a measure of how rapidly this happens, which is a measure of the contortion. Also note from the above expressions that for a "smooth" line, the euclidiean dimension is 1, and therefore its length is a constant and does not vary as the measurement scale is varied. For a thorough discussion of fractal geometry see the references (Mandelbrot, 1983) and (Peitgen et al., 1988).

One way to compute the fractal dimension of an arbitrary contorted curve is to use a computer code which actually implements the line segment approximation to the curve. Once a table of length L vs. measurement scale is calculated, the results are plotted on a log-log graph. Taking the log of eqn. 2 we see that the resulting slope from the graph is equal to 1-D, (see fig 2.)

$$\log L = (1-D)\log\varepsilon + \log C \qquad (3)$$

This was the approach taken with the flame photograph data. From the film negatives the seed interface was digitized and the resulting file of sequential (x,y) points was operated on by the algorithim. In this method it is the fractal dimension of the intersection of the contorted seed interface and the laser sheet that is being measured. This intersection is a curve and therefore has a fractal dimension between 1 and 2. What is really desired is the fractal dimension of the actual seed interface surface, which thus has a fractal dimension between 2 and 3. In this analysis it was assumed that the fractal dimension for the surface was equal to the fractal dimension of the curve plus one, based on the analogous relationship in euclidiean geometry.

$$D_{surface} = D_{curve} + 1 \qquad (4)$$

If the fractal surface is isotropic then this result should hold (Sreenivasan, 1986). In the case of jet flames there is symmetry about the jet axis so there is expected to be some slight dependence of the measured fractal dimension on the orientation of the intersecting laser sheet.

IV. EXERIMENTAL METHOD AND RESULTS

a. The experimental set-up used in this study consisted of a Nd-YAG pulsed laser, a vertical burner assembly with various nozzel sizes, and a large format Hasselblad camera which was synched to the laser pulse, (Chen & Roquemore, 1986). The flow was seeded by mixing the fuel with either preformed particles or $TiCl_4$ gas which reacted with the water formed from combustion to form micron sized TiO_2 particles. Since the various seeds rapidly lose their light scattering ability at known temperatures, the seed/no-seed interface is assumed to approximately represent an isotherm, (see fig. 3). The interface is recorded on film by pulsing a thin sheet ($\sim$ 1mm) of short duration ($\sim$ 10ns) laser light through it in synch with the camera shutter. Thus a virtually instantaneous 2-D slice of the seed interface surface is obtained, (see fig. 4). Approximately 500 photos of turbulent jet methane diffusion flames under different flow conditions and seeding arrangements were taken. The original plan to process the seed interface data was to digitize the photos by hand. However, this idea was dropped in favor of writing a computer code to find the interface, thus avoiding the error due to the human subjectivity in determining exactly where the interface was when it tended to get blurry.

In order to implement the computer code, the images from the film negatives were first digitized onto a 575 by 385 pixel array of a photodiode array electronic camera (Photometrics Sys.), by projecting the film image onto the array via a negative enlarger (see fig. 5). This system was devised by personnel at Systems Research Labs and their help was greatly appreciated. Once the image was recorded on the 575 by 385 array, a threshold intensity was set such that all pixels above the threshold intensity were set to white and all those below it were set to black, thus defining the seed interface objectively and removing the ambiguity due to blurry seed regions. At this stage a modified contour level program devised by Larry Goss of SRL was used to retrieve the sequential (x,y) data points describing the thresholded seed interface. This data was then sent to the line segment approximation program that determines the fractal dimension.

Due to problems with using the enlarger to project the film images onto the photodiode array of the electronic camera, the method used to digitize the

images from the film was very tedious and very sensitive to adjustments in the system. This unforeseen problem arose too late to switch over to the hand tracing method, and is the reason that only about 20 images were analyzed. The computer based image analysis method is still felt to be superior to the hand tracing based method since the enlarger system was peculiar to the circumstances (flame images recorded on film as an intermediate step), and could be eliminated from the method in the future. That is, if the flame images were recorded directly by the electronic camera there would be no need for the enlarger system and thus none of the associated problems.

b. The images analyzed in the study were of turbulent methane diffusion jet flames anchored on a 10 mm diameter ASME specification contoured nozzel. The Reynolds number based on the nozzel diameter and cold flow properties at the nozzel ranged from 7,000 to 10,000. The laser sheet was angled at 45 degrees to the jet axis at approximately 75 mm downstream of the nozzel, (see fig. 6). A typical result from the fractal analysis program is shown in figure 7. Note that there is a strong linear correlation in the data, but there is also a significant amount of scatter, especially at the larger length scales. This is directly due to the finite length of the data record. As the length of the measurement scale in the line segment approximation scheme approaches the size of the largest features in the flow (on the order of the nozzel diameter), the approximated curve length increases and decreases as large objects in the flow are "hit and missed" respectively by the line segments. If the data record was very large compared to the largest features in the flow, these fluctuations would average out and the graph would smooth out toward a constant value. The measurement scale at which this happens is called the outer cutoff (ε_o). Since the curves analyzed were closed, it was thought that "walking around" the curves many times and then dividing the calculated length by the number of times the curve was circled would smooth out the graphs and make the outer cutoff visible, but this was not the case. At the small length scales the approximate curve length tends to level off toward a constant value, (see fig.7). This is because the small measurement scales are resolving the smallest features of the flow. The scale at which this happens is termed the inner cutoff (ε_i), signifying the physical limit of fractal behavior due to the smoothing of small scales by molecular diffusion effects. The fractal plot of an idealized physical object would apppear as shown in figure 8.

The results of the analysis are presented in Table 1. The inner cutoff was visible on most of the graphs and was taken as 2.5 mm. The outer cutoff was not readily seen, but was taken as 15.0 mm. The average diameter of the seed image was approximately 50 mm. Using the above cutoffs as the assumed region of fractal behavior, the average fractal dimension of the seed interfaces was 2.40. This result compares well with the results obtained by Sreenivasan for turbulent nonreacting flows (Sreenivasan, 1986), but there is significant room for error in the present results due to the small sample size and the problems encountered with the image enlarger system. With the analysis system in its present state however, flame pictures could be recorded directly with the digital camera and processesed quickly, yielding much better statistics. The error present in the entire system was assessed by analyzing a photo of a geometric construction (Koch curve) of known fractal dimension (D = 1.5). Depending on the values chosen for the inner and outer cutoffs, the computed fractal dimension was between 1.48 and 1.52, representing a total error of $\pm$ 4%. However, for physical objects the inner and outer cutoffs are less well defined, resulting in a larger error.

As mentioned before, a large number of seeded flame pictures were developed this summer. Some of these will be analyzed by the system at Cornell using several different fractal dimension algorithims.

V. INTERPRETATION OF THE SEED IMAGES

a. In turbulent flows the inner cutoff should be of the order of the Kolmogorov scale, and the outer cutoff of the order of the turbulence integral scale, since it is assumed that it is the turbulent flow that causes the distortion of the reaction zone. The fact the inertial subrange of the turbulence cascade process follows a self-similar mechanism as energy passes through the different sized turbulent eddies is the underling reason to expect turbulent interfaces to be self-similar and thus approachable with fractal geometry techniques, (Srennivasan, 1986; Gouldin, 1986). In the case of turbulent flames however, there is a large drop in the turbulent Reynolds number as fluid elements near the hot reaction zone, thus raising the question of

whether or not the reaction zone becomes smoothed out. Although photos of seed interfaces tend to support this, the interpretation of exactly what the seed interface represents is not yet clear since different seeds yielded different flow images.

Various seeds were used for the flow visualization (reacting $TiCl_4$, preformed TiO_2, Al_2O_3, and SnO_2), and all gave different images. The last two seeds retain their light scattering ability to temperatures near the adiabatic flame temperature, so it was thought that they would yield a more accurate picture of the reaction zone. The problem however is that these seeds are preformed refractory based seeds and it is very hard to seed the flow consistently with them. Because of this inconsistency, the interpretation of the refractory seeded flows was not clear. In the future an agitated seeder box design will be tried at Cornell in order obtain seeded flame pictures with the refractory based seeds.

From all the seeding methods used, the seed interfaces showed a general shear layer appearance (see fig. 4.). This is somewhat expected since the mean jet profile contains a strong velocity gradient perpendicular to the jet axis. The shearing effect of this velocity gradient is probably enhanced in the reaction zone since there is a dramatic increase in the dynamic viscosity there, however there could also be dynamical effects from flame induced turbulence which are less well understood.

Since the seed originates from the fuel side of the reaction zone, the seed interface represents fuel rich fluid elements at a temperature of approximately 1,100 °K. The seed is expected to follow the fluid elements' motion since they are around 1 micron in diameter and their Schmitt number is very large (ie., seed particles are dominated by momentum rather than diffusion). The question of whether the seed interface follows the shape of the reaction zone is addressed in figure 9. Since the seed interface approximately follows an isotherm (Vilimpoc et al., 1987), the question is how much change is there in the isothermal contours between 1,100 °K and 2,200 °K. Since the seed interface is rich in fuel and at high temperature, the reaction zone will definitely try to move with it as the interface is contorted by the turbulent shear layer (fig. 9.). The problem is that the diffusion of products out of the

reaction zone makes the flame structure "thick" and thus allows for changes in the shape of the isotherms. For now the shape of the reaction zone is still in question, but it is known that the isotherms in a turbulent diffusion jet flame are contorted, and fractal in nature. This is a first step in the analysis of the turbulent flame structure and may be useful in determining the rates of turbulent diffusion of reactants, oxidizer, and products.

VI. RECOMENDATIONS:

a. At the present time the application of the fractal dimension data to turbulent diffusion flames is not as well developed as for premixed flames (Gouldin, 1986). However the notion of the increase in surface area due to the fractal nature of the surface still applies and can be used to estimate the effective area for the diffusion of chemical species. It may also be able to relate the fractal dimension of different isothermal surfaces to the temperature and concentration gradients occuring in the local flame structure, thus determining the relative importance of the various transport mechanisms.

b. Due to time constraints only about 20 flame images were analyzed this summer. As previously mentioned, the transfer of the images from the film negatives onto the photodiode array by the enlarger was the major cause of difficulty. By recording the flame images directly with the photodiode camera and thus bypassing the enlarger system, the raw data would be much more uniform from image to image, and the analysis time would be greatly reduced. As a follow-up to this summer's work it is suggested that the photodiode camera system be used to evaluate the fractal dimension of the seed interface of turbulent flames under various conditions. Due to the quick processing time of the this system, good statistics could be obtained at each flame condition.

The photodiode system should also be used to assess the difference in seeding techniques. Once an agitated seeder is built that can adequately seed the flow with refractory seeds, the fractal dimension obtained with these seeds should be calculated since their interfaces are expected to lie closer to the reaction zone. Also, if the resolution of 2-D Rayleigh scattering data is deemed

acceptable at high temperatures, fractal dimensions based on this data should be carried out since it would remove the ambiguities associated with the seeding techniques.

Table 1

Data analyzed for fractal character was Roll #2 of B/W film shot on 7/14/88

Frame	D	Re
1	2.454	7,000
4	2.420	8,000
5	2.406	"
6	2.405	"
7	2.480	9,000
8	2.377	"
9	2.347	"
10	2.314	10,000
11	2.432	"

Computer Program Parameters:

ε_i = 2.5mm

ε_o = 15.0mm

50 measurement scales used, from 0.8mm to 30mm, equally spaced.

Size of the seed images was approximately 50mm in diameter

Average Fractal Dimension = 2.402

ACKNOWLEDGMENTS

I wish to thank the Air Force Systems Command and the Air Force Office of Scientific Research for sponsorship of this research. I would also like to thank Universal Energy Systems for putting together the Graduate Student Research Program and for helping make all the admistrative details go smoothly.

Aside from the research, my stay in Ohio this summer was extremely rewarding due to the influences of many different people at Wright-Patterson AFB who went out of their way to help me with the research. Dr. W.M. Roquemore provided much needed guidance for the work and raised many key questions concerning the interpretaion of the seed interface, and his input was greatly appreciated. I also benefied from various discussions with Dr. Lea Chen who was visiting from the University of Iowa. I would also like to thank Dave Peltier and Curtiss Reeves of W-P AFB for their paticence and help with taking endless flame photos and with setting up a digitizing system respectively.

Last, but by no mean least, I would like to thank the people who had to put up with me on a daily basis. Larry Goss, Tzong Chen, Mike Post, Viroj Vilimpoc, and everyone else associated with Systems Research Labs at W-P AFB were exceptionally helpful with the project, and it could have not been done without them. They never hesitated to take time from there own projects to help me with my own. Thanks to them this summer's work was not only rewarding, but also enjoyable on a daily basis.

REFERENCES

Barnard, J. A., and Bradley, J. N., Flame and Combustion, New York, NY, Chapman and Hall Co., 1985.

Chen, L. D., and Roquemore, W. M., "Visualization of Jet Flames," Combustion and Flame, Vol. 66, pp. 81-86, 1986.

Gouldin, F. C., "An Application of Fractals to Modeling Premixed Turbulent Flows," Cornell U. College of Engineering Report E-86-01, 1986.

Hilton, S. M., "Measurements to Determine the Fractal Character of Premixed V-Flames," M.Eng. Report, Cornell U., 1987.

Mandelbrot, B. B., The Fractal Geometry of Nature, New York, NY, W.H. Freeman and Co., 1983.

Peitgen, Heinz-Otto, and Deitmar Saupe, The Science of Fractal Images, New York, NY, Chapman and Hall Co., 1985.

Sreenivasan, K. R., and Meneveau, C., "The Fractal Facets of Turbulence," Journal of Fluid Mechanics, Vol. 173, pp. 357-386, 1986.

Vilimpoc, V., Goss, L. P., Lynn, W. F., and Sarka, B., "Simultaneous Thin-Filament Pyrometry and Reactive Mie Scattering Measurements on a H Jet Diffusion Flame," In-house Systems Research Labs publication, Dayton, OH, 1986.

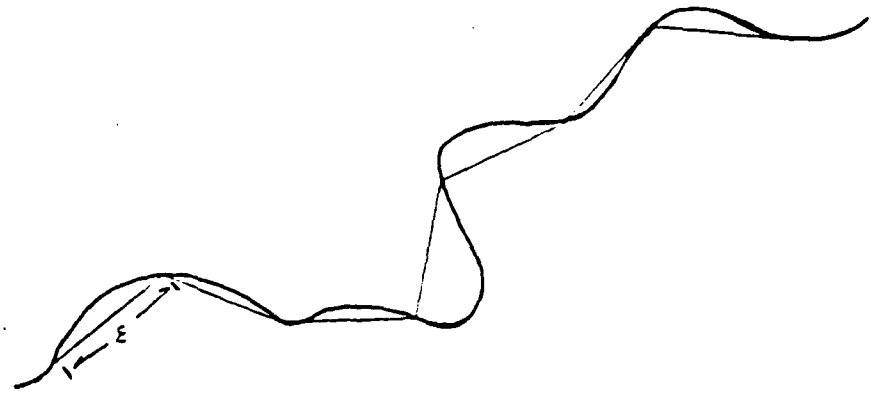

Line-Segment Approximation to a Contorted Curve
(Figure 1.)

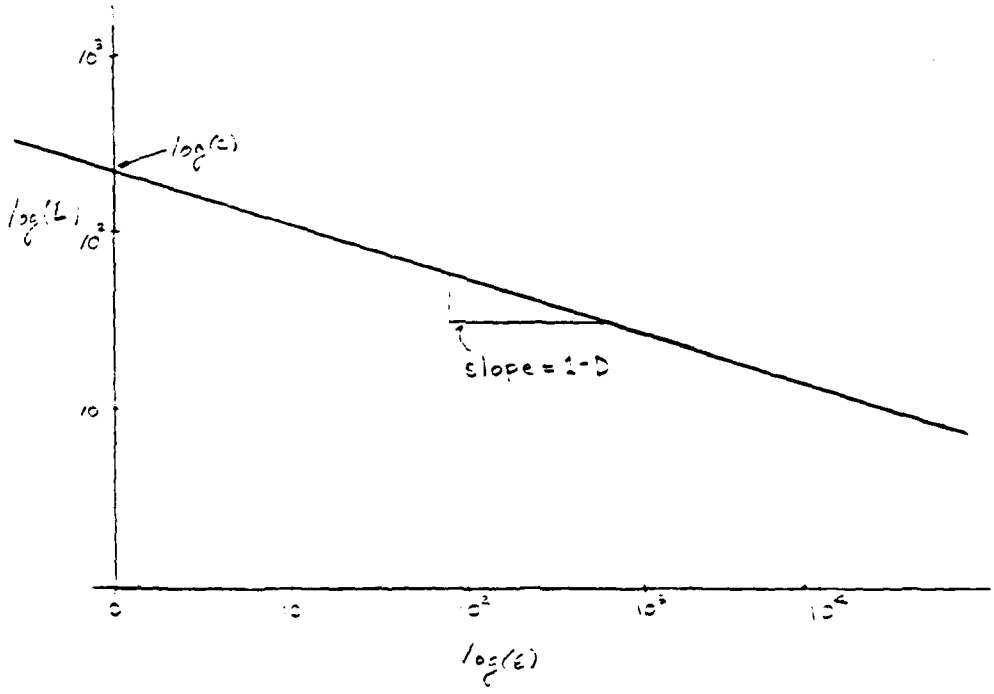

Variation of the measured length of a Fractal curve with the measurement scale used. (note log-log scaling)
(Figure 2.)

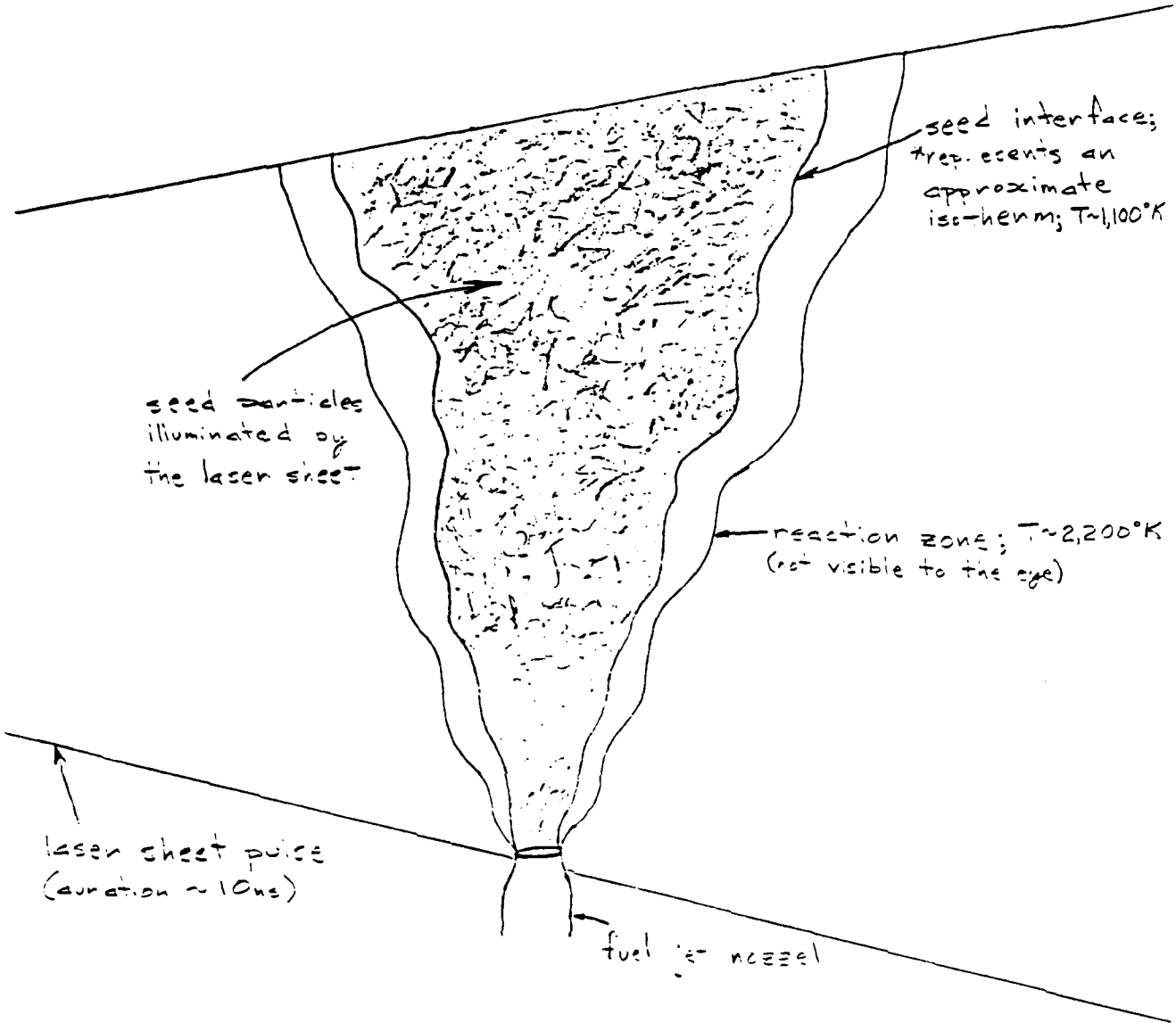

Illumination Technique for Viewing Flame Structure

(Figure 3.)

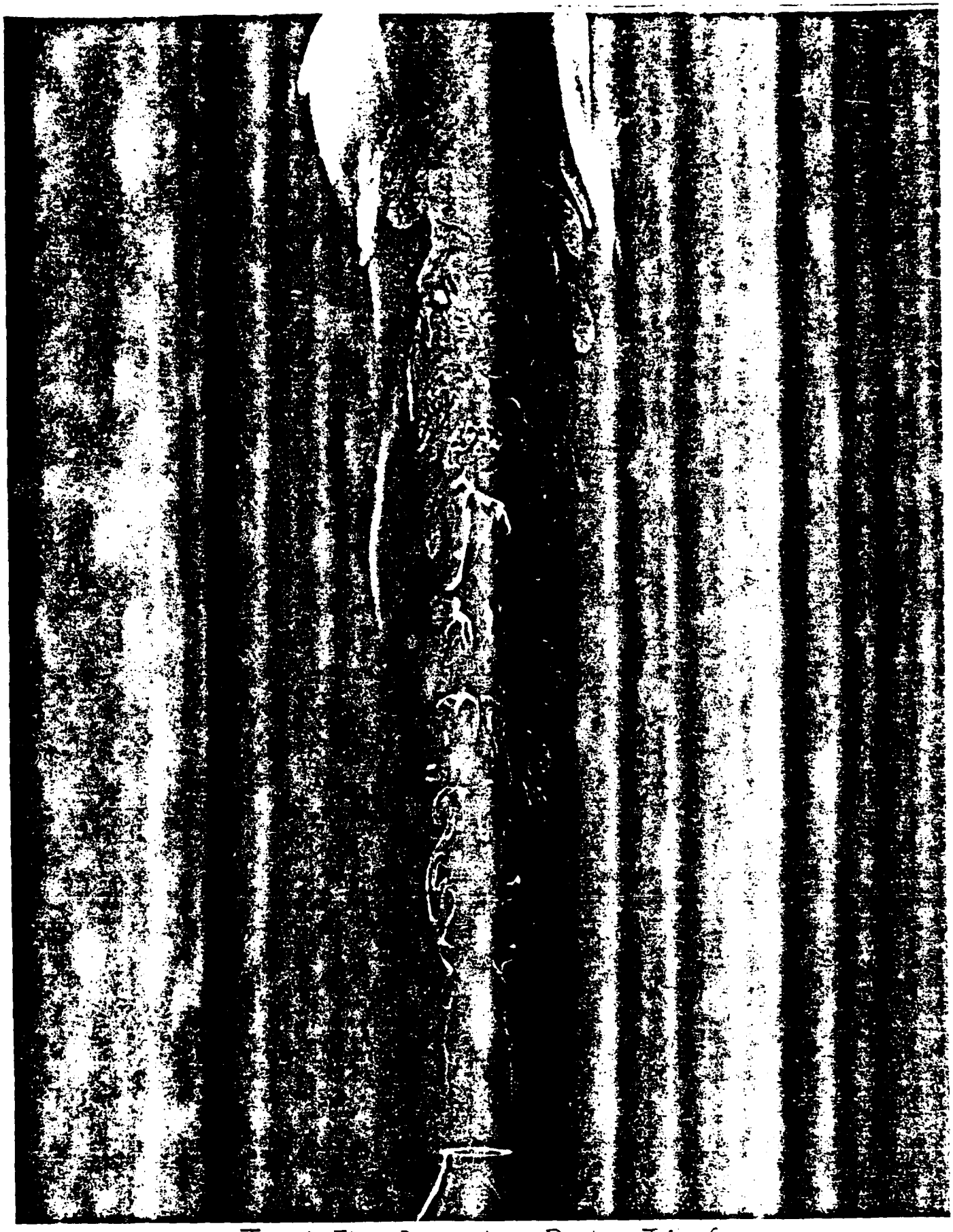

Typical Flow Image Using Reacting Tilia Seed
(Figure 4.)

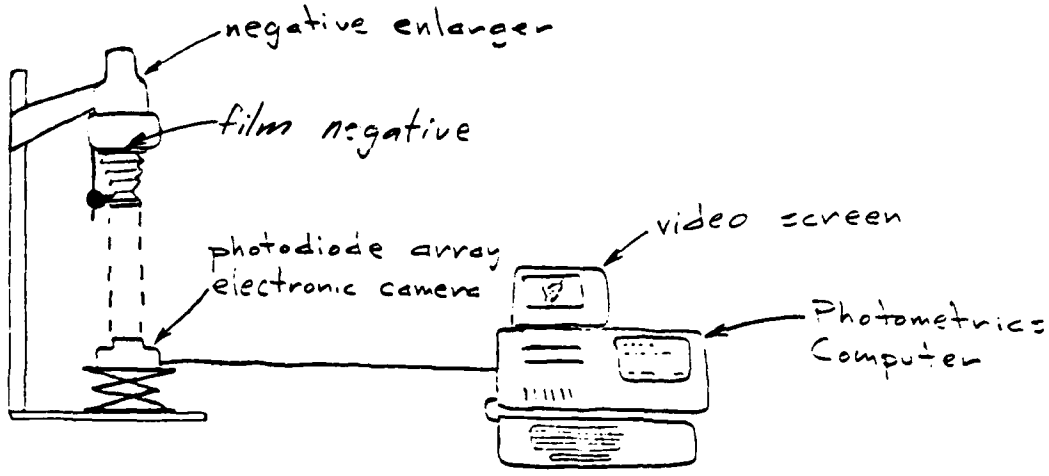

Enlarger Set-Up
(Figure 5.)

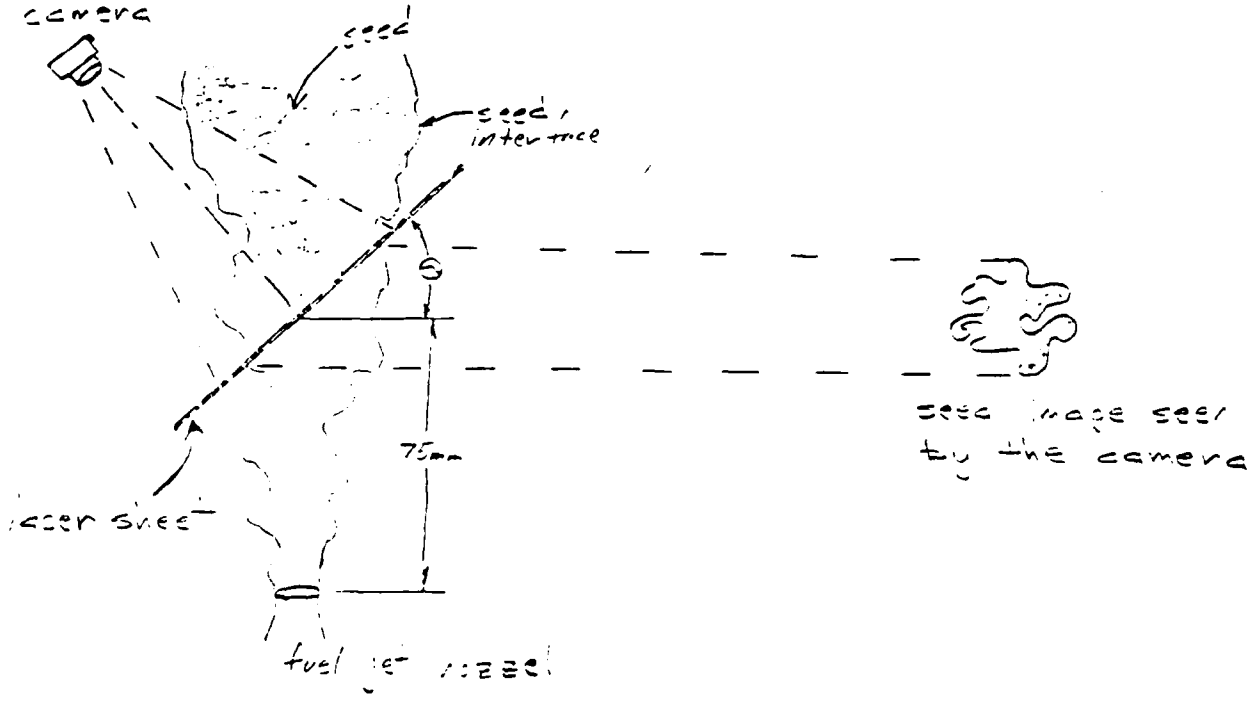

Orientation of Seed Images Analyzed
(Figure 6.)

LEN= length of seed interface in mm
EPS = measurement scale size in mm

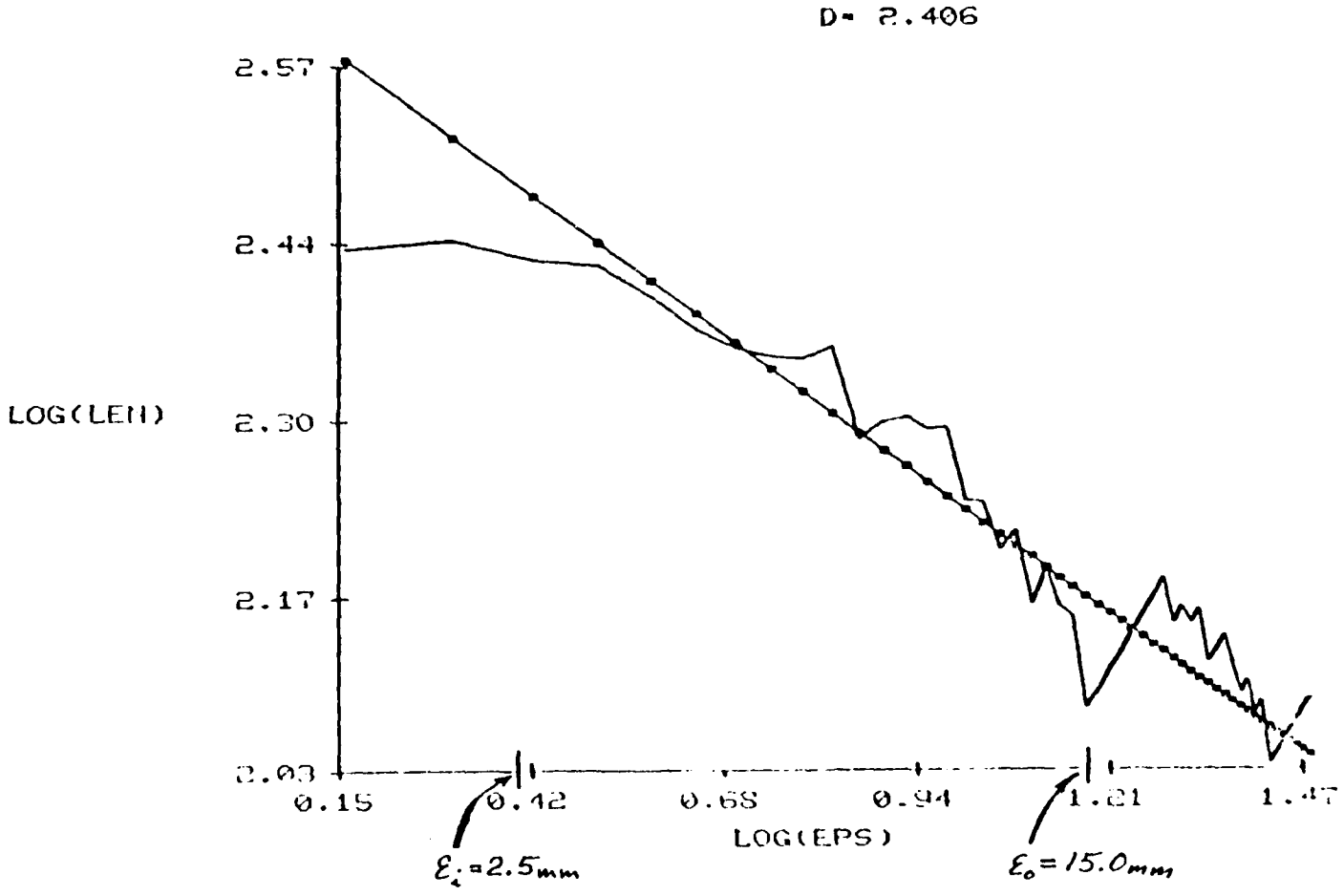

Typical Output from the Fractal Analysis Program
(Figure 7.)

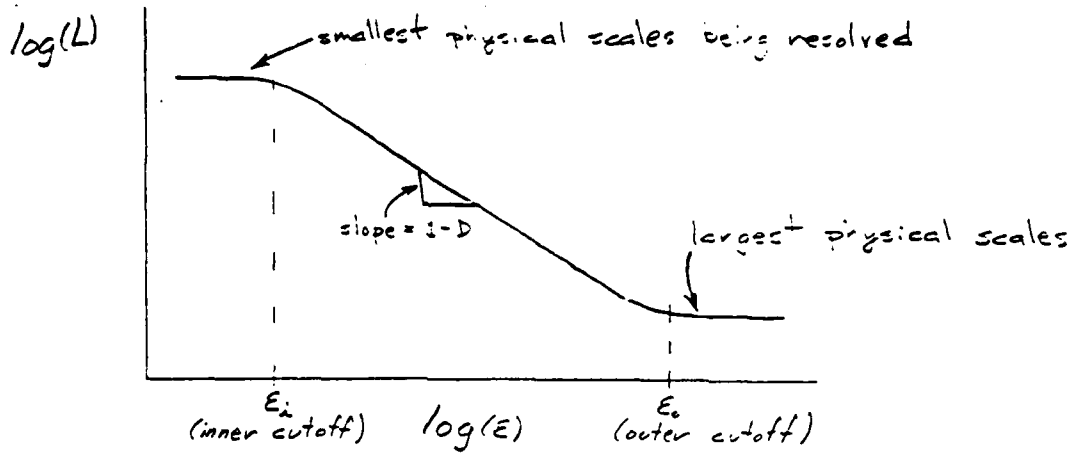

Fractal Behavior of an Idealized Physical Object

(Figure 8.)

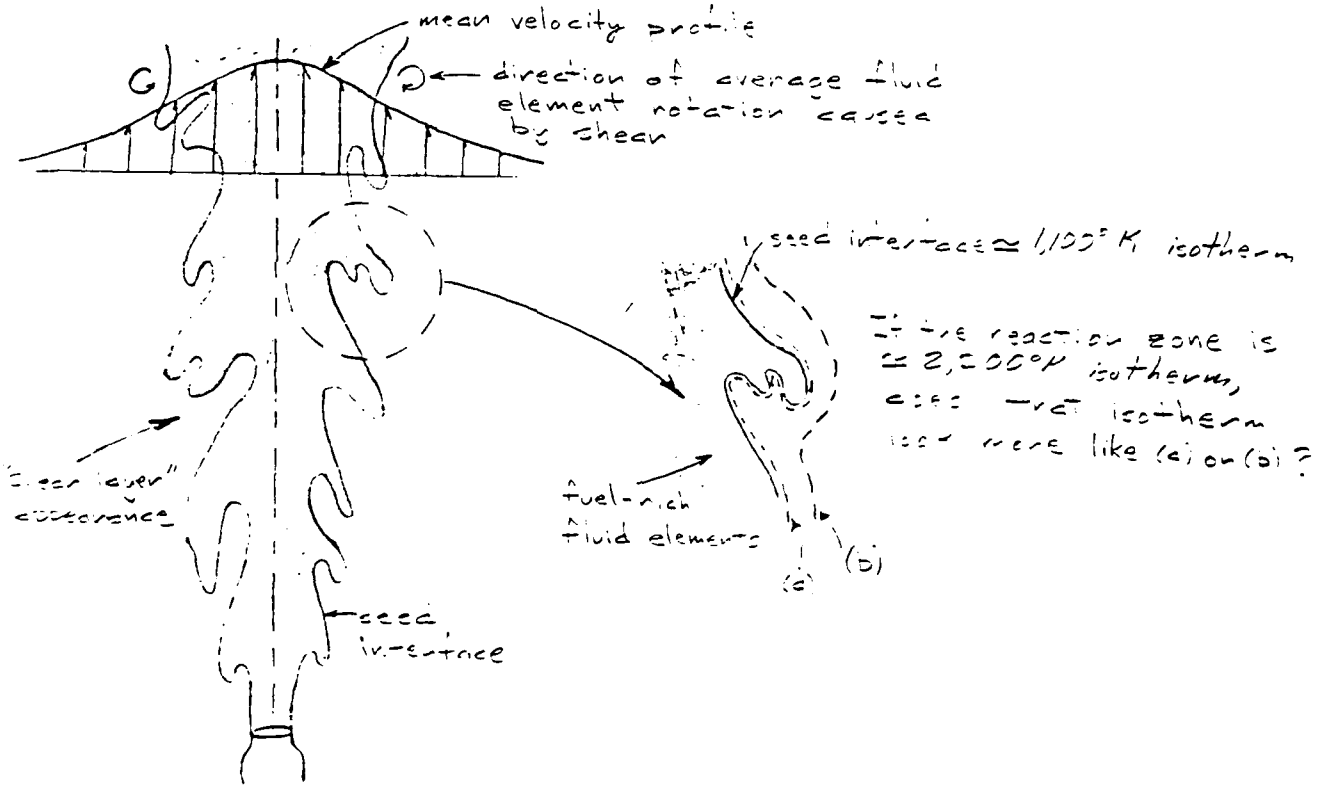

Flow Visualization Interpretation

(Figure 9.)

APPENDIX MAY BE OBTAINED FROM

UNIVERSAL ENERGY SYSTEMS, INC.

OR FROM THE AUTHOR

1988 USAF-UES SUMMER FACULTY RESEARCH PROGRAM/

GRADUATE STUDENT RESEARCH PROGRAM

Sponsored by the

AIR FORCE OFFICE OF SCIENTIFIC RESEARCH

Conducted by the

Universal Energy Systems, Inc.

FINAL REPORT

Thermionic Emission vs Drift-Diffusion and the Placement of the Spike Layer for the BICFET

Prepared by:	John Bambery
Academic Rank:	Graduate Student
Department and	Physics Department
University:	Indiana University of Pennsylvania
Research Location:	WPAFB, Avionics, Electronics Technology Division, Electronics Research Branch, Device Research Group
USAF Researcher:	Dennis Whitson and Gary McCoy
Date:	September 26, 1988
Contract No:	F49620-88-C-0053

Thermionic Emission vs Drift-Diffusion and the Placement of the Spike Layer for the BICFET

by

John Bambery

ABSTRACT

The analytical program for the BICFET was rewritten in such a way as to allow one to easily change the material system being used and to be able to implement new equations without a significant rewrite of the program. New options were also included in the program.

It was found that the inclusion of all three valleys in AlGaAs was necessary to correctly treat parameters such as the density of states effective mass when the value of the Al mole fraction, x was around 0.45.

In order to correctly calculate the electron and hole mobilities it is necessary to bring in their dependence on the electric field, the impurity concentration and the Al mole fraction. These changes affected the drift-diffusion velocity and therefore the gain and the current values.

The placement of the spike layer in either the semiconductor or the semi-insulator had a decided impact on the gain and behavior of the device, especially at high values of x.

At large values of x the drift-diffusion velocity was dominant and had a profound effect on the gain and the functioning of the device.

ACKNOWLEDGMENTS

I would like to thank the Air Force Systems Command and the Air Force Office of Scientific Research for sponsorship of my research effort. The Avionics Laboratory of Wright Patterson Air Force Base has an environment quite conducive to scientific research. I would also like to thank the AADR group and Gary McCoy for the support and encouragement which made the summer both productive and enjoyable.

Special thanks go to Ben Carroll for his help in using the computer system and his exemplary patience in answering all my questions about the VAX machines.

In addition, acknowledgement should go to Dr. Dennis Whitson whose guidance was an essential part of the project.

I. INTRODUCTION

The tasks for which I took responsibility during the summer research program were largely oriented toward computer programming. A basic understanding of many programming concepts was derived from two computer classes in Fortran and Basic. My current level of understanding of the necessary Fortran concepts can largely be attributed to an independent study project concerning the determination of an average index of refraction for HgCdTe samples. This study was under the direction of Dr. Larry Freeman at Indiana University of Pennsylvania (IUP).

My knowledge of the computer program to model the BICFET and my direction throughout the summer research program came from Dr. Dennis Whitson. The theoretical work and any conceptual difficulties were dealt with by him. Dr. Whitson is on leave from IUP under the auspices of the AFOSR Resident Research Program. He first came to Wright-Patterson Air Force Base (WPAFB) in the summer of 1986 under the Faculty component of the summer program administrated by UES. He is carrying on a research program at WPAFB to model Heterojunction devices such as the BICFET and resonant tunneling diodes. The modeling includes both an analytical approach such as reported here and finite difference numerical modeling.

I will continue to develop this computer model of the BICFET at IUP since I will be doing my M.S. research under Dr. Whitson's guidance.

II. OBJECTIVES OF THE RESEARCH EFFORT

The objective of the summer research effort was to rewrite the analytical programs modeling the bipolar inversion channel field effect

transistor (BICFET). The aim was to include some new options in the analysis and to write the program in such a way as to allow one to easily change the material system being used (GaAs/AlGaAs in this case) and to be able to implement new equations without a significant rewrite of the program.

The new options include:

1) Effects of using all three valleys instead of the one valley approximation;
2) Effects on the electron and hole mobilities in the semi-insulator due to the: (a) electric field, (b) impurity concentration and (c) Al mole concentration,x;
3) Effects of placing the spike layer in either the semi-insulator or the semiconductor;
4) Thermionic emission vs drift-diffusion;
5) PNP BICFET vs NPN BICFET.

III. MATERIAL PARAMETERS

All the material dependent parameters have been calculated in a sub-program callled GAASPAR so that only this sub-program needs to be changed when it is desired to try a new material with the BICFET equations.

The energy gaps of the three valleys of AlGaAs vary with the Al mole fraction (1). For GaAs the existence of the upper two valleys (X and L) can be largely ignored for many applications, however in general for AlGaAs this is not the case. In thermal equilibrium the electron population of each of the valleys varies with the value of x (the Al mole fraction) due not only to the change in energy gap but also the

change (Eq. 1) in the effective mass (2) where m^*_Γ, m^*_X, and m^*_L are

$$m^*_\Gamma = 0.067 + 0.083X$$
$$m^*_X = 0.85 - 0.14X \qquad m^*_L = 0.56 + 0.1X \tag{1}$$

respectively the density of states effective masses for the Γ, X, and L valleys. The total electron population, n_o, is found by adding the populations of the Γ valley, n_Γ, the X valley, n_X, and the L valley, n_L, (Eq. 2) where $N_C = 2(2\pi m^*_n k_B T/h^2)^{3/2}$, E_c is the conduction band

$$n_o = n_\Gamma + n_X + n_L = N_C \exp[(E_F - E_c)/k_B T] \tag{2}$$

edge of the lowest valley and m^*_n is the density of states effective mass for all the electrons. The population in each valley is determined (3) by the position of its conduction band edge with respect to the Fermi level, E_F, and the effective density of states (which in turn is determined by the density of states effective mass). Eq.3 gives the

$$n_\Gamma = 2(2\pi m^*_\Gamma k_B T/h^2)^{3/2} \exp[(E_F - E_c + E_{G1} - E^\Gamma_G)/k_B T] \tag{3}$$

density for the Γ valley (there are equivalent expressions for the other two valleys) where E_{G1} is the smallest energy gap of the three valleys and is given in Eq. 4. It is seen from Eq.'s 2, 3 and 4 that a

$$E_{G1} = E^\Gamma_G \qquad 0 \le X \le 0.45$$
$$E_{G1} = E^X_G \qquad 0.45 \le X \le 1 \tag{4}$$

reasonable definition for a density of states effective mass for the 3-valley system would be:

$$m^{*3/2}_n = m^{*3/2}_\Gamma e^{(E_{G1} - E^\Gamma_G)/kT} + m^{*3/2}_X e^{(E_{G1} - E^X_G)/kT} + m^{*3/2}_L e^{(E_{G1} - E^L_G)/kT} \tag{5}$$

The fraction of electrons in each valley as a function of x is shown in Fig. 1; while the density of states effective mass as a function of x is seen in Fig. 2. The one valley approximation assumes that for x < 0.45 the Γ valley determines all the material properties and for x > 0.45 the X valley does. From these figures it is seen at

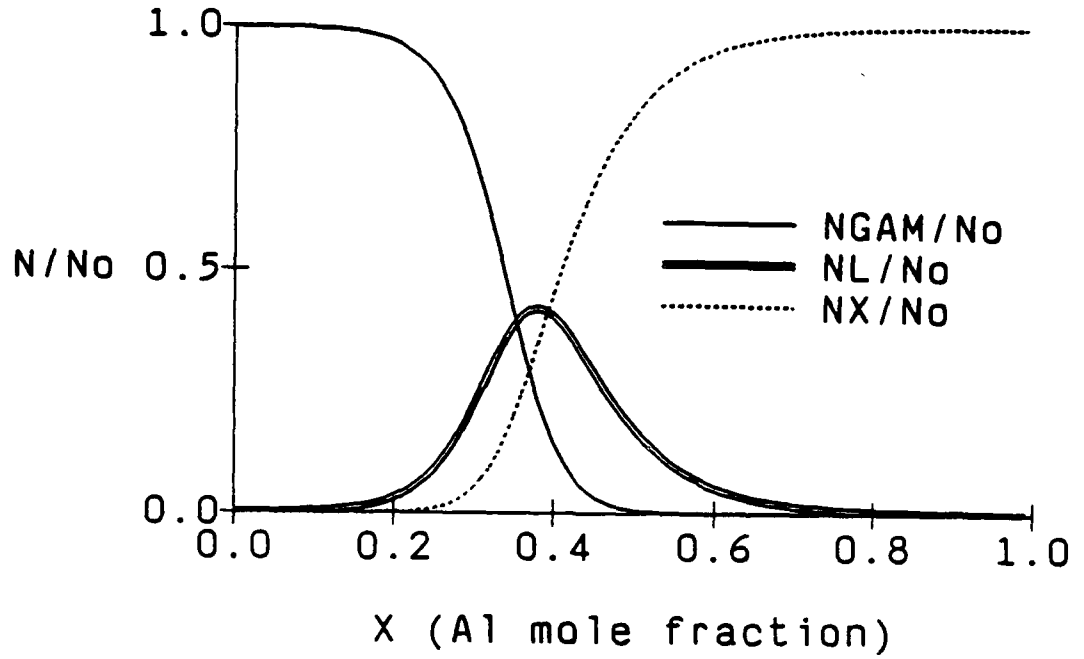

Fig. 1 Fraction of the electrons in each of the valleys. No, NGAM, NL, and NX are respectively the density of all the electrons, the electrons in the Gamma valley, the L valley and the X valley.

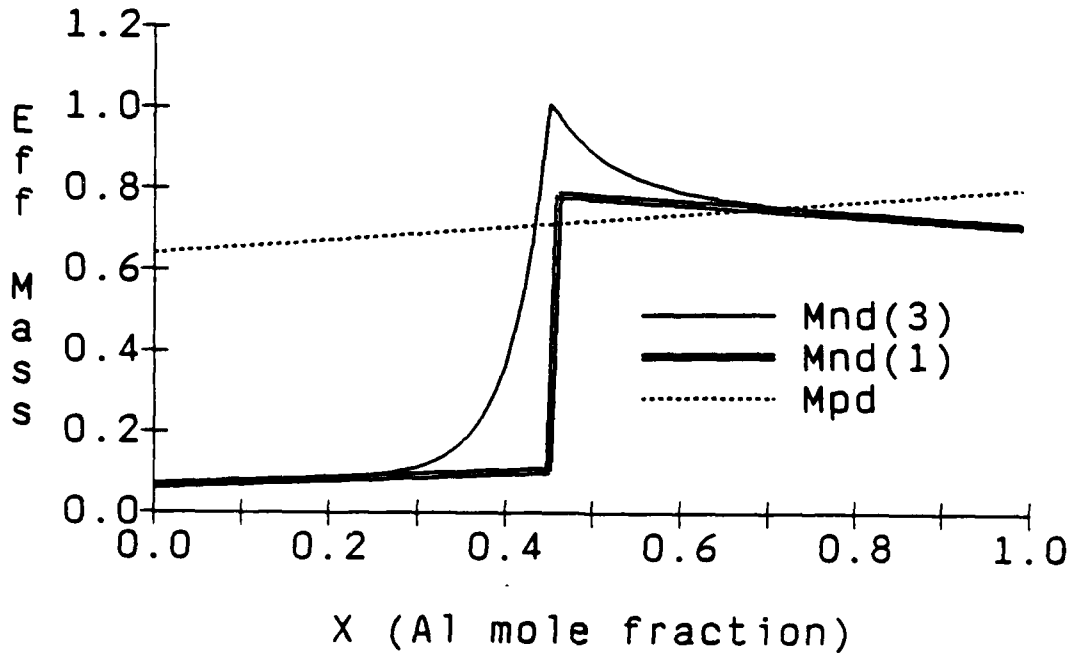

Fig. 2 Effective masses vs the Al mole fraction, x. Mnd(3), Mnd(1) and Mpd are respectively the effective mass for electrons considering all 3 valleys, electrons assuming one valley dominates and holes.

once that neglecting the L valley and assuming the one valley approximation can cause considerable error when x is around 0.45.

For the case of the holes a similar approach can be used to define a density of states effective mass. From noting that the two valence band edges are coincident we can define the hole density of states effective mass as given in Eq. 6 where m_h^* is the heavy hole density of

$$m_p^{*3/2} = m_h^{*3/2} + m_l^{*3/2} \qquad (6)$$

states effective mass and m_l^* is the light hole density of states effective mass. These masses are also a function of x as given in Eq. 7. Because the heavy holes are much larger than the light holes they dominate the hole properties.

$$m_h^* = 0.62 + 0.14x \;\; ; \;\; m_l^* = 0.087 + 0.063x \qquad (7)$$

Some of the important transport parameters that are affected by the size of the effective mass include the thermal velocities, the effective densities of states and the mobilities. The equation for the thermal velocity is given in Eq. 8 and its dependence on x due to the changing effective mass is shown in Fig. 3. While the hole thermal velocity

$$v_t = (K_B T / 2 m^* \pi)^{1/2} \qquad (8)$$

doesn't change very much, the electron thermal velocity changes significantly with the value of x.

The electron mobilities not only have a strong x dependence (Fig.s 4 and 5) but also depend strongly on impurity concentration (Fig.4) and electric field (Fig.5). The hole mobilities are smaller but have similar dependencies. The equations for these dependencies are taken mainly from Schuelke (1) and Shur(3). Since the dopant level in the semi-insulator is on the order of E17 and the electric field in the semi-insulator can be as large as 100 kV/cm it is seen from these Fig.'s that these effects

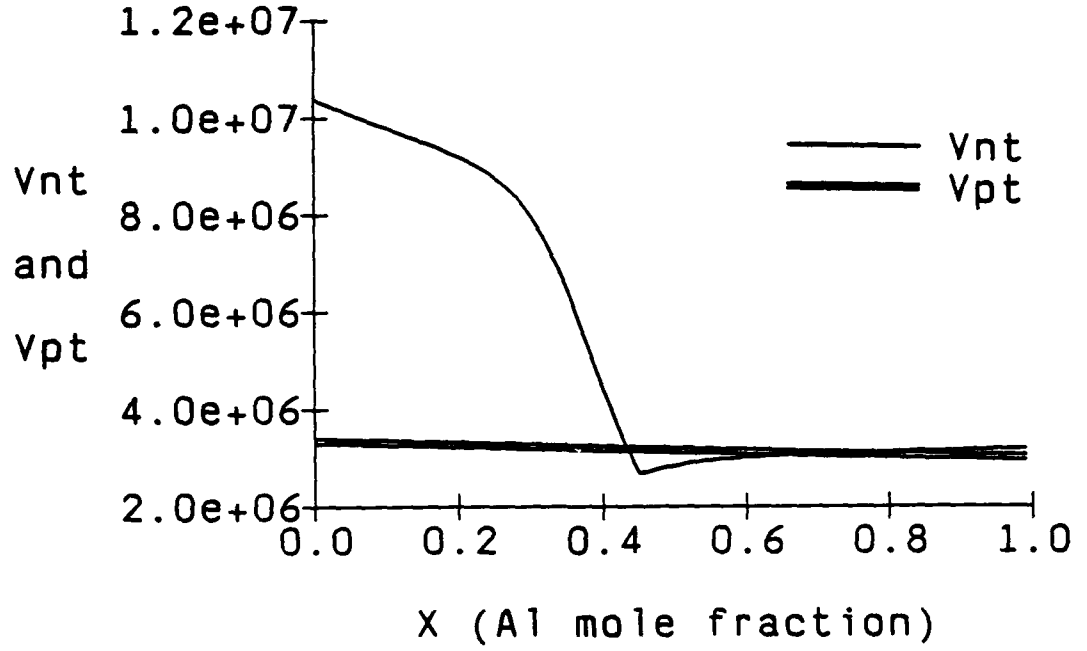

Fig. 3: Thermal velocities vs the Al mole fraction, x. Vnt (Vpt) is the thermal velocity for electrons (holes) in AlGaAs.

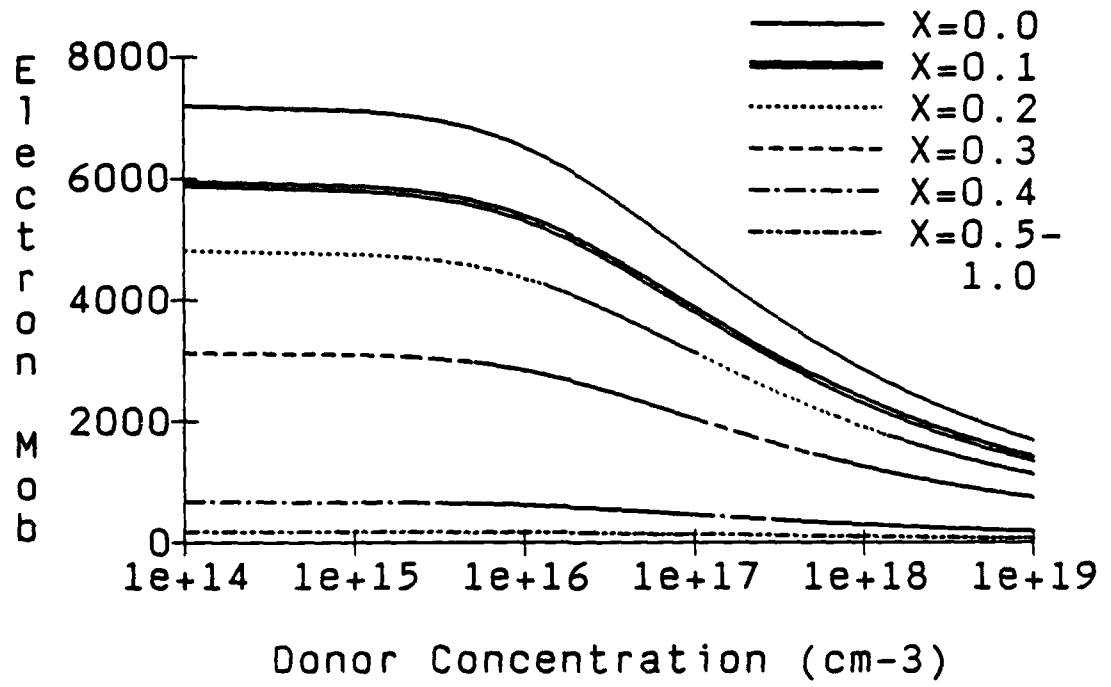

Fig. 4: Electron mobility vs donor concentration with the Al mole fraction, x as a parameter and the electric field equal to 1.0 KV/cm.

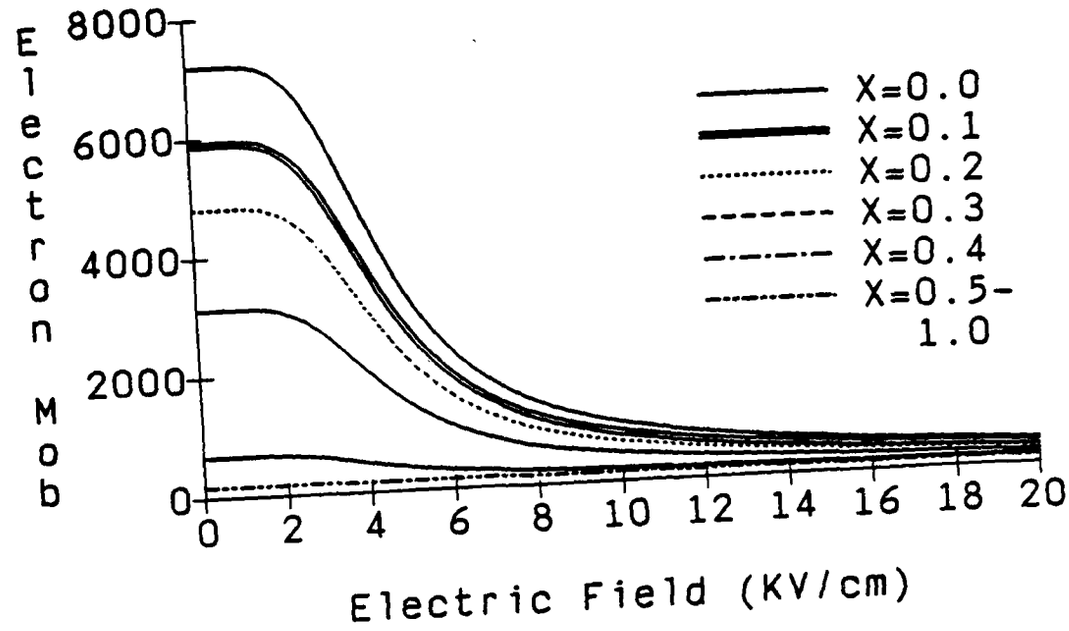

Fig. 5: Electron mobility vs electric field with the Al mole fraction, x as a parameter.

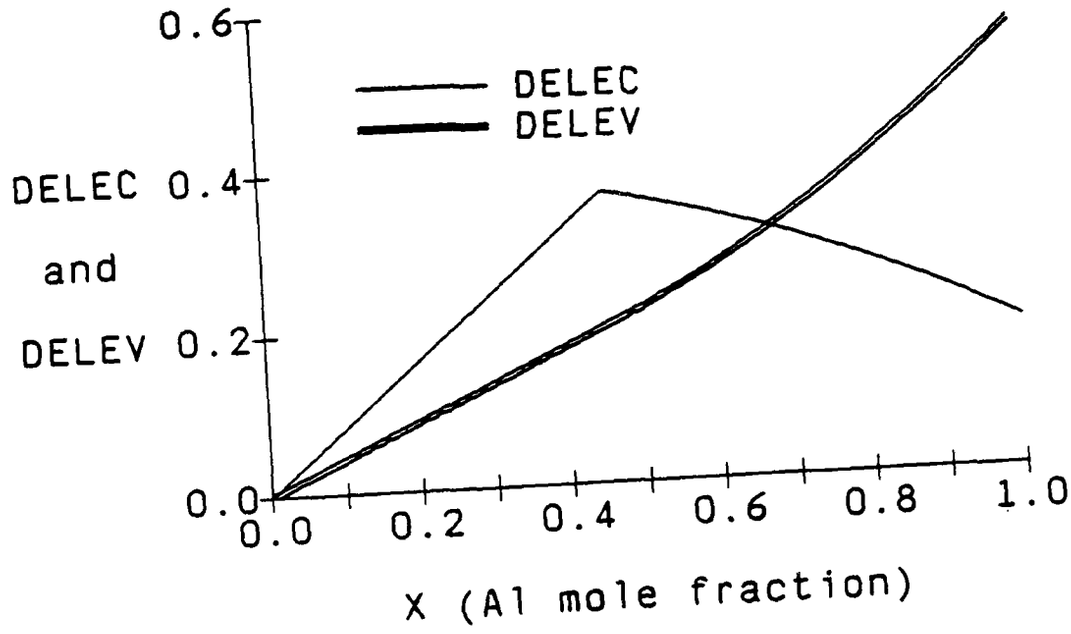

Fig. 6: Conduction band discontinuity (DELEC) and valence band discontinuity (DELEV) vs the Al mole fraction, x.

can not be ignored as was done in previous analytical models (4,5,6).

The gain of the BICFET depends exponentially on the band discontinuity (ΔE_V for the NPN and ΔE_C for the PNP) which depends strongly (see Fig. 6) on the Al mole fraction (7). It is assumed that $\Delta E_V = 0.35\,\Delta E_G^{\Gamma}$ (where ΔE_G^{Γ} is the total band discontinuity for the Γ valleys) and that $\Delta E_C = \Delta E_G - \Delta E_V$ where ΔE_G is the total band discontinuity when the band gap is taken from the valence band to the lowest conduction band valley (X-valley for $x > 0.45$).

IV SPIKE LAYER IN SEMI-INSULATOR OR SEMICONDUCTOR

The placement of the spike layer in either the semiconductor (case 1) or the semi-insulator (case 2) affects the gain and the operation of the BICFET. In Fig. 7 it is seen that for case 1 there are two effects that are important: (1) the mobile holes do not stay in just the lightly doped region of the semiconductor but also move into the heavily doped spike layer and (2) the fraction of acceptors in the spike layer that are ionized will change as the band diagram is altered by a variety of changing conditions. These two effects change the charge balance in Eq. 9 by increasing the positive charge and reducing the negative charge in

$$Q_e = qN_A/\left(1+g\,e^{[\beta(\epsilon_p-\Delta E_i)]}\right) - qd_1N_{d2} - qd_2p_o - \left(2q\epsilon_2/\beta\right)^{\frac{1}{2}}\left[p_o+\beta\phi_s N_{d4}\right]^{1/2} \qquad (9)$$

the spike layer. The amount of emitter charge, Q_e , is determined by the difference between the negative charge in the spike layer (first term on right) and the positive charge in the semi-insulator (qd_1N_{d2}), the spike layer (qd_2p_o) and the semiconductor (fourth term) where N_A is the acceptor density; d_1 is the thickness and N_{d2} is the donor density

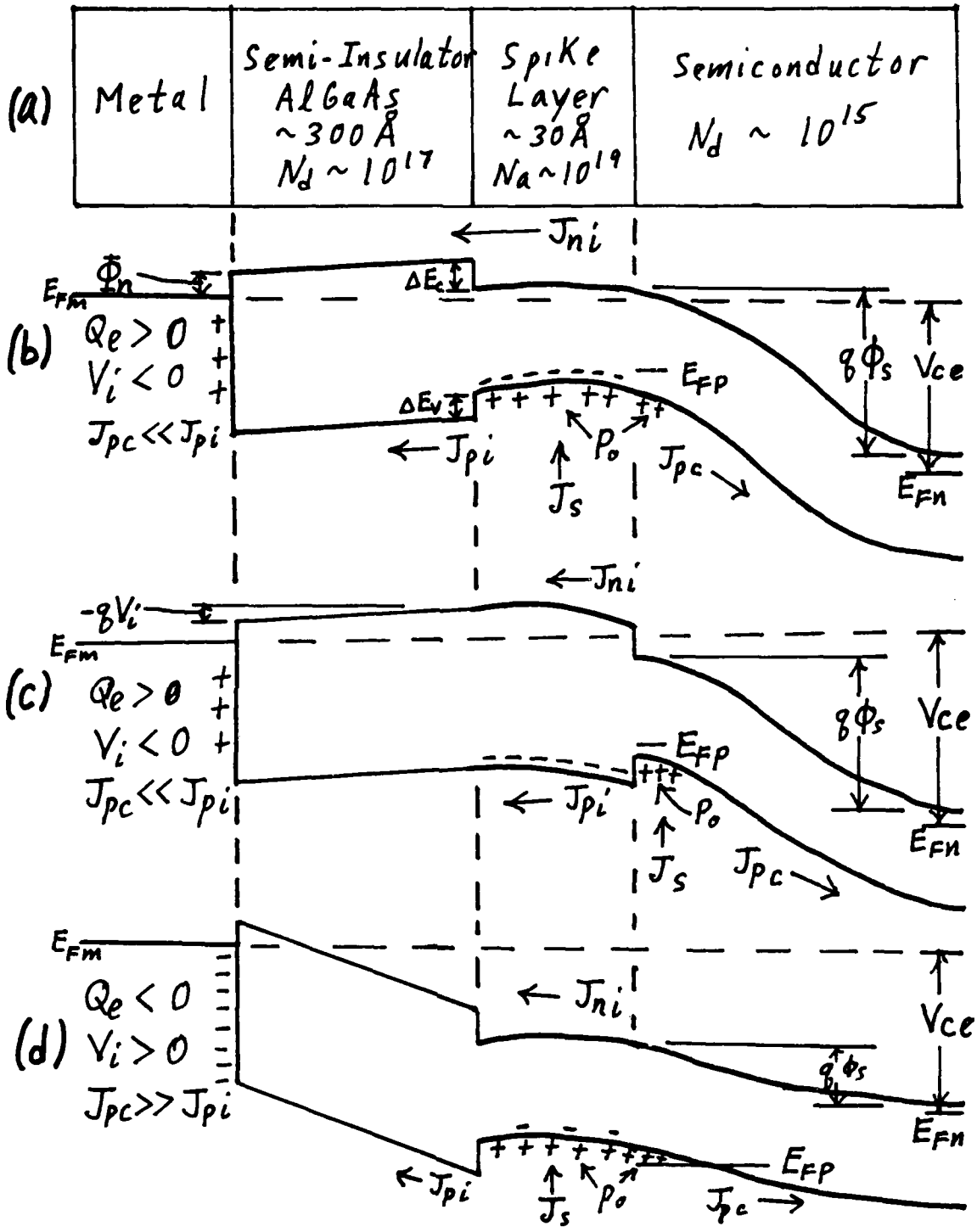

Fig. 7: (a) Structure of the BICFET; (b) Band diagram when the spike layer is in the semiconductor; (c) Band diagram when the spike layer is in the semi-insulator; (d) Band diagram when Qe < 0.0.

of the semi-insulator; d_1 is the thickness and p_o is the hole concentration in the spike layer and the inversion layer.

The high frequency properties of the BICFET should improve with an increase in p_o since this would decrease the channel resistance. At the same time one would like to be able to increase the current gain. However, as can be seen in Fig. 8 and Eq. 10 the gain varies inversely

$$G = \frac{V_n}{V_p} \frac{N_c}{p_o} e^{(\Delta E_v - \Phi_n)/kT} \qquad (10)$$

with p_o . In Fig. 8 it is also seen that the gain decreases with an increase in N_A and is less for case 2 than case 1. For case 1 the holes actually in the spike layer have a mobility that is reduced quite substantially by impurity scattering, however the number of holes and their distribution in the lightly doped semiconductor will be the same for both cases. Therefore, for a given p_o the resistance of the channel will be approximately the same for both cases. For case 1 there will be a lower resistance channel (the lightly doped semiconductor) in parallel with a higher resistance channel (the spike layer itself) and thus a slightly lower resistance than for case 2.

The design of a BICFET might proceed in the following manner. First, p_o is chosen to give a required conductivity in the channel and then the acceptor density is found (Fig. 8). Next the Al mole fraction, x, is calculated or picked from a graph to give the required gain. For example, let us take p_o = E19. For case 1 this would require N_A = 1.1E14 cm-2 (3.7E20 cm-3 for 30 Angstroms) while for case 2, N_A = 2.9E12 cm-2 (9.7E18cm-3 for 30 Angstroms). For case 1 this concentration (3.7E20 cm-3) is probably too large (unless one wanted to increase the spike layer width substantially) and in this instance the spike layer should probably go in the semi-insulator. Growth

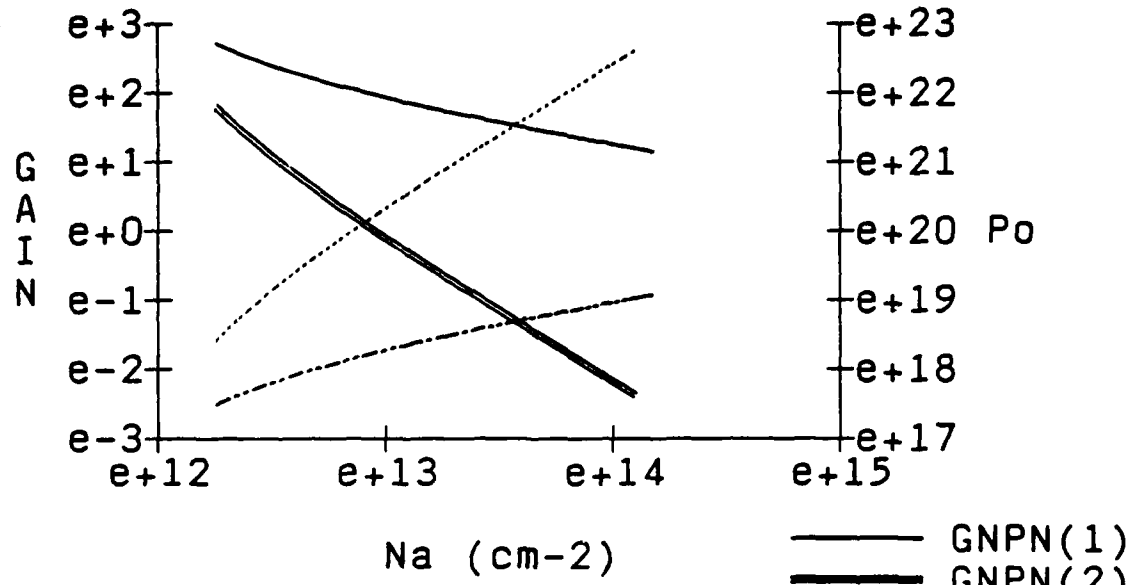

Fig. 8: Current gain, GNPN, and inversion charge density, Po, vs spike layer density, Na. The symbol (1), (2) indicates that the spike layer is in the semiconductor, semi-insulator. Vce = 2.0, Js = 0.01 and x = 0.3.

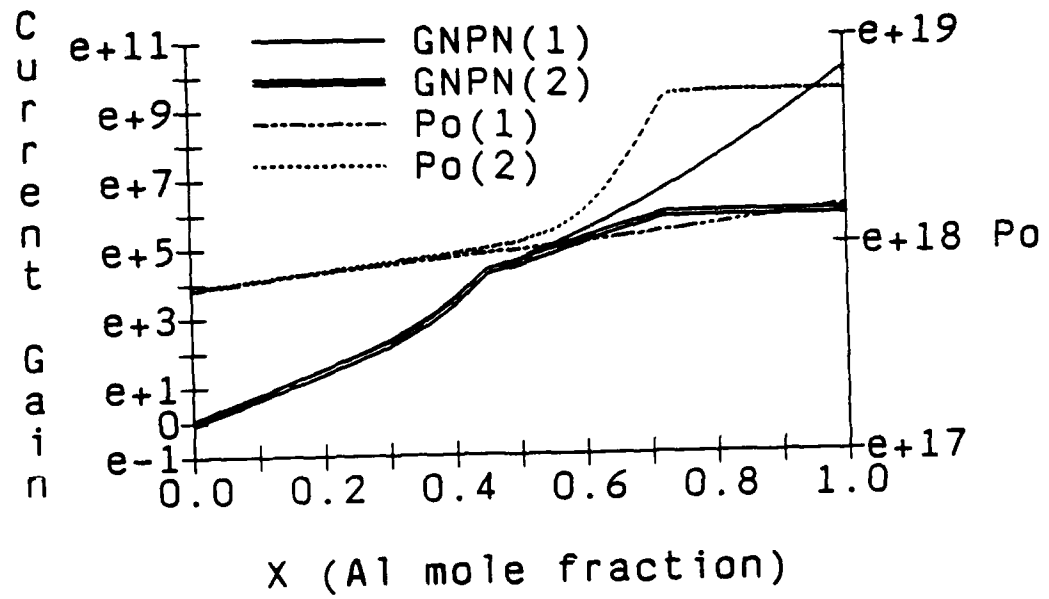

Fig. 9: Current gain (Jni/Js), GNPN, and inversion charge density, Po, as a function of the Al mole fraction, x. The symbol (1) indicates that the effective velocity is calculated using only the thermal velocity while (2) indicates that both the thermal velocity and the drift-diffusion velocities were used. The spike layer is in the semiconductor, Vce = 2.0 and Js = 75.

capabilities need to be considered when deciding on where to place the spike layer.

V THERMIONIC EMISSION VS DRIFT-DIFFUSION

In their paper (4) Taylor and Simmons asserted that the drift diffusion component of the effective velocity was negligible compared to the thermionic emission component. This turns out to be true for x values around 0.3 which they were concerned with, but for higher values of x, the drift diffusion component becomes dominant.

Using the drift diffusion equation one can show that

$$J_{ni} = q V_n N_c e^{(qV_i - \Phi_n)/kT} \tag{11}$$

$$J_{pi} = q V_p p_o e^{(qV_i - \Delta E_v)/kT} \tag{12}$$

$$1/V_n = \frac{1}{V_{nt}} + \frac{1}{V_{nd}} \; ; \; \frac{1}{V_p} = \frac{1}{V_{pt}} + \frac{1}{V_{pd}} \tag{13}$$

$$V_{nd} = \frac{D_n}{d_1}\left(-\frac{qV_i}{kT}\right)\frac{1}{1 - e^{qV_i/kT}} \tag{14}$$

where Jni (Jpi) is the electron (hole) current density, v_n (v_p) is the effective electron (hole) velocity, v_{nt} (v_{pt}) is the electron (hole) thermal velocity, v_{nd} (v_{pd}) is the electron (hole) drift-diffusion velocity, and D_n (D_p) is the electron (hole) diffusion coefficient in the semi-insulator. The equation for v_{pd} is the same as Eq. 14 with D_n replaced by D_p. The variables V_i, Φ_n and ΔE_v are defined in Fig. 7.

In Fig. 9 we see that when the drift diffusion velocity is taken into consideration the gain flattens out at higher x values, while it continues to go up when one considers only the thermal velocity. The controlling velocity is the smaller of the two and in Fig. 10 it is seen that the point at which v_{nd} takes control depends on both the x value and the input current. When v_{nd} controls the behavior of the device a

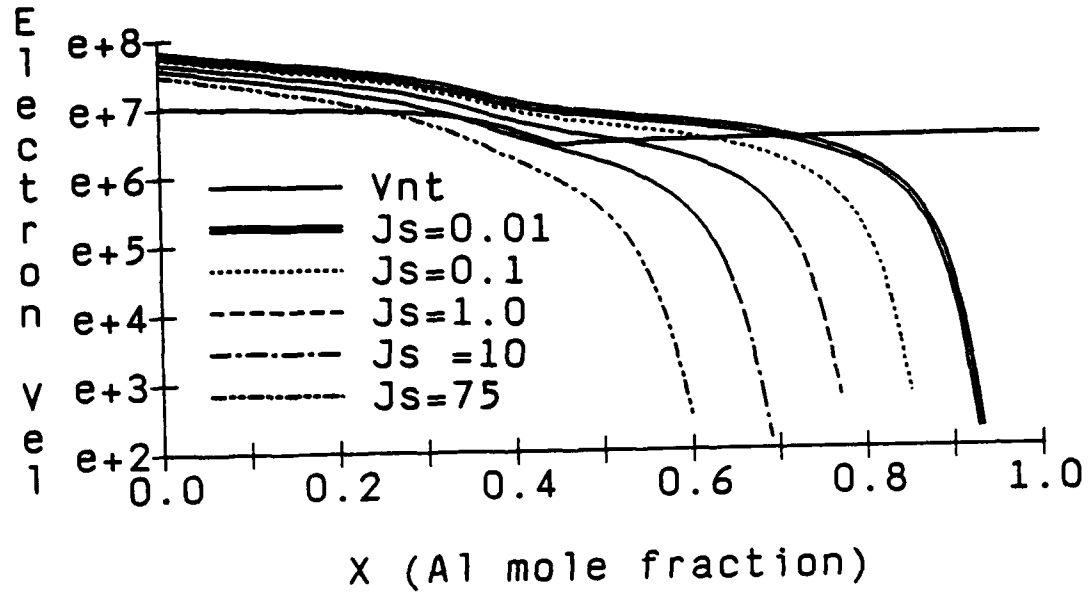

Fig. 10: Electron drift-diffusion velocity, Vnd, vs the Al mole fraction, x with the source current, Js as a parameter and electron thermal velocity, Vnt, vs x. The spike layer is in the semiconductor and Vce = 2.0.

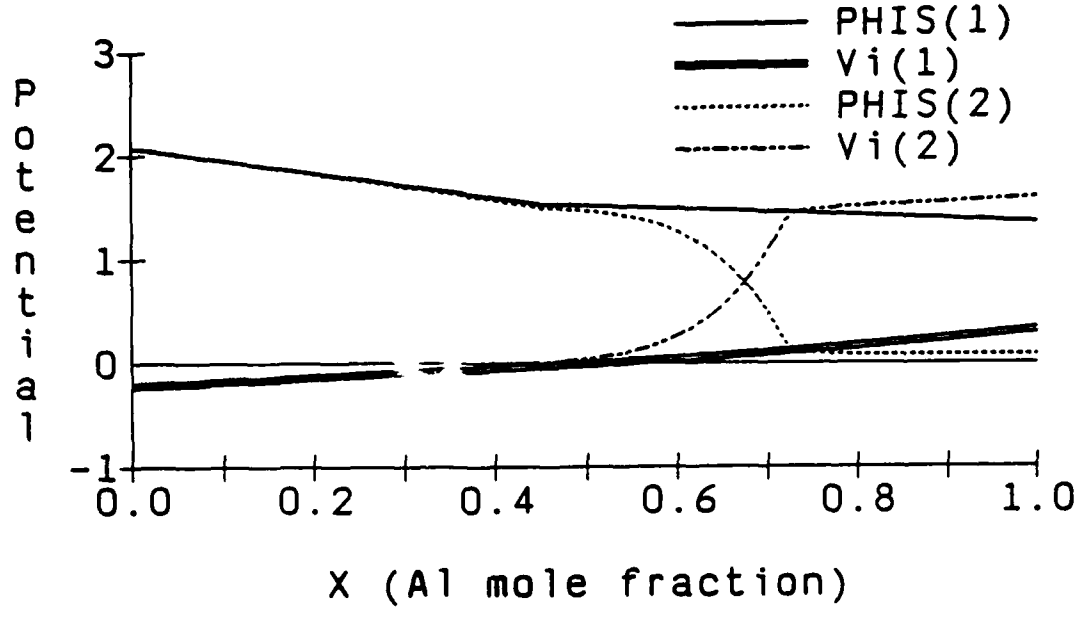

Fig. 11: Voltage drop across the semi-insulator, Vi, and surface potential of the semiconductor (ϕ_s), PHIS vs the Al mole fraction, x. The symbol (1) indicates that the effective velocity is calculated using only the thermal velocity while (2) indicates that both the thermal velocity and the drift-diffusion velocities were used. The spike layer is in the semiconductor, Vce = 2.0 and Js = 75.

number of other things are happening, for example ϕ_s becomes quite small and V_i' becomes positive and large (Fig.11). This causes Jpi to become very small while Jpc goes from being essentially zero to the size of Js, i.e. the hole current is no longer flowing thru the semi-insulator but thru the semiconductor because of the changing potentials V_i' and ϕ_s. Also, p_o increases rapidly and then flattens out (Fig. 9) and the fraction of ionized acceptors in the spike layer drops dramatically which increases the positive charge and decreases the negative charge in the spike layer. In order for charge balance to occur as given in Eq. 9, Q_e must become more negative which causes V_i' to become more positive. Notice that when only the thermal velocity is considered in each of these Fig.'s none of these effects occur.

Since v_{nd} essentially goes to zero as x increases one might also expect Jni and the gain to go to zero instead of flattening out as shown in Fig. 9. However, when V_i' becomes positive v_{nd} is given by Eq. 15 and Jni by Eq. 16. It is seen that Jni is almost a constant and since

$$V_{nd} \cong \frac{D_n}{d_1}\left(\frac{qV_i'}{kT}\right) e^{-qV_i'/kT} \qquad (15)$$

$$J_{ni} \cong q\left(\frac{D_n}{d_1}\right)\left(\frac{qV_i'}{kT}\right) N_c\, e^{-\Phi_n/kT} \qquad (16)$$

Js is constant, the gain would also be essentially constant.

When the density in the spike layer is increased there occurs a decrease in the fraction of acceptors ionized and an increase in p_o. It would seem, therefore, that the effects described above would be accentuated as N_A is increased.

It is interesting to see what happens to the gain when Jc (the collector current) is increased. In Fig. 12 we see that the current gain decreases rapidly when Jc reaches a certain value. At which value this occurs depends on the value chosen for Φ_n, the metal

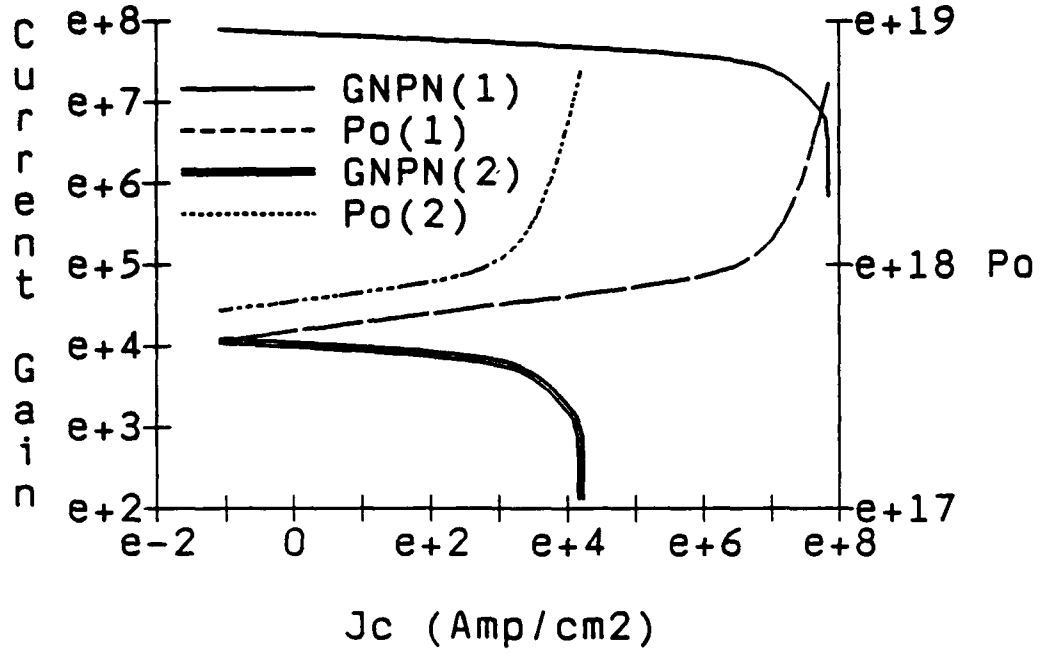

Fig. 12: Current gain (Jni/Js), GNPN, and inversion charge density, Po, as a function of the collector current, Jc. The symbol (1) indicates that $\Phi_n = 0.02$ and (2) that $\Phi_n = 0.24$. The spike layer is in the semiconductor, Vce = 2.5 and x = 0.8.

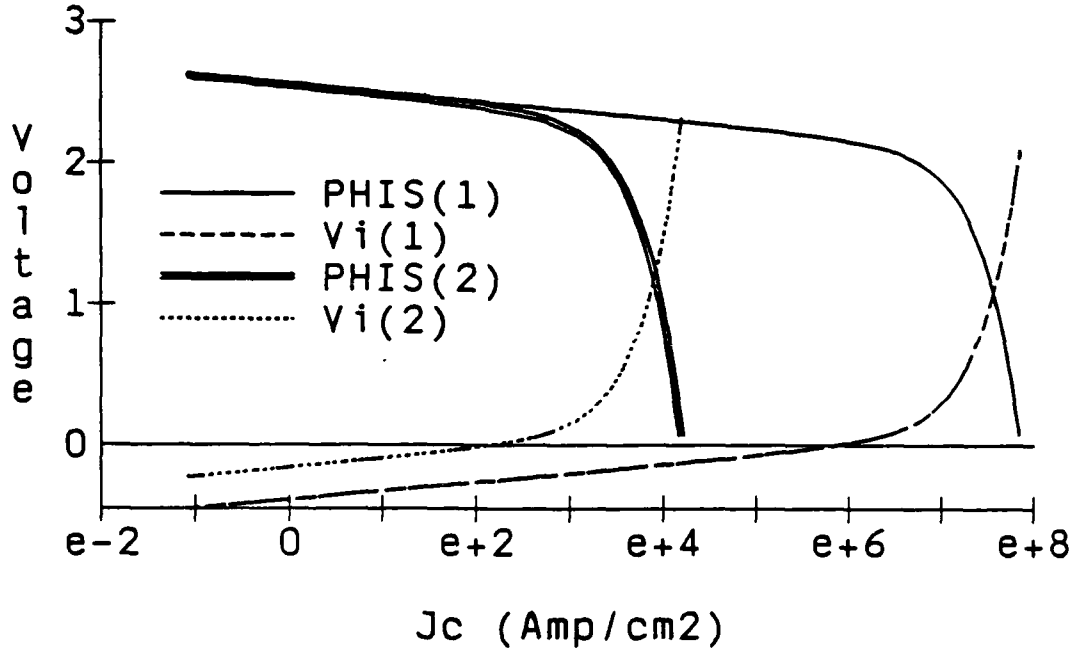

Fig. 13: Voltage drop across the semi-insulator, Vi, and surface potential of the semiconductor (ϕ_s), PHIS vs the collector current, Jc. The symbol (1) indicates that $\Phi_n = 0.02$ and (2) that $\Phi_n = 0.24$. The spike layer is in the semiconductor, Vce = 2.5 and x = 0.8.

semi-insulator contact potential and x. From Fig. 13 we see that the same physical processes are occuring as discussed above, i.e. V_t' is going positive due to v_{nd} becoming very small,etc.

It should be noted that all the above results were under the assumption that the spike layer was in the semiconductor, but the results also qualitatively apply to the case of the spike layer in the semi-insulator. However, in the latter case the effects don't come into play until higher values of x and Jc are reached.

In Taylor and Simmons' paper (4) it was assumed that Dn = 220 and Dp = 10 (GaAs values). This choice only slightly changes the ratio v_n/v_p (which affects the gain in Eq. 10) at lower values of x, but it is found that at higher values of x it is necessary to correctly calculate the diffusion coefficients using their x, impurity concentration, and electric field dependencies.

VI RECOMMENDATIONS

1. Do more modeling with this program, e.g., what happens to v_{nd} as N_A is changed.
2. Include recombination in the model. This effect is probably quite important at low values of Jc.
3. Model the PNP BICFET more extensively.
4. Include the change in activation level for the donors as a function of x. This effect could be important especially for the PNP BICFET.
5. Get the finite element program PUPHS (from Purdue University) up and running. The above analytical model could then be checked for accuracy and a parameter such as Φ_n could be found as a function of x.

REFERENCES

1. Schuelke, R.J., "Numerical Simulation of Semiconductor Heterostructures", Ph.D. Thesis, Purdue University, Dec. 1984.

2. Adachi, S., "GaAs, AlAs, and Al Ga As: Material parameters for use in research and device applications", J. Appl. Phys., 58(3), R1-R29, Aug. 1985.

3. Shur, Michael, GaAs Devices and Circuits, Plenum Press, 1987.

4. Taylor, G.W. and J.G. Simmons, "The Bipolar Inversion Channel Field-Effect Transistor (BICFET)- A new Field-Effect Solid-State Device: Theory and Structures", IEEE Transactions of Eletron Devices, ED-32, 2345-67, Nov. 1985.

5. Whitson, D.W. and W.D. Schmidt, "Analytical Computer Modeling of the NPN BICFET Device", Final report, 1986 USAF-UES Summer Faculty Research Program, Air Force Office of Scientific Research, Contract No. F49620-85-C-0013.

6. Whitson, D. W., "Effects on the BICFET of the Fermi Distribution Factor and the Al Mole Fraction", Final report, 1987 USAF-UES Mini-Grant Follow-On to Summer Faculty Research Program, Air Force Office of Scientific Research, contract No. F49620-85-C-0013/SB581-0360.

7. A.J. Hill and P.H. Ladbrooke, Electronics Letters, 22(4), 218, 1986.

1988 USAF-UES SUMMER GRADUATE STUDENT RESEARCH PROGRAM

Sponsored by the

AIR FORCE OFFICE OF SCIENTIFIC RESEARCH

Conducted by the

Universal Energy Systems, Inc.

FINAL REPORT

Finite Elements Simulation of the Resonant Tunneling Diode

Prepared by:	Kevin Lyle Carmichael
Academic Rank:	Masters Graduate Student
Departmment and	Physics Department
University :	Wright State University
Research Location:	WPAFB,Avonics Electronics Technology Divison
USAF Researcher:	Gary McCoy, Dennis Whitson
Date:	September 22, 1988
Contract No:	F49620-88-C-0053

Finite Elements Simulation of the Resonant Tunneling Diode

by

Kevin Lyle Carmichael

ABSTRACT

At the current time there is a great deal of interest in developing electronic oscillators which can operate in the frequency range above 200 Ghz. It is believed that for a device to accomplish this it must have a region of negative differential resistance. One such device that shows such a region is the resonant tunneling diode. In this project the resonant tunneling diode is investigated to understand the device and to find improvements which could help make the device more applicable.

The analysis of this device is done using a program called SEQUAL. SEQUAL is a finite difference algorithm which was developed specifically to for heterostructure devices. The program self-consistently solves Poisson's equation and Schrodinger's equation to yield information pertaining to the device such as the electrostatic potential, electric field and the electron distribution. The total analysis of this device was completed using information obtained from the SEQUAL program.

ACKNOWLEDGMENTS

I would like to thank the Air Force Systems Command and the Air Force Office of Scientific Research for sponsoring this research program of which I was partly involved. The Avionics Laboratory of Wright Patterson Air Force Base provided an ideal environment for the development of this project from both an experimental and theoretical aspect. I would also like to thank Gary McCoy and the AADR group for their advice and direction concerning this project.

In addition, special thanks are offered to the system operator, Ben Carroll who gave me assistance innumerable times on the VAX machines.

Finally , Dennis Whitson deserves the utmost thanks for his daily guidance. With his help I was able to accomplish a great deal of work, making this a most productive effort.

I. INTRODUCTION

My responsibilities for this summer involved a great deal of programing. The bulk of my experience with fortran comes from two programming classes that I took several years ago. In addition to the classes, I have had a great deal of experience programming with a number of personal projects I have undertaken.

My knowledge of programs that I used to model these devices came primarily from debugging the problems that arose when they were compiled on the VAX computer for the first time. Knowledge of the heterostructure device physics necessary to study these devices was acquired from Dr. Dennis Whitson.

Dr. Whitson is on leave from Indiana University of Pennsylvania and is currently working at Wright Patterson Air Force Base under a AFOSR Resident Research Program. He is working on research in modeling heterostructure devices such as the resonant tunneling diode.

I am continuing research on the resonant tunneling diode as work towards my Masters thesis under Dr. Whitsons supervision.

II. OBJECTIVES OF THE RESEARCH EFFORT:

The primary objective of this summer research project was to implement several computer programs written in fortran but on a different computer system. The problem being that the fortran language was not exactly compatible between the two machines. In conjunction with the existing programs a handful of secondary programs had to be generated to help run the original programs. Also even after the programs were running correctly, they had to be understood. There are always a number of problems involved in using a program that is not familiar.

The next task that was addressed was the problem of the resonant tunneling diode. The analysis of this device provides the motivation for using the fore mentioned programs and is the center of attention of this effort.

Several other devices were studied with these programs, however they were not focused upon because they were more complicated in nature. For the purpose of learning the program and devices of this nature the simplicity of the resonant tunneling diode was thought adequate.

III. COMPUTER PROGRAMS

In this section I would like to address some of the accomplishments and limitations of the total software package as it evolved over the summer project. It should be noted here that the evolution process is by no means over. Both programs that are currently running (FISH1D and SEQUAL) along with the programs to come (1DPUPHS and 2DPUPHS) will surely have to be adapted to be practical.

In the theoretical analysis of GaAs/ALGaAs heterostructures a method for constructing a conduction band profile must be available. There are several ways to accomplish this with varying degrees of sophistication. The crudist method is to create a "flatband" profile. This is simply a profile with the conduction band equal to zero in the GaAs region and the conduction band to the appropriate conduction band offset in the AlGaAs region. This of course does not account for the band bending that will occur near interfaces of different material and different doping densities. The way around this is to solve Poisson's equation across the entire device. The program FISH1D was developed to do this provided the analysis is restricted to the equilibrium case. FISH1D takes in information on initial doping densities, material types, temperature and cross sectional area along with one dimensional user defined space grid and uses this information to solve Poisson's equation. The program output includes electrostatic potential, electric field, electron and hole densities, dopant and ionized dopant densities and other important parameters as a function of distance across the device.

When analyzing heterostructures it is often necessary to stray from classical mechanics in favor of quantum mechanics. This is the motivation for SEQUAL. SEQUAL is a program that is extremely versatile in that it was written as a post processor. By this it is meant that a previous program has already been run to generate a classical conduction band profile which is then fed into SEQUAL as input. SEQUAL then adjusts the classical parameters to include the quantum effects. By doing this SEQUAL is not contingent on any particular program. All that is truly necessary is a conduction band profile, even a flat band is sufficient although this will increase processing time as will be explained shortly.

SEQUAL's main objective is to determine a conduction band profile consistent with quantum mechanics. The main problem is that the input band profile is often calculated using classical mechanics. What is required to solve this problem is a consistent solution of Schrodinger's equation and Poisson's equation. This is accomplished by an iteration scheme. Schrodinger's equation is first solved using the classical conduction band profile to determine the wavefunctions for the electrons. Once this is known a charge distribution can be generated and used to recalculate the electrostatic potential using Poisson's equation. The potential is then fed back into Schrodinger's equation, thus completing the loop.If this procedure is repeated a consistent solution of both equations is approached. At the specified level of convergence the program jumps out of the iteration loop and the desired conduction band is known and can be used to

calculate other output parameters.

In theory this is the extent of these programs, however actually carrying out these calculations can be more complicated than appears on the surface. First, there is the problem of setting up the finite difference grid. Both FISH1D and SEQUAL provide a automatic grid function. Neither, however were found to work adequately , which brings us to the next problem. When using a finite difference grid care has to be taken not to let the potential change too greatly between two consecutive points. On the devices we studied to keep this criteria at dissimilar material interfaces it was necessary to define extra grid points which are within .1 angstroms of the interfaces. The next problem is not as easily overcome. When calculating the number of transmitted electrons an integration over energy space is required. The problem arises with the number of energy nodes that have to be taken into the integration. For a relatively low bias this is not a problem but for biases over 0.5 volts the number of energy nodes to be integrated over is large enough to cause unmanageable run times. In the future something will have to be done on this problem in order to fully investigate these devices.

IV. Resonant Tunneling Diode

The concentration of this effort was done primarily on the resonant tunneling diode (RTD). The QWITT diode was also looked into somewhat but was put on a lower priority until the simpler RTD was understood. The QWITT diode is a form of the RTD which has a non-symmetric drift region on one side of the diode. The analysis of these devices are quite similiar however,therefore the main analysis will be limited to the symmetric RTD and references will be made to the non-symmetric diode where needed.

The construction of the RTD consists of two regions, the drift region and the potential well. Generally the outside drift regions are n-doped GaAs and the potential barriers are Al Ga As. In the work done here the mole fraction was limited to 0.45 so that only direct band transitions to the gamma valley will occur. In figure 1 the drift regions extend from 0 to 1025 angstroms and 1175 to 2200 angstroms with the potential well sandwiched in between. The dimensions here vary somewhat but the three layers that construct the potential well are often under 100 angstroms. With dimensions this small it is not surprising that classical mechanics is insufficient to describe these devices.

To understand negative differential resistance in the RTD a quantum mechanical approach is necessary. This device can be modeled simply as a double barrier. Electrons, represented by wavefunctions, are injected from the contacts with a spectrum of wavevectors. The electrons encounter the potential barrier and are partially transmitted, the rest are reflected back into the contact. Of those that are transmitted some are again transmitted through the second barrier. The electrons in between

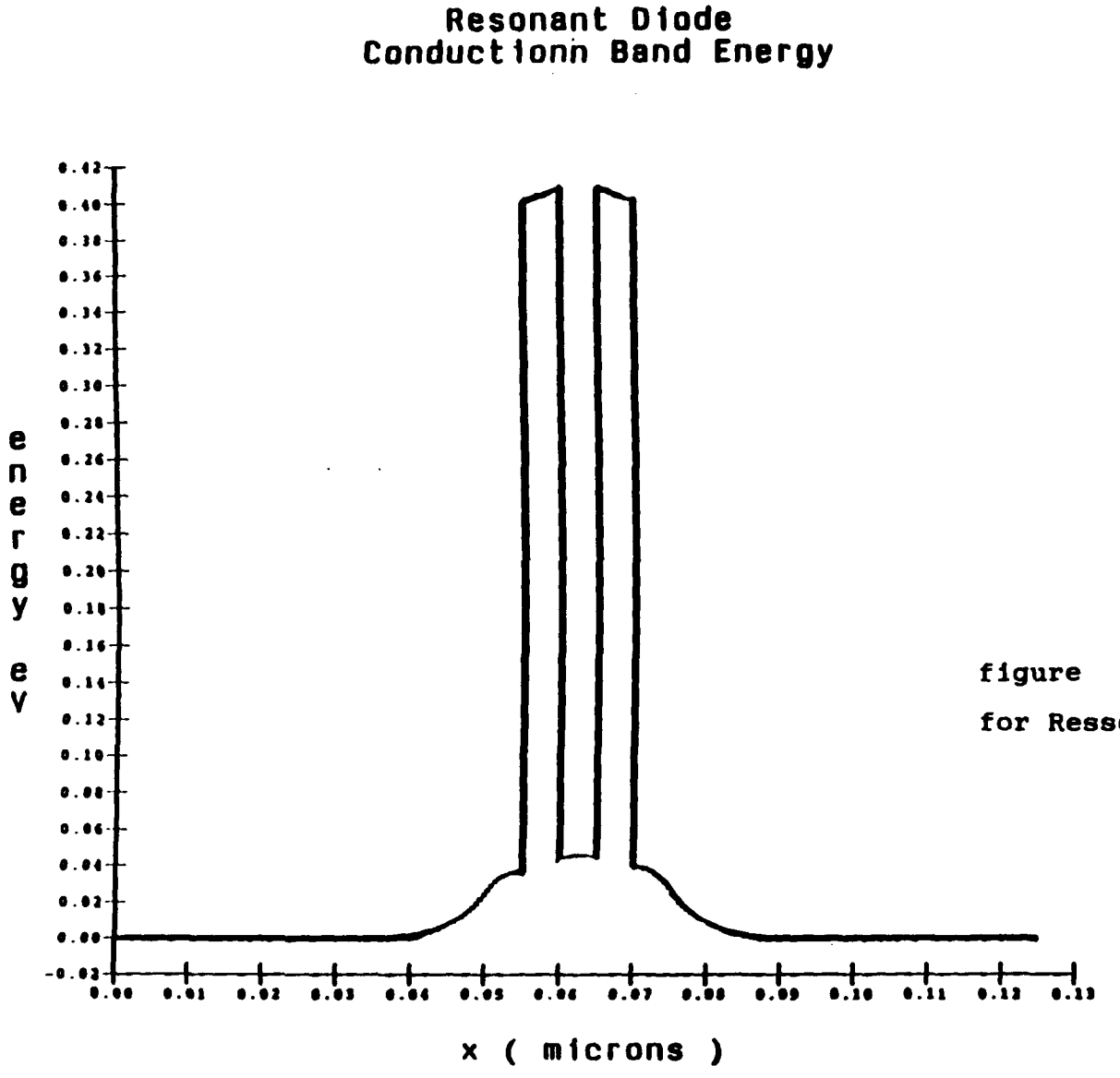

figure 1. Conduction Band Profile for Ressonant Tunneling Diode

the two barriers continuously reflect between them until they are transmitted out of it. Electrons in the well whose wavefunctions meet the boundary conditions can have a transmission coefficient close to unity. These electrons are said to have a resonant energy and the wavefunction peaks in the well to form quasi-bound energy states. It is these quasi-bound energy states along with the electron distribution which are directly responsible for the NDR region. The number of electrons available is governed by Fermi-Dirac statics so that as you go above the Fermi energy the electron distribution drops off sharply. The transmission coefficient depends mainly on the quasi-bound energy states that are present in the well and secondarily on the relative height difference of the barriers. These two concepts can be combined together to understand negative differential resistance.

At equilibrium the quasi-bound state is significantly above the quasi-fermi level. Since the electrons are primarily of energy close to the fermi level, there are not many electrons available at the quasi-bound energy to tunnel into the well. When the device is put under bias the right side is held at ground while the left side is pulled down to the appropriate voltage as can be seen in figures 2 and 3. When this is done the quasi-bound state is pulled down toward the quasi-fermi level. This causes an increasing number of electrons to be at the quasi-bound energy and therefore a larger number to be transmitted through the device. This initial increase in the current can be seen in the current verus voltage which is given in figure 4. The current is determined at any particular voltage by calculating a transmission coefficient for each energy then multiplying it times the available

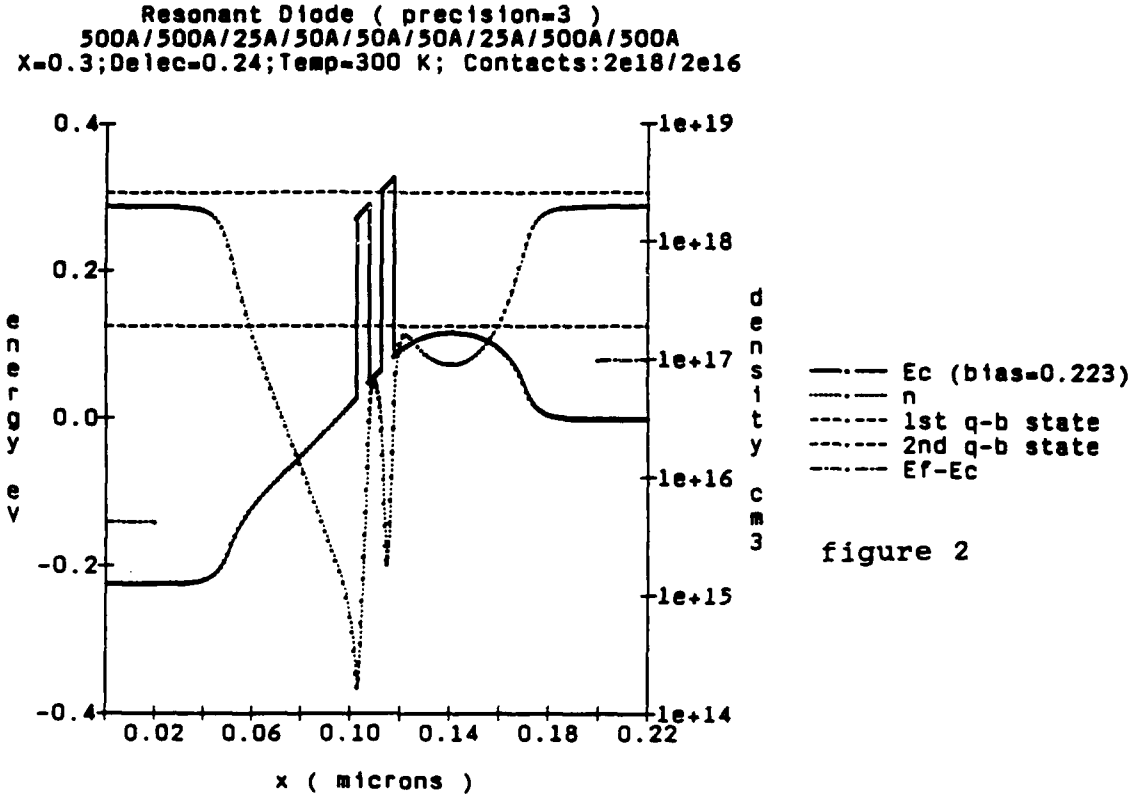

figure 2

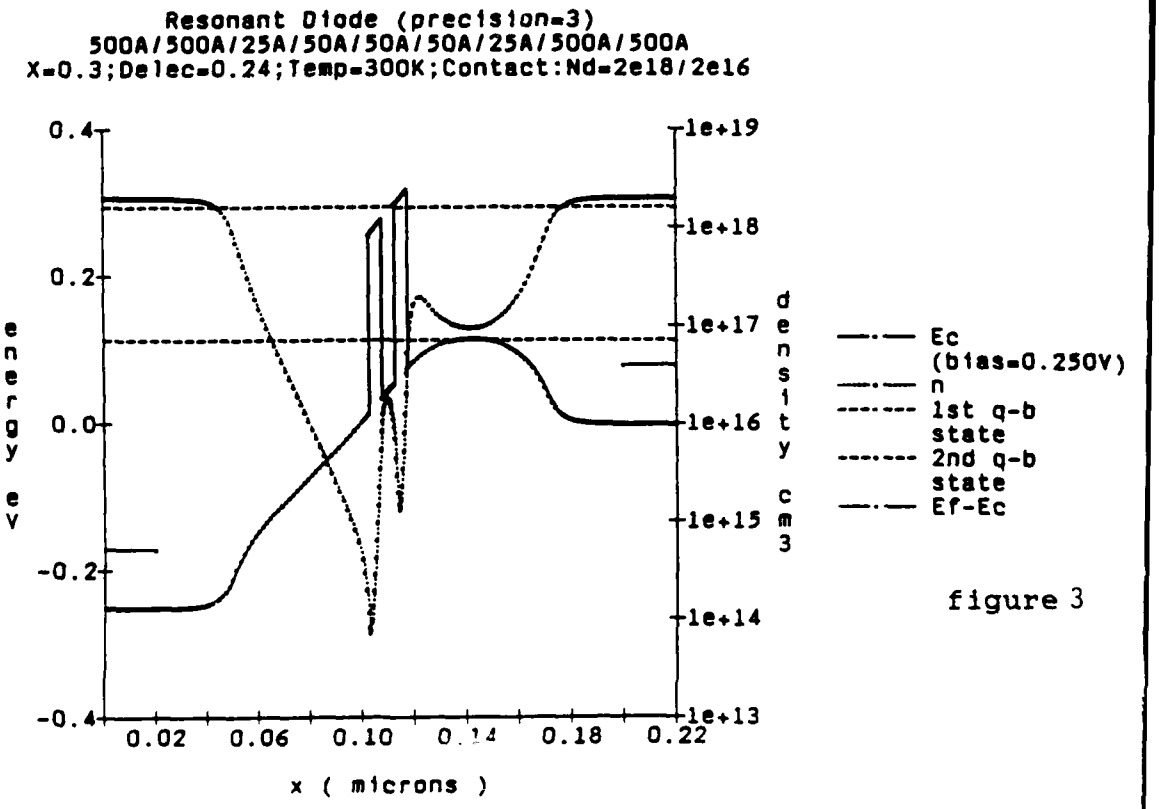

figure 3

Conduction Band, Electron Density Quasi-Bound States and Quasi-Fermi Level for a) C 223 V and b) 0.25 V

electrons at that energy. The sum of all electrons transmitted yields the current. The maximum current available occurs when this relationship is optimized. For the device we modeled the maximum current occurred at 0.223 volts while the minimum occurred at 0.25 volts. Note that the maximum does not occur when the bound state energy equals the fermi energy but at a bias slightly less, due to the transmission coefficient degrading as the bias increases. As the bias is increased further the current will decrease and the NDR region begins. In figure 4 this is the region between 0.223 and 0.25 where the graph has a negative slope. The current drops because the quasi-bound state is pulled below the fermi-level so that there are not many electrons that can tunnel through at the resonant energy. As the two energies are further separated the current continues to drop until the bias is sufficient to pull the barriers down low enough to allow electrons to pass over the top. At this point the current increases proportional to the voltage increase and the NDR region is finished. Developing these programs to the point they can predict this NDR region in these devices is the biggest accomplishments of this summer project.

Due to the time limitations of this appointment a complete investigation could not be accomplished.There are several areas in which calculations have been made but a complete understanding is not in hand. In light of this I would now like to present the rest of the calculations on the resonant tunneling diode.

One very important parameter to understand is the transmission coefficient. In figures 5 and 6 the transmission coefficient has been plotted as a function of energy.

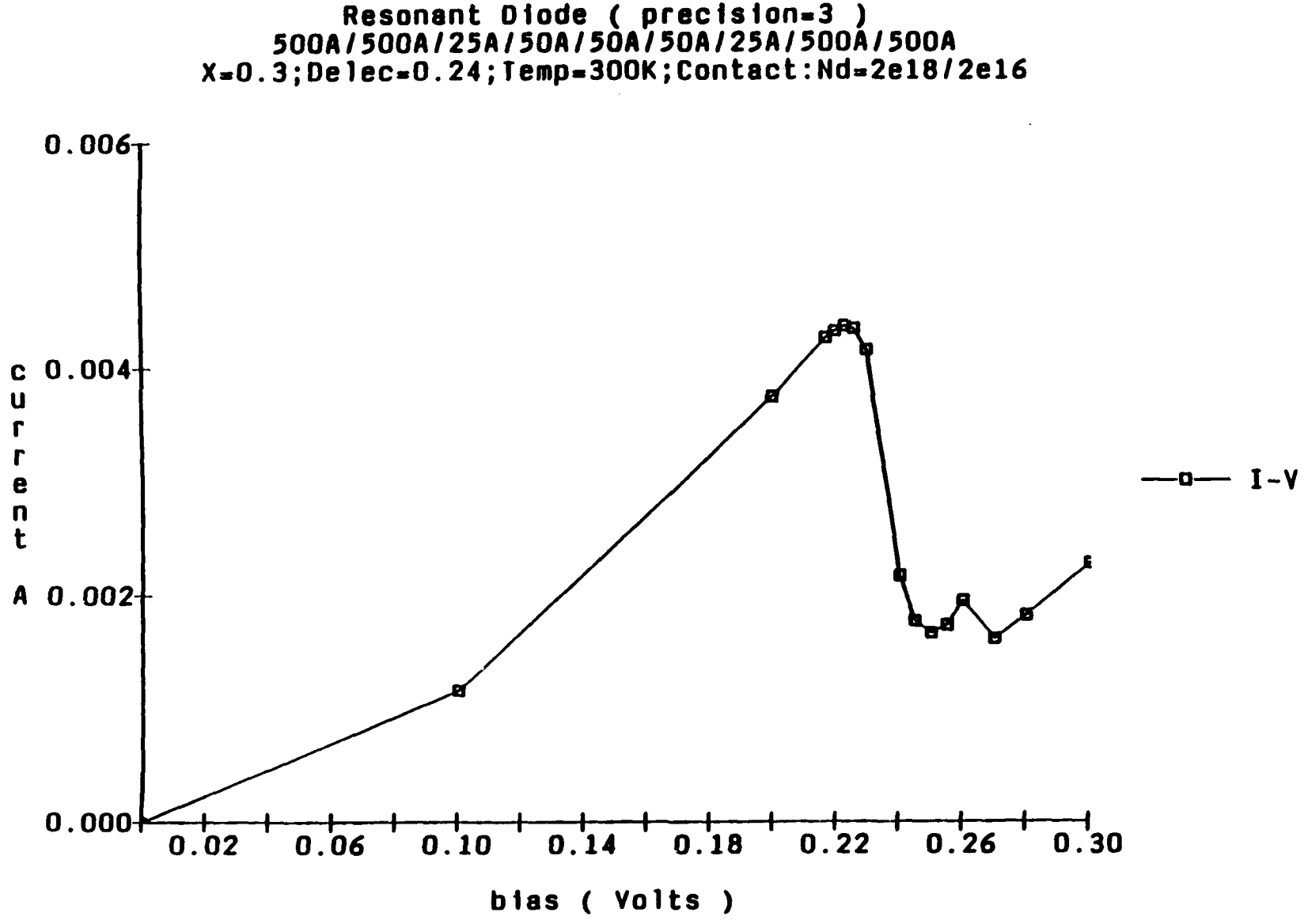

figure 4. Current vs. Voltage for Resonant Tunneling Diode

Only two of this type of graph are included here due to space limitations. The two that are included are the plots for the maximum current (fig.5) and the minimum current (fig.6). There appears to be a fair amount of interesting structure contained here, unfortunately I am not sure exactly what it is. There are basically two main peaks in all the graphs from this set. For these graphs included here the peak energies can be read to be approximately 1.25 eV and 3 eV. These match the energies of the two quasi-bound states rather well which does not seem unreasonable. The interesting feature that can be seen here is that at the lower of the two biases (fig.5) there is a second peak which is very close to the 1.25 eV peak. As the voltage across the device is increased to 0.25 V this secondary peak drops away until it can just be seen as a shoulder in figure 6. As of this writing this is not understood well but I believe it could be understood with more analysis.

The final calculation that I will present here is a plot of both the energy at which the transmission coefficient is a local maximum and the value of that maximum for each of the two quasi-bound energy states. These quantities are plotted as a function of bias and is shown here as figure 7. Considering this graph, there are some interesting features that are worthy of a note. First, notice that the

transmission coefficient of the first state disappears at the same bias that there is a jump in both parameters of the second bound state. This may well be physical although again it is not currently understood by myself. Weather or not it is physical, it is

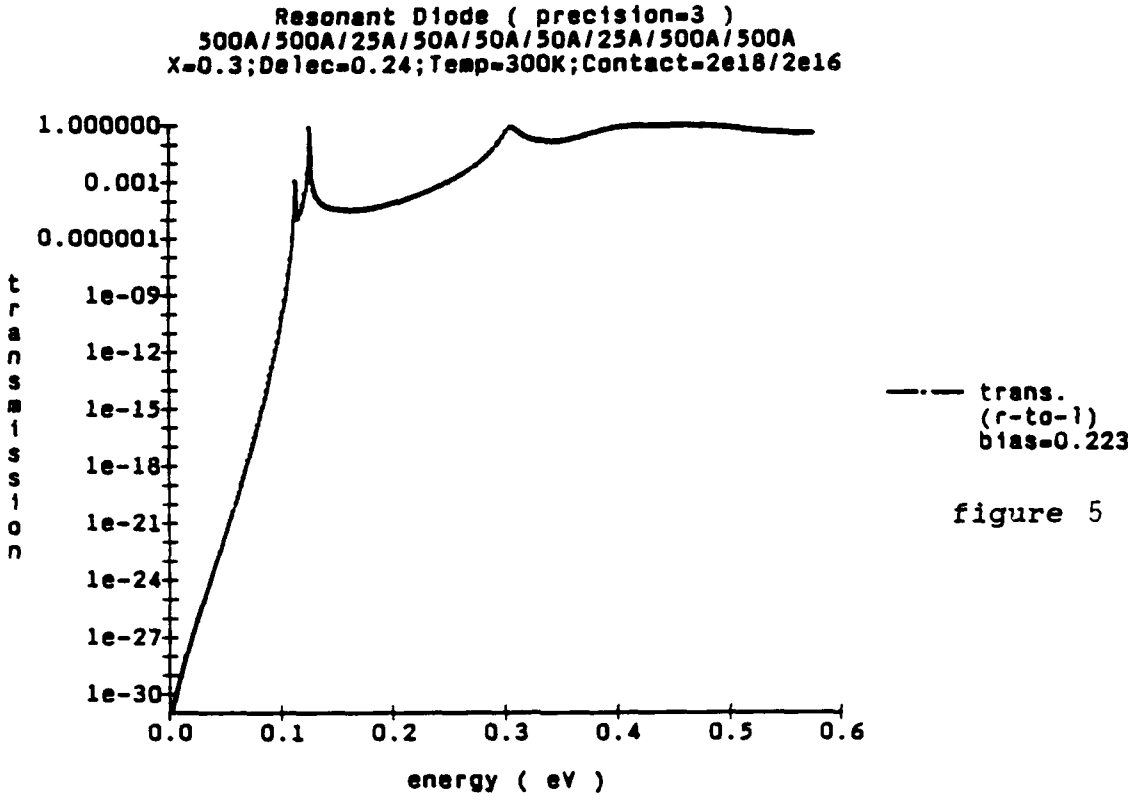

figure 5

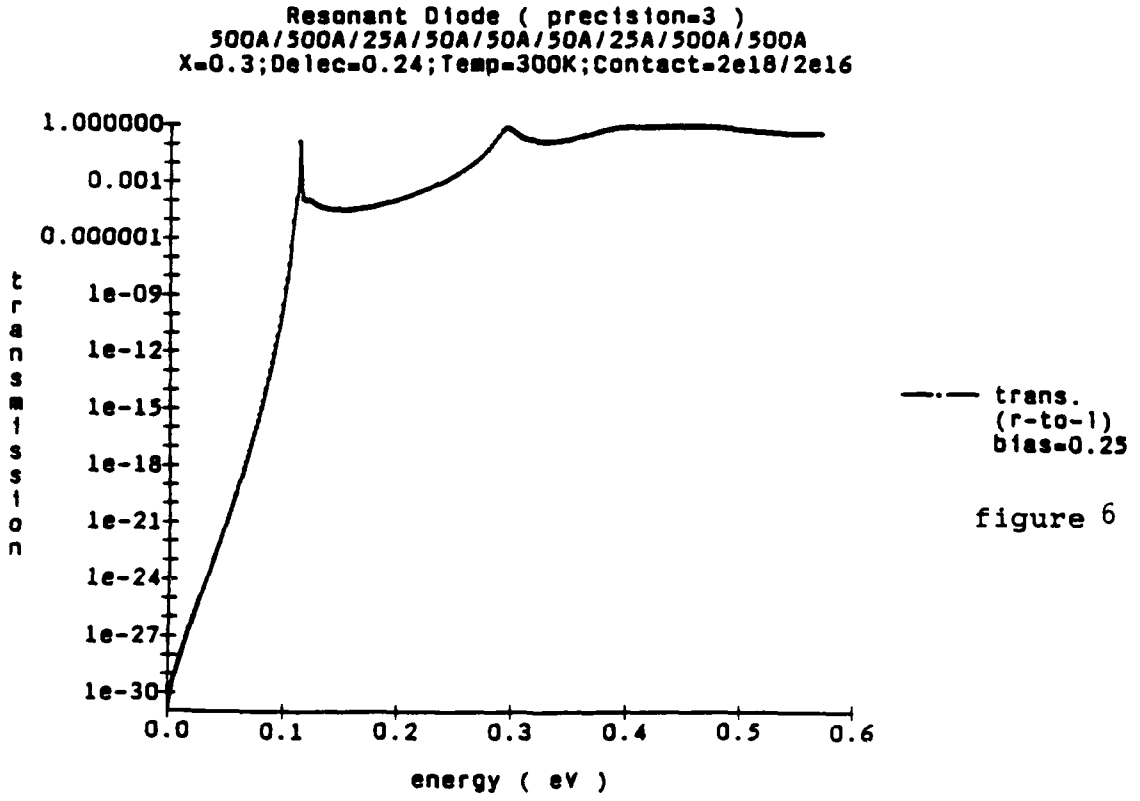

figure 6

Transmission Coefficient vs. Electron Energy for a) 0.223 and b) 0.25

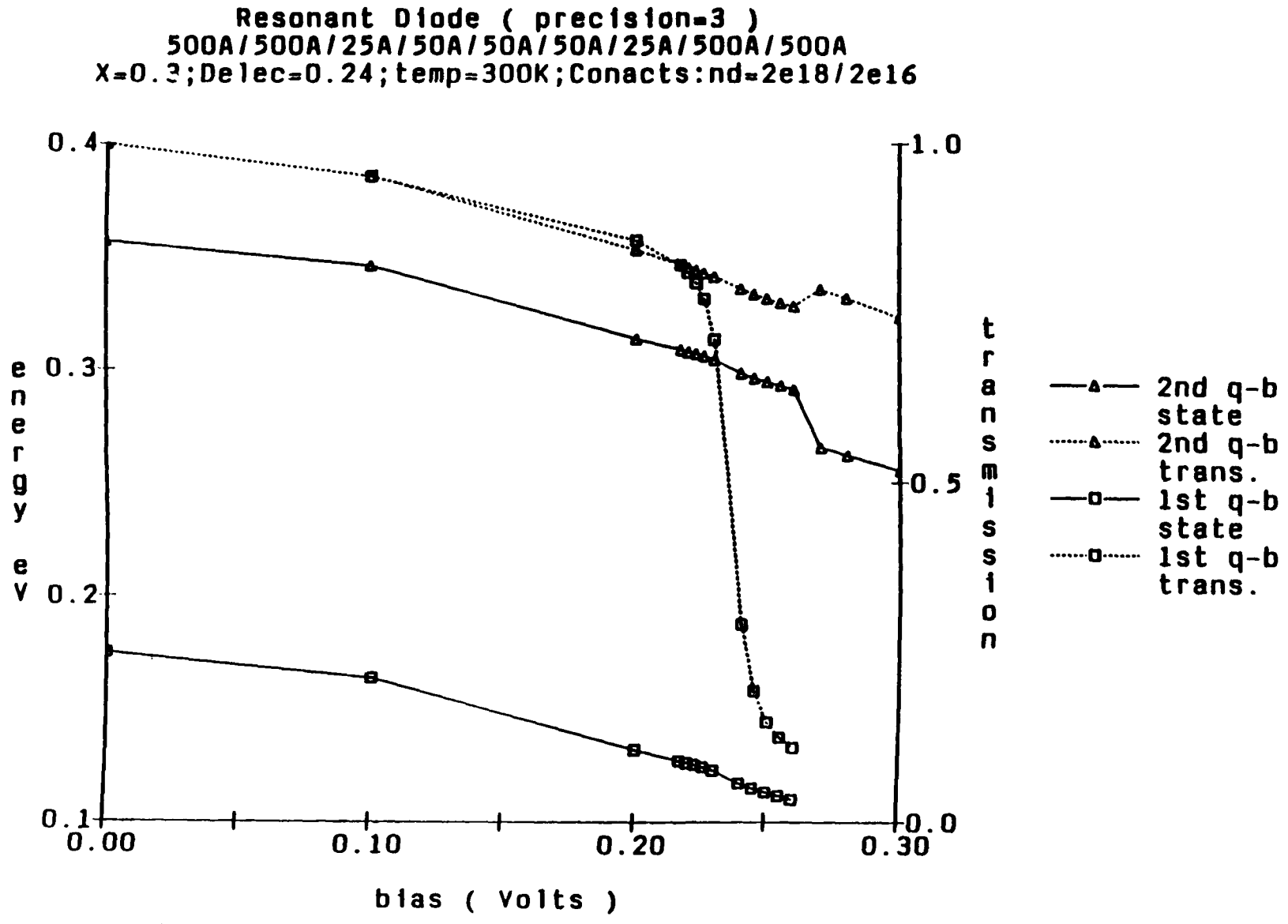

figure 7 Transmission Coefficient(dotted) and Quasi-Bound Energy(solid) vs. Bias

interesting that the lowering of this energy at which we have transmission combined with the raising of the transmission coefficient should imply a rise in the current at this particular voltage. Checking the I-V curve (figure 2) this peak is easily seen at this voltage. This at least implies some consistency to the algorithms used here in this report.

V. RECOMMENDATIONS:

a. The investigation of heterostructure devices in general is an integral part of the advancement in high speed electronics. The progress made during this appointment would suggest that a continued effort in this field would be a rewarding choice.

b. A consideration should be given to a wider range of devices. There are several new devices which needed to be analyized. In conjuction with this the programs used in this report are very useful for predicting new structures .

c. Several programs currently exist from the Purdue group which I did not have time to implement. These include a one and two dimensional non equilibrium Poisson's equation solver as well as a Monte Carlo simulation. These programs have many applications to this work and would be very useful once they were on line.

REFERENCES

1. McLennan, Michael James, "Quantum Ballistic Transport in Semlconductor Heterostructures",M.S. Thesis, Purdue University, Dec. 1984

2. Cahay, M.,McLennan,M., Datta, S., Lundstrom, M.S., "Importance of Space-Charge Effects in Resonant Tunneling Devices", J. Appl. Phys. Lett., 50(10), March 1987

3. Lundstrom, M., Datta, S.,Bandyopadhyay, S., Sorlie, P., Klausmeier-Brown,M., Maziar, C., Cahay, M., "Physics and Modeling of Heterostructure Semiconductor Devices", Annual Report, October 1985

4. Lundstrom, M., Datta, S . Bandyopadhyay, S.,Das, A., Klausmeier-Brown,M., Maziar,C., Cahay, M.,McLennan, M., "Physics and Modeling of Heterostructure Devices",Annual Report, October 1986

1988 USAF-UES SUMMER FACULTY RESERCH PROGRAM/

GRADUATE STUDENT SUMMER SUPPORT PROGRAM

Sponsored by the

AIR FORCE OFFICE OF SCIENTIFIC RESEARCH

Conducted by the

Universal Energy Systems, Inc.

FINAL REPORT

SOFTWARE TOOLS MODELING LOW VOLTAGE BEAM STEERING DEVICES

Prepared by:	Daniel B. Cook
Academic Rank:	Bachelor of Science
Department and	Department of Electo-Optics
University:	The University of Dayton
Research Location:	AFWAL/AARI-2
	Wright-Patterson AFB, Dayton, Ohio
USAF Researcher:	Dr. Paul F. McManamon
Date:	July 15, 1988
Contract Number:	F49620-88-C-0053

SOFTWARE TOOLS MODELING LOW VOLTAGE BEAM STEERING DEVICES

by

Daniel B. Cook

ABSTRACT

Computer models of two distinct and promising beam steering devices were performed. The multiple stage Wollaston prism beam steering device, utilizing ferro-electric crystals, was found to give beam steering accuracy within an average of one arc-second. The optical phase array, with its piston and gradient phase array patterns, was also computer modeled, and it was shown that with small enough radiating nematic liquid crystal elements, there is no difference in far-field patterns between the two phase pattern types. A user-friendly computer program was written which transformed wavefront phase patterns into far-field beam patterns.

I. INTRODUCTION:

With the ever-increasing use of lasers in the defense scenario, it has become increasingly important to design an efficient, quick, and lightweight beam steering device. Because of the speed requirement, electro-optical methods offer the only feasible means of designing a realistic beam steering device. Also, the need to incorporate the device on airborne or space-borne systems adds the requriement of low voltage demand. For this reason liquid crystals, with their inherent speed and efficiency, have shown great promise as the electro-optic material from which to build a beam-steering device. As a Summer Faculty Researcher, Dr. Mohammad Karim surveyed fast liquid crystal materials and their possible use in beam steering devices. As his graduate assistant, I designed computer models of these devices to prove their feasibility. Two design approaches utilizing liquid crystals were investigated by Dr. Karim and myself. The first design, the optical phase array, has been of great interest to Air Force Wright Avionics Laboratory for some time. The second design, the multiple stage Wollaston prism beam steering device, was first conceptualized over twenty years ago (Soref and McMahon, 1966; Kulcke et. al., 1966), but only recently has the technology evolved so that the design could meet both the speed and size requirements desired.

I am a Master of Science candidate student in the Department of Electro-Optics at the University of Dayton. I have experience programming in the Pascal, C , Fortran, and BASIC languages. I was introduced to the area of beam agility by my professor, Dr.

M. Karim, and it was at his suggestion that I apply for the Summer fellowship from UES. Apart from the standard amount of research done in the undergraduate years, this fellowship has awarded to me the first opportunity to perform new and valuable research. The nature of the Air Force research on this project was such that both a theorist and a software designer were needed to fully investigate new technologies. It is in this way that I came to be involved with the project.

II. OBJECTIVES OF THE RESEARCH EFFORT:

The prime goal of the summer project was to explore potential systems of low-voltage, broad-band beam steering devices, and in particular, to explore the system known as the optical phase array. As the research progressed, one other beam steering device, the multiple stage Wollaston prism beam steering device, was deemed to meet the potential requirements of the project. These requirements were:

50000 resolvable angular spots
20 degree cone field-of-view
50 cm. x 50 cm. aperture
switching speed around 1 millisecond
uniform broad-band performance around thre
distinct wavelength bands:
0.7-1.1 microns
4.2-4.5 microns
9.5-11.5 microns

As the field was narrowed to these two systems by Dr. Karim, it became my task to design computer models to simulate their performance. My last objective of the research effort was to provide a user-friendly computer program and an associated user's manual which would transform wavefront phase delay patterns at an aperture into far-field beam patterns.

III. THE MULTIPLE STAGE WOLLASTON PRISM BEAM STEERING DEVICE:

a. The Wollaston prism operates on one simple principle: an incoming beam of linearly polarized light will be deflected either above or below the horizontal, depending on its polarization relative to the optic axis of the prism (Soref and McMahon, 1966). A beam of light cannot pass through a Wollaston prism undeviated. The amount of deviation caused is dependent only on the internal angle of the prism and the extraordinary and ordinary indices of refraction of the material from which the prism is made. The multiple stage Wolaston prism beam steering device (WPBSD) is simply a series of Wollaston prisms placed in series, and constructed so that each prism has twice the deflecting power of the previous stage. Each prism is separated by a ferroelectric liquid crystal (FLC) half-wave retarder. In this way, each prism may deviate an incoming beam either up or down, depending on whether the FLC has caused the polarization of the beam to represent an extraordinary or an ordinary ray. The purpose of giving each prism twice the deflecting power of its previous neighbor is to enable the device to have binary characteristics. For example, if the maximum deviation is 10 degrees in either direction, then the last stage would have the power to deflect a beam 5 degrees either direction, its closest neighbor 2.5 degrees either direction, the next stage 1.25 degrees either direction, etc. Obviously the greater the number of stages, the higher accuracy of beam deflection. For a 16-stage device with a maximum deflection of 10 degrees either way, the device would have an ideal pointing accuracy of 0.55 arc-

seconds, and 65536 resolvable angular spots. The main advantages of the WPBSD are that the FLC retarders between each stage have a switching speed on the order of a few hundred nanoseconds, and cooling of the system would be facilitated because the heat loss from the beam is dissipated over 16 separated stages. The disadvantages of the WPBSD are that the extraordinary and ordinary exiting beam from each prism are not deviated exactly opposite in magnitude (causing appreciable differences compounded over 16 stages), and that propagating a beam through 16 separate prisms is bound to give appreciable transmission losses. The first program that I wrote for the WPBSD created a 16-stage device and calculated the optimum prism material and the optimum internal prism angle that would cause the least difference between extraordinary and ordinary exiting beams for each stage. From this information, the minimum prism thickness and minimum prism aperture were calculated for each stage, giving a final device thickness of no less than 5.6 cm., using readily available prism materials. It must be noted that only the wavelength band centered around 1.06 microns was taken into account, since the index of refraction values of prism materials are not tabulated for wavelengths greater the around 2 microns.

Although the difference in exit angle of the extraordinary and ordinary rays was minimized for each prism, a difference still remained, so that the pointing accuracy of the WPBSD was nowhere near the ideal, and also changed with desired deflection angle, most notably around 0 degrees deflection, where the 16th (and most significant) stage switched from deflecting down to deflecting up. To alleviate this problem, the vernier-type

accuracy of the earlier stages is utilized. For example, if one wanted to deflect to +9.5 degrees, and the WPBSD deflected to +9.3 degrees instead, then if the WPBSD were instructed to deflect to +9.7 degrees, then possibly the desired +9.5 degree deflection would result. The second program I wrote for the WPBSD took a desired deflection angle, calculated the actual deflection angle from the WPBSD, and then adjusted appropriate stages of the device so that the desired deflection angle resulted. This is what I called the "trained" WPBSD as opposed to the "untrained" WPBSD from earlier programs.

b. Please refer to Figure 1. Note that the untrained WPBSD displays an erratic pattern of deflection error, while the trained WPBSD is much more predictable. Note also that (illusions of scaling aside) the trained WPBSD had far greater accuracy than did the untrained version. Finally, note that at the central wavelength 1.06 microns (the wavelength for which the prism angles were optimized) on the trained WPBSD, the deflection error is nearly negligible, and increases only as the wavelength moves away from center. Calculations showed that at a distance of 100 miles, the average error in targeting (wavelength = 1.06 microns) would be on the order of 13.5 inches.

IV. THE OPTICAL PHASE ARRAY:

a. The optical phase array works on the principal of constructive interference of light beams propagated through an array of elements, each of which contributes a certain phase to an incident beam. One way of introducing this desired phase shift across a beam of light is by making the array from nematic

liquid crystal layers (NLC). The phase pattern produced by the array of NLCs dictates the resulting far-field pattern. There are two basic phase patterns which are used. One is known as the piston phase pattern, in which each NLC contributes a constant phase "plateau" to the beam. This stair-step pattern attempts to emulate the constant slope phase pattern which an ideal deflector would cause. The second type of phase pattern contributed by the NLCs is known as the gradient or echelle pattern. This pattern uses a gradient across each NLC to emulate the ideal constant slope. Theoretically, this pattern should exactly emulate the ideal deflector. There are two distinct disadvantages to the two phase patterns: the first is that the NLCs have typically slow switching speeds (on the order of 50 milliseconds). The second being that each NLC must be electronically adressed. This causes each NLC to be separated from its neighbors by a gap which is taken up by electrodes, etc. Also, since each NLC is on the order of 20 microns wide, creating a 50 cm. x 50 cm. aperture filled with these NLCs would require addressing 0.625 billion separate elements. My job was to investigate the differences in far-field patterns caused by the gradient and piston type phase patterns, and then to create a user-friendly program which would plot these far-field patterns, along with an associated user's manual.

b. The piston phase array, since it requires only one electrode per radiating element, is the more desirable to the designer who must address an appreciable amount of the elements. Therefore it is desirable to show that, as the number of radiating elements

approaches some limiting factor, the difference between the piston and gradient phase patterns is negligible. Since present technology can produce NLCs 20 microns wide, and the ultimate desire (since switching speed increases as width decreases) is to produce NLCs 1 micron wide, I computed far-field patterns of both phase pattern types for NLCs ranging in width from 20 microns down to 1 micron. Results show that even at an NLC width of 20 microns, the far-field patterns created by the two phase pattern types were essentially identical.

The final program written computed far-field diffraction patterns of both phase pattern types, according to inputs given by the user. The user could simulate either a one-dimensional or a two-dimensional phase array. The user inputs included:

ratio of NLC width to width of NLC+electrodes
actual width of NLC
phase pattern type
amount of phase difference across entire array
operating wavelength

The program constructed the appropriate amplitude and phase members of each array, (refer to Figure 2) and performed the Fourier transform on the array to produce the far-field pattern. Due to memory and speed constraints, the one-dimensional array model used 819 radiating elements, and the two-dimenional array used 13 x 13 elements. The percentage of the transmitted beam residing in the main lobe was computed, along with the deflected position of the main lobe. Refer to Figures 3 and 4 for example output from the program. The program was written in the ASYST language, and a listing of the program follows.

V. RECOMMENDATIONS:

For both types of beam steering devices, theory is borne out well, it is the present state of materials technology which hinders further investigation:

a. For the Wollaston prism beam steering device, it is essential to determine the index of refraction of the typical prism materials for all the desired wavelength bands. Current data only supports computer modeling at the wavelength band centered around 1.06 microns. Also, transmission characteristics of each type of prism material must be given before this type of beam deflector could be given serious consideration. It is not known whether present materials technology could support it, but if the prisms could be constructed properly, the WPBSD could be reduced in overall thickness from 6 cm. down to possibly 1 cm., enabling it to be a very feasible device.

b. Technology must also advance sufficiently so that the optical phase array could be considered a feasible beam steering device. Present switching speeds are still around 50 milliseconds, far too slow for reasonable defensive beam steering. Also, the amount of electrical connections needed to properly address the array becomes a formidable problem with each decrease in NLC size. This effect must be taken into account before any further investigation of other problems with the optical phase array are considered.

VI. REFERENCES:

Kulckle, W., Kosanke K., Max, E., Habegger, M. A., Harris, T. J., and Fleisher, H., "Digital Light Deflectors", Appl. Opt., Vol. 5, 1966, p. 1657.

Soref, R. A., and McMahon, D. H., "Optical design of Wollaston-prism digital light deflection", Appl. Opt., Vol. 5, 1966, p. 425.

ACKNOWLEDGEMENTS

I wish to thank the Air Force Systems Command and the Air Force Office of Scientific Research for sponsorship of the research. I also with to thank the work done by Universal Energy Systems, Inc., especially Mr. Rodney Darrah and Mr. Milton Danishek, in administering this program.

This being my first experience with new and valuable research, I wish to thank a few people for the patience and invaluable lessons they gave me. These would include Ms. Carol Heben, 1st Lt. Larry Myers, and Dr. Paul F. McManamon. Most especially, I would like to thank Dr. Mohammad Karim, my professor and Summer Faculty Research Program sponsor, for introducing me to the program, and for providing me with interesting and valuable research topics.

```
\ PROGRAM INITIALIZATION

16 GRAPHICS.DISPLAY.MODE
GRAPHICS.DISPLAY
-1 2 FIX.FORMAT

18 2 23 77 WINDOW (SPECS)
22 1 23 78 WINDOW (SPLIT1)
24 0 24 79 WINDOW (SPLIT2)

  DEF.VUPORT
  VUPORT.CLEAR
  (SPLIT2)  SCREEN.CLEAR

: BLACK       0 ;
: BLUE        1 ;
: GREEN       2 ;
: CYAN        3 ;
: RED         4 ;
: MAGENTA     5 ;
: BROWN       6 ;
: WHITE       7 ;
: GRAY        8 ;
: LT.BLUE     9 ;
: LT.GREEN    10 ;
: LT.CYAN     11 ;
: LT.RE       12 ;
: LT.MAGENTA  13 ;
: YELLOW      14 ;
: I.WHITE     15 ;

: 3DVU
   0.0 0.3 VUPORT.ORIG
   0.6 0.7 VUPORT.SIZE
;

: XCROSS
  0.61 .65 VUPORT.ORIG
  0.4  .35 VUPORT.SIZE
;

: YCROSS
  0.61 0.3 VUPORT.ORIG
  0.4  .35 VUPORT.SIZE
;

: SPECS.WIN
  0.0 0.04 VUPORT.ORIG
  1.0 0.26 VUPORT.SIZE
;

: UPPER
  0.0 0.5 VUPORT.ORIG
  1.0 0.5 VUPORT.SIZE
;

: LOWER
  0.0 0.0 VUPORT.ORIG
  1.0 0.5 VUPORT.SIZE
;

: 1DLOWER
  0.0 0.7  VUPORT.ORIG
  1.0 0.35 VUPORT.SIZE
;

: 1DUPPER
  0.0 0.65 VUPORT.ORIG
  1.0 0.35 VUPORT.SIZE
;

: 1DSPECS.WIN
  0.0 .51 VUPORT.ORIG
  1.0 .46 VUPORT.SIZE
;

: 2DSPECS.WIN
  0.0 .04 VUPORT.ORIG
  1.0 .46 VUPORT.SIZE
;

3  STRING $RATIO
6  STRING $WIDTH
8 STRING $XDELAY
8 STRING $YDELAY
6  STRING $LAMBDA
10 STRING $TYPE
11 STRING FILENAME

REAL SCALAR RATIO
REAL SCALAR WIDTH
REAL SCALAR XDELAY
REAL SCALAR YDELAY
REAL SCALAR LAMBDA
REAL SCALAR FACTOR
REAL SCALAR OFFSET
REAL SCALAR YOFFSET
INTEGER SCALAR ESCAPE.FLAG
INTEGER SCALAR BOUND
INTEGER SCALAR ARRAY.TYPE
INTEGER SCALAR XMAXPOS
INTEGER SCALAR YMAXPOS
INTEGER SCALAR CODE
INTEGER SCALAR PLOT.TYPE
REAL SCALAR PERCENTAGE
REAL SCALAR XANGLE
REAL SCALAR YANGLE
REAL SCALAR MAX

DIM( 64 , 64 ) COMPLEX ARRAY IMAGE2
DIM( 2048 )    COMPLEX ARRAY IMAGE1
DIM( 64 , 64 ) REAL ARRAY PHASE2
DIM( 2048 )    REAL ARRAY PHASE1
DIM( 10 )      INTEGER ARRAY CELL
DIM( 128 )     REAL ARRAY P1
DIM( 128 )     REAL ARRAY P2
DIM( 64  )     REAL ARRAY AMP1
DIM( 64  )     REAL ARRAY AMP2
```

```
: CLEAR.KEYS
   132 0 DO
      ' FUNCTION.KEY.DOES NOP
   LOOP
;
: FF.QUIT
   SCREEN.CLEAR
   (SPLIT2) SCREEN.CLEAR BELL ." QUIT?"
   PCKEY ?DROP 89 = IF BYE THEN
;
: READ.FILE
   NORMAL.DISPLAY
   (DEF) SCREEN.CLEAR
   ." HERE IS A LIST OF NLC OPTICAL PHASE GRATING" CR
   ." FILES WHICH HAVE BEEN PREVIOUSLY SAVED:" CR
   CR DIR *.NLC
   CR CR
   " PLEASE ENTER THE NAME OF THE FILE YOU WISH TO REVIEW." CR
   ." (NO .NLC EXTENSION IS NECESSARY)
   "INPUT FILENAME "!=
   FILENAME
   0 "LEFT"
   ".NLC" "CAT
   FILENAME "!=

   SCREEN.CLEAR
   16 GRAPHICS.DISPLAY.MODE
   GRAPHICS.DISPLAY
   (SPLIT2)
   FILENAME DEFER> FILE.OPEN
   1 SUBFILE
   UPPER
   DIM( 30000 ) INTEGER UNNAMED.ARRAY
   FILE>ARRAY
   DIM( 30000 ) UNNAMED.ARRAY
   RESTORE.VUPORT
   2 SUBFILE
   LOWER
   DIM( 30000 ) UNNAMED.ARRAY
   FILE>ARRAY
   DIM( 30000 ) UNNAMED.ARRAY
   RESTORE.VUPORT
   FILE.CLOSE
ONERR: (DEF) SCREEN.CLEAR
        ." CAN'T FIND THE DESIRED FILE " FILENAME "TYPE ." ON DISK." CR
        ." PLEASE CHECK THE AVAILABLE FILES GIVEN, AND TRY AGAIN." CR
        CR
        ." TYPE ANY KEY TO CONTINUE " BELL PCKEY ?DROP DROP
        "FILE.OPEN IF FILE.CLOSE THEN
        ?YSELF
;

: WRITE.FILE
   FILE.TEMPLATE
      INTEGER DIM( 30000 ) SUBFILE
      INTEGER DIM( 30000 ) SUBFILE
   END

   (SPLIT2)
   SCREEN.CLEAR
   10 EMIT FILENAME DEFER! FILE.CREATE
   10 EMIT FILENAME DEFER! FILE.OPEN
   UPPER
   1 SUBFILE
   0 DIM( 30000 ) INTEGER UNNAMED.ARRAY !=
   DIM( 30000 ) UNNAMED.ARRAY
   STORE.VUPORT
   DIM( 30000 ) UNNAMED.ARRAY
   ARRAY>FILE
   LOWER
   2 SUBFILE
   0 DIM( 30000 ) UNNAMED.ARRAY !=
   DIM( 30000 ) UNNAMED.ARRAY
   STORE.VUPORT
   DIM( 30000 ) UNNAMED.ARRAY
   ARRAY>FILE
   FILE.CLOSE

ONERR)
          (SPLIT2)  SCREEN.CLEAR  ." DISK ERROR. CHECK FILE NAME"
          ." TYPE ANY KEY TO CONTINUE"
          BELL PCKEY
          ?DROP DROP
          "FILE.OPEN IF FILE.CLOSE
          THEN

;

: SAVE.NAME
   (SPLIT2) SCREEN.CLEAR
   ." NAME OF NEW FILE ? ( NO .NLC EXTENSIONS, PLEASE ) "
   "INPUT FILENAME "!=
   FILENAME
   0 "LEFT"
   ".NLC"
   "CAT
   FILENAME "!=
;: SAVE.SCREEN
  SAVE.NAME
  WRITE.FILE
;

: SPECS.SETUP
  (SPLIT2)
  UPPER VUPORT.CLEAR
  LOWER VUPORT.CLEAR
  FILE.OPEN SPECS.PIC

  1 SUBFILE
  DIM( 30000 ) INTEGER UNNAMED.ARRAY
  FILE>ARRAY
  1DSPECS.WIN
  DIM( 30000 ) UNNAMED.ARRAY
  RESTORE.VUPORT
  2 SUBFILE
  DIM( 30000 ) UNNAMED.ARRAY
  FILE>ARRAY
  2DSPECS.WIN
  DIM( 30000 ) UNNAMED.ARRAY
  RESTORE.VUPORT
```

```
    FILE.CLOSE
;

: 1D.FULL.PLOT
    1DUPPER
    1.0 1.0 DATA.SIZE
    AXIS.DEFAULTS
    HORIZONTAL GRID.OFF
    NO.LABELS
    AXIS.FIT.OFF
    VERTICAL AXIS.FIT.OFF
    PHASE1
    cyan axis.color
    1.white color
    white label.color
    Y.AUTO.PLOT
    white color
    NORMAL.COORDS
    0 CHAR.DIR
    0 LABEL.DIR
    .4 .07 POSITION
    " FAR-FIELD INTENSITY" LABEL
    .55 .125 POSITION
    .550 .2 DRAW.TO
    blue color
    OUTLINE
;

: 1D.NEARBY.PLOT
    1DLOWER
    AXIS.DEFAULTS
    1.0 1.0 DATA.SIZE
    HORIZONTAL GRID.OFF
    NO.LABELS
    AXIS.FIT.OFF
    VERTICAL AXIS.FIT.OFF
    PHASE1
    cyan axis.color
    white label.color
    1.white color
    Y.AUTO.PLOT
    white color
    NORMAL.COORDS
    .4 .07 POSITION
    0 CHAR.DIR 0 LABEL.DIR
    " HIGHER-ORDER TERMS" LABEL
    .55 .125 POSITION
    .55 .2 DRAW.TO
    blue color
    OUTLINE
;

: 1D.PERCENT.FIND
    PHASE1
    PHASE1
    0.0SUM
    /
    PHASE1 !=
    PHASE1 SUB[ XMAXPOS 10 - , 20 ]  0.0SUM
    100 * PERCENTAGE !=
    PHASE1 [ XMAXPOS ]
    MAX !=
;

: 1D.CLIP
    0. PHASE1 sub[ XMAXPOS 10 - , 20 ] !=
;

: 1D.ANGLE.FIND
    LAMBDA
    WIDTH /
    10 bound /
    2DE *
    4!
    real
    /
    XMAXPOS 1024 - *
    180 * PI / XANGLE !=
;

: 1D.MAX.FIND
    0. MAX !=
    2048 1 DO
       PHASE1 [ I ]
       MAX >
       IF
          I XMAXPOS !=
          PHASE1 [ I ] MAX !=
       THEN
    LOOP
;

: 1D.SPECS.PLOT
    SPECS.WIN
    (SPECS:  SCREEN.CLEAR
    ." RATIO OF LC WIDTH TO FULL CELL:  " RATIO .
    ."          WAVELENGTH: " LAMBDA . ." MICRONS." CR
    ." APERTURE WIDTH OF LC CELLS:      " WIDTH . ." MICRONS." CR
    ." PERCENTAGE OF BEAM IN MAIN LOBE: " PERCENTAGE . CR
    ." LOCATION OF DEFLECTED BEAM:      " XANGLE . ." DEGREES." CR
    STYPE "TYPE ." PHASE ARRAY.
    XDELAY . ." RADIANS TOTAL PHASE ACROSS ARRAY."
    blue color
    OUTLINE
;

: 1D.TRANS
    REAL
    Z=POL
    FFT
    1022 ROTATE
;

: CELL.MAKE
    RATIO 1 MODULO ABS
    10 *
    BOUND !=
    0 BOUND = IF
                 10 BOUND !=
              THEN
    0 CELL !=
    BOUND 1 - 1 DO
      I CELL [ I ] !=
    LOOP
    BOUND 10.0 /
    RATIO !=
    RATIO "," $RATIO "!=
;
```

```
       XDELAY *   *
       PHASE1 !=
    THEN
;

: 1C.PHASE.MAKE
    REAL
    1 ARRAY.TYPE =
    IF
       2048 RAMP
       1 -
       2048 *
       8192 /
       XDELAY *
       *
       PHASE1 !=
    ELSE
       2048 RAMP 2048 *
       10 /       0.5 -
       FIX        REAL
       10.0 *     8192 /
       XDELAY *     *
       PHASE1 !=
    THEN
;

: 2C.PHASE.MAKE
    REAL
    1 ARRAY.TYPE =
    IF
       2048 RAMP 1 -
       4096 *
       8192 /
       XDELAY *
       *
       PHASE1 !=
    ELSE
       2048 RAMP  4096 *
       10 /         0.5 -
       FIX          8192 /
       10.0 *       REAL
       XDELAY *       *
       PHASE1 !=
    THEN
;

: 3C.PHASE.MAKE
    REAL
    1 ARRAY.TYPE =
    IF
       2048 RAMP 1 -
       6144 *
       8192 /
       XDELAY *
       *
       PHASE1 !=
    ELSE
       2048 RAMP    6144 *
       10 /         0.5 -
```

```
: X1.AMP.MAKE
    REAL
    CELL
    0 1 DO
      DUP
      CATENATE
    LOOP
    SUB[ 1 , 2048 ]
    DUP
;

: X2.AMP.MAKE
    REAL
    CELL
    10 1 DO
      DUP
      CATENATE
    LOOP
    SUB[ 2049 , 2048 ]
    DUP
;

: X3.AMP.MAKE
    REAL
    CELL
    11 1 DO
      DUP
      CATENATE
    LOOP
    SUB[ 4097 , 2048 ]
    DUP
;

: X4.AMP.MAKE
    REAL
    CELL
    11 1 DO
       DUP
       CATENATE
    LOOP
    SUB[ 6145 , 2048 ]
    DUP
;

: X1.PHASE.MAKE
    REAL
    1 ARRAY.TYPE =
       IF
          2048 RAMP 1 -
          8192 /
          XDELAY *
          *
          PHASE1 !=
       ELSE
          2048 RAMP
          10 /       0.5 -
          FIX        REAL
          10.0 *     8192 /
```

```
       FIX          REAL
       10.0 *       8192 /
       XDELAY *       *
       PHASE1 !=
    THEN
;

: 1C.EXPON
    ZPOL
    PHASE1 !=
    1C BOUND /
    2DE * 4!
    .0 *
    ) sweep /
    FACTOR !=
    2048 1 DO
      -2 PI *
      FACTOR
      I 1024 -   *
      *
      OFFSET *
      PHASE1 [ I ] *
      PHASE1 [ I ] !=
    LOOP
    PHASE1
    Z=POL
    IMAGE1 *
    IMAGE1 !=
;

: X1.EXPON
    0. image1 !=
    0. PHASE1 !=
    -3072 OFFSET !=
    1d.expon
;

: X2.EXPON
    -1024.offset !=
    1d.expon
;

: X3.EXPON
    1024 OFFSET !=
    1d.expon
;

: X4.EXPON
    3072 OFFSET !=
    1d.expon
;

: BLAZED
    1 ARRAY.TYPE !=
    " BLAZED" STYPE "!=
;
: PISTON
    0 ARRAY.TYPE !=
    " PISTON" STYPE "!=
;
: 1D.MENU
```

```
    0 $228 !=
    0 $22C !=1ag !=
    CLEAR.KEYS
    (SPLIT2' SCREEN.CLEAR 8 SPACES
    ." 41: new 1D array    #41 Scr Print    49: save    HOME)
    array
    ?error
    code !=
    code case
            71 of 2 escape.flag !=   endof
            41 of 1 escape.flag !=   endof
            49 of save.screen        endof
            76 of ###.quit           endof
            myself
         endcase
;
0 ESCAPE.FLAG !
  1+
  myself
then
: TYPE.MENU

    0 CODE !=
    (SPLIT2' SCREEN.CLEAR
    22 SPACES
    ." 67: blazed          68: piston"
    clear.kbuf
    KEY
    TOKEN
    CODE !=
    CODE CASE
            67 OF BLAZED  ENDOF
            68 OF PISTON  ENDOF
            myself
         ENDCASE
;
: 2D.CLIP
    PHASE2 [ YMAXPOS , XMAXPOS ]   DUP
    PHASE2 [ YMAXPOS , XMAXPOS ] !=
    0. PHASE2 [ YMAXPOS , XMAXPOS ] !=
    PHASE2 ()MAX ()MAX  1.0 *     )
    IF
       1.0    PHASE2 ()MAX ()MAX    *
       PHASE2 [ YMAXPOS , XMAXPOS ] !=
       DROP
    ELSE
       PHASE2 [ YMAXPOS , XMAXPOS ] !=
    THEN
;

: X.CROSS

    SCREEN.VIEWPORT.CLEAR
    AXIS.DEFAULTS
    HORIZONTAL NO.LABELS
    HORIZONTAL GRID.OFF
    AXIS.FIT.OFF
    VERTICAL AXIS.FIT.OFF
    PHASE2
    1SECT' [ YMAXPOS , ' ]
```

```
white LABEL.COLOR
1.WHITE COLOR
Y.AUTO.PLOT
blue color
OUTLINE
WHITE COLOR
NORMAL.COORDS
.3 .07 POSITION
" X CROSS-SECTION" LABEL
NORMAL.COORDS
.548 .10 POSITION
.548 .20 DRAW.TO
;

: Y.CROSS

  YCROSS VUPORT.CLEAR
  AXIS.DEFAULTS
  HORIZONTAL NO.LABELS
  HORIZONTAL GRID.OFF
  AXIS.FIT.OFF
  VERTICAL AXIS.FIT.OFF
  PHASE2
  1SECTC ( , IMAIPOS )
  cyan axis.color
  white label.color
  1.white color
  Y.AUTO.PLOT
  blue color
  OUTLINE
  NORMAL.COORDS
  white color
  .3 .07 POSITION
  " Y CROSS-SECTION" LABEL
  normal.coords
  .548 .1  POSITION
  .548 .2  DRAW.TO
;


: XYZ.PLOT
  STACK.CLEAR
  3avu vuport.clear
  clear.axis.defaults
  .05 .05 data.origin
  phase2
  1.white color
  argn.plot
  blue color
  outline
  (split2:
;
: CONT.PLOT
  CODE
  STACK.CLEAR
  3avu vuport.clear
  clear.axis.defaults
  HORIZONTAL GRID.ON
  VERTICAL   GRID.ON
  phase2
  1.white color
  7 contour.plot
  blue color
  outline
  white color
  WORLD.COORDS
  IMAIPOS 0 POSITION
  IMAIPOS 5 DRAW.TO
  0 YMAIPOS POSITION
  5 YMAIPOS DRAW.TO
  (split2:
;
: 2D.SPECS.PLOT
  SPECS.WIN
  (SPECS:  SCREEN.CLEAR
  -1 2 fix.format
  ratio ." ratio       " cr
  lambda ." slambda    " cr
  width ." swidth      " cr
  xdelay ." sxdelay    " cr
  ydelay ." sydelay    " cr
  ." RATIO OF LC WIDTH TO FULL CELL:    " $RATIO .TYPE
  ."          WAVELENGTH: " $LAMBDA .TYPE ." MICRONS." CR
  ." LOCATION OF DEFLECTED BEAM:        " $ANGLE .
  TYPE ." DEGREES." CR
  ." APERTURE WIDTH OF LC CELLS:        " $WIDTH .TYPE ." MICRONS."
  CR
  ."          X - $XDELAY .TYPE CR
  ." PERCENTAGE OF BEAM IN MAIN LOBE:   " PERCENTAGE .
  ."          Y - $YDELAY .TYPE CR
  $TYPE .TYPE ." PHASE ARRAY."
  24 SPACES ." RADIANS TOTAL PHASE ACROSS ARRAY."
  blue color
  OUTLINE
;
: 2DMENU
   0 escape.flag !
   0 code !
   CLEAR.EVE
   (SPLIT: SCREEN.CLEAR
   ." 42: new 2D-plot  43: xyz  44: contour  Prt Sc: print  49: save"
   ."  HOME: main menu"
  cursor.off
  echo
  "droc
  code !
  code case
          71 of 2 escape.flag !     endof
          42 of 1 escape.flag !     endof
          43 of xyz.plot            endof
          44 of cont.plot           endof
          49 of save.screen         endof
          79 of 44.quit             endof
          eveil
        endcase

0 escape.flag @
  if
    eveil
  then
```

```
: 2D.PERCENT.FIND

  PHASE2
  PHASE2
  ()SUM ()SUM
  /
  PHASE2 !*
  PHASE2 SUB( YMAIPOS 2 - , 4   IMAIPOS 2 - , 4 )  ()SUM ()SUM
  10  *
  PERCENTAGE !*
  PHASE2 ( YMAIPOS , IMAIPOS )
  MAX !*
;

: 2D.ANGLE.FIND
  LAMBDA
  WIDTH /
  10 BOUND /
  0.5 0 fix
  fsqrt
  /
  DUP
  IMAIPOS 32 - *
  180 * PI /
  XANGLE !*
  YMAIPOS 32 - *
  180 * PI /
  YANGLE !*
;

: 2D.MAX.FIND
  0. MAX !*
  65 1 DO
  65 1 DO
     PHASE2 ( J , I )
     MAX  )
     I*
       PHASE2 ( J , I )
       MAX !*
       I IMAIPOS !*
       J YMAIPOS !*
     THEN
  LOOP
  LOOP
;

: AMP.MAKE

  CELL
  7 1 DO
       CELL
       CATENATE
    LOOP
  SUB( 1 , 64 )
  AMP1 !*

  CELL
  13 1 DO
       CELL
       CATENATE
    LOOP
  SUB( 65 , 64 )
  AMP2 !*
;

: 2D.AMP1

  AMP1  AMP1 ( I ) *
  65 2 DO
       AMP1
       AMP1 ( I )
       *
       LAMINATE
  LOOP
  DUP
;

: 2D.AMP2
  AMP2 AMP2 ( I ) *
  65 2 DO
       AMP2
       AMP2 ( I )
       *
       LAMINATE
  LOOP
  DUP
;

: 2D.AMP3
  AMP3  AMP3 ( I ) *
  65 2 DO
       AMP1
       AMP3 ( I )
       *
       LAMINATE
    LOOP
    DUP
;

: 2D.AMP4
  AMP4  AMP4 ( I ) *
  65 2 DO
       AMP2
       AMP4 ( I )
       *
       LAMINATE
    LOOP
    DUP
;

: PHASE.MAKE

: ARRAY.TYPE *
  IF
    REAL
    128 RAMP 128 /
    XDELAY *
    PI !*
    128 RAMP 128 /
    YDELAY *
    PI !*
  ELSE
    128 RAMP 1 - 1.0078740 *
    10       0.5 -
    FIX   REAL
    10.0 * 128 /
    XDELAY *
    PI !*
    128 RAMP 1 - 1.0078740 *
    10       0.5 -
    FIX   REAL
    10.0 * 128 /
    YDELAY *
    PI !*
  THEN
;
```

```
PHASE.MAKE

: ARRAY.TYPE *
  IF
    REAL
    128 RAMP 128 /
    XDELAY *
    PI !*
    128 RAMP 128 /
    YDELAY *
    PI !*
  ELSE
    128 RAMP 1 - 1.0078740 *
    10       0.5 -
    FIX   REAL
    10.0 * 128 /
    XDELAY *
    PI !*
    128 RAMP 1 - 1.0078740 *
    10       0.5 -
    FIX   REAL
    10.0 * 128 /
    YDELAY *
    PI !*
  THEN
;


: 2D.PHASE1

  P1  SUB( 1 , 64 ) P2 ( I ) *
  65 2 DO
       P1 SUB( I , 64 )
       P2 ( I )
       *
       LAMINATE
  LOOP
  *
  PHASE2 !*
;


: 2D.PHASE2
  P1 SUB( 65 , 64 ) P2 ( I ) *
  65 2 DO
       P2 ( I )
       P1 SUB( 65 , 64 )
       *
       LAMINATE
  LOOP
  *
  PHASE2 !*
;

: 2D.PHASE3
  P1 SUB( 1 , 64 ) P2 ( 65 ) *
  65 2 DO
       P1 SUB( I , 64 )
       P2 ( 65 )
       *
       LAMINATE
  LOOP
  *
  PHASE2 !*
;


: 2D.EXPON
  IMAGE
  PHASE2 !*
  1* BOUND /
  0.5 *
  FIX
  I *
  ! SWAP

  FACTOR !*
  65 1 DO
     65 1 DO
     FACTOR
     I 32 - *
     OFFSET *
     FACTOR
     J 32 - *
     YOFFSET *
     *
     -2 PI *
     *
     PHASE2 ( J , I ) *
     IMAGE ( J , I ) !*
     LOOP
  LOOP
  PHASE2
  IMAG.
  IMAGE *
  IMAGE2 !*
;

: 2D.EXPON1
  0.0 IMAGE !*
  0.0 PHASE2 !*
  DFFSET !*
  YOFFSET !*
  2D.EXPON
;
```

```
: 2D.EXPON2
  32 OFFSET !=
  32 YOFFSET !=
  2D.EXPON
;

: 2D.EXPON3
  -32  OFFSET !=
  -32 YOFFSET !=
  2D.EXPON
;

: 2D.EXPON4
  32 OFFSET !=
  -32 YOFFSET !=
  2D.EXPON
;

: 2D.TRANS

  REAL
  I=POL
  2D.FFT
  31 ROTATE TRANS[ I , 2 ]
  31 ROTATE TRANS[ I , 2 ]
;


: 2D.DRIVER

  STACK.CLEAR
  16 GRAPHICS.DISPLAY.MODE
  GRAPHICS.DISPLAY
  SPECS.SET
  (SPLIT2) SCREEN.CLEAR
  ." 1. RATIO ? " $INPUT
  IF RATIO !=
     ELSE 1.0 RATIO !=
     THEN
  SCREEN.CLEAR
  ." 2. CRYSTAL SIZE ? " $INPUT
  " WIDTH !=
     ELSE 10.0 WIDTH !=
     THEN
  TYPE.MENU
  0. IMAGE1 !=
  0. PHASE1 !=
  SCREEN.CLEAR
  ." ENTER THE TOTAL PHASE DELAY ACROSS THE X-DIRECTION, IN RADIANS. "
  $INPUT
  IF XDELAY !=
     ELSE 0.0 XDELAY !=
     THEN
  SCREEN.CLEAR
  ." ENTER THE TOTAL PHASE DELAY ACROSS THE Y-DIRECTION, IN RADIANS. "
  $INPUT
  IF YDELAY !=
     ELSE   0.0 YDELAY !=
     THEN
  SCREEN.CLEAR
```

```
  ." WHAT IS THE OPERATING WAVELENGTH ( IN MICRONS ) ? "
  $INPUT
  IF LAMBDA !=
     ELSE 1.0e LAMBDA !=
     THEN
  SCREEN.CLEAR
  CELL.MAKE
  APP.MAKE
  PHASE.MAKE
  ." NOW COMPUTING TRANSFORM #1 OF 4."
  2D.APP1
  2D.PHASE1
  PHASE1
  2D.TRANS
  2D.EXPON1
  SCREEN.CLEAR
  ." NOW COMPUTING TRANSFORM #2 OF 4."
  2D.APP2
  2D.PHASE2
  PHASE2
  2D.TRANS
  2D.EXPON2
  SCREEN.CLEAR
  ." NOW COMPUTING TRANSFORM #3 OF 4."
  2D.APP3
  2D.PHASE3
  PHASE3
  2D.TRANS
  2D.EXPON3
  SCREEN.CLEAR
  ." NOW COMPUTING TRANSFORM #4 OF 4."
  2D.APP4
  2D.PHASE4
  PHASE4
  2D.TRANS
  2D.EXPON4
  SCREEN.CLEAR
  ." NOW COMPUTING PERCENTAGES, MAX, CROSS-SECTIONS, ETC."
  IMAGE2
  DUP
  CONJ
  *
  IMAG
  PHASE2 !=

  2D.MAX.FIND
  2D.ANGLE.FIND
  2D.PERCENT.FIND
  2D.CLIP

  UPPER VLPORT.CLEAR
  LOWER VLPORT.CLEAR
  0.CROSS
  Y.CROSS
  2D.GRAPH.PLOT

  2GRAPH

  1 ESCAPE.FLAG !
;
```

```
    ayself
  then
;

: 1D.DRIVER

  STACK.CLEAR
  16 GRAPHICS.DISPLAY.MODE
  GRAPHICS.DISPLAY
  SPECS.SET!"
  (SPLIT2  SCREEN.CLEAR
  ." 1. RATIO ? "  $INPUT
  IF RATIO !=
     ELSE 1.0 RATIO !=
     THEN
  SCREEN.CLEAR
  ." 2. CRYSTAL SIZE ? " $INPUT
  IF WIDTH !=
     ELSE  10.0 WIDTH !=
     THEN
  TYPE.MENU
  0. IMAGE1 !=
  0. PHASE1 !=
  SCREEN.CLEAR
  ." ENTER THE TOTAL PHASE DELAY ACROSS THE ARRAY, IN RADIANS.  "
  $INPUT
  IF XDELAY !=
     ELSE 0.0 XDELAY !=
     THEN
  SCREEN.CLEAR
  ." WHAT IS THE OPERATING WAVELENGTH ( IN MICRONS ) ? " $INPUT
  IF LAMBDA !=
     ELSE 1.0  LAMBDA !=
     THEN
  SCREEN.CLEAR
  CELL.MAKE
  (SPLIT2  SCREEN.CLEAR ." NOW COMPUTING TRANSFORM #1 OF 4"
  1D.APP.MAKE
  1D.PHASE.MAKE
  PHASE1
  1D.TRANS
  1D.EXPON
  SCREEN.CLEAR ." NOW COMPUTING TRANSFORM #2 OF 4"
  2D.APP.MAKE
  2D.PHASE.MAKE
  PHASE2
  2D.TRANS
  2D.EXPON
  SCREEN.CLEAR ." NOW COMPUTING TRANSFORM #3 OF 4"
  3D.APP.MAKE
  3D.PHASE.MAKE
  PHASE3
  3D.TRANS
  3D.EXPON
  SCREEN.CLEAR ." NOW COMPUTING TRANSFORM #4 OF 4"
  4D.APP.MAKE
  4D.PHASE.MAKE
  PHASE4
  4D.TRANS
  4D.EXPON
```

```
  SCREEN.CLEAR ." NOW COMPUTING PERCENTAGES, MAX, ETC."
  IMAGE1
  DUP
  CONJ
  *
  ZMAG
  PHASE1 !=


  1D.MAX.FIND
  1D.ANGLE.FIND
  1D.PERCENT.FIND
  UPPER VLPORT.CLEAR
  LOWER VLPORT.CLEAR
  1D.FULL.PLOT
  1D.CLIP
  1D.MEARF.PLOT
  1D.SPECS.PLOT
  (SPLIT2
  CURSOR.OFF

  1D.MENU

  1 escape.flag !
    if
      ayself
    then
;


: RESTORE.KEYS
  0 ESCAPE.FLAG !
  (SPLIT2) SCREEN.CLEAR  8 SPACES
  ." #10) another file review      Prt Scr  print      HOME) main menu"
  CURSOR.OFF
  PCKE
  "DROP
  CODE !=
  CODE CASE
        F10  OF   1 ESCAPE.FLAG !=      ENDOF
        ^    OF   2 ESCAPE.FLAG !=      ENDOF
        MYSELF
      ENDCASE
;
: MAIN.KEYS
    PCKE
    "DROP
    CODE !=
    CODE CASE
            F1  OF                  ENDOF
            F2  OF                  ENDOF
            F10 OF                  ENDOF
            ^P  OF                  ENDOF
            MYSELF
        ENDCASE
;
```

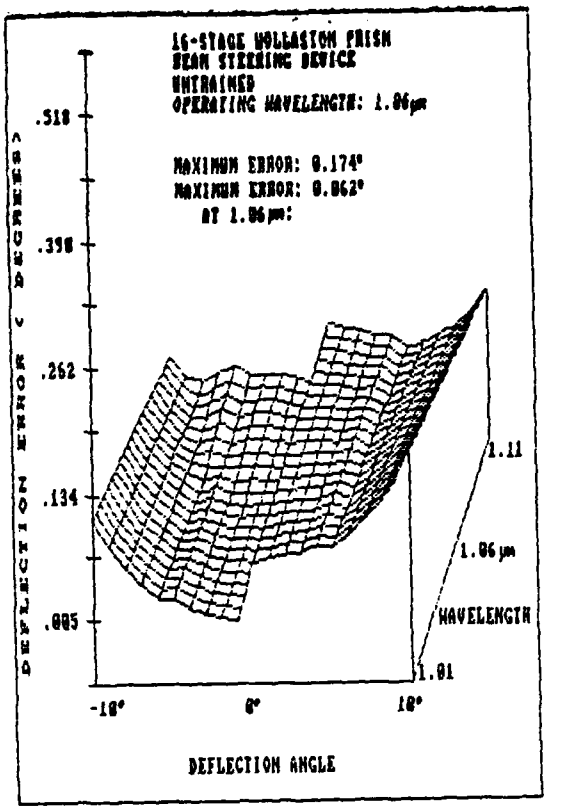

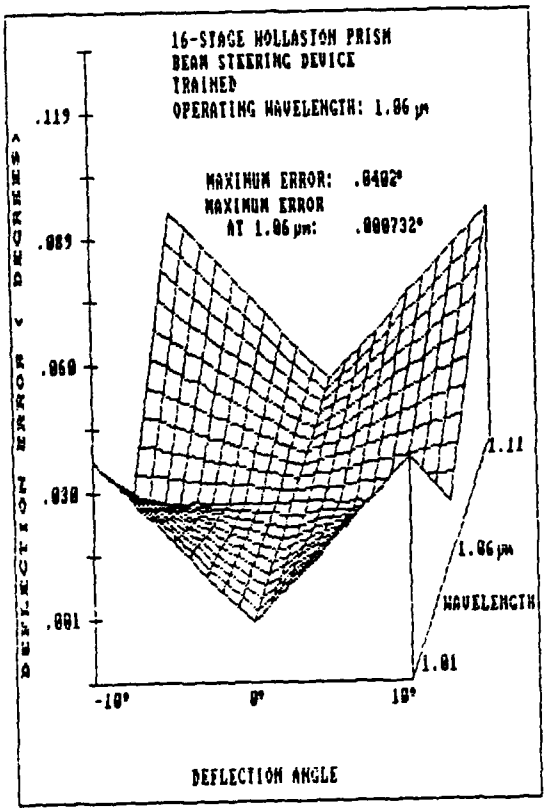

FIGURE 1: ANGULAR DEFLECTION ERROR VERSUS INPUT WAVELENGTH AND DESIRED DEFLECTION ANGLE, UNTRAINED AND TRAINED WOLLASTON PRISM BEAM DEFLECTORS.

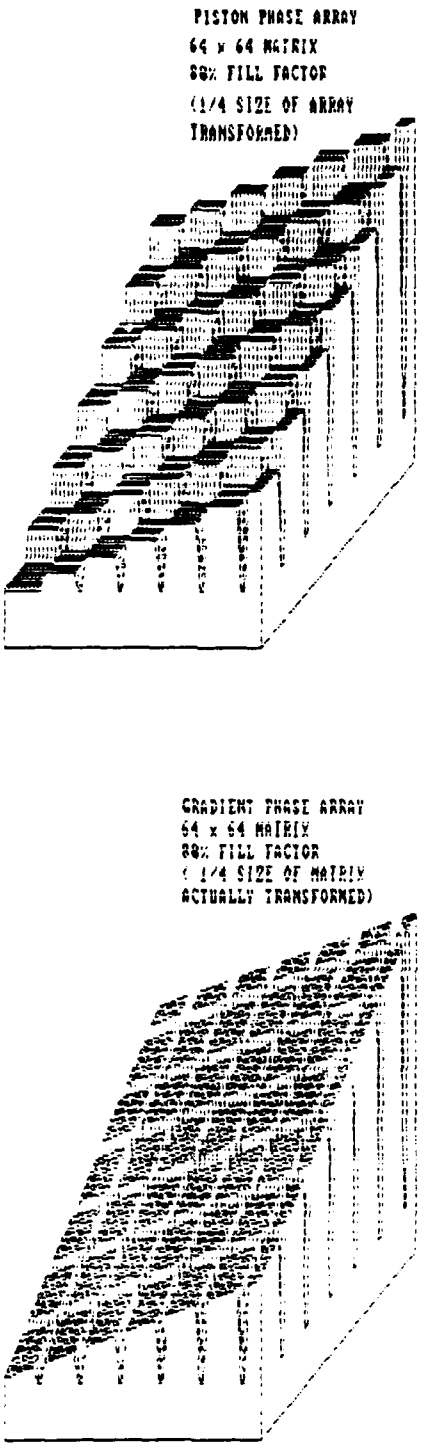

FIGURE 2: COMPARISON OF PISTON VERSUS GRADIENT PHASE PATTERNS FOR A TWO-DIMENSIONAL PHASE ARRAY.

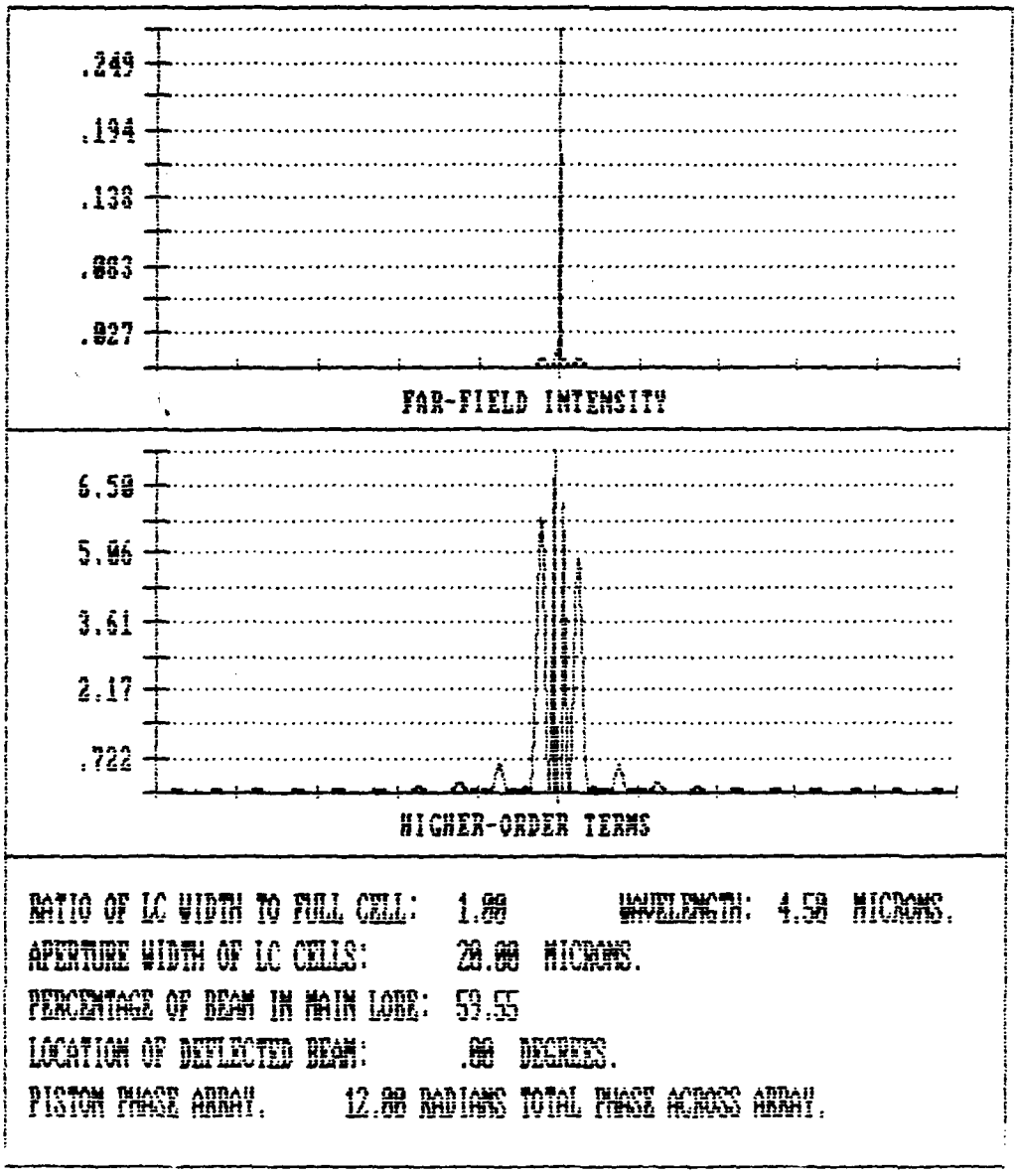

FIGURE 3: EXAMPLE OUTPUT FROM THE FAR-FIELD PATTERN PROGRAM, MODELING A ONE-DIMENSIONAL OPTICAL PHASE ARRAY.

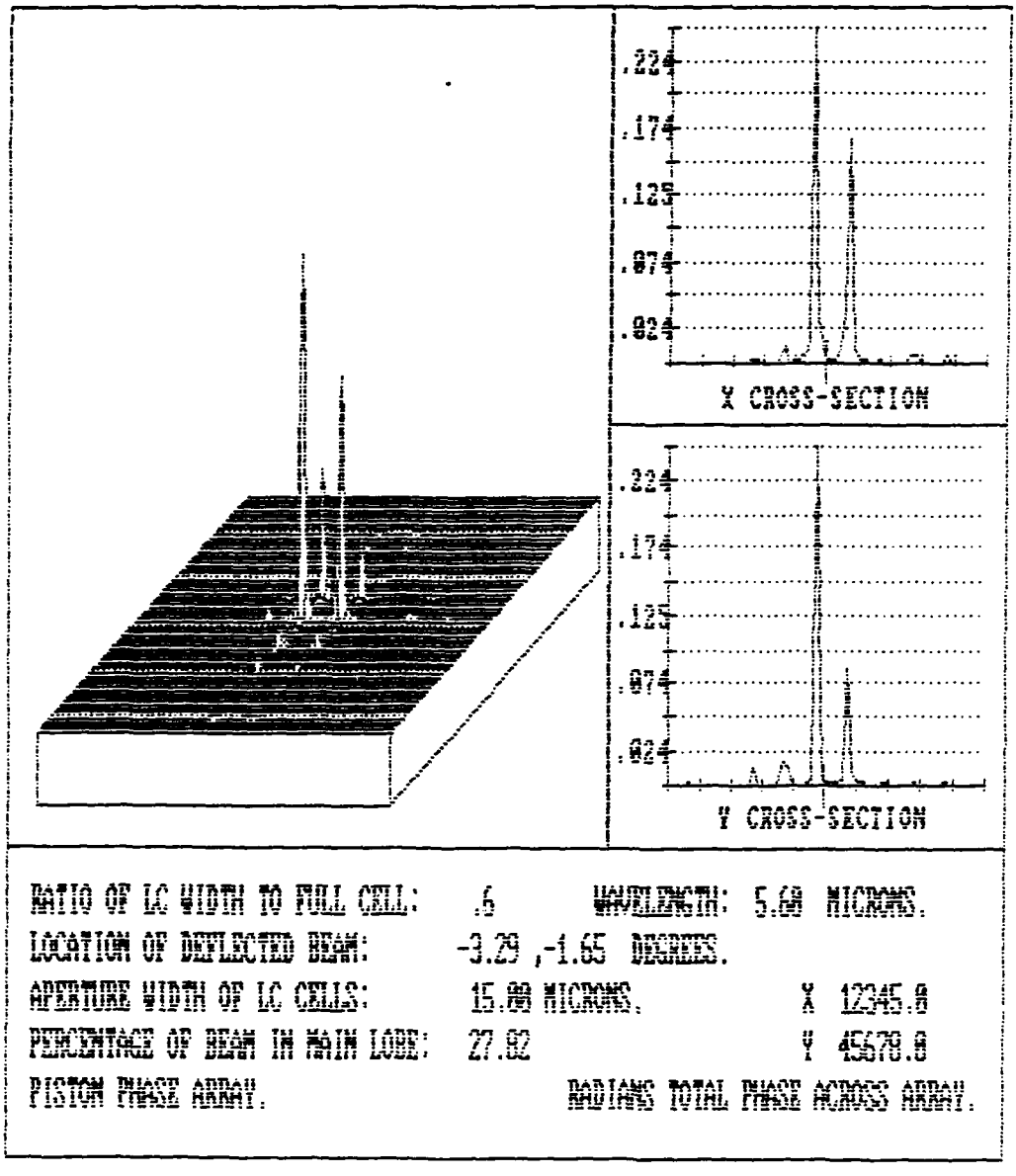

FIGURE 4: EXAMPLE OUTPUT FROM THE FAR-FIELD PATTERN PROGRAM, MODELING A TWO-DIMENSIONAL OPTICAL PHASE ARRAY.

1988 USAF-UES SUMMER FACULTY RESEARCH PROGRAM/

GRADUATE STUDENT RESEARCH PROGRAM

Sponsored by the

AIR FORCE OFFICE OF SCIENTIFIC RESEARCH

Conducted by the

Universal Energy Systems, Inc.

FINAL REPORT

ACQUISITION OF DIGITAL RADAR DATA FOR USE ON THE IMPROVED ISAR SOFTWARE

Prepared by:	Ed Grissom
Academic Rank:	Graduate Student
Department and University:	Electrical Engineering, Tennessee Technological University
Research Location:	AFWAL/AAWP-1 WPAFB Dayton, Ohio 45433-6543
USAF Researcher:	Dr. James B.Y. Tsui
Date:	September 8, 1988
Contract No:	F49620-88-C-0053

Edward Grissom

ABSTRACT

ACQUISITION OF DIGITAL RADAR DATA FOR USE ON THE IMPROVED ISPX SOFTWARE

The methods used to acquire radar signals in a digital form are explained. A set of programs developed to capture, transfer, and process the digital data are described, along with instructions for their use. Several improvements to the ISPX software are introduced and explained.

Acknowledgements

I wish to thank the Air Force Office of Scientific Research for sponsorship of this research. Universal Energy Systems must be mentioned for their concern and help to me in all administrative and directional aspects of this program.

My summer was an enriching experience due to all of the help and support given me by the members of the Passive ECM group. I wish to thank Dr. Jim Tsui for giving me such an interesting project, and to Mrs. Tsui and Mr. and Mrs. Gerd Schrick for their hospitality and graciousness in invinting me to their homes. A special thank you is reserved for F. Bryan Loucks for keeping my social agenda full and insuring there was never a dull moment during my stay in Dayton.

I. INTRODUCTION

The acquisition of real world radar data in a discrete time form is required for any computer analysis of radar signals. The Passive ECM Group at Wright-Patterson Aeronautical Laboratory has been developing a package of radar signal analysis routines which were tested and evaluated based on computer generated data. Due to the high frequency of radar signals, no method for capturing real world signals had been developed.

My research interests have been in the area of specialized hardware for digital signal processing. My work as a technician in a lab devoted to computer aided hardware development uniquely qualifies me to work on both the hardware and software aspects of radar signal acquisition and analysis.

II. OBJECTIVES OF THE RESEARCH EFFORT

As of the beginning of my assignment as a participant in the 1986 Graduate Student Research Program (GSRP) there was no method for acquiring radar frequency data in a discrete time format. In addition to this, the Interactive Signal Processing Executive (ISPX) analysis software was lacking a method for

determining the exact frequency of peaks in the spectrum of a signal. As I became familiar with the ISPX package, I encountered a number of deficencies in the program's ability to manipulate data.

My research effort for the 1988 GSRP was to remedy the deficencies in the ISPX software, and to develop a method for obtaining real world radar data using available equipment.

III. OBTAINING DIGITAL DATA:

Equipment and Programs Needed

(1) HP 54D111 Digitizing Oscilloscope

(2) TN1000 Tuner and Mixer

(3) HP 9836 or 9826 personal computer (PC)

(4) HP-IB cables

(5) Signal Source (Frequency Generator or Antenna)

(6) Cabling for the signal source, and two equal length coax cables for the connection from the mixer outputs to the O-scope inputs.

(7) 4 - 120 VAC outlets

(8) HP Basic Boot Disk and "NEWTN" control program.

(9) DS/DD Data Storage Diskette(s)

Set-up

Connect All Power Cabling Connect HP-IB to Scope, Tuner, and PC . Connect Signal Source to Tuner (RF IN, not REF IN) and connect channel 1 and 2 on the scope to the tuner outputs. The channels on the tuner are I and Q, I is on the left and should go to channel 1. Insert the Basic boot disk and power up all components. (NOTE: There are two power switches and two power cables on the Tuner). Insert "NEWTN" disk and 'LOAD "NEWTN"'. Press 'RUN' on the PC Press 'REC', 'SETUP', and 'EXIT' to initialize the scope.

To manually set the tuner center frequency, press 'MODE' then 'MAN FREQ' then enter the frequency in MHz (5.5 GHz = 5500). To scan a range of frequencies, press 'MODE' then 'BAND' to set the limits of the scanned band. Press 'MODE', 'SCAN' to choose step size and start the scan. You should use a manual frequency setting for the best results in data acquisition. Adjust scope sensitivity, trigger level, and time base for the desired display. Auto Scale does not always give the best possible display and may not find the

signal. Note that the display is only a small portion of the acquired waveform. Adjust the parameters accordingly.

Acquisition and Storage

All acquisition is done from the 'REC' mode. In 'REC' mode, local control of the scope is occasionally disabled. Front panel (local) control of the scope can be regained by pressing the front panel "LOCAL" button or by pressing 'GO LOCAL' on the PC . In the upper right corner of the scope display is a Remote/Local status indicator. No indication means the front panel controls are enabled. "R" or "RL" generally mean it is OK to go to local control. "RT" means the scope is talking to the PC . You are hereby warned that going to local control while the scope is talking to the PC will result in loss of data.

Press 'DIGITIZE' to obtain data. 'DIGITIZE' sets the scope for single shot acquisition and arms the trigger. When the trigger is activated, the scope displays the captured waveform and also stores both channels in the waveform memories. You may press 'DIGITIZE' as many times as you wish to capture new data. Note: previous data is lost if not 'TRANSFER'ed to the PC . Also: new data is not displayed until the

scope displays "Stopped". If the scope displays "Awaiting Trigger" or "Running", the waveform memories have not been updated.

Press 'TRANSFER' to bring the contents of both waveform memories to the RAM on the PC . It takes approximately 2 min. to transfer the data. Do NOT go to local mode during the transfer or data will be lost. "TRANS DONE" is displayed when the transfer is complete.

Once the data is in RAM on the PC it may be listed on the screen. Press 'LIST' to enter list mode. Press K0 (default '1') to change the beginning point of the list and K1 (default '8192') to change the stopping point of the list. Press 'LIST' to begin the output. Eighteen lines of three columns are displayed; Channel 1, Channel 2, and Point #. Channels 1 and 2 are integers between 0 and 256 (8 bit digitizations). 0 is the bottom of the channel display and 256 is the top of the display no matter what settings are chosen for the offsets, sensitivity, and timebase. To continue with another 18 lines, press 'CONT'. To abort the listing, press K0('ABORT') immediatley after 'CONT'.

RAM Data may be stored to diskette by inserting the Data Diskette and pressing 'STORE A:'. You are prompted for a filename. The storing takes about 2

min. The scope may be adjusted (in LOCAL mode) during this process. Previously stored Data on Disk can be loaded to RAM with 'LOAD'. You are prompted for a filename. The RAM data can be sent to the waveform memories on the scope with the 'PLOT' command. Note: Waveform memory is displayed by separate commands from the Channel 1 and 2 display on the scope.

The 'REC' mode is exited by pressing 'EXIT' and the Tuner program is exited by pressing 'QUIT'.

IV. CONVERTING AND TRANSFERRING DATA

Equipment and Programs Needed

(1) HP 9836 PC

(2) HP Basic Boot Disk and "NEWTN" Program Disk.

(3) Terminal Emulation Software ('boot:' and 'term:' disks)

(4) 1 - 120 VAC outlet

(5) RS-232 Cabling for connection to host computer

(6) Diskette with binary data (from "NEWTN" program) and blank formatted diskettes for ASCII data

Converting

Plug in, connect up, and turn everything on. "NEWTN" stores data in three files. The extensions 'DAT', 'HED', and 'PRE' are used to distinguish between the files. 'PRE' is used to store the preamble information needed by the scope to re-construct the waveform. 'HED' is used to store the information needed to align and locate the data by the 'CH' and 'ISPX' software on the VAX. The first two bytes are a binary integer representing the center frequency of the tuner when the acqusition was made. The next two lines are ASCII characters containing the xinc, xorg, xref, yinc, yorg, and yref data for both channels from the 54D111 scope. 'DAT' contains the 16384 data points stored as 2-byte words. The first 8192 points are from channel 1 and the last 8192 points are from channel 2.

Boot the Basic System on the HP9836. 'LOAD "DATCON"' from the program disk. Remove the program disk and insert the binary data disk in Drive 0 (right hand drive). Insert the blank disk in Drive 1. Press 'RUN' and enter the filename (without the 'DAT' extension) of the binary data. "DATCON" will read the binary information on Drive 0 and write it in ASCII format on Drive 1. The conversion takes approximately 2.5 min. The ASCII data normally takes up just under half of the space on a DS/DD disk so that only two

ASCII files may be recorded per diskette. If you reuse an ASCII disk, 'PURGE' the original ASCII files before attempting to write new ones.

Transferring

Insert the 'boot:' disk of the terminal emulation software in drive 0 and the 'term:' disk in drive 1. Re-boot the system. A default (enter) answer to the three questions is sufficient to get the program running. Press 'enter' to bring up the host computer prompt. Log in and, if necessary, set the terminal characteristics on the HP and the host computer to match.

Move to the directory where you wish to store the data. To run the ISPX software on the data, the best place to store the data is in the directory [isu.rajan.data2]. Prepare the host computer to retrieve the data. On a UNIX system this is done by:

```
% cat > fname
```

where fname is the name of the file where you wish the data to be stored. On a VMS system use:

```
$ copy SYS$INPUT fname
```

Set up the HP to transmit the ASCII data. This is done by pressing K0 twice, then 'filer' (↵). Insert

the ASCII data disk and press 'Volumes'. A list of Volume Names (prefixes) will be displayed. Note the prefix for the data disk (probably B9826: or B9836:) and press any key to return to the file transfer menu.

Enter the prefix and press 'Prefix' TAB down to 'File to Upload', enter the file name and press 'Upload'. The computer should display the file as it is transmittted. You must transfer both the header file ('HED') and the data file ('DAT') separately. You should name the files fname.DAT and fname.HED. This will take 10 min. (or more) for the data files depending on system and system load.

When transfer is complete, the disk drive light will no longer blink. Terminate the input for the host computer; ^d for UNIX, ^Z for VMS. Be sure to log out before shutting off the equipment.

V. USING THE ISPX PACKAGE:

Formatting the data

The data should be saved in two files (fname.DAT and fname.HED) in the directory [tsui.rajan.data2] on the EW1 VAX. Since the ISPX software handles at most 512 points at a time, the data must be broken into chunks before it may be used. Another consideration is

that the two channels may not be aligned in time or the channel offsets on the scope may not have been equal. The program CH.FOR takes care of these problems. Enter "RUN CH.EXE" to run the program. CH will prompt you for an input filename; enter the filename, do not include the extension. The program automatically adds the proper extension for the file it needs. (.DAT or .HED) CH will then ask you for an output filename. If you enter "FOO", it will store the data, in the proper format, in the directory [tsui.rajan], as "FOO.DAT". CH will then prompt "REAL or COMPLEX". Normally, you will use complex since this gets both the I and the Q channels. If you just want the I channel, select REAL. CH then reads the header file, writes a statement telling you how to convert the periodogram into actual frequencies and then reads the data. You will need this information later. CH checks the alignment of the data in the time domain and adjusts the two channels so they line up properly. You are then prompted with the current starting point and length. You may change this by entering any number but 1. You will then be prompted for a starting point and length. You may list the data and if it is not acceptable, go back and choose another starting point and length.

Once you have the desired chunk of data, you may save it in a number of formats. If you choose to save

the data as fractional counts, CH will divide each 8 bit data point by 256 to obtain a number between 0 and 1. There will be no negative numbers in this data. Normally, 0 volts corresponds to 128 counts or .50000 fractional counts. This method will leave a large DC component in the spectrum of the signal unless it is taken into account by ISPX. The other format is in actual voltage levels. CH uses the header information to determine the voltage levels and offsets (which can be ignored) to output the actual voltage level at the input of the scope. One consideration while using this method is that the data is saved in a F10.7 format and small voltages may lose some of their accuracy.

Running the improved ISPX software

First set the default directory to [tsui.rajan]. Your data files (output from CH) should be automatically stored in this directory. Type "run work". The ISPX software will load and prompt you for a terminal type. You may load your data files by using the 'file I/O' menu choice. Most of the improvements in the ISPX software are in the vector manipulation menu choice. This is a new menu item not found in previous editions of ISPX. The choices under this category include vector addition, multiplication, inner product, shifting,

reversal, convolution, scaling, conjugation, and many other useful manipulations.

There are several methods available for computing the PSD of a data sequence. The choices under '(B) PSD Method' are Fourier, ARMA, Adaptive, and Prony. The Fourier methods and the ARMA methods seem to work well. The Adaptive and Prony methods are not complete as of this writing.

After using one of the methods to compute a spectral estimate, you can use the 'find peaks' menu choice under vector manipulations to find the relative frequency of the spectral peaks. The relative frequency will be a fraction, between -.5 and .5 . To determine the actual frequency of the signal at the peak, you must recall the information given by the CH program. You must multiply the relative frequency by the sampling frequency (1/sample interval) and then subtract from the center frequency of the tuner. Note that this means negative relative frequencies are above the tuner center frequency and that positive relative frequencies are below the tuner center frequency. The 'find peaks' software includes the ability to search for a peak between two points, or in each of several sections of the data. You may specify the threshold for peaks in absolute values or in percentage of the maximum. The software will also output a line

spectrum, with a line at each detected peak. The 'peak of peaks' choice is still in the developmental stage. Its function is to find all of the peaks, and by using the width and height of the peaks, determine the most prominent peak of all the peaks.

VI. RECOMENDATIONS

(1) The "NEWTN" program should be expanded to include the data conversion program "DATCON". Although this will restrict "NEWTN" to be run only on the HP 9836 PC, it will reduce the time consuming data conversion process.

(2) The "NEWTN" program should also be expanded to include the functions of the "CH" program (in FORTRAN on EW1). Since only a small portion of the 8192 points are used by the ISFX software, there is no reason to store and transmit all 8192 points. This will greatly reduce the time required for transmission of the data, and will allow more data sets to be stored on the same diskette.

(3) The 'peak of peaks' routine should be completed and tested. It seems to be a viable method for detecting true peaks in a spectrum.

(4) The adaptive method and Prony's method for spectral estimation on the ISPX software do not work. These methods may be the best spectral estimators for certain classes of data. The programs should be checked and put into working condition.

1988 USAF-UES SUMMER FACULTY RESEARCH PROGRAM

GRADUATE STUDENT RESEARCH PROGRAM

Sponsored by the

AIR FORCE OFFICE OF SCIENTIFIC RESEARCH

Conducted by the

Universal Energy Systems, Inc.

FINAL REPORT

Prepared by :	Robert Y. Li, Ph. D. / Yuhong Yu Li
Academic Rank:	Assistant Professor / Graduate Student
Department and	Electrical Engineering / Computer Science
University:	University of Nebraska, Lincoln
Research Location:	AFWAL/AARA Wright-Patterson AFB Dayton, OH 45433-6543
USAF Researcher:	James D. Leonard
Date:	August 15, 1988
Contract No:	F49620-87-R-0004 / F49620-88-C-0053

SAME REPORT AS
PROF. ROBERT LI
AVIONICS LABORATORY # 82

1988 USAF-UES SUMMER FACULTY RESEARCH PROGRAM

GRADUATE STUDENT RESEARCH PROGRAM

Sponsored by the

Air Force Office of Scientific Research

Conducted by

Universal Energy Systems, Inc.

FINAL REPORT

A Proposed Turbulence Monitoring Facility For Wright-Patterson Air Force Base

Prepared By:	Randal L. Mandock
Academic Rank:	Graduate Student
Department and University:	School of Geophysical Sciences Georgia Institute of Technology
Research Location:	AFWAL/AARI Wright-Patterson Dayton, OH 45433
USAF Researcher:	Jan Servaites
Date:	29 September 1988
Contract No.	F49620-88-C-0053

A PROPOSED TURBULENCE MONITORING FACILITY FOR WRIGHT-PATTERSON AIR FORCE BASE

by

Randal L. N. Mandock

ABSTRACT

A study was undertaken to develop a plan for the characterization of atmospheric turbulence to support infrared sensor and laser beam propagation research at Wright-Patterson Air Force Base. To accomplish this assignment, I: surveyed the topography and physical environment of the AFWAL test range in Area "B"; visited the NOAA Wave Propagation Laboratory in Boulder, Colorado, and the Georgia Tech Research Institute at Georgia Tech, Atlanta, Georgia; and wrote three proposals to monitor atmospheric turbulence.

The facility proposed in this report is designed to monitor turbulence during routine testing and special experiments. This facility is expected to provide information on the behavior of the refractivity structure parameter along a slant-path propagation range and at a well-characterized horizontal propagation range on Wright Field.

I. INTRODUCTION

Seeing along a slant path through the atmosphere is a function of the integral of the atmospheric turbulence refractivity structure parameter, CN2 (Lutomirski, 1978; Walters, 1981), and other scattering and absorption effects. Aside from diffraction effects, the ability to resolve an image is limited by the degree of defocusing induced by the medium separating the image and detector. When the medium is the atmosphere, such factors as aerosol concentration, gas molecules, turbulence, and others all work together to influence the propagation of electromagnetic (EM) energy. My concern is with the effect of atmospheric turbulence on the ability to see a target.

The Electro-Optics Sensor Evaluation/Analysis Group (AARI) of the Avionics Laboratory of Air Force Wright Aeronautical Laboratories (AFWAL) at Wright-Patterson Air Force Base (WPAFB) is concerned with the potential impact that atmospheric turbulence will have on laser imaging and other future electro-optical systems that will require evaluation. The Laser Hardened Materials Technical Area (MLPJ) of the Materials Laboratory at WPAFB is interested in understanding the effects of atmospheric turbulence on its propagating laser beams. The Communications Technology Group (AAAI) of the Avionics Laboratory at WPAFB needs to know the effect of scintillation on optical communications links. These diverse interests could be addressed by establishing a facility to quantify and monitor the degradation of electro-optical systems by atmospheric turbulence. Such a facility would be capable of deriving predictive relationships from measured data, but would also be flexible enough to perform routine monitoring during tests.

The basis for my assignment to AARI was to sketch out the preliminary design for a facility to characterize atmospheric turbulence to support sensor and other research at WPAFB. My background includes experience in remote sensing of the solid earth, studies of millimeter wave propagation through the atmosphere, the spectral analysis of nuclear radiations, and data processing. I am currently acquiring the components to build an acoustical imaging Doppler interferometer for a doctoral thesis. The millimeter wave experience and my interest in the turbulent scattering of acoustic energy contributed to my assignment to AARI.

II. OBJECTIVES OF THE RESEARCH EFFORT

Currently, there is no atmospheric turbulence monitoring facility in the Department of Defense capable of fully documenting variations in CN2 along a slant beam path. Additionally, only limited results are available for the variability of CN2 in the vertical; e.g., CN2 is proportional to the minus 4/3 power of height during the daytime (Shapiro et al., 1981). No predictive models exist for the horizontal variation of CN2 during nonneutral conditions, whereas the assumption for propagation along a horizontal path under neutral conditions is CN2 constant. Thus, a facility such as the AFWAL Turbulence Monitoring Site (ATMS) proposed here would be of research as well as operational value.

My assignment as a participant in the 1988 Graduate Student Research Program was to develop a plan for the characterization of atmospheric turbulence to support sensor and other research at WPAFB. To accomplish this assignment, I was to survey the topography and physical environment of Area "B". Facilities and instrumentation at AARI had to be checked. Meetings were to be arranged with potential users of atmospheric turbulence information at WPAFB to define their needs. Visits to the Wave Propagation Laboratory (WPL) of the National Oceanic and Atmospheric Administration (NOAA) Environmental Research Laboratories and Georgia Tech were planned for consultation with turbulence experts. If available, instrumentation was to be borrowed from government laboratories for summer use and anticipated follow-on research. Finally, I was to use this equipment to acquire and analyze turbulence data concurrent with my other activities.

III. SURVEY OF TOPOGRAPHY AND PHYSICAL ENVIRONMENT ON AFWAL TEST RANGE

To survey the topography of the AFWAL test range, I requested a recent map of Area "B" from the Environmental Planning group of civil engineers in Area "C". I then walked various sections of the beam path and observed the remainder by automobile. I walked and photographed large segments of the target area on Wright Field. I concluded that the slant beam path can be instrumented with a row of micrometeorological (micromet) towers and that the target area on Wright Field is sufficiently level for propagation experiments at constant altitude over distances on the order of 1 km.

I used a Weathermeasure Model 8297 surveying compass and the services of an airman to determine the effective height of representative trees in a loose shelterbelt along the southern boundary of Wright Field. At Site S1 a tall tree was found to be 10 m and an average tree 6 m. These trees were located 10-11 m south of the fence along the southern boundary. At Site S2 a tall tree measured 21 meters and was located 57 m south of the fence along the southern boundary; an average tree measured 12 m and was located 10 m south of the fence along the southern boundary. I do not consider the tall tree at Site S2 to be part of the shelterbelt because of its distance from the southern boundary and its separation from the shelterbelt by a highway. From these measurements, I conclude that the average height of the shelterbelt ranges from 6 to 12 m; I will take 12 m to be a conservative estimate for calculation of the recirculation region. Both Sites S1 and S2 were located 13 m north of the fence along the southern boundary.

I measured the height of grass on Wright Field to be between 15 and 30 cm. Plate (1971) shows that this situation corresponds to an aerodynamic roughness length of 3-4 cm.

IV. REVIEW OF FACILITIES AND INSTRUMENTATION AT AARI

A tour of the machine shop and electro-optical laboratories showed them to be well-equipped and adequate for constructing optical turbulence measurement devices. Items that could be put to immediate use include a Spectra Physics 133 He-Ne laser (133-1867) and five SDC detector/preamp (SD 100-41-11-231) units. The Meteorological Measurement and Control Package (MMAC PAC) should be adequate to provide rough estimates of some turbulence parameters.

V. MEETINGS WITH POTENTIAL USERS OF ATMOSPHERIC TURBULENCE INFORMATION

I organized three 2-hour meetings with representatives of MLPJ, AAAI, AARI, and AAWP (Passive Electronic Countermeasures Branch) to determine whether their organizations have a need for measurements on atmospheric turbulence.

I presented a 2-hour seminar entitled "An Introduction to Atmospheric Turbulence" to representatives of MLPJ and AAAI. The audience was composed of engineers and physicists who believe that atmospheric turbulence degrades the performance of their laser technology. The definitions of CN2 and the inertial subrange of turbulence were developed. At the end of the seminar I passed out a "Survey on the Need for Turbulence Information" to selected members of the audience. Results of the survey suggested that atmospheric turbulence is presently degrading the performance of laser-hardening devices, modified electro-optic sensors, and optical communications links at AFWAL. The surveys expressed the need for a turbulence measurement facility on the AFWAL test range at Wright Field.

I arranged for representatives of AARI, AAAI, MLPJ, and Georgia Tech to attend a 30-minute presentation of my proposals for ATMS and follow-on research. The results of this meeting are

financial support for a fellow graduate student at Georgia Tech, a newly-established link between Georgia Tech and MLPJ, and a possible source for follow-on research support for myself.

VI. RESULTS OF VISITS TO NOAA/WPL AND GEORGIA TECH

I visited NOAA/WPL during the final week in July. During that visit I received guidance on how to select instrumentation to measure turbulence parameters, how to incorporate this instrumentation into a measurement program, and how to acquire and analyze the data taken by this program. I toured a WPL atmospheric acoustics laboratory, the Table Mountain Research Facility, and the Boulder Atmospheric Observatory.

Three visits to Georgia Tech provided overall direction for the research component of ATMS. The researchers at Georgia Tech discussed the present state of knowledge about the prediction of the properties of turbulence in the surface boundary layer (SBL). They stressed that information on electro-optical degradation by turbulence is useless to the battlefield commander if he is unable to anticipate its effect on his systems. He requires the ability to gather reliable information which will inform him of systems performance not at the time of measurement, but at the time of deployment. Sections II and VII discuss present capabilities for doing this. Sections VIII, IX, and X are the results of the visits to NOAA/WPL and Georgia Tech.

VII. PRESENT STATE OF KNOWLEDGE REGARDING CN2 IN THE SURFACE BOUNDARY LAYER

The meteorological literature contains references to work that has been done in an attempt to predict CN2 by using measurements of averaged micromet parameters. During my 10-week assignment I was able to review four such references. Tatarskii (1961) demonstrates how CT2 (the temperature structure parameter for turbulence) can be determined from measurement of the mean temperature at two heights by using either an equation, for the case of unstable stratification, or a figure, for the case of stable stratification. Wyngaard et al. (1971) describe an indirect method of determining CN2 by measuring mean values of the lapse rate of temperature and of the vertical gradient of the horizontal component of the mean wind. The gradient Richardson number (Ri) can be calculated from these parameters and from a knowledge of the mean temperature at the level of interest. CT2 can be found in a table once Ri is known. A simple relation can then be used to convert CT2 to CN2 when the mean pressure is measured. Kaimal (1973) derives a relationship for CT2 in the surface layer which is based on Ri, sensor height, and the variance of potential temperature. This relationship is for a stably stratified surface layer. Kohsiek (1988) discusses a method of determining CN2 under convective conditions by measuring turbulent fluxes at 5 Hz with dry and wet bulb thermocouples and fast response anemometers mounted at six levels of a meteorological mast.

There are numerous problems with all of these methods of deriving CN2 from low frequency data. Simple logarithmic relationships and gradient transfer theories assume the restrictive case of neutral stability. Such stability conditions occur for only a few minutes diurnally near sunrise and sunset (Walters and Kunkel, 1981), thereby limiting the applicability of these theories. Other assumptions are seldom satisfied for battlefield operations: stationary conditions, homogeneous turbulence, and flat, nonsloping terrain which is removed from obstacles to the wind flow (Biltoft, 1985). The advection of microscale convective plumes across an isolated measurement point imposes a requirement for long averaging times. However, long averaging times can filter out rapidly changing events.

The presence of convective plumes can cause CT2 to vary over two orders of magnitude in just a few seconds; CT2 is larger within the plume. A high density of plumes therefore represents a worst-case situation for EM wave propagation, while their absence combined with near-neutral

stability represents a best-case scenario. Herein lies the need for an appropriately-equipped turbulence monitoring site at a wave propagation test range which possesses a sloping beam path. The structure of the SBL under unstable (plume generating) conditions is not well understood, although the SBL is the most intensely studied region of the atmosphere. It is my belief that progress has been impeded by the absence of detailed information on the structure of convective plumes in the SBL. The following three sections detail a plan to instrument Wright Field with the best equipment available to allow characterization of plume structure, spatial and temporal distribution, intensity, and effect on EM wave propagation in the SBL.

VIII. PROPOSAL TO MONITOR ATMOSPHERIC TURBULENCE ALONG THE BEAM PATH (TMAB)

Atmospheric turbulence is expected to vary along a slant beam path in both the horizontal and vertical directions. This anisotropy has been addressed in the mean (i.e., for long averaging times) by assuming a constant C_N^2 along a constant-altitude, although sloping, path. Real beam paths, such as that at WPAFB, are not constant-altitude and do not traverse homogeneous terrain. Therefore the assumption of a constant C_N^2 in the mean is not valid.

TMAB is designed to monitor spatial and temporal variations in C_N^2 along a real slant beam path. It will initially be outfitted with the following components:

A. 22 tower-mounted Atmospheric Instrumentation Research, Inc. (A.I.R.) CT-1A-T Temperature Structure Function Sensors.
B. 1 Radian Corporation (Radian) Echosonde PS/2 single-axis sodar system located 140 m west of the nominal sensor location in Building 620.
C. 1 Radian Echosonde PS/2 three-axis sodar system located near the Environmental Monitoring and Control System (EMACS) on the AFWAL test range at Wright Field.
D. 2 Ochs Optical Systems Model IV path-averaged C_N^2/wind sensor systems.

TMAB will provide 22 point determinations of C_T^2 at 100-meter intervals along the beam path. Sampling will occur at 10 m above ground level except over a wooded area, where data will be taken at 5 m above the canopy. Since the characteristic dimension of a convective plume in the SBL is 100 m and its horizontal lifetime is hundreds to thousands of meters (personal communication with J. C. Kaimal and J. E. Gaynor of WPL), this arrangement should be appropriate for the detection of convective plumes in the SBL. The towers can be as sophisticated as reinforced steel structures with guy wires, or as simple as 10-meter telephone poles. Data transmission can be accomplished via either shielded cable or telemetry. The CT-1A-T is a pair of Kaimal-Ochs 12-micron platinum wire probes which provide values of C_T^2 averaged over 30 seconds. The normal probe separation is one meter, but can be any value within the inertial subrange (see Section IX). Clifford et al. (1971) used a separation of 40 cm to estimate C_N^2 at a height above the ground of 1.6 m. A potentially more economical alternative to the CT-1A-T would be to send AARI personnel to WPL (contact G. R. Ochs) for training in the construction of fine-wire temperature sensors (Lawrence et al., 1970).

The primary purpose for the Radian Echosonde PS/2 sodar systems is to determine average values for C_T^2 in 20 vertical range gates. Parameters of secondary importance to be measured by the single-axis sodar are vertical Doppler wind vectors and their variances (sigma) in 20 range gates. Secondary parameters to be measured by the three-axis sodar include vertical and horizontal Doppler wind vectors, vertical and horizontal sigmas, and horizontal wind components in 20 range gates. The gated C_T^2 averages will provide turbulence profiles in the vertical at point locations near the sensor platform in Building 620 and at the target site near EMACS. The sodars, when used in conjunction with the 22 point C_T^2 sensors, will determine if C_T^2 interpolations and correlations are possible along the slant beam path. The Doppler velocities will provide information on vertical motions of air masses, the wind shear profile at the target

site, and horizontal mean winds. A potentially more economical alternative to the Radian Echosonde PS/2 sodar systems would be to contract W. D. Neff at WPL to build equivalent or superior systems.

The Ochs Optical Systems Model IV path-averaged CN2/wind sensor system consists of a separate optical transmitter and optical receiver (Ochs and Cartwright, 1985). The system measures path-averaged values of CN2 and crosswind over optical paths from 200 to 1500 m, with a path averaging interval which can be set to 1, 10, or 100 seconds. The CN2 and crosswind measurements are weighted most heavily along the middle 1/3 of the optical path, thereby avoiding the strongest effects of optical turbulence which are produced near the transmitting aperture (Clifford and Lading, 1983; Clifford, 1978). The system uses a 0.94 micron (infrared) light-emitting diode (LED) at the focus of a 15-cm diameter concave mirror. This extended light source is incoherent, safe for the human eye, and resists the saturation of scintillations commonly found with laser scintillometers (Wang et al., 1978).

There is no better alternative to the Model IV for measuring CN2 directly. All coherent scintillometer systems saturate with increasing path length or CN2 (Clifford, 1978). When the variance of the log-amplitude fluctuations (ex2) exceeds about 0.3, a plot of ex2 versus path length (or CN2) initially increases, then levels off and eventually decreases. This is the saturation phenomenon. Strohbehn (1978) explains it as follows. When the lateral coherence length is longer than the width of a Fresnel zone (i.e., the coherent scattering case), the scintillations are dominated by turbulent eddies with scale sizes of about the same dimension as a Fresnel zone. No saturation is expected for this situation. However, when the lateral coherence length is shorter than the width of a Fresnel zone, the scintillations are independent of CN2 and the path length, and the ex2 curve flattens. The scintillations are then dominated by eddies of about the same size as the lateral coherence length.

Since the Model IV is range-limited to 1.5 km and the optimum path length is 900 to 1200 m, one Model IV transmitter will be located on the sensor platform in Building 620. The optical path will be along a line from the sensor platform to EMACS. I propose to locate the receiver for this transmitter on the roof of Hangar 4 away from any heat source. It should be mounted on a solid platform, such as cement, bricks, or a steel structure, to minimize vibration; spurious vibrations would interfere with the minute turbulence-induced fluctuations in the received intensity. The other transmitter will be located at EMACS, and its receiver mounted adjacent to the first on the roof of Hangar 4. The path length for the first Model IV is 1 km, while that for the second is about 1.3 km.

A subsequent addition to each of the 22 towers is a TSI, Inc., Model 1755 constant-temperature anemometer with a Model 1210-T1.5 cross-flow (for vertical mounting) tungsten hot-wire general purpose probe. This anemometer (which is known as a hot-wire anemometer) will provide useful information on spatial variations in the energy spectrum of turbulence. An alternative to both the CT-1A-T and TSI Model 1755 is an Applied Technologies, Inc., sonic anemometer/thermometer. This is a 10-Hz sensor which will probably outperform the wire sensors, although it requires a greater capital outlay.

A final recommended sensor package to supplement components A-D above is an A.I.R. Advanced Tethersonde System AIR-3A-1R. This system can be used to verify meteorological conditions at any point along the beam path at any altitude of interest.

IX. PROPOSAL TO MONITOR ATMOSPHERIC TURBULENCE ON AFWAL TEST RANGE AT WRIGHT FIELD (WFTT)

The Wright Field Tower Triangle (WFTT) will be the primary component of a wave propagation test site located on Wright Field. The purpose of WFTT is two-fold: to fully document the target end of the beam path during testing of sensors located in Building 620, and to acquire turbulence data which are expected to allow a predictive model for the spatial and temporal variation of CN2. The model is intended to provide values of CN2 from the measurement of gross meteorological

parameters (e.g., horizontal wind speed). Additional tests involving horizontal beam paths up to 1.5 km in length will traverse the triangle, with supplemental sampling at various distances from it.

I recommend the following components for WFTT:

A. 1 Ochs inner scale device.
B. 5 A.I.R. CT-1A-T sensors for determination of turbulence outer scale.
C. 3 meteorological towers (tower triangle) instrumented at 2, 5, and 10 meters.
   i. Instrumentation on each tower at 2 meters (mounted on rotating boom).
      a. 1 A.I.R. Lyman-Alpha Hygrometer AIR-LA-1.
      b. 1 Ophir IR-1100 Optical Hygrometer.
      c. 1 TSI Model 1755 constant-temperature anemometer with Model 1210-T1.5 cross-flow probe.
      d. 1 fine-wire temperature sensor located in gap of Lyman-Alpha hygrometer.
      e. 1 wind vane/anemometer (e.g., R. M. Young Propvane Model 35003 or 8002).
   ii. Instrumentation on each tower at 5 meters.
      a. 1 Applied Technologies SWS-211/3S sonic anemometer/thermometer.
      b. 1 Ophir IR-1100 Optical Hygrometer.
      c. 1 Ochs Optical System Model IV path-averaged CN2/wind sensor.
      d. 1 12-micron fine-wire temperature sensor located at 2 cm from sonic anemometer path.
   iii. Instrumentation on each tower at 10 meters.
      a. 1 Applied Technologies SWS-211/3S sonic anemometer/thermometer.
      b. 1 Ophir IR-1100 Optical Hygrometer.
      c. 1 12-micron fine-wire temperature sensor located at 2 cm from sonic anemometer path.
D. Meteorological instrumentation either centered in tower triangle or incorporated into EMACS.
   i. 1 Radian Echosonde PS/2 three-axis sodar system.
   ii. 1 A.I.R. Intellisensor digital barometer AIR-D8-2A.
   iii. Standard EMACS pyranometers, pyrgeometer, and pyrradiometer.
E. 2 Ochs path-averaged CN2 profilers.
F. 1 Ochs Optical System Model IV path-averaged CN2/wind sensor.
G. Several A.I.R. CT-1A-T sensors for point measurements of CT2.

The triangle configuration of micromet towers was chosen to provide the capability for three-dimensional modeling. The goal is to predict CN2 from horizontal (one-dimensional) variations in wind speed. A one-dimensional measurement of the horizontal wind field would thus allow the prediction of the three-dimensional turbulence spectrum. The three-dimensional spectrum will give an estimate of how the one-dimensional spectrum varies across the battlefield.

Components A and B are needed to provide definitive values for the inner and outer scales of turbulence. These scales demarcate the inertial subrange of the turbulence spectrum; i.e., the range for which the structure function of temperature is proportional to the 2/3 power of scale size. Hocking (1985) remarks that the inner scale defines the approximate transition between the inertial and viscous ranges of turbulence, while the outer scale corresponds to the largest scale size for which turbulence may be considered to be isotropic (Clifford, 1978). According to Hill and Clifford (1978), the ratio of the inner scale to the Kolmogorov microscale is 7.4 for air. For a value of the Kolmogorov microscale equal to 0.2 cm (Mandock, 1986), the inner scale is found to be on the order of 1 cm. Tatarskii (1971) gives the relationship between the height, z, of a sensor above the ground and the outer scale, Lo, as Lo = 0.4z in the SBL. The inner scale places a lower limit on the length of propagation path in the SBL; i.e., for inertial subrange behavior, the size of the Fresnel zone must be larger than the inner scale. The outer scale places an upper limit on the agreement between measurement and inertial subrange behavior.

The Ochs inner scale device (Ochs and Hill, 1985) consists of a 3-mW He-Ne laser with a 1 mrad beam divergence (e.g., AARI's Spectra Physics 133-1867), a 0.94 micron LED transmitter, and 2 photodiodes (e.g., AARI's SDC detector/preamp SD 100-41-11-231). The technique requires two

optical paths, each about 260 m long. An alternative to this technique of measuring the inner scale is described in Ochs and Hill (1985). This alternative requires two hot-wire anemometers, but produces only a local value of inner scale, rather than a path-averaged value.

I recommend that CT2 be measured continuously at 2 m above the ground by five CT-1A-T sensors with horizontal probe spacings of 0.5, 0.75, 1.0, 2.0, and 3.0 m. Since CT2 is assumed constant for scales within the inertial subrange, the outer scale will be given approximately by the greatest distance for which CT2 remains constant. Clifford et al. (1971) determined the outer scale by measuring the temperature structure function for averaging times which varied from 10 to 100 seconds. On log-log plots of three of these 5-point functions, versus probe spacing, the curves followed a 2/3 slope until they began to roll over at a spacing corresponding to the outer scale. The outer scale was found to be about 1-2 m at a sensor height of 1.6 m above ground. A potential problem with using the CT-1A-T sensor for this type of measurement is its relatively slow frequency response of 25 Hz. This response limits the probe spacing to a minimum of 0.4 m, assuming a maximum wind speed of 11 miles per hour (mph). A better alternative is to train AARI personnel, in accordance with the recommendation in Section VIII, in the construction of 2.5-micron fine-wire temperature sensors. These sensors will allow a minimum spacing of 0.2 m for maximum wind speeds of 22 mph and a response time of 100 Hz. Lawrence et al. (1970) report a minimum frequency response of 200 Hz for this type of sensor.

The location of the tower triangle was chosen to miminize the effects on the wind field of such obstacles as the Air Force Museum Hangars 487 and 489, a 6-foot fence along the northern boundary of the test range, and the shelterbelt of trees located along the southern boundary. It should not cross paved surfaces or be located on a downslope. The proposed location for the northeastern tower (T1) is 100 feet south of the fence along the northern boundary. It is to be located at the intersection of a circular arc of 1000-foot radius centered on the southwestern corner of Building 487 and a line drawn perpendicular to the fence. The northwestern tower (T2) is to be located 200 m west of T1 at the intersection of a westerly-bearing chord and the 1000-foot arc. The southern tower (T3) is to be located at the intersection of lines 200 m in length drawn from T1 and T2. T3 will be located about 72 feet north of the east-west cement road accessing EMACS.

The location of WFTT will determine the directional dependence of the aerodynamic surface roughness, zo, and other turbulence parameters on the presence of the obstacles mentioned above. According to Hosker (1984), the maximum extent of the cavity or recirculation region downwind of a two-dimensional obstacle is about 13H, where H is the height of the obstacle above ground. For rounded obstacles, such as the hangars, the cavity length is about 10H. The 1000-foot distance from the 75-foot Hangar 487 is slightly greater than 13H. WFTT is probably beyond the cavity of Hangar 487, but zo may still be influenced by the hangar when the mean wind is from the north. This situation might not be serious, however, since the prevailing winds are from the southwest. The 6-foot fence is about 17H from T1 and 63H from T2. They are expected to have no influence on the tower measurements. The 12-m shelterbelt is located about 36H from WFTT, and is expected to have no influence on tower measurements (Plate, 1971).

The instruments on each tower at 2 m are fast response to measure subrange-scale turbulence. They will be mounted on a rotating boom which can be oriented into the mean wind throughout the measurement period. The AIR-LA-1 has a frequency response of 500 Hz. It requires calibration every 3 to 6 hours to provide absolute humidity measurements and correct for drift. The source and detector windows of the AIR-LA-1 require cleaning approximately every 6 hours. The IR-1100 measures absolute humidity at 10 Hz and is used at this level to calibrate the AIR-LA-1. The TSI Model 1755 has a 25 kHz frequency response; the Model 1210-T1.5 cross-flow probe has a 4 micron tungsten wire sensor element. The fine-wire temperature sensor commonly has a 2.5 micron platinum sensor element with a minimum frequency response of 200 Hz (Lawrence et al., 1970). The prop-vane anemometer has a 1-m distance constant and is used to verify values for the mean wind measured by the hot-wire anemometer.

The instruments on each tower at 5 m have intermediate response speeds (25 Hz or less). They are expected to provide subrange measurements for mean wind speeds less than 10 m/s. The SWS-

211/3S operates at 10 Hz. The manufacturer claims that it will provide absolute virtual temperature measurements in addition to wind speeds. If the claim is true, then this instrument will eliminate the need for the 12-micron fine-wire temperature sensor which is to be located 2 cm from the sonic path. The sonic anemometer must be carefully leveled and requires ambient temperature and relative humidity information for calibration. The IR-1100 is used at this level to measure fluctuations in absolute humidity and should be mounted as near to the sonic anemometer as possible, without interfering with the air flow. The Ochs Model IV will be aligned following Kaimal and Gaynor (1983). The purpose for these instruments in the triangle is to measure the mean surface wind speed and direction and the convergence within the triangle. Each leg of the optical triangle measures path-averaged crosswind and CN2. The 200-m spacing is designed to provide information on the direction and speed of convective plumes advecting across the triangle. The 12-micron fine-wire temperature sensor is to be placed very near to the sonic path to provide correlations between fluctuating temperatures and wind velocity components. It is expected to have a 25-Hz frequency response. An A.I.R. FT-1A-T 25-Hz temperature sensor located 4 cm (the smallest scale size detectable for a 1 m/s wind) from the sonic path would be a possible alternative to the 12-micron fine-wire temperature sensor.

The instruments on each tower at 10 m have the same characteristics as those mounted at 5 m.

The three-axis sodar in component D.i. can be either a unit independent of the one specified in VIII.C., or it can be the same one. The advantage of a single sodar on the Wright Field test range is a smaller initial capital outlay. The advantage of two independent units, one centered in the tower triangle and the other outside the triangle, is the ability to make simultaneous profiles of CT2 both inside and outside of a convective plume. I recommend this latter arrangement, especially if W. D. Neff builds the devices.

The AIR-DB-2A is a microprocessor-controlled digital pressure transducer with 10-Hz frequency response. When located near the midpoint of a horizontal propagation path, this transducer is capable of measuring the pressure fluctuations produced by turbulence. The 10-Hz output will also be averaged and used to convert values of CT2 to CN2.

The radiometers listed in D.iii. are routinely deployed at EMACS during sensor tests. They are used in turbulence monitoring to measure net radiation, to determine upwelling and downwelling fluxes of solar and terrestrial radiation, and to infer the presence of cloud cover.

The Ochs path-averaged CN2 profilers were built by G. W. Ochs of WPL early this year for measuring horizontal variations in CN2 along a 600-m path. Whereas the Model IV determines path-averaged values of CN2 weighted most heavily along the middle 1/3 of the path, the CN2 profiler is designed to produce weighted values of CN2 along 3 segments of the path. It uses three different apertures to produce weighting functions along the first, middle, and final third of the optical path. Using infrared LED transmitters, like the Model IV, the CN2 profiler is safe for use around unprotected eyes. Two of these devices will be able to profile a 1200-m path, which is about the maximum horizontal distance over a homogeneous surface at the Wright Field test range. Should longer ranges be required, the maximum range for each profiler can be determined by first measuring CN2 along a 600-m path. The separation between transmitter and receiver is then extended until CN2 begins to fall off. This event can be observed by measuring CN2 for a 24-hour period at each separation distance and comparing the resulting curves. The greatest value of CN2 that can be measured for a given path length, L, can be found from (Ochs and Cartwright, 1985)

$$L = 0.54\, D^{5/8}\, \lambda^{1/8}\, (C_n^2)^{-3/8}, \qquad (1)$$

where D is the transmitter and receiver aperture diameter, λ is the optical wavelength, and C_n^2 is CN2. The falloff in CN2 for path lengths greater than the maximum is caused by the saturation of scintillations discussed in Section VIII. To reduce the interference caused by spurious vibrations, the transmitter and receiver units must be mounted on a solid, vibration-free surface, such as cement blocks or a steel platform.

The Ochs Model IV will provide path-averaged measurements of crosswind and CN2 along paths up to 1.5 km. It will be supplemented by a number of point measurements of CT2 by CT-1A-T sensors distributed along the propagation path. I recommend a 100-m sample interval for the point measurements.

X. PROPOSED UES FOLLOW-ON RESEARCH - PARTIAL SITE CHARACTERIZATION OF WRIGHT FIELD TEST RANGE FOR TURBULENCE MONITORING OF SENSOR TESTS

The follow-on research that I propose will determine the variance of intensity and angle-of-arrival fluctuations of a He-Ne laser beam to infer the behavior of CN2 at WFTT. If AARI instrumentation (EMACS and MMAC PAC) and personnel can be made available, I additionally would like to instrument a 10-m tower at EMACS to observe micrometeorological parameters at WFTT.

The primary objective of the follow-on research is to measure three optical turbulence parameters:

1. The variance of intensity fluctuations, given by Phillips and Andrews (1981) as

$$\sigma_I^2 = \exp(\sigma_{\ln I}^2) - 1, \tag{2}$$

where $\sigma_{\ln I}^2 = \tilde{\sigma}_{\ln I}^2 (0.5\, C_n^2\, k^{7/6}\, L^{11/6})$,

$\tilde{\sigma}_{\ln I}^2$ is a normalized variance depending on the ratio of Fresnel zone to inner scale, k is the wave number of the optical beam (radians/meter), and L is the path length.

2. The variance of angle-of-arrival fluctuations, derivable from Tatarskii (1971) as

$$\sigma_\alpha^2 = 0.54\, C_n^2\, L\, r^{-1/3}, \tag{3}$$

where r may be interpreted as the spacing between sensors in an array.

3. The phase structure function, again derivable from Tatarskii (1971) as

$$D_\phi(r) = 1.09\, C_n^2\, k^2\, L\, r^{5/3}. \tag{4}$$

Values for CN2 will then be calculated from each of the three parameters and compared.

Instrumentation for these measurements is presently available at AARI. The light source and receivers will consist of AARI's Spectra Physics 133-1867 He-Ne laser and five SDC detector/preamp SD 100-41-11-231 photodiodes. The 1-milliradian divergence of the 0.8-mm beam exiting the laser will provide a spherical wavefront. To assure that only coherent portions of the wavefront are sampled, each photodiode must be stopped down to a 1-mm aperture diameter. A restricted field of view for the photodiode array will be required for operation in daylight. I will supply the data acquisition system.

The equipment will be located on Wright Field near EMACS. The photodiodes will be mounted in a linear array with an adjustable spacing between each receiver. This spacing is irrelevant for

the irradiance calculation, but it is critical for the angle-of-arrival and structure function measurements. One Fresnel zone has been chosen as the appropriate distance, r, for the receiver spacing. At a laser frequency of 0.6328 microns, r is 0.80, 1.12, and 1.38 cm for path lengths of 100, 200, and 300 m, respectively. I measured the diameter of the photodiode at its largest dimension to be about 0.95 cm and the diameter of the socket to be about 1.02 cm. If these dimensions cannot be reduced, the minimum path length will be about 163 m. I will initially plan for a minimum path length to correspond to the minimum practical photodiode spacing. If meteorological conditions are expected to remain uniform for 3 or 4 days, I plan to vary the path length over a range of distances until saturation of scintillations occurs.

A secondary objective of the follow-on research is to use standard AARI anemometers (Weathertronics 2030 or 2031) and wind vanes (Weathertronics 2020) to measure fluctuating horizontal wind speeds and directions. From these measurements, I will calculate 20-minute averages, variances, vertical gradients, and spectra. I will attempt to estimate an aerodynamic roughness length following a graphical method outlined in Biltoft (1985). The 10-m tower will be instrumented with identical instruments at heights of 2, 5, and 10 m to provide the necessary measurements.

XI. DATA ACQUISITION AND PROCESSING

There are two approaches to data acquisition and processing: routine and experimental monitoring. Routine monitoring assumes that adequate information on turbulence is obtained by sampling with a frequency that corresponds to scale sizes which fall within the inertial subrange, typically ranging from 1 cm to several meters in the SBL. For a 10-m/s wind speed, a 100-Hz frequency response will provide information on scale sizes of about 20 cm.

Routine monitoring for TMA8 is estimated to produce about 2 million samples per hour (sph) of raw data. This assumes a 25-Hz frequency response for 22 CT-1A-T units, 180 sph for the single-axis sodar, 300 sph for the three-axis sodar, and 72 sph at a 100-second averaging time for each of the Ochs Model IV systems.

Using a maximum frequency response of 100-Hz, routine monitoring for WFTT is estimated to generate about 9.2 million sph of raw data . This assumes 12 sph for the Ochs inner scale device, one-half million sph for the outer scale determination, about 8 million sph for the three towers in the tower triangle, a 10-Hz frequency response for the digital barometer, 300 sph for the three-axis sodar, 216 sph at a 100-second averaging time for the two Ochs CN2 profilers, 72 sph for the Ochs Model IV, and one million sph for 10 CT-1A-T point sensors.

The total raw data acquisition for both TMA8 and WFTT is therefore slightly in excess of 22 megabytes per hour. This figure can be reduced by one or two orders of magnitude through the judicious application of Fourier transforms, averaging, and grab-sampling to the raw data (Kaimal and Gaynor, 1983). Storing only processed data will prove profitable for TMA8 and WFTT during routine monitoring.

However, a substantial amount of information will be lost if these techniques are applied to WFTT during experimental phases of data acquisition. I estimate a raw data acquisition rate of about 600 megabytes per hour for WFTT under experimental conditions. This estimate assumes a 500-Hz frequency response for the AIR-LA-1 and fine-wire temperature sensors and a 25 kHz frequency response for the TSI anemometer.

The number of data channels associated with each site will influence the type of analog-to-digital (A/D) conversion capability required. Without the AIR-3A-1R Tethersonde System, TMA8 is expected to require a minimum of 34 and a maximum of 78 channels of A/D conversion. WFTT is expected to require 78 channels of A/D conversion. This results in a minimum of 112 and a maximum of 156 channels of A/D conversion required for the proposed data acquisition scheme. (These figures do not include data recorded by EMACS, since EMACS is already an independent operational system.)

To place these figures in perspective, both my acoustical Doppler interferometer and my proposed UES follow-on research are expected to require 180-megabyte data-acquisition rates per hour for raw data. Transforming and averaging is expected to reduce the figure for follow-on research by as much as four orders of magnitude. (These figures do not include EMACS data.)

XII. CAPITAL OUTLAY

A figure for capital outlay is somewhat difficult to calculate in this case because several of the instruments are expected to be fabricated in AARI and WPL laboratories. This instrumentation includes the sodars, fine-wire temperature sensors, Ochs Model IV and CN2 profilers, and the Ochs inner scale device. Assuming that only the Ochs instruments and 9 fine-wire temperature sensors will be constructed by government personnel, the estimated total capital outlay for TMAB instrumentation is $110,000, and $259,000 for WFTT. This brings the total commercial instrument cost for the proposed facility to $369,000.

XIII. STATUS OF BORROWED INSTRUMENTATION AND DATA ANALYSIS

Due to my late start on the summer project, I am sorry to say that I was unable to borrow equipment from government laboratories. However, EMACS was calibrated and tested during my final week at WPAFB. Data from those runs is presently being edited, and I expect to receive about 24 hours of data by 31 October. I plan to perform whatever analysis is possible on this data, and intend use it to initiate a WPAFB data base for teaching purposes at Georgia Tech.

XIV. RECOMMENDATIONS

The majority of my recommendations are contained within the body of this report. However, I have a few suggestions which have a bearing on the research I accomplished.

The intercommunication established by the Georgia Tech group between AARI, MLPJ, AAAI, and the Georgia Tech Research Institute (GTRI) may be the first interdisciplinary approach of its kind with respect to wave propagation through the real atmosphere. MLPJ and AAAI have an immediate need for a facility such as that proposed here. One Georgia Tech student in the School of Geophysical Sciences is already in the process of beginning doctoral thesis research with MLPJ as a result of my summer effort, and I am encouraging UES follow-on research for partial site characterization at Wright Field in the summer of 1989. Enthusiasm is high among the participants in the five meetings that were held this summer. Externally, WPL and GTRI personnel are looking forward to continuing involvement with this summer's project.

Considering the high degree of interest in this project generated at MLPJ, UES follow-on research would be appropriate. No costly equipment will be needed; I am assured that any specialized instrumentation I might require will be made available by WPL and GTRI if I submit my request early enough. Details for a mini grant can be arranged through Professor G. W. Grams (a Fellow of the Summer Faculty Research Program and my supervisor on the project) at Georgia Tech.

The importance of my research and the proposed facility which resulted from it rests in its uniqueness. To the best of my knowledge, no comparable facility exists anywhere in the U. S. Department of Defense. The AFWAL Turbulence Monitoring Site is proposed to be of research as well as operational value. Continued interest generated by UES, GTRI, and WPL might go a long way in making the proposed facility a showpiece among interdisciplinary research centers.

ACKNOWLEDGEMENTS

I acknowledge the assistance of A1c Dan Smith, Gerald R. Ochs, J. Chandran Kaimal, John E. Gaynor, Reginald J. Hill, William D. Neff, Richard B. Fritz, Jim Churnside, John Hines, Christopher A. Biltoft, Steve Conally, Randy Horn, Jan Servaites, Jeff Sweet, Peter Land, Robert W. McMillan, James J. Gallagher, Ronald A. Bohlander, Robert G. Roper, George Chimonas, C. Gerald Justus, Bob Duckworth, and Gerald W. Grams during my summer effort.

I thank the Air Force Systems Command, the Air Force Office of Scientific Research, and AFWAL/AARI for sponsorship of this research. Universal Energy Systems must be mentioned for its concern and help to me in all administrative and directional aspects of this program.

REFERENCES

Biltoft, C.A., "Notes on Atmospheric Stability, Turbulence, and Its Measurement," Tech. Rpt. DPG Doc. No. DPG-TR-85-204, US Army Dugway Proving Ground, Dugway, UT, March 1985, pp. 1-42.

Clifford, S.F., G.M.B. Bouricius, G.R. Ochs, and M.H. Ackley, "Phase Variations in Atmospheric Optical Propagation," J. Opt. Soc. Am., 1971, Vol. 61, pp. 1279-1284.

Clifford, S.F., "The Classical Theory of Wave Propagation in a Turbulent Medium," In Laser Beam Propagation in the Atmosphere, Edited By J.W. Strohbehn, New York, NY, Springer-Verlag, 1978, pp. 12, 39, 40.

Clifford, S.F. and L. Lading, "Monostatic Diffraction-Limited Lidars: The Impact of Optical Refractive Turbulence," Appl. Opt., 1983, Vol. 22, pp. 1696-1701.

Hill, R.J. and S.F. Clifford, "Modified Spectrum of Atmospheric Temperature Fluctuations and Its Application to Optical Propagation," J. Opt. Soc. Am., 1978, Vol. 68, pp. 892-899.

Hocking, W.K., "Measurement of Turbulent Energy Dissipation Rates in the Middle Atmosphere by Radar Techniques: A Review," Radio Sci., 1985, Vol. 20, pp. 1403-1422.

Hosker, R.P., "Flow and Diffusion Near Obstacles," In Atmospheric Science and Power Production, Edited By D. Randerson, USDOE Rpt. DOE/TIC-27601, NTIS, 1984, pp. 258, 262.

Kaimal, J.C., "Turbulence Spectra, Length Scales and Structure Parameters in the Stable Surface Layer," Boundary Layer Meteorol., 1973, Vol. 4, pp. 289-309.

Kaimal, J.C. and J.E. Gaynor, "The Boulder Atmospheric Observatory," J. Appl. Meteorol., 1983, Vol. 22, pp. 863-880.

Kansiek, W., "Observation of the Structure Parameters CT2, CTQ, and CQ2 in the Mixed Layer Over Land," Appl. Opt., 1988, Vol. 27, pp. 2236-2240.

Lawrence, R.S., G.R. Ochs, and S.F. Clifford, "Measurements of Atmospheric Turbulence Relevant to Optical Propagation," J. Opt. Soc. Am., 1970, Vol. 60, pp. 826-830.

Lutomirski, R.F., "Atmospheric Degradation of Electrooptical System Performance," Appl. Opt., 1978, Vol. 17, pp. 3915-3921.

Mandock, R.L., The Kolmogorov Turbulence Spectrum and a Note on Its Effect on Millimeter Waves, unpublished manuscript, Georgia Tech Res. Inst., Georgia Inst. of Technology, Atlanta, GA, 1986.

Ochs, G.R. and W.D. Cartwright, "Optical System Model IV for Space-Averaged Wind and CN2 Measurements," Tech. Memo. ERL WPL-52, Nat. Oceanic and Atmos. Admin., Boulder, CO, October 1985.

Ochs, G.R. and R.J. Hill, "Optical Scintillation Method of Measuring Turbulence Inner Scale," Appl. Opt., 1985, Vol. 24, pp. 2430-2432.

Phillips, R.L. and L.C. Andrews, "Measured Statistics of Laser-Light Scattering in Atmospheric Turbulence," J. Opt. Soc. Am., 1981, Vol. 71, pp. 1440-1445.

Plate, E.J., Aerodynamic Characteristics of Atmospheric Boundary Layers, USDOE TID-25465, NTIS, 1971, pp. 27, 28, 167.

Shapiro, J.H., B.A. Capron, and R.C. Harney, "Imaging and Target Detection With a Heterodyne-Reception Optical Radar", Appl. Opt., 1981, Vol. 20, pp. 3292-3313.

Strohbehn, J.W., Laser Beam Propagation in the Atmosphere, New York, NY, Springer-Verlag, 1978, p. 79.

Tatarskii, V.I., Wave Propagation in a Turbulent Medium, New York, NY, McGraw-Hill, 1961, pp. 191-196.

Tatarskii, V.I., The Effects of the Turbulent Atmosphere on Wave Propagation, Jerusalem, Israel Program for Scientific Translations, Ltd., 1971, pp. 86, 239, 289.

Walters, D.L., "Atmospheric Modulation Transfer Function for Desert and Mountain Locations: Transverse Coherence Length Measurements," J. Opt. Soc. Am., 1981, Vol. 71, pp. 406-409.

Walters, D.L. and K.E. Kunkel, "Atmospheric Modulation Transfer Function for Desert and Mountain Locations: The Atmospheric Effects on Transverse Coherence Length," J. Opt. Soc. Am., 1981, Vol. 71, pp. 397-405.

Wang, T., G.R. Ochs, and S.F. Clifford, "A Saturation-Resistant Optical Scintillometer to Measure CN2," J. Opt. Soc. Am., 1978, Vol. 68, pp. 334-338.

Wyngaard, J.C., Y. Izumi, and S.A. Collins, "Behavior of the Refractive-Index-Structure Parameter Near the Ground," J. Opt. Soc. Am., 1971, Vol. 61, pp. 1646-1650.

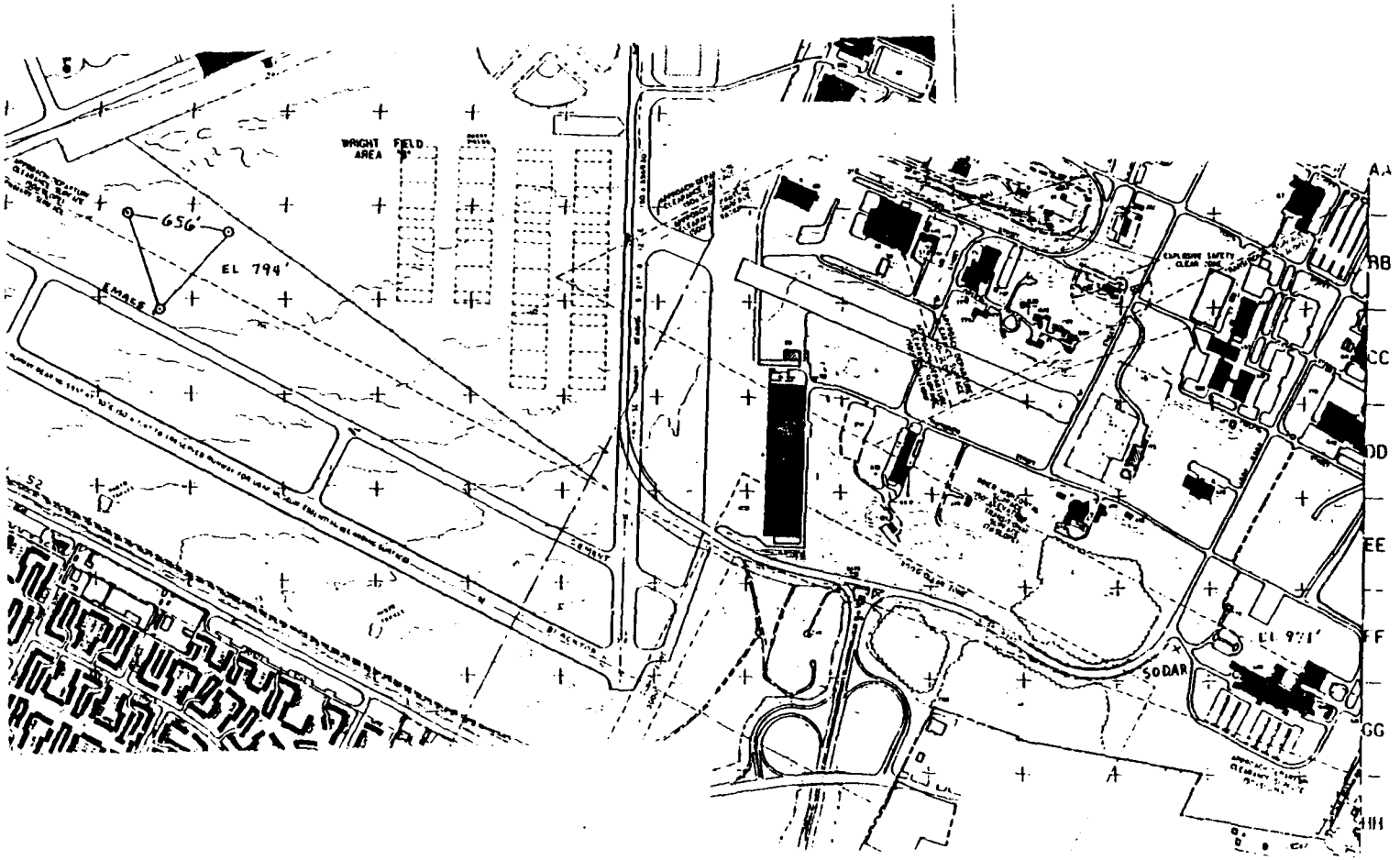
WRIGHT FIELD AREA
656'
EL 794'
SMAGE
SODAR
AA
BB
CC
DD
EE
FF
GG
HH

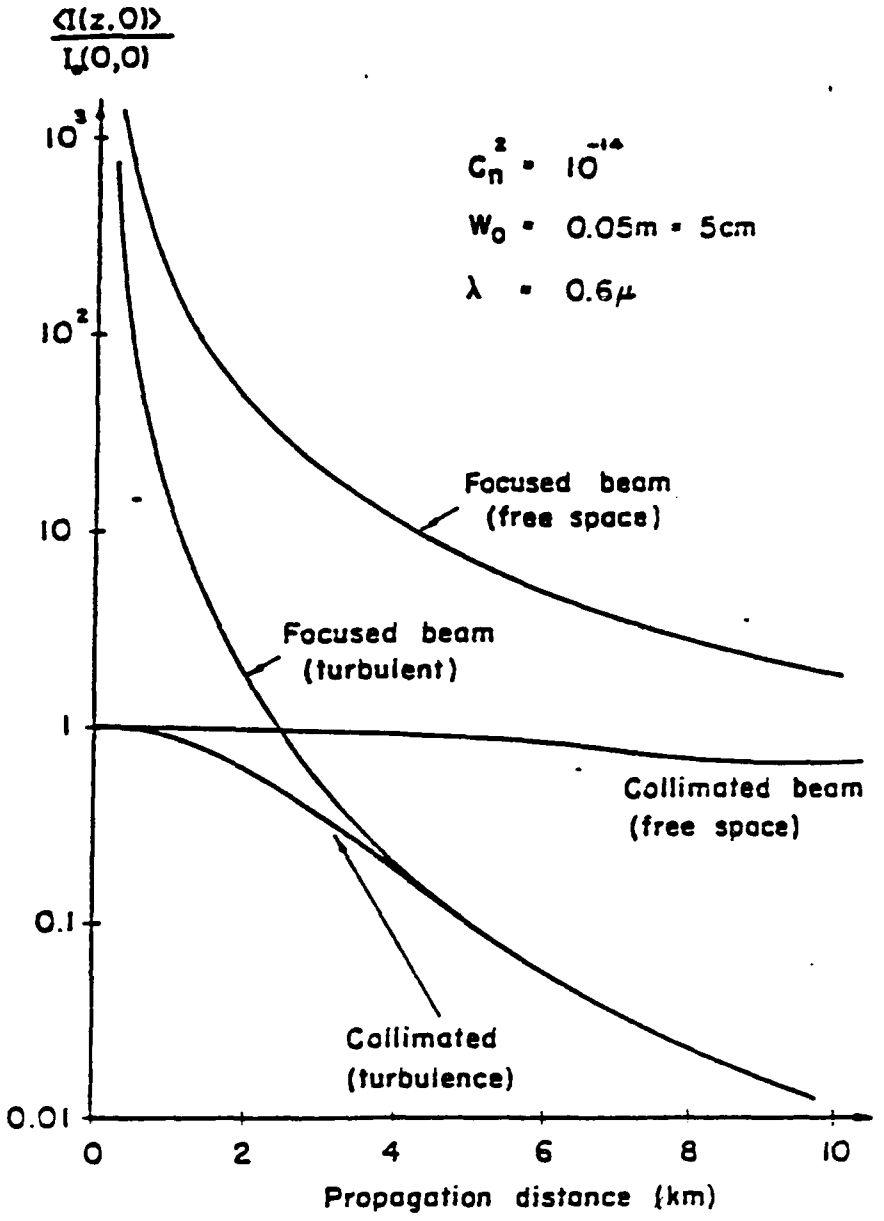

Fig. 5.2. Average intensity $\langle I \rangle$ of collimated and focused beams on the beam axis as a function of distance

A typical form for the average intensity of a beam propagating through atmospheric turbulence is given in the weak fluctuation approximation by

$$\langle I(L,p) \rangle = \frac{W_0^2}{W_{LT}^2} \exp\left[- \frac{2p^2}{W_{LT}^2} \right]$$

where $W_{LT}^2 = W^2/(1-f)$

and $f = 1.36\, C_n^2\, k^{7/6}\, L^{11/6}\, \Phi(L)$

(From Ishimaru, A., "The Beam Wave Case and Remote Sensing," In Laser Beam Propagation in the Atmosphere, Edited By J.W. Strohbehn, New York, NY, Springer-Verlag, 1978, pp. 129-170.)

1988 USAF-UES SUMMER FACULTY RESEARCH PROGRAM

GRADUATE STUDENT RESEARCH PROGRAM

Sponsored by the

AIR FORCE OFFICE OF SCIENTIFIC RESEARCH

Conducted by the

Universal Energy Systems, Inc.

FINAL REPORT

Lightwave Systems and Device Database Development

Prepared by:	Phillip E. Pace
Academic Rank:	Student
Department and	Electrical and Computer Engineering
University:	The University of Cincinnati
Research Location:	AFWAL / AAWP-1 Wright Patterson A.F.B. Dayton, Ohio 45432
USAF Researcher:	Dr. James Tsui
Date:	8/15/88
Contract No:	F49620-88-0053

Lightwave Systems and Device Database Development

by:

Phillip E. Pace

ABSTRACT

Conventional receiver architecture and signal processing techniques are reaching their limits in terms of speed and throughput and new optical designs are offering great promise in terms of these eliminating these limitations. Lightwave system designers are now faced with the problem of staying abreast of the current and future state of optical devices and sub-system technologies. A composite, categorized, and up-to-date database development has been researched and constructed which details the various optical computing and processing components available for systems development along with a brief description of their general capabilities.

ACKNOWLEDGMENTS

I wish to thank the United States Air Force Systems Command and the Office of Scientific Research for the sponsorship of this research. I also wish to especially thank The Universal Energy Systems for their support in giving me direction and handling all the administrative responsibilities.

My experience in the Electronic Warfare Division / Passive ESM branch proved to be very valuable in understanding what is needed in terms of future technology and systems development. I would like to thank Dr. James Tsui and his entire staff for all their support and understanding.

For his patience and faith in me and his confidence in my potential, I would especially like to thank my academic advisor, Dr. P. A. Ramamoorthy. Without his guidance and support none of this effort would have been possible and I am deeply grateful.

I. INTRODUCTION

The Electronic Warfare - Passive ESM (Electronic Support Measures) branch of the USAF Aeronautical Laboratories at Wright Patterson Air Force Base are particularly interested in developing receivers for radar, IR, optical and UV detection and warning. The current (and future) electronic density within the combat environment is pushing the performance of digital ESM receivers beyond their capabilities. Optical processing and computing remain a valid alternative for receiver systems design because of the inherent advantages over current implementation.

The first advantage lies in the massive parallel processing that may be easily implemented resulting in a large increase in computational speed. Additional advantages include extremely high throughput (due to the computations being accomplished at the speed of light), the ease of interconnectability (ie. for implementation of neural architectures) and the powerful operations available, ie. a lens taking the 2-D Fourier transform.

My research interests have been in the area of optical processing devices for receiver design. My work on a special lightwave systems and device database have contributed to my assignment at the Passive ESM branch of the USAF Aeronautical Laboratories.

II. OBJECTIVES OF THE RESEARCH EFFORT

The main problem facing optical system designers today is keeping track of the available lightwave devices and their corresponding performance specifications so that new and different approaches to system architectures may be developed that exploit the advantages that are being offered. The problem with this is that it combines two separate areas of research.

One separate area is the semiconductor device technology area where the research interest is only at the device level. The second separate area is the systems processing and computing area in which the research is directed towards the overall architecture of the system design. In order for the future lightwave systems designer to function, a knowledge of both areas is mandatory.

My assignment as a participant in the 1988 Graduate Student Research Program was to construct a composite database of the current lightwave device research and technology. This is necessary so that new receiver system architectures may be developed (not just conventional schemes being implemented optically). Since this bridge between the two separate areas of technology is constantly being torn due the rapid development of lightwave device technology, it was decided

that this effort should be continuously updated and in the future to also add the individual device system performance, analysis and design BIBO parameters useful in systems development.

III. CATEGORIES

The two different types of optical processing are incoherent processing (optical waves with 2 or more wavelengths present) and coherent processing (monochromatic optical waves). The optical processing devices in existence today, can basically be grouped into 4 categories.

Integrated Optical Devices -	devices fabricated in GaAs, Si, GaAlAs, ZnCd, InP and other types of compounds
Interface Devices -	optical hybrid equipment and connectors
Lasers -	solid and gas type lasers
Geometrical Components -	transparent objects that deflect, transmit and reflect

Detailed below is a composite of the various devices and systems used and a brief description of their function.

IV. Integrated Devices

IV-1. Light Waveguides and Couplers

These are the interconnection elements for various devices of an optical integrated circuit. Waveguides can be planar (symmetric or asymmetric) or rectangular. System analysis parameters include whether a certain mode or modes can exist, the guide cutoff frequency, the volume and surface scattering losses, the absorption losses and the radiation losses.

Waveguides

Planar symmetric - bordering layers have identical index of refraction

Planar asymmetric - one bordering layer has index of refraction much larger than the other border

Rectangular waveguide - channel guide or 3-D guide

Rectangular striploaded - optical stripline

Couplers

Direct focusing - endfire approach that matches beam-field to the waveguide mode field. Useful for coupling gas laser beams to IOC waveguides.

End-Butt - parallel approach useful for waveguide to waveguide coupling and heterostructure laser to waveguide.

Prism - couple light into a waveguide that is buried within a OIC, with only the surface exposed.

Microlenses - used on coupling into single mode fiber end. Has to perform wavefront matching of the radiation field to the mode carried in the fiber.

Grating - connects a particular waveguide mode with an unguided optical beam which is incident at an oblique angle.

Tapered - based on the principle that a waveguide which is below cutoff transfers its energy into radiation modes. Guide thickness is tapered in coupler region to produce a reduced-height waveguide with a decreasing cutoff wavelength.

Fiber to waveguide couplers

Butt - fiber directly butted in contact with the waveguide, without any interfacing device in an end-on alignment.

Tapered film fiber - fiber connected to a tapered section of waveguide through a substrate or through the surface.

Waveguide to Waveguide

Dual channel directional - parallel channel optical waveguides closely spaced so that energy is transferred from one to the other by optical tunneling (coherent synchronous coupling).

IV-2. Electro-Optic Switches and Modulators

Usually these devices can function as either a switch or a modulator. The device is considered a modulator if its primary function is to impress information on a light wave. The device is considered a switch if it changes the spatial

position of the light or else turns it off or on.
The operation is based on the electro-optic effect (Pokels effect + Kerr effect) which is the change in the index of refraction produced by the application of an electric field.
System analysis parameters include modulation depth (modulation index), bandwidth, insertion loss, power consumption and isolation.

Single Waveguide Modulator Structures

Phase modulators - the electric field causes a change in phase of lightwaves traveling along the guide that is proportional to the voltage (requires phase coherent detection).

Polarization modulators - the electric field causes a change in the polarization of the lightwaves proportional to the voltage (requires a polarization analyzer for detection).

Intensity modulators - the structure guides the lowest order mode with no electric field and when the electric field is applied the mode becomes transmissive.

Electro-absorbtion modulators - the electric field produces an intensity modulation but is based on the Franz Keldysh effect (no Pockel's effect) and is characterized by large changes in the device absorption.

Dual Channel Waveguide Modulators

Mach-Zehnder modulators - the interference is produced between phase coherent lightwaves by traveling over different

path lengths. By applying voltage to the electrodes, the path lengths can be varied. Single mode, multimode and birefringement fibers can be used for the paths and are sensitive to external vibration and pressure changes.

Bragg effect modulator - the voltage applied to the electrodes changes the index of refraction and forms an optical grating pattern in the guide which changes the direction of propagation of the light beam.

Reflection modulators - the electo-optic effect reduces the index of refraction of the device to the point where total internal reflection of an incident optical beam occurs.

Lightwave Crossbar - composed of non-linear material, light is injected into one row and one column waveguides representing two input values. The addition of the two fields together cause the non-linear material at the intersection to switch states. The other sites lack intensity and do not switch states. Probe beams in the third dimension can be modulated by the non-linear patches.

IV-3. Acoustic - Optic Modulators

In these types of modulators, acoustic waves produce the desired grating pattern in the index profile. The acousto - optic effect is the change in the index of refraction caused by mechanical strain which is introduced by the passage of an acoustic - strain wave. The resulting index variation is periodic with a wavelength equal to that of the acoustic wave.

Bragg type modulator - based on diffraction which takes place when long interaction lengths between the optical and acoustic beams cause multiple diffraction. Used as a modulator, beam deflector and as a optical switch.
Raman Nath modulator - have a smaller modulation index than that of the comparable Bragg modulators and cannot be used as an optical switch because the diffracted light is distributed over many orders at different angles.

IV-4. Integrated Lasers

From the principles of light emission in semiconductors it is possible to design a light source in such a way that stimulated emission of photons will dominate over both spontaneous emission and absorption. With a resonant reflecting structure generating optical feedback, a lasing mode can be established and coherent optical emission will result. System analysis parameters include the optical modes supported, the lasing threshold, output power, stability, efficiency and environmental temperature requirements.

Discrete laser diode - small, simple in construction, pn junction laser with flowing junction current. Used in fiber optic signal transmission applications.
Electron-Beam pumped laser - pumped by a high-energy electron beam impinging on the semiconductor crystal rather than by a flowing junction current.

Tunnel injection laser - pumped by a current of electrons or holes which reach the active region by tunneling through an energy barrier.

Distributed feedback laser - doesn't use the reflecting structure as the lasers above do. Uses distributed feedback from a Bragg type diffraction grating.

Excimer laser - high average power in the UV region with radiation at 193 nm (ArF) and 248 nm (KrF). Pulse duration 10-30 nsec with beam divergence from 2 to 5 mrad.

Fabry - Perot - dual channel device where feedback is provided by the channels and coupling region.

IV-5. Optical Detectors

Detectors in IOC must have high sensitivity, short response time, large quantum efficiency, and low power consumption. Factors that pertain to the system analysis include cutoff frequency, linearity and noise.

Photodiodes -(discrete, pyroelectric, Schottky-Barrier, light emitting, avalanche) Current is modulated by the absorption of photons of light.

Photovoltic - large bandwidth device that generates a voltage when illuminated.

Photoconductive - device in which the resistance is proportional to the intensity of light impinging upon it.

IV-6. Specialized Multi-Element Compounds

Whole receivers, antenna systems, transmitters and various specialized components can be integrated with uses ranging from telecommunications to military to medical.

RF Spectrum Analyzer - light from a laser source is coupled into a planar waveguide passing first through a collimating lens then through a Bragg-type acousto-optic modulator. The RF signal to be analyzed is applied to an acoustic transducer that generates sound waves causing them to have a time varying period. This makes the deflection angle of the optical beam at the output of the modulator a function of the input rf signal.

Analog to digital converter - this device incorporates two 3 dB couplers and a phase shifter formed in a pair of straight waveguides. The devices now are capable of one-bit electro-optical A to D conversion at 100-200 MHZ.

V. Interface Devices and Systems

V-1. Systems

Spatial light (valve) modulators (SLM) - acts as a piece of film whose transmittance or reflectance may be varied spatially and temporally by electronic or optical means. The two types are the optically addressed and the electrically addressed. The SLM can be used as a polarization modulator, hologram media, storage device, analog multiplication, optical phase conjugation, crossbar interconnection for

linear and nonlinear spectral estimation, real-time diagnostic expert system, image amplifier, wavelength converter, incoherent to coherent image converter, cross correlator and convolver. Different types include deformable surfaces, GaAs, magneto-optic, micro-channel, micromechanical, multiple quantum well, membrane, electron beam addressed electro-optic crystal (DKDP), pockels readout optical modulator (PROM), single crystal ferroelectrics (Photo Titus), ceramic photoelectrics, ruticon and the liquid crystal.

Optical phased lock loop - has the same function as the electronic PLL. Contains an optical oscillator whose output phase and / or frequency is steered to keep it in sync with the reference signal.

Optical wavelength synthesizer - optical device that allows a wide variety of signals to be set up simultaneously.

Fiber ring resonator - device for non-linear phase modulation in which the intensity transfer function has resonances at integral multiples of two pi (zero transmission in optimal coupling conditions). Phase modulator is usually a piezoelectric cylinder in which a voltage is applied to change the length of the cylinder and the fiber. Resonator is excited by a single mode laser and the polarization is adjusted to the polarization eigen mode of the fiber. Important in spectral analysis or when the piezoelectric transducer is a control element in various sensor configurations.

Beam splitters and deflectors - used in beam manipulation, beam deflection, interferometry, imaging and recording. Analysis parameters include polarization, transmission tolerance, scatter and absorption loss, useable clear Polarizer - selectively transmits (or lets through) a specific polarization. Used as detectors, polarization analyzers, laser beam attenuators and filters. Analysis parameters include polarization, spectral range, transmittance, acceptance angle and extinction ratio.

VIII. RECOMMENDATIONS

The number of different lightwave devices now available is numerous. The progression of new fabrication techniques, devices and system components is moving along at a rate so rapid that a way of categorizing the system level performance parameters of each of these as they are developed seems imperative if new advanced system architectures (such as parallel distributed processors) are to be developed.

Further database development including the system level input and output parameters and the interface specifications for each individual entry, would make the lightwave system designers job much easier. In addition, the new designs could also take advantage of the current technology that is (or will be) available more readily, enhancing the capabilities of future systems.

Dye Laser - laser wavelength can be tuned over a significant range by varying the dye solution.

VII. Geometrical Components

Included in this category are the various geometrical optic devices made from fused silica, borosilicate or plastic used for light beam deflection and transmission. Analysis parameters include radius of curvature, surface quality, surface figure tolerance, number of edge chips, angular tolerance (prisms), transmittance and polarization.

Mirrors -devices that reflect or diffract light. Used in various system designs to reflect light back into the system, set up a resonating cavity, beam deflection and to direct light to and from various components.

Prisms - used as a dispersion element in laser cavities, couple light into integrated guides and devices, decomposition of light into its various spectral components. Types include right-angle prisms, Littrow prisms, Brewster angle prisms, dove prisms, Porro prisms.

Lenses - standard configurations include plano convex, bi-convex concave, bi concave, cylindrical and aplanatic achromats. Analysis parameters include diffraction effects, spherical aberrations, focal length, radius of curvature, clear aperture, surface figure and the thickness. Used for phase transformation, Fourier transformation, image formation, focussing and collimating.

V-2. Interface Devices

Fiber optics - interconnection waveguide structure that can operate in single mode (633 nm) or multimode. No outside EM interference, high bandwidth and very low losses. Used for telecommunication and pulse compression. Always experience some degree of linear birefringence (due to fiber bending and lateral pressure) and circular birefringence (induced by magnetic field - Faraday effect).

Diffraction grating - glass or plastic material which is etched or cut to cause grooves to diffract light in a specified way. Used in optical filters and hologram writing.

Hologram - 2D or 3D, computer generated or media wavefront recording produced by holography.

VI. Lasers

Lasers in this category are the structures **not** fabricated in semiconductor material. Analysis parameters used to characterize lasers are the peak output power, efficiency, spectral range, beam divergence and pulse repetition frequency.

Ruby Laser - common laser using a three-level energy system with a maximum emission power output at .6943 micro meters.

Nd:Yag, Nd:Glass Laser - four energy level system with maximum output power at 1.06 micro meters.

CO 2 laser - continuous output power in the range of 150 KW at 10.6 micrometers.

REFERENCES

Leith, E. "Fundamentals of Modern Holography", The International Society For Optical Engineering , Aug. 18 1987.

Marom,E. and Konforti,N., "Dynamic Optical Interconnections", Optics Letters, July 1987.

Chang,C.L. and Tsai, C.S. "Electro-Optic Analog-To-Digital Converter Using Channel Waveguide Fabry-Perot Modulator Array", Applied Physics Letters, July 1983.

Hunsperger, Robert G., Integrated Optics : Theory and Technology, Springer Verlag, New York 1984.

Gowar, John, Optical Communication Systems, Prentice Hall International, Englewood Cliffs, N.J. 1984.

Goodman, Joesph H., Introduction to Fourier Optics, McGraw Hill, New York, 1968.

Yariv, A., Introduction to Optical Electronics, Holt, Rinehart and Winston Inc., New York 1971.

1988 USAF-UES SUMMER FACULTY RESEARCH PROGRAM/

GRADUATE STUDENT RESEARCH PROGRAM

Sponsored by the

AIR FORCE OFFICE OF SCIENTIFIC RESEARCH

Conducted by the

Universal Energy Systems, Inc.

FINAL REPORT

A Study of Sky Backgrounds and Sub-Visual Cirrus

Prepared by:	Eric O. Schmidt
Academic Rank:	Graduate Student
Department and	Atmospheric Sciences Department
University:	Georgia Institute of Technology
Research Location:	AFWAL/AARI-3 Wright-Patterson AFB Dayton, OH 45433
USAF Researcher:	Jan Servaites

Date:	September 23, 1988
Contract No.:	F49620-88-C-0053

A Study of Sky Backgrounds and Sub-Visual Cirrus

by

Eric O. Schmidt

ABSTRACT

A complementary set of instruments was set up to facilitate the observation of natural sky background radiance levels and the detection of sub-visual cirrus clouds Wright-Patterson Air Force Base. Two coordinated camera/photometer systems were used to look at the solar aureole and at the sky background. A frequency-doubled Nd:Yag lidar was used for sub-visual cirrus detection and the other instruments coordinated with synoptic data to try to characterize the clouds.

Sub-visual cirrus were detected on the afternoon of the final day of the experiment in a band ahead of a cold front. The detection of the incidence and continued presence of an optically thin, yet physically thick smoke layer due to forest fires in the northwestern U.S. was a bonus for the experiment. The natural photometric background levels were determined for a variety of weather conditions and the range, resolution and photon noise levels measured.

I. INTRODUCTION:

Sub-visual cirrus clouds have been cited (Schmidt et al, 1988) as the probable source of the 11 μm "window-fill" phenomenon which degrades the performance of airborne and space borne sensors. Detection of cirrus clouds and the middle atmosphere via a LIDAR (LIght Detection And Ranging Device) is limited by the natural sky background, i.e. the photon noise produced by direct and scattered radiation. Characterization of these effects is necessary to understand the effects the atmosphere has on sensors and our environment.

The Atmospheric Sciences Department of the School of Geophysical Sciences at the Georgia Institute of Technology, in conjunction with the Electromagnetics Laboratory/Electro-Optics Division of the Georgia Tech Research Institute is currently involved in efforts to utilize the 100-inch optical collimator at Wright-Patterson Air Force Base as the collector for an atmospheric LIDAR system, the "MegaLIDAR" system. Because of the greater collecting area this system should be able to measure atmospheric parameters up to 100 km altitudes versus altitudes of 20-25 km obtained with typical lidars. Operation of the MegaLIDAR on a frequent basis will allow verification of properties and models of the middle atmosphere, including gravity wave modeling. Determination of sky background characteristics under different cloud-cover conditions is important for qualification of operational limitations.

My research interests have been in the area of the detection, characterization and modeling of visible and sub-visual cirrus clouds. Previous work on the characteristics of sub-visual cirrus clouds via coordinated radiometric and spectrometric measurements has contributed to my understanding of cirrus clouds and the efforts of this study.

II. OBJECTIVES OF THE RESEARCH EFFORT:

The methods of detecting sky background radiance levels are well-known, involving the use of radiometric and/or photometric sensors. Detection of sub-visual cirrus clouds has also been done by means of a LIDAR (Uthe and Russell, 1976); however, this was done in the tropics, not at mid-latitude locations. To date there has been little coordinated effort in the area of detection and characterization of sub-visual cirrus using multi-sensor techniques. Coordinating photometric information with satellite imagery, ground-based camera images and synoptic data, parameters can be determined when the LIDAR has verified the presence of sub-visual cirrus. Computer analysis of the video and digital images is an alternate detection method and provides unique information on the extent and uniformity of sub-visual cloud bands.

My assignment as a 1988 Fellow in the Graduate Student Research Program was to determine the natural sky background under a variety of weather conditions and to detect and parameterize sub-visual cirrus. Information on the natural sky background variability was gained by means of two Pritchard photometers. Video imagery was obtained simultaneously from two CCD (charge-coupled device) cameras: a solar aureole camera with occultation disk, and an all-sky camera with a 160° field-of-view (FOV). The 8-12 μ/m band radiometer was not available for use during the experiment period, so the study is limited to measurements in the visible region of the spectrum. The cameras were not in the original plan; however, they provide avenues for future work.

Further research work and computer analysis of the data recorded during the two-week observation period will begin at the Georgia Institute of Technology upon my return. A proposal for a mini-grant

under Dr. Gerald Grams will be submitted. The MegaLIDAR. proof-of-concept test will be run in October, 1988 at Wright-Patterson AFB, Building 622.

III. NATURAL SKY BACKGROUND

a. The natural sky background and its effect on the range and noise of LIDAR systems is important in the field of remote sensing, particularly among people with an interest in the "MegaLIDAR" project. Ground-based LIDAR systems are currently operated primarily at night due to the uncertainty in the background photon levels. To study the effects of the daytime versus nighttime sky on the performance of LIDAR systems, two coordinated camera and photometer systems were set up.

One camera looked at the overhead sky with a small FOV (6° or 3°) and was coordinated with a vertically pointing all-sky camera with a 160° FOV. The all-sky camera was connected to an animation system that was driven by a Commodore-64 computer which sent a signal to the animation system once per minute. Upon receiving this signal, the animation system read the time and date from a clock and transposed it onto 3/4" video tape as part of the frame header. The video recorder simultaneously recorded a frame of the input video signal from the all-sky camera (a Sony color CCD). This time-lapse system was set up on the roof of the Mobile Infrared Laboratory (MIRL) each morning and allowed to run until dark. A shadow-band stand was used to block the sun throughout the day and neutral density filters were used to adjust the input intensity levels to acceptable values, according to the camera sensitivity and the extent of the solar halo.

The second camera/photometer system was an off-vertical system, designed to scan the region near the sun to look at the solar aureole,

i.e. to determine the variation of intensity with angle away from the sun. Hall (1968) and Watt (1980) have been able to derive particle size distributions and cirrus properties from the slope and variability of the solar aureole. In an attempt to improve upon their efforts, a super-VHS video recorder was used to record the input images from the GE TN2500 CCD camera (17 mm, f2.7 lens). A 9° solar occultation disk was used with the camera seated on a telescope mount. In order to obtain useful aureole information and to calibrate the camera images, the photometer elevation angle was frequently adjusted. It was set-up with a 2° or 6° FOV and two neutral density filters (ND 4 + ND 2) so that it could safely scan across the sun. Using the viewing objective of the photometer, the sensor was pointed ahead of the sun and the Earth's rotation used to scan at a known rate. The photometer covered 15° of sky in approximately one hour while the video recorder could run for two. Once the sun was scanned, the photometer would be re-set for another scan and the process repeated so that several scans could be made every day. At night the photometer filters were removed and the field-of-view widened to accomodate the sensitivity range of the instrument (the vertically pointing photometer also used a ND 4 filter during the day and was opened up to a 3° FOV without filtering at night.)

b. Using secant scaling to determine the variation of sky background with zenith angle (as per Chapman, 1931), the typical ratio of off-axis (approximately 65° zenith angle) to vertical photometer readings should be 2.4:1. Excluding the presence of clouds and the sun, this reasonably agrees with the results obtained (day and night). Light pollution at night is a problem under certain sky conditions as was evidenced by the

photometer readings when the smoke layer was overhead. The off-axis:vertical ratio was about 3.5:1 in this case, indicating an increase in the amount of light received of 50% over the norm. The smoke particles probably reflected light incident from the city of Dayton into the FOV of the off-axis photometer. We believe that this increase is also indicative of a nonspherical smoke particle habit (shape). Spherical particles should uniformly scatter obliquely incident radiation; however, this type of uniform scattering would merely support a secant law effect. Only nonspherical particles can enhance scattering at oblique angles (Takano and Liou, 1988).

The calibration and coordination of the video images recorded by the two camera systems will be done by "frame- grabbing": digitizing an image recorded on tape and storing it in a computer file. The variation of the sky background can then be analysed in more depth. However, such an effort falls beyond the scope of the summer project and will be pursued as a follow-on task.

IV. LIDAR DETECTOR SYSTEMS

a. The LIDAR system itself could also be used to determine the photometric sky background, but only at a single wavelength (0.53 μm). The laser in the LIDAR system is a doubled Nd:Yag that has a 0.25" beam at the aperture with a 2 milliradian divergence at the 1/e point. The system is capable of operating at 20 Hz with a 20 nanosecond pulse width and 35 mJoules/pulse (it also emits 135 mJ/pulse at 1.06 μm, but we were not set up to utilize that frequency). The LIDAR system schematic is shown in Fig. 1, incorporating a 14" Celestron collecting telescope, the laser, a fitted photomultiplier tube and a linear amplifier. The output is passed into a transient recorder and digitizer which operates

at 10 MHz, then into an IBM AT personal computer, where the files are stored. Continuous operation of the system is possible and a display of the raw data as it is collected is provided. Another utility of the system allows the user to re-scale the raw data files and to apply corrections for the $1/r^2$ decrease in the beam intensity and for the exponential decrease in the molecular density of the atmosphere ($e^{-z/H}$). This "range-converted" display can also be re-scaled, and it provides a first-look at the scattering ratios of features in the atmosphere.

b. Figure 2 shows a typical cloud at the top of the boundary layer during the day. The curve is distributed about the value 1, since this occurs when scattering is equal to that of a purely molecular atmosphere (no clouds and/or aerosols). Peak readings indicate that the cloud scatters approximately 15 times more efficiently than the background atmosphere. Another feature seen in Figure 2 is the exponential growth of noise. Since the signals at high altitudes are very small and an exponential correction is being applied (the smallest noise representing the integer mode of the calculation), they tend to be exaggerated. This is very obvious during the day, and less obvious at night (see Fig. 3). In addition to a decrease in noise at night, the range of the LIDAR system also increases. The daytime scan in Fig. 2 is only accurate to approximately a 5.5 km altitude while the nighttime scan on the same day shown in Fig. 3 is accurate to about 16 km (or better). The reduction in noise is typically greater than a factor of 5-10. The dark current noise was also measured (at 66° F) and found to be a maximum of $\pm$18 counts/sec (or photons/sec) over the diurnal observation period. The mean quiescent nighttime background photon levels during the ten day experiment period

were found to be 2140 (±18) counts/sec, while the daytime levels peaked at 3280 (±18) counts/sec in the early afternoon. This gives a 1.5:1 ratio of daytime to nighttime photometric background levels at 0.53 μm (near the peak of the solar spectrum at 0.55 μm).

V. SUB-VISUAL CIRRUS

a. The LIDAR is the primary means by which sub-visual cirrus are detected, though the measurement of the solar aureole and multi-spectral satellite techniques are being developed as useful, operational methods. The LIDAR was operated for ten days in the MIRL facility in front of Building 622 at WPAFB during both daylight and nighttime hours. A two man system was required to satisfy the safety office concerns for air traffic in the WPAFB area. This limited most observation periods to 3-4 hours, mostly in the afternoon and evening hours. We believe that the presence of sub visual cirrus clouds should be associated with discontinuities or "breaks" in the tropopause, i.e. the Inter-Tropical Convergence Zone (ITCZ), south of the jet cores, and near frontal boundaries. This is in agreement with evidence provided at the July 1988 FIRE meeting (Starr and Cox, 1985).

b. The detection of sub-visual cirrus clouds is weather dependent. During the time the experiment was in operation, two fronts passed through the Dayton area. We were not able to detect sub-visual cirrus on the first occasion due to manpower constraints; however, on the second occasion high altitude cirrus streaks were observed to move through the area with the prevailing winds. Camera images verify the presence of the thin clouds and their apparent absence as well. Figure 4 shows an example of a cloud observed when the LIDAR was apparently looking at a visually clear sky. The cloud feature seen in Fig. 4 is approximately

0.5 km thick and at an altitude of 11.25 km, with a scattering ratio of about 12:1 (versus 4:1 as expected for a typical cirrus cloud at that altitude). This moderately high scattering ratio is indicative of the possible presence of nonspherical ice crystals. The LIDAR was set-up to view at an angle of approximately 3° from the vertical, so that specular reflections are not a problem for this system. Therefore, we conclude that sub-visual cirrus clouds were observed for about 2.5 hours with a prevailing wind from the southeast at 5 knots (and high altitude winds of approximately 50 knots from the west-southwest). This indicates the presence of a sub-visual cirrus cloud band that is approximately 240 km wide. There was a frontal passage 24 hours later, accompanied by rainfall. This finding, though solitary, agrees with the expectations that we have concerning the presence of these types of clouds; therefore, we conclude that sub-visual cirrus clouds are associated with frontal systems.

VI. SMOKE LAYER DETECTION

a. An unexpected result of our experiment was the observation of a smoke layer from fires in the western United States. The incidence of the smoke layer and its persistence and properties were monitored for several days. The LIDAR monitored the thickness and persistence of the smoke layer via the scattering ratio. The optical depth will be derived after some post-operation analysis. In addition to the LIDAR, the all-sky and aureole cameras and the photometers were running.

b. Figure 5 shows the range-converted display of the smoke layer between a 3-5.5 km altitude range. The r^2 increase in scattering ratio near the ground is an artifact of the saturation of the linear amplifier.

The smoke itself appears to be in three levels or layers and is located 1.5-2 km above the boundary layer. Synoptic information for this period of time does not indicate the presence of any inversions in the altitude region where the smoke layering is located. It was originally detected on September 8th and persisted until heavy rains on the afternoon and evening of September 12th. The smoke layer was optically thin as is evidenced by Fig. 6, where a thin cloud was observed overhead through the smoke layer. The night before the smoke layer was detected the sky was very clear and stars could be seen to within 10° of the horizon. On the nights that the smoke layer was present (especially the first night) no stars could be seen below approximately a 45° zenith angle. The ratio of the vertically pointing photometer to the off-axis photometer (viewing at a 65° zenith angle) at night was 3.5:1, not 2.4:1 as expected, a factor of 50% increase. GOES satellite photographs taken near sunrise and sunset (large oblique incidence and reflectance angles) show the plumes of the forest fires and indicate the presence of the smoke layer as it apparently follows the polar jet stream. This is only seen in the visible photographs, not in the infrared images (to date).

VII. RECOMMENDATIONS:

a. The operation of a LIDAR such as the MegaLIDAR during daylight hours is feasible; however, the range and resolution will suffer due to increased background photon noise. As was discussed earlier, the range reduction is about a factor of three from night to day time observations with a factor of 5-10 increase in noise. This means that daylight observations should occur either late or early in the day. If 90 km is the expected nighttime altitude of maximum sensing, then this means that 30 km is the maximum altitude to be expected in daytime. One feature of

the MegaLIDAR system that will help to reduce the stray photon noise is the long "telescope" path (the mirror is at the bottom of a 150' shaft built in the center of Building 622, WPAFB). The use of baffles will help reduce the amount of extraneous noise, both external and internal.

Synoptic data was obtained from the base weather station and I attended a weather briefing every day that provided educational and stimulating discussions. The Weather Office provided temperature, pressure and dew point soundings, as well as GOES photographs, and charts at 200-, 300-, 500-, 700-, 850-mb, and surface. The satellite photographs provided the crucial link for the identification of the smoke layer. This type of information should be monitored on a daily basis to ensure optimal operating conditions for the MegaLIDAR and other LIDAR systems, as well as identification of features of interest to observers.

b. A bonus was obtained during the experiment as the presence of a smoke layer from forest fires in the northwestern United States was first detected and then monitored for several days with the full complement of instruments operating during both daylight and nighttime hours. The moon was in its new phase in the middle of the ten day period so that there was no extraneous light from it to affect the LIDAR or the photometers. Consequently, the nighttime photometer measurements were solely measurements of the effects of the smoke. Derivation of parameters of interest (optical depth, particle size and density, and nonsphericity) for the smoke particles will be done as follow-on work. In addition to providing information about the smoke particles, we believe that the scattering effect seen is analogous to that seen in the infrared near sub visual cirrus, i.e., scattering of infrared radiation incident from warm, lower clouds into the FOV of sensors by hexagonal crystals may be the

primary cause of the 11 μm window-fill phenomenon. The properties of smoke in the atmosphere are also important in modeling the effects of "nuclear winter" on our environment.

c. Computer analysis of satellite images stored on magnetic tape is an important area of work to be pursued in the next year. Previous work by Schmidt, et al, (1988) has indicated the existence of a linear relation between the 7.2 and 11.2 micrometer channels of a cold optics radiometer when a radiometric "knee" (a feature associated with sub-visual cirrus) was detected. This indicates the possibility of multi-spectral detection of sub-visual cirrus with verification by the LIDAR. AVHRR, VAS, GOES, and DMSP images in both the infrared and visible are being collected and archived for analysis at Georgia Tech. Analysis of the images to look for the presence of the smoke layer will also be pursued.

d. Analysis of the all-sky and aureole camera images is also an area of interest. Photographic detection and parameterization of cirrus clouds has been done by Hall (1968) and we are looking to improve on this method by using frame-grabbing (or image digitization) to store the images on a computer to allow digital analysis of the observations. Information on the smoke layer, sub-visual cirrus, typical cirrus, and low and mid-level clouds can be uniquely gained through calibration with the photometers for both camera systems. A study of the variation of the background photon noise levels can also be gained from analysis of the camera images. Comparison of the results with the background radiance levels predicted by atmospheric model codes, initialized with the synoptic information gathered is planned. This means that a unique "equivalent cloud" detection method can be explored through follow-on work.

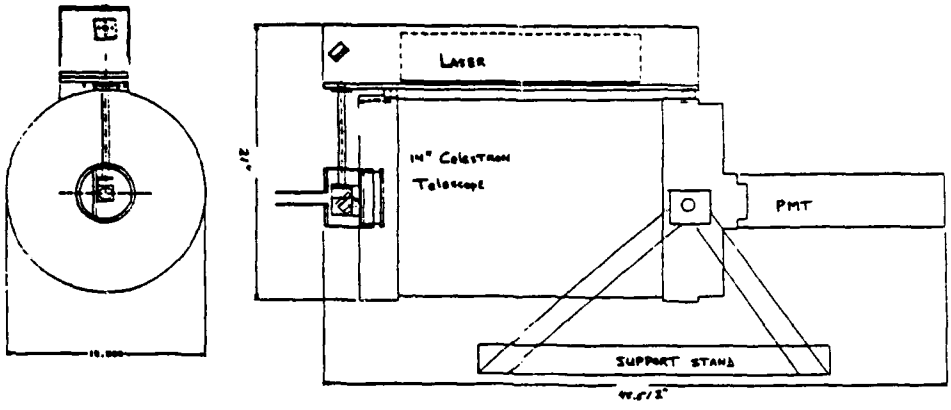

Figure 1. Sub-visual Cirrus lidar ("mini-lidar").

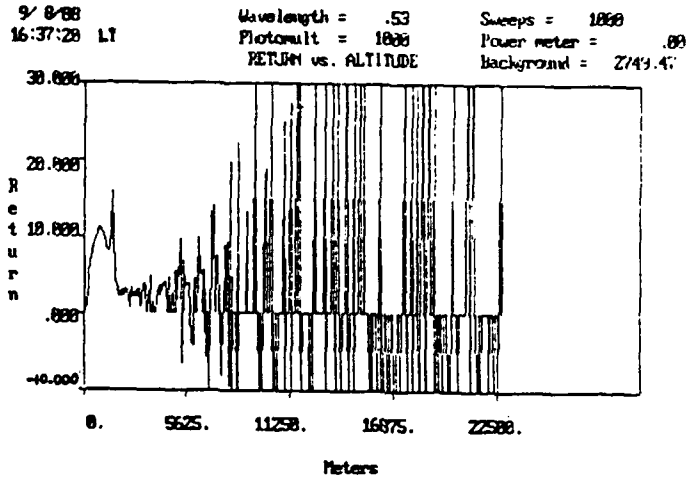

Figure 2. Typical daytime lidar scan showing cloud at top of boundary layer.

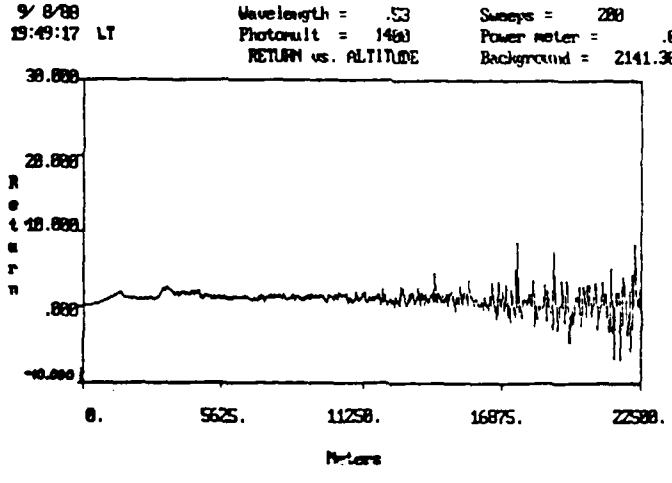

Figure 3. Nighttime lidar scan showing increased range and reduced noise levels.

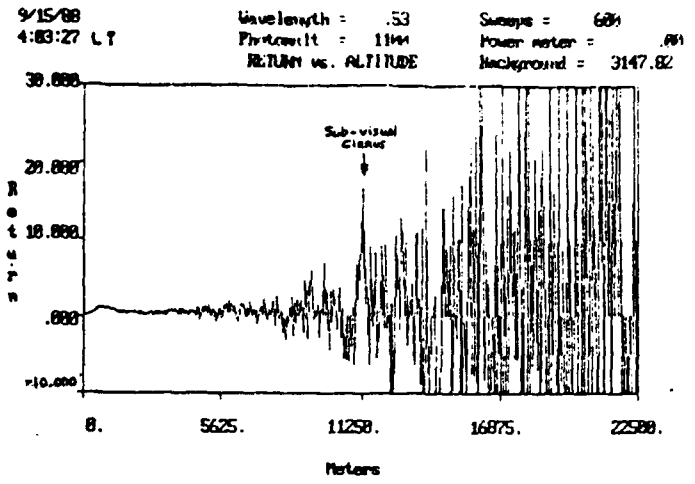

Figure 4. Sub-visual cirrus cloud detected during day.

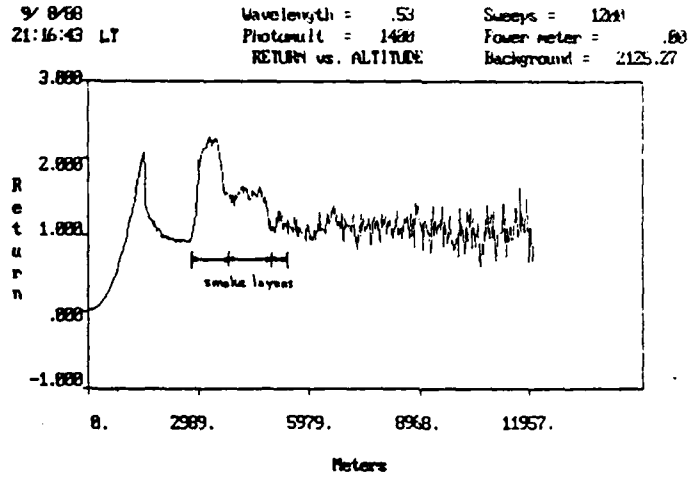

Figure 5. Three-level smoke layer detected on 9/8/88.

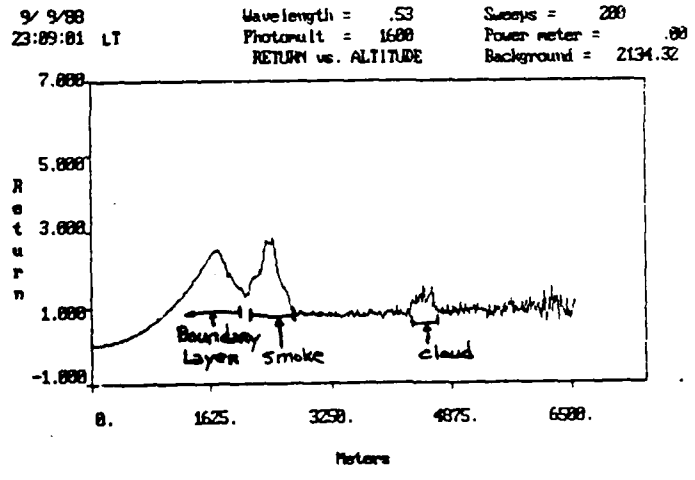

Figure 6. Optically thin smoke layer detected below cloud.

Acknowledgements

I wish to thank the Air Force Avionics Laboratory at Wright-Patterson AFB, the Air Force Systems Command, and the Air Force Office of Scientific Research for sponsorship of this research. Universal Energy Systems, Inc. must be mentioned for their concern and help in the administrative and directional aspects of this program.

My experience and work at the laboratory was rewarding and useful because of the help and efforts of many people. Jan Servaites provided me with equipment, contacts and the means to accomplish what I set out to try to do. Bill Lanich provided me with encouragement and a stimulating research atmosphere. The help of Maj. Bob Hughes, Maj. Willis Shanor, SSgt. Foster and 21t. Steve Finney was invaluable in overcoming obstacles that arose in obtaining support data and provided excellent educational opportunities with their discussions of current and future weather conditions. The personnel at AARI-2 and AARI-3 were of great help and encouraged my efforts in all ways. Thanks goes to Richard Hill for his technical expertise and for listening. Of course, this project could not possibly have succeeded without the encouragement and support of Dr. Gerald Grams, who has encouraged me at every turn, and other people at Georgia Tech: Clyde Wyman, Ed Patterson; my colleagues Christoph Vogel, Capt. Jason Tuell and my fellow GSRP Fellow, Randal Mandock.

REFERENCES

Schmidt, E., "High Altitude Cirrus Effects on Spectral Measurements," Proceedings of the 1988 SPIE Technical Symposium, Vol. 924, (1988).

Uthe, E.E. and Russell, P.B., "Lidar Observations of Tropical High-Altitude Cirrus Clouds," IAMAP Symposium on Radiation in the Atmosphere, Garmisch-Partenkirsch, Germany 19-28 August 1976.

Hall, Jr., F.F., "The Effect of Cirrus Clouds on 8-13 mm Infrared Sky Radiance," Appl. Opt. 7, 891 (1968).

Chapman, S., "The Absorption and Dissociative or Ionizing Effect of Monochromatic Radiation in an Atmosphere on a Rotating Earth," Parts I&II, Proc. Phys. Soc. 43, pp. 26 & 483 (1931).

Takano, Y. and Liou, K-N., "SOLAR RADIATIVE TRANSFER IN CIRRUS CLOUDS I. Single-Scattering and Optical Properties of Hexagonal Ice Crystals," J.A.S., 1988 (in publication).

Starr, D. and Cox, S.K., "Cirrus Clouds, Part 1; A Cirrus Cloud Model," J.A.S., 42, 1985.

Watt, A.D., Circumsolar Radiation, National Technical Information Service (NTIS) SAND80-7009, Apr. 1980.

2034s

1988 USAF-UES SUMMER FACULTY RESEARCH PROGRAM /

GRADUATE STUDENT SUMMER SUPPORT PROGRAM

Sponsored by the

AIR FORCE OFFICE OF SCIENTIFIC RESEARCH

Conducted by the

Universal Energy Systems, Inc.

FINAL REPORT

ADAPTIVE ARRAY ARCHITECTURES with LOW-SENSITIVITY TO RANDOM ERRORS IN THE STEERING VECTOR ELEMENTS

Prepared by:	Tien N. Tran
Academic Rank:	Graduate student
Department and	Electrical and Computer Engineer Department
University :	University of Cincinnati
Research Location:	Avionic Laboratory,
	Wright-Patterson AFB, Dayton, OH
Date:	October 6, 1988
Contract No.:	F49620-88-C-0053

ADAPTIVE ARRAY ARCHITECTURES with LOW-SENSITIVITY TO RANDOM ERRORS IN THE STEERING VECTOR ELEMENTS

by

Tien N. Tran

ABSTRACT

Adaptive Arrays and Beam Forming are used extensively to enhance a desired signal and adaptively cancel or null jammers and other interferring signals. In adaptive processing using the Applebaum adaptive array approach, a steering vector is used to steer the array in the direction of the desired signal. It has beeen shown by Compton, Jr. that errors in the steering vector elements can cause a rapid drop in the output signal-to-interference-plus-noise ratio (SINR) and that the drop becomes larger as the number of elements in the array is increased. In this report, we show that the sensitivity of the output of the array processor to errors in the steering elements can be minimized by going for alternate architectures. We also point out other advantages of such architectures.

ACKNOWLEDGMENTS

The author sincerely appreciates the Air Force Systems Command and the Air Force Office of Scientific Research for giving him the opportunity to acquire new knowledge. Most of all, he also would like to thank everyone at Avionic Lab, Wright-Patterson AFB for the warm welcome and a wonderful summer.

in other armed services to go for adaptive arrays consisting of larger (64 to 256) number of sensors. Several researchers have presented various methods to reduce the problem. Hence architectures or approaches that will minimize the sensitivity of the array output to element variations are needed. Hong et. al. [11] propose to combine Widrow and Applebaum methods; a middle of the road solution since while the LMS portion reduces the effect of steering error, it also lessens the optimality of the Applebaum array. Random noise injection was also considered but this will also lead to desensitivity of array to interested signals. In the next section, we propose altenative architectures for the beamforming arrays and discuss their advantages.

II PROBLEM FORMULATION AND SOLUTION

Consider and adaptive linear array with N elements with half wavelength spacing as shown in Fig. 1. Denoting by $\tilde{x}_j(t)$, the analytic signal received by element j ($1 \leq j \leq N$), W_j the complex weight for the j-th signal, $\tilde{s}(t)$ the array output, $W = [w_1, w_2, \ \ldots \ w_N]^T$ the weight vector, $W_s = [w_{s1}, w_{s2}, ..., w_{sN}]^T$ the steering vector, $X = [\tilde{x}_1(t), \tilde{x}_2(t), ..., \tilde{x}_N(t)]^T$ the signal vector, $\phi = E(x^* x^T)$ the covariance matrix where T denotes transpose and * complex conjugate, W is calculated from the sensor signal as

$$W = \Phi^{-1} W_s \tag{1}$$

If the received signal $\tilde{x}_j(t)$ consists of the desired signal $\tilde{d}_j(t)$, one interference signal $\tilde{t}_j(t)$ and the thermal noise $\tilde{n}_j(t)$, the expressions for the output desired signal power P_d, output inteference power P_i), output noise power P_n and output SINR as

I. INTRODUCTION

During the last twenty years, different approaches have been proposed for designing systems that can track a desired signal and provide protection against jamming and other interference signals. Such systems are highly useful in defense radar and communication applications. Beam forming, that is, the mixing of weighted and delayed version of signals at an array of sensors is one such technique that leads to an increase in the signal-to-interference-plus-noise (SINR) ratio of the received signal. The weights are adapted in real time to account for the time varying characteristic of the jamming and interfering signals.

The methods by Applebaum [1], [2] and Widrow, et al [3] and their variations [?] for example are used quite frequently for adaptive beam forming. The Applebaum method uses a steering vector in the feedback loop of the adaptive beam forming network while the method of Widrow relies upon a reference signal to track the desired signal.

Compton, Jr. considered the effects on array performance of random steering vector errors [4] and the effect of beam forming errors [6] (i.e. when the supplied look direction is different from the actual desired signal arrival angle). He showed that very small errors in the steering vector can cause large degradation in the output SINR and the situation becomes worse as more elements are added to the array and as the received desired signal power becomes larger (the subjects of error, imperfection or precision requirements are explored to some extents also by other researchers in [7], [8], [9], [10]). However, there is a great push in the Air Force and perhaps

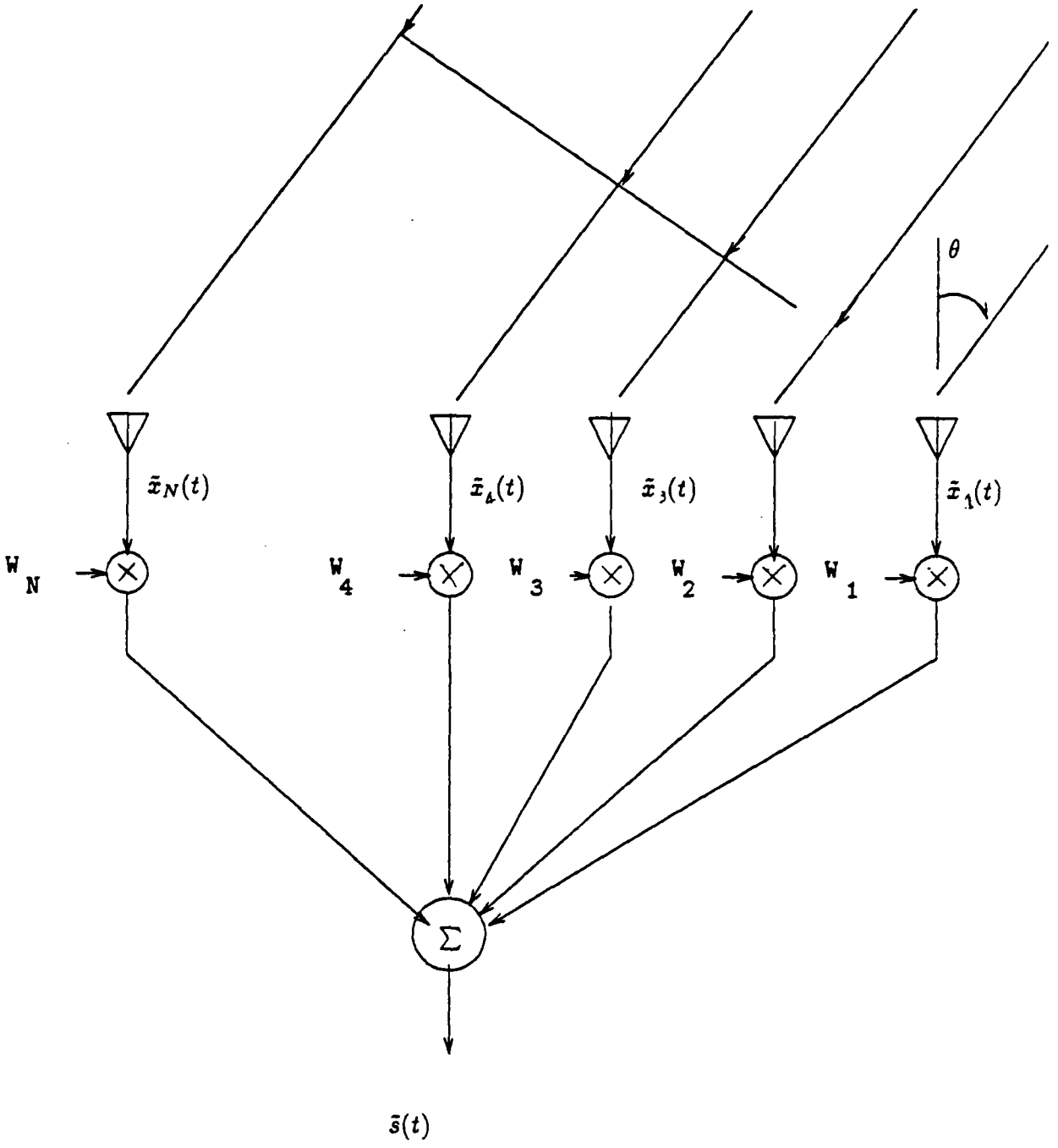

Fig. 1: An N-element adaptive beam forming array.

a function of errors in the steering elements are given by [4]:

$$P_d = \left(\frac{K_s^2}{2\sigma^2}\right)\left[W_o^T\Phi_o^{-1}\Phi_{do}\Phi_o^{-1} + 2\sigma_w^2 Trace(\Phi_o^{-1}\Phi_{do}\Phi_o^{-1})\right] \quad (2)$$

$$P_i = \left(\frac{K_s^2}{2\sigma^2}\right)\left[W_o^T\Phi_o^{-1}\Phi_{io}\Phi_o^{-1} + 2\sigma_w^2 Trace(\Phi_o^{-1}\Phi_{io}\Phi_o^{-1})\right] \quad (3)$$

$$P_n = \left(\frac{K_s^2}{2\sigma^2}\right)\left[W_o^T\Phi_o^{-1}\Phi_o^{-1} + 2\sigma_w^2 Trace(\Phi_o^{-1}\Phi_o^{-1})\right] \quad (4)$$

$$SINR = \frac{P_d}{(P_i + P_n)} \quad (5)$$

The expressions have been calculated assuming the errors in the steering vector elements to be random with zero mean and variance σ_w^2, where K_s is an arbitrary constant, $\phi_{do}, \phi_{io}, \phi_{no}$ are the normalized covariance matrices respectively of the desired signal, interference and noise, Φ_o is the sum of these three matrices and $\frac{1}{\sigma^2}$ is the input SNR. (The reader can refer to ref. [4] for a complete description of all the variable involved).

In Fig. 2, we show the output SINR as a function of σ_w^2 for the case where a desired monochromatic (fractional bandwidth $B_d = 0$) signal arrives at the broadside ($\theta_d = 0^o$) with a SNR of 0dB and no interference. This is the case where SNR is zero dB or noise is equal to signal, a bad scenerio but in this case there are still some advantages in using more elements on the array. In Fig 3, all other factors remain the same as Fig 2 except that the SNR improved to 10 dB, still a less than normal situation. From the figure, it is obvious that the higher value of N or the number of sensor elements on the beam forming array, the smaller the tolerance of the array for the error in the steering vector (represented by variance σ_w). Fig. 4 describes a better

situation for the received signal where the SNR is 20 dB. One concludes that with this type of arrangement (Fig 1 beam former) the more element sensors one has on the array the worse his system performs except with very small or no steering vector errors. In real life scenerio, besides having signal of 20 to 30 dB over noise, one also has interference or jamming signal from friendly or unfriendly sources. As shown in Fig 5 and 6, when with interference ($B_i = 0$) at $\theta_i = 30^o$ with interference to noise ratio (INR) of 40dB, the tolerance of large arrays for steering vector error becomes even more critical; giving the same error variance σ_w, one probably may be better off with a small array or even just one sensor than a larger array.

Thus efforts to increase the accuracy of adaptive FIR steering beamformers by increasing the number of sensors, and consequently the number of elements in the weight vector array, would meet with limited success due to the fact that the detrimental effects of random steering errors on the beamformer performance also increase with the number of sensors. This self-defeating phenomenon points to the need of a new approach to better adaptive FIR steering beamformer array performance.

Current beamformers use direct form (Fig 1) realizations for combining the sensor inputs to evaluate the accuracy of the particular pole (steering angle) realization. Such a realization have an inherent limitation - that of sparse pole realizations in the z-domain [12]. This leads to greater sensitivity of their performance to round-off errors due to finite precision, since the probability and closeness of their achieving a particular performance point (pole) is limited by how close a value the selected precision allows. If the density of realizations of pole realizations in the z-domain were to be higher, this sensitivity is mitigated, since the probability and closeness of achiev-

ing a particular pole realization is better. This is the approach we take, and propose the cascade form realization of the FIR beamformer as a improved alternative. The cascade form realizations are characterized by the higher density of pole realizations which is what this effort is aimed at achieving. Put it another way, with cascade form, large numer of elements arrays are less sensitive to error in the steering vector. Furthermore, cascade structure beam forming array such as one in Fig 7 would not change the beam forming array algorithm considerably.

For the direct form beam forming array the steering vector is represented by:

$$W_s = K_s W_o \left[1, e^{j2\pi \sin\theta_d}, e^{j2\pi \sin\theta_d}, ..., e^{j(N-1)\pi \sin\theta_d}\right]^T \tag{6}$$

and the signal:

$$X = [\tilde{x}_1(t), \tilde{x}_2(t), ..., \tilde{x}_N(t)]^T \tag{7}$$

Output of the array may be in the form

$$y(t) = K_s W_o \left[\tilde{x}_1(t) + \tilde{x}_2(t)e^{j\pi \sin\theta_d} + ... + \tilde{x}_N(t)e^{j(N-1)\pi \sin\theta_d}\right] \tag{8}$$

While the output of the cascade form such as in Fig 7 will be:

$$\begin{aligned} lllly(t) &= K_s W_o \left\{[\tilde{x}_1(t), \tilde{x}_2(t)][1, e^{j\pi \sin\theta_d}]^T, [\tilde{x}_3(t), \tilde{x}_4(t)][1, e^{j\pi \sin\theta_d}]\right\} \left\{1, e^{j2\pi \sin\theta_d}\right\}^T \quad (9) \\ &= K_s W_o \left\{[\tilde{x}_1 + \tilde{x}_2(t)e^{j\pi \sin\theta_d}], [\tilde{x}_3(t) + \tilde{x}_4(t)e^{j\pi \sin\theta_d}]\right\} \left\{1, e^{j2\pi \sin\theta_d}\right\}^T \quad (10) \\ &= K_s W_o \left[\tilde{x}_1(t) + \tilde{x}_2(t)e^{j\pi \sin\theta_d} + ... + \tilde{x}_N(t)e^{j(N-1)\pi \sin\theta_d}\right] \end{aligned}$$

which is similar to output of direct form.

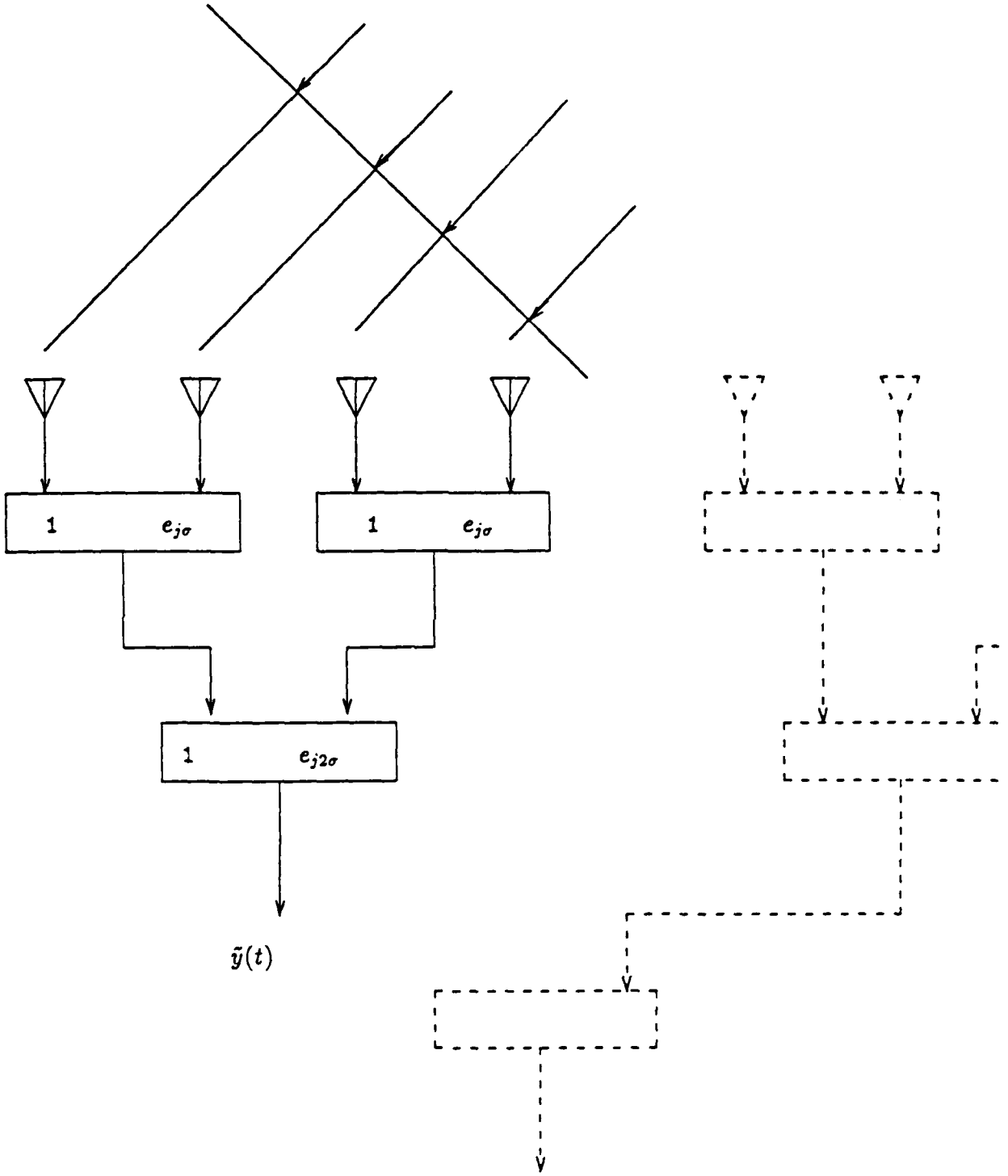

Fig. 7: Cascade structure beam array

Fig 8, 9 and 10 is the SINR of the cascade form with σ_w^2 for the fractional bandwidth $B_d = 0$, signal arrival angle $\theta_d = 0°$ with a SNR of 0, 10dB and 20 dB, respectively with no interference, for array of 2, 4, 8, 16, 32 and 64 sensors with 2 sensor sub unit. Fig. 11 and 12 show SINR of arrays of 3, 9, 27 and 81 sensors with 3 sensor sub unit.

IV FUTURE RESEARCH

From initial research, we conclude that the sensitivity of Applebaum array to steering vector error is due to array structure similar to the same effect in digital filters; for digital filters realizations, altenate architectures have been proposed and used to reduce the effect of error in the coefficient due to quantization, precision limitation, etc. Thus, changing the beam forming algorithm to accommodate for the steering vector error may not be necessary or effective as a change in the array architecture. Cascade structure is one candidate form for the problem solution. One such structure is shown in Fig 7. While the array in Fig 7 is sub-divided into basic unit of two inputs and two steering weights each, this is not necessary the optimal form: three inputs basic unit or other arrangements probably would do as well. Further simulation would have to be done to check the effect of interference signals on different forms of cascade structure; from the interference signal consideration, an interferencing signal will be canceled by and at each sub unit separately or is it a join effort of the whole array.. Also, the cascade form with clear division or isolation of input sensors from second stage while easier to put in mathematical form and to simulate, is not necessary the optimal way either.

References

[1] Applebaum, S.P. "Adaptive Array," IEEE Trans. Antennas and Propagation, Special Issus on Adaptive Antennas, vol. AP-24, pp. 585-598, 1976.

[2] Applebaum, S.P. and D.J. Chapman, " Adaptive arrays with main beam constraints," IEEE Trans. Antennas and Propagation, vol. AP-24, pp. 650-662, 1976.

[3] Widrow, B. Mantey, P.E. Griffiths, L.J., and Goode, B.B., "Adaptive Antennas Systems," Proceedings of the IEEE, Dec 1967.

[4] R.T. Compton, Jr., "The Effect of Random Steering Vector Errors in the Applebaum Adaptive Array," IEEE Trans. on Aerospace and Electronic Systems, vol. AES-18, no. 5, September 1982.

[5] R.T. Compton, Jr., "The power inversion adaptive array-concept and preformance," IEEE trans. on Aerospace and Electronic Systems, vol. AES-15, pp. 803-814, November 1979.

[6] R.T. Compton, Jr., "Pointing Accuracy and dynamic Range in a Steereed Beam Adaptive Array," IEEE Trans. Aerospace and Electronic Systems, vol. AES-16, pp. 280-287, May 1980.

[7] Neil K. Jablon, "Adaptive Beamforming with the Generalized Sidelobe Canceller in the Presence of Array Imperfections," IEEE Trans. Antennas and Propagation, vo. AP-34, N0. 8, August 1986.

[8] Lal C. Godara, "Error Analysis of the Optimal Antenna Array Processors," IEEE Trans. on Aerospace and Electronic Systems, vol. AES-22, no. 4, July 1986.

[9] Richard M. Davis, Patrick Jone-Shyan Sher, "Quantization Noise in Adaptive Weighting Networks," IEEE Trans. on Aerospace and Electronic Systems, vol. AES-20, no. 5, September 1984.

[10] Ramon Nitzberg, "Computational Requirements for Optimal Weights in Adaptive Processing," IEEE Trans. on Aerospace and Electronic Systems, vol. AES-16, No. 4, July 1980.

[11] Young J. Hong, Donald R. Ucci, Chien-Chung Yeh, "An Adaptive Array with Steering Vector and Reference Signal," Intl. Comm. Conf. 1986.

[12] L.R. Rabiner and Bernard Gold, *Theory and Application of Digital Signal Processing,"* Prentice-Hall 1978.

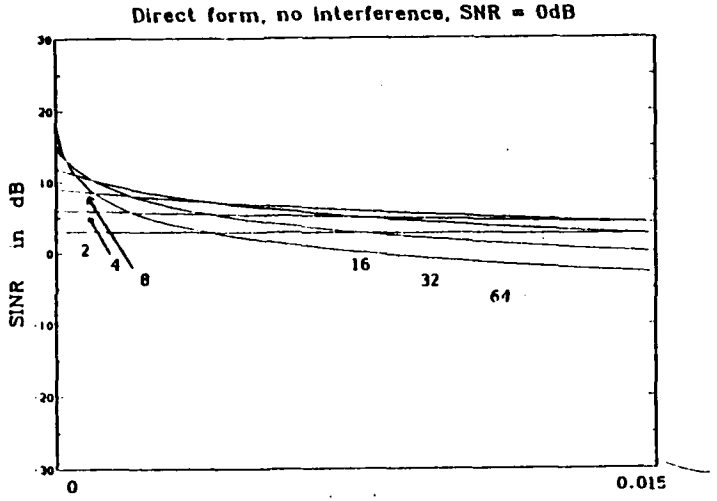

Fig. 2: Direct form array, SINR vs σ_w^2. No interference, $\theta_d = 0°$, $B_d = 0$, SNR = 0 dB.

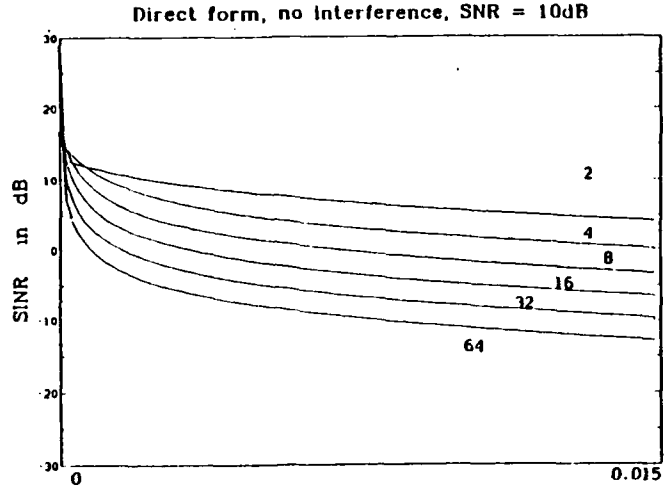

Fig. 3: Direct form array, SINR vs σ_w^2. No interference, $\theta_d = 0°$, $B_d = 0$, SNR = 10 dB.

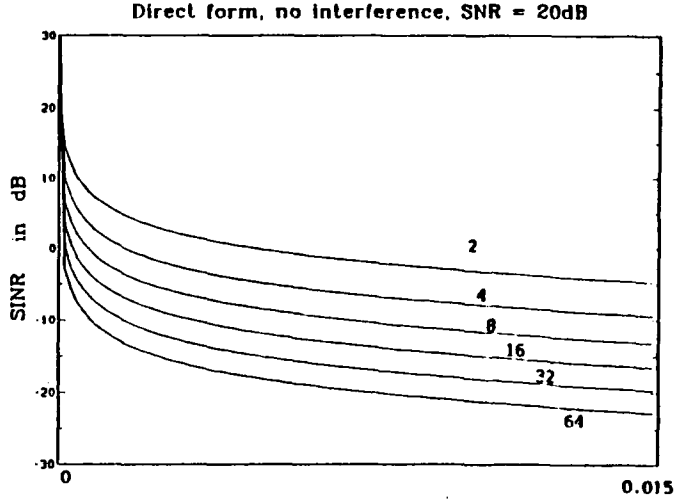

Fig. 4: Direct form array, SINR vs σ_w^2. No interference, $\theta_d = 0°$, $B_d = 0$, SNR = 20 dB.

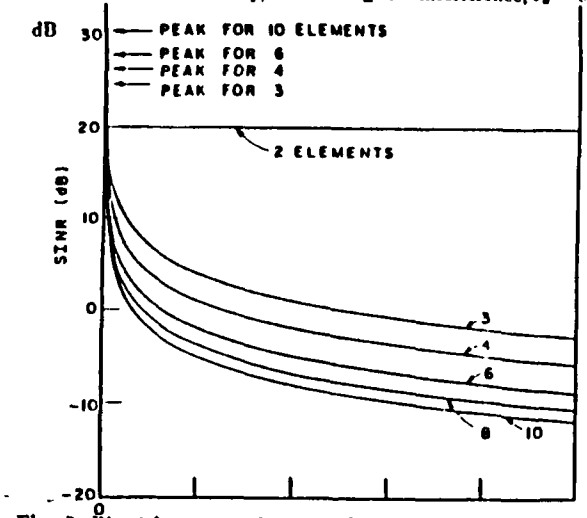

Fig. 5: Direct form array, SINR vs σ_w^2, $\theta_d = 0°$, $B_d = 0$, SNR = 10 dB. Interference 40dB, $\theta_i = 30°$, $B_i = 0$.

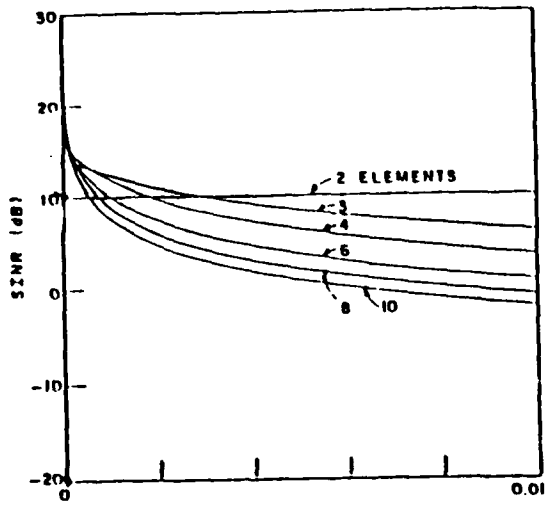

Fig. 6: Direct form array, SINR vs σ_w^2, $\theta_d = 0°$, $B_d = 0$, SNR = 20 dB. Interference 40dB, $\theta_i = 30°$, $B_i = 0$.

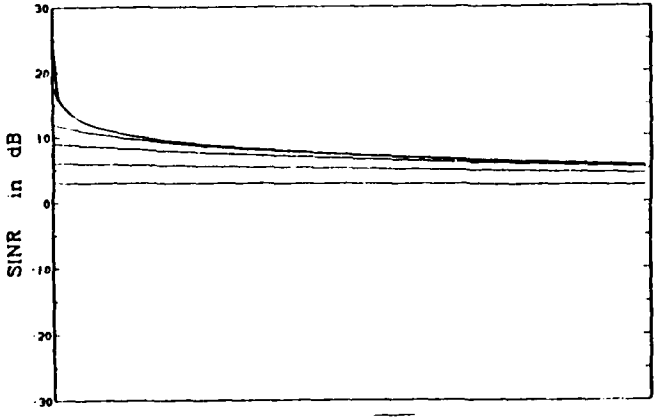

Fig. 8: Cascade form array, 2 sensors sub unit, SINR vs σ_w^2. No interference, $\theta_d = 0°$, $B_d = 0$, SNR = 0 dB.

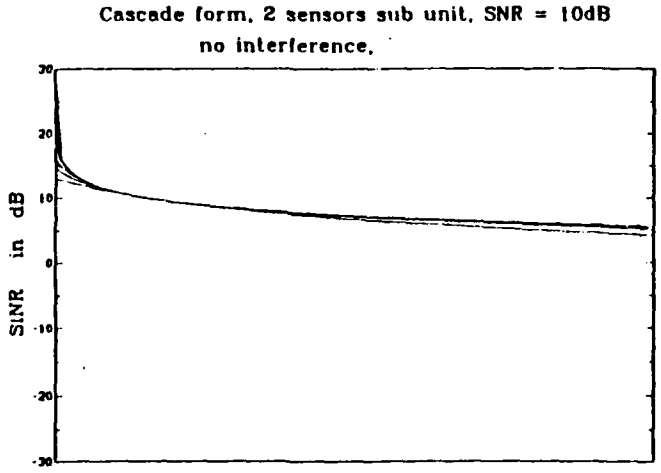

Fig. 9: Cascade form array, 2 sensors sub unit, SINR vs σ_w^2. No interference, $\theta_d = 0°$, $B_d = 0$, SNR = 10 dB.

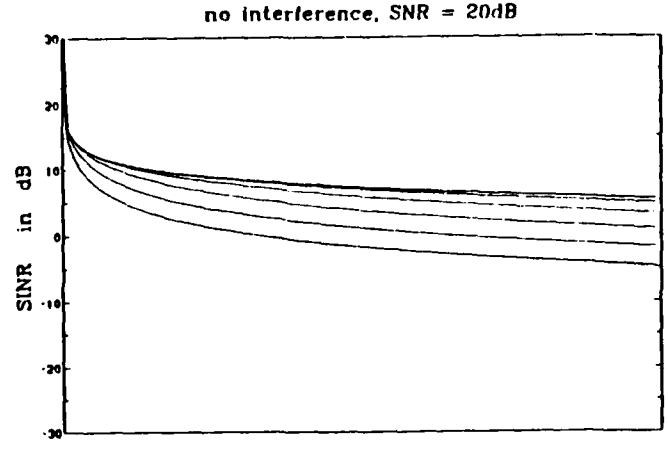

Fig. 10: Cascade form array, 2 sensors sub unit, SINR vs σ_w^2. No interference, $\theta_d = 0°$, $B_d = 0$, SNR = 20 dB.

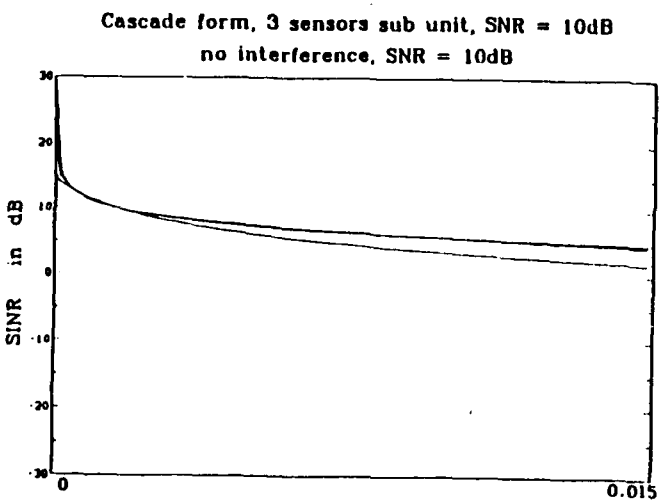

Fig. 11: Cascade form array, 3 sensors sub unit, SINR vs σ_w^2. No interference, $\theta_d = 0°$, $B_d = 0$, SNR = 10 dB.

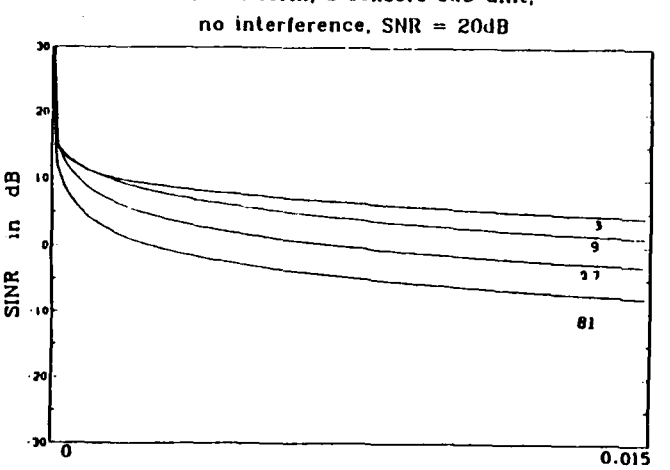

Fig. 12: Cascade form array, 3 sensors sub unit, SINR vs σ_w^2. No interference, $\theta_d = 0°$, $B_d = 0$, SNR = 20 dB.

1988 USAF-UES SUMMER FACULTY RESEARCH PROGRAM/
GRADUATE STUDENT RESEARCH PROGRAM

Sponsored by the
AIR FORCE OFFICE OF SCIENTIFIC RESEARCH
Conducted by
Universal Energy Systems, Inc.

FINAL REPORT

Extraction of Circuit Definitions from VHDL Specifications

Prepared by:	John P. Van Tassel
Academic Rank:	Master's Candidate
Department and University:	Computer Science and Engineering
	Wright State University
Research Location:	AFWAL/AADE
	Wright-Patterson AFB
	Dayton, Ohio
USAF Researcher:	Dr. John Hines

Date:	26 August 88
Contract No:	F49620-88-C-0053

Extraction of Circuit Definitions from VHDL Specifications

by

John P. Van Tassel

ABSTRACT

The report that follows is a discussion of the results of the research conducted under government contract project # 210, contract number F49620-88-C-0053 on the formal verification of digital circuit designs specified in the VHDL description language. It describes a method of logic extraction using executable Prolog grammars, and the extensions of such a scheme to mechanical theorem proving. The work included here was conducted in cooperation with Dr. David Hemmendinger, and should be viewed in conjunction with his report.

ACKNOWLEDGMENTS

I would like to thank the Air Force Systems Command, the Air Force Office of Scientific Research, and Universal Energy Systems for putting together the program that made it possible for the work presented here to be conducted. I am also indebted to Dr. David Hemmendinger for suggesting this project and providing guidance during its undertaking. Dr. John Hines was most obliging in providing support and ideas during the course of the project. Darrell Barker, Capt. Mike Dukes, and Capt. Jack Ebel provided invaluable input on the nuts and bolts aspects of VLSI design and their implementation VHDL. I am also grateful for the systems support given Ben Carroll and his group. It proved to be of tremendous assitance in the development of the tests and software and is greatly appreciated.

I. INTRODUCTION

The goal of the fellowship this summer was to look at methods of formal verification of VLSI design. Although not an electrical engineer, I have been working in the areas of logic and concurrent programming for the past year, and became convinced by the arguments of Dr. Hemmendinger that the design language VHDL lent itself to a formal analysis of the type applied to concurrent programs. With the drive to standardize VHDL, there is also a clear need for some sort verification process beyond simulation. To that end the project presented here was undertaken.

The bulk of the literature on VLSI verification centers on the simulation approach. Specifically, that one builds a state machine description of the circuit, and gives it a "complete" set of input to discover its correctness. Conversely, some take the proof theoretic approach and quickly become mired in human directed mechanical proofs that are obscure to those not familiar with such methods. After looking at VHDL and some of the newer automated proof systems, specifically Cambridge LCF and its derivative HOL, it seemed possible to automatically extract descriptions of circuits that would be understandable to such mechanical provers.

In order to accomplish the derivation of such descriptions, a method had to be implemented for extracting the first-order logic definitions of circuits. To that end, an executable Prolog grammar was developed to parse VHDL specifications. A description of the results of the utilization of that grammar follows.

II. OBJECTIVES

With the broad task of investigating VLSI verification as the objective of the effort, it became clear that the whole needed to be broken down into subgoals. Specifically, to

1. Become familiar with the current literature on hardware verification.
2. Gain an understanding of VHDL.
3. Apply some of the ideas found in (1) to VHDL to perhaps gain new insight on the problem.

In the process of familiarizing ourselves with VHDL, we found some bugs in the Beta version of the VHDL 1076 simulator. While finding and documenting them increased our knowledge of the language and led to some interesting questions about it, the whole process did leave some doubts as to the actual implementation of some of the attributes mentioned below, particularly the process model. Where there was confusion, the Language Reference Manual was followed as closely as possible.

Having arrived at (3) above, it became clear that the VHDL assert statement was a powerful meta-statement for describing the workings of the circuit in question. The fact that these assertions, and eventually, the theorem proving definitions, had to be extracted on the fly, led to the development of an executable Prolog grammar for the parsing of VHDL descriptions. The rapid prototyping provided by Prolog made much of the work presented here possible.

III. THE GRAMMAR

The basic construction of the grammar was taken directly from the context-free definition of the language found in the VHDL Language Reference Manual. The grammar in the LRM could not be translated directly into Prolog grammar notation, and obtain complete determinism in its execution. As a consequence, modifications were made that, while preserving the meaning of the original, optimized its execution.

The VHDL statements that are currently supported are signal and variable assignments, *if* and *case* conditionals, as well as the *block*, *process* and *architecture* statements. The assertions formed are put together in the same pass as the parsing of the VHDL code, and therefore are not terribly expensive to generate. The primary

assumption made was that the VHDL had already been analyzed. Although the grammar will generally not parse VHDL that is incorrect, it was not implemented to guard against possible infinite evaluations if given bad code.

IV. THE ASSERTION STATEMENTS

Once a workable program had been developed, it became possible to develop and try out ideas on how the assertion statements should look. The signal assignment statement was chosen as the first primitive operation to look at. A sample one might look like:

```
Output <= In1 and In2 after 40 ns;
```

where Output, In1, and In2 are all signals. It is an example of inertial delay, namely that Output gets the result of anding In1 and In2 if and only if those signals have been held stable for 40 ns. As an assertion, it would take the form:

```
ASSERT (NOT (In1'STABLE(40ns) AND
             In2'STABLE(40ns))
        OR
        (Output = (In1'DELAYED(40ns) and In2'DELAYED(40ns))));
```

Although not immediately discernable, this is a simple if-then construct stating that if both In1 and In2 have been stable for 40 ns, then Output is equal to the and of In1 and In2 40 ns ago. A less complicated variation of the same signal assignment is simply to switch from inertial to transport delay:

```
Output <= transport In1 and In2 after 40 ns;
```

The result is:

```
ASSERT (Output = (In1'DELAYED(40ns) and In2'DELAYED(40ns)));
```

where no statement of stability is needed. The value of Output takes on whatever the result of anding In1 and In2 is after 40 ns.

With the underlying logic of basic signal assignments in place, we can look at their incorporation into more complex VHDL statements, in particular, *if* and *case* statements. *If* statements provide a construction similar to the one used in signal

assignments. Specifically, if we wanted to say:

```
if A then
  B;
elsif C then
  D;
else
  E;
end if;
```

The corresponding assertion would look like:

```
ASSERT ((NOT A OR B) AND
        ((A AND NOT C) OR D) AND
        ((A AND C) OR E));
```

Note that the assertion statement takes into account information implicit in the construction of the *if* statement. *Case* statements are a special case of *if* statements, and as such have assertions that look much the same. For example,

```
case A is
  when B => C;
  when D => E;
end case;
```

Looks like

```
ASSERT ((NOT (A = B) OR C) AND
        (NOT (A = D) OR E));
```

when made into an assertion.

So far, we have seen individual sequential statements, but VHDL descriptions are certainly made up of more than these. It is the case, however, that when constructing an assertion to deal with the a block of statements, the whole is made up of the conjunction of the individual parts. For example, the code:

```
architecture PROCESS_IMPL of CONTROLLED_CTR is
signal ENIT, ENIT1, STRB : BIT;
begin
 DECODE:
   process (STRB)
        variable CONREG : BIT := '0';
     begin
       if (STRB = '1') then
          CONREG := CON;
          case CONREG is
            when => CONSIG <= "1000" after ENCDEL;
            when => CONSIG <= transport ENIT after ENCDEL;
                        ENIT1 <= CONSIG after IENDEL;
          end case;
       end if;
     end process DECODE ;
 STRB <= STRB1 after100 ns;
end PROCESS_IMPL ;
```

produces the following assertions (edited and highlighted for clarity):

```
-----------------------------------------------------------------
-- For process DECODE the following can be asserted:
-----------------------------------------------------------------
ASSERT
   (
      (
         ( NOT (strb = '1') OR
            (
               (conreg  = con)
               AND
               (
                  ( NOT (conreg = '0') OR
```

```
            (
               (
                  ( NOT TRUE OR
                     (consig  = "1000")
                  )
               )
            )
         )
         AND
         ( NOT (conreg = '1') OR
            (
               (
                  (consig  =
                     enit'DELAYED(encdel)
                  )
               )
               AND
               (
                  ( NOT consig'STABLE(iendel) OR
                     (enit1 = consig'DELAYED(iendel))
   ];
-----------------------------------------------------------------
-- For architecture CONTROLLED_CTR(PROCESS_IMPL),
-- the following assertion has been made:
-----------------------------------------------------------------
ASSERT
   (
-----------------------------------------------------------------
-- Remember, assertions made on process DECODE
-- are also implicitly true.
-----------------------------------------------------------------
```

```
(
   (
      ( NOT
         strb1'STABLE(100ns) OR
         (strb  = strb1'DELAYED(100ns))
];
```

It is obvious that these assertions should be universally true. They are also a first step towards the extraction of a logical definition of the circuit that is understandable to a theorem prover. They were particularly helpful in finding out what certain VHDL statements meant. Although Version 1 of the simulator was not obtained until the last week of the project, the grammar required little or no modification to agree with it.

V. THE HOL DESCRIPTIONS

The next phase of the project is to go in a direction similar to H.G. Barrow's *Verify* program. Namely, determining logically if two definitions of a circuit, one derived from the circuit itself, the other given as the specification, agree. While *Verify* utilized Prolog exclusively for this, we feel that the product HOL, developed by Michael Gordon at Cambridge, provides the most promise in the area. Although not intimately familiar with HOL and Cambridge LCF at present, I am able to describe how the signal assignment statements mentioned earlier should look. For example, transport delay can be expressed as

```
Out <= transport In after 40 ns;
```

and its corresponding HOL statement might look like

```
!t. Out t = ((t < 40) => F | In (t - 40))
```

where (!) is universal quantification and (|) is the conditional operation. The statement reads "for all times t, Out at time t is In at time t - 40 as long as t is greater than 40, else it is false (0)." Inertial delay takes on a more complicated syntax. A simple statement like

```
Out <= In after 40 ns;
```

becomes

$$!t.\ Out\ t = (!t'.\ (((t' =< t) \wedge (t' >= t - 40) \wedge (In\ (t - 40) = In\ (t'))) => In\ (t - 40) \mid Out\ t))$$

meaning "for all times t, Out at time t is In at time t - 40 as long as In remained constant (stable) over the interval t', else it stays the same."

I have been able to extract statements that look like the above by changing only the syntax of the statements output from the grammar, while leaving the grammar itself unchanged. Currently, we are trying to get a copy of HOL in order to become more familiar with it, and to discover how to best construct statements of the kind mentioned above. It should also be possible to construct HOL theories to expand the default set included with the product. These new items would be specific to the nature of the construction of VHDL statements, as well as the underlying implementation of the language.

VI. RECOMMENDATIONS

The work this summer has been particularly fruitful. We have become aquainted with VHDL and its simulator, a program has been written to extract logical definitions of circuits described in VHDL, and a method to utilize those definitions in the verification of circuit designs has been proposed. Along the way, we became aquainted with the literature on verification, and similar efforts in the area. The work shows promise but was naturally limited by the time frame of the contract.

As a consequence, we propose to continue the work through the support of a mini-grant. As mentioned by Dr. Hemmendinger in his report, this would include further development of the grammar, more work on the translation to HOL, and the development of HOL theories to make the verification possible.

REFERENCES

1. H. G. Barrow, "VERIFY: A program for proving correctness of digital hardware designs", *Artificial Intelligence*, vol. 24, 1984, pp. 437-491.
2. G. Birtwistle and P. A. Subrahmanyam, *VLSI Specification, Verification, and Synthesis*, Academic Press, New York, 1987.
3. D. Borrione, *From HDL Descriptions to Guaranteed Correct Circuit Design*, North-Holland, Amsterdam, 1987.
4. E. M. Clarke, E. A. Emerson, and A. P. Sistla, "Automatic verification of finite-state concurrent systems using temporal logic specifications", *ACM Trans. on Programming Languages and Systems*, vol. 8, no. 2, 1986, pp 244-263.
5. M. Fujita, H. Tanaka, and T. Moto-oka, "Verification with Prolog and temporal logic", *Computer Hardware Description Languages and Their Applications (Proc. of the 6th Int. Symp. on CHDL's)*, ed. T Uehara and M. Barbacci, North-Holland, Amsterdam, 1983, pp. 103-114.
6. A. Galton, ed., *Temporal Logics and Their Applications*, Academic Press, 1987.
7. Institute of Electrical and Electronics Engineers, *IEEE Standard VHDL Language Reference Manual*, IEEE Press, New York, 1988.
8. G. Milne, and P. A. Subrahmanyam, *Formal Aspects of VLSI Design*, Academic Press, New York, 1987.
9. B. Mishra and E. M. Clarke, "Automatic and hierarchical verification of asynchronous circuits using temporal logic", *Technical Report CMU-CS-83-155*, Carnegie-Mellon Univ, Pittsburgh, 1983.
10. B. Moszkowski, *Executing Temporal Logic Programs*, Cambridge University Press, 1986.
11. T. Uehara, T. Saito, F. Maruyama, and N. Kawato, "DDL verifier and temporal logic", *Computer Hardware Description Languages and Their Applications (Proc. of the 6th Int. Symp. on CHDL's)*, ed. T Uehara and M. Barbacci, North-Holland, Amsterdam, 1983, pp. 91-101.

1988 USAF-UES SUMMER FACULTY RESEARCH PROGRAM

GRADUATE STUDENT RESEARCH PROGRAM

Sponsored by the

AIR FORCE OFFICE OF SCIENTIFIC RESEARCH

Conducted by

UNIVERSAL ENERGY SYSTEMS, INC.

FINAL REPORT

Applications of Evolutionary Learning Strategies to Pattern Recognition Tasks

Prepared By:	Mateen M. Rizki, Ph.d. and Michael Zmuda
Academic Rank:	Assistant Professor and Graduate Student
Department and	Computer Science Department
University:	Wright State University
Research Location:	AFWAL/AAAT-3 Wright-Patterson AFB, OH 45433
USAF Researcher:	Louis Tamburino, Ph.D.
Date:	24 August 1988
Contract No.	F49620-88-C-0053

SAME REPORT AS
PROF. MATEEN RIZKI
AVIONICS LABORATORY # 85

1988 USAF-UES SUMMER FACULTY RESEARCH PROGRAM

GRADUATE STUDENT RESEARCH PROGRAM

Sponsored by the

AIR FORCE OFFICE OF SCIENTIFIC RESEARCH

Conducted by

UNIVERSAL ENERGY SYSTEMS, INC.

FINAL REPORT

A Computer Model for Air-To-Air Combat (Force on Force) Assessment

Prepared By:	*Patrick J. Sweeney, Ph.D. and* Kathy Bennett
Academic Rank:	Professor and Graduate Student
Department and	Engineering Management and Systems
University:	University of Dayton
Research Location:	AFWAL/FIAA Wright-Patterson AFB, OH 45433
USAF Researcher:	Jack M. Byrnes
Date:	22 July 1988
Contract No.	F49620-88-C-0053

SAME REPORT AS
PROF. PATRICK SWEENEY
FLIGHT DYNAMICS LABORATORY # 94

1988 USAF-UES SUMMER FACULTY RESEARCH PROGRAM

GRADUATE STUDENT SUMMER SUPPORT PROGRAM

Sponsored by the

AIR FORCE OFFICE OF SCIENTIFIC RESEARCH

Conducted by the

Universal Energy Systems, Inc.

FINAL REPORT

Prepared by:	Susan M. Dumbacher
Academic Rank:	Graduate Student
Department and	Aerospace Engineering Department
University:	University of Cincinnati
Research Location:	AFWAL/FIGXC
	Wright Patterson AFB
	Dayton, Ohio 45433
USAF Researcher:	Arthur Finley Barfield
Date:	28 Sept 88
Contract No:	F49620-88-C-0053

EVALUATIONS OF SUBOPTIMAL FILTERS AS APPLIED TO LARGE FLEXIBLE SPACE STRUCTURES

by

Susan M. Dumbacher

ABSTRACT

With the reality of space existence so near at hand, it is imperative that man keep up with the technology required to achieve these lofty goals. With this in mind, the topic of structural control of Large Flexible Space Structures (LFSS) is indeed an important one. To separate the fields of structures and controls in this case would be to ignore the problem as a whole and, hence, it is desired to effectively control a LFSS with the minimum structural weight required. From this standpoint, various parameters of the LFSS and, in particular, modal positions and velocities, must be determined to utilize effective feedback control to damp out unwanted vibrations. The purpose of this study is to evaluate the possible types of estimation of these modal positions and velocities and, specifically, to investigate the performance and robustness of suboptimal/decentralized filters as opposed to centralized filters.

ACKNOWLEDGEMENTS

I wish to thank the Air Force Systems Command and the Air Force Office of Scientific Research for sponsorship of this research. I would also like to extend my appreciation to Adolph Harris and to UES for all their administrative efforts.

I have received a great deal of support from the Flight Dynamics Labratory, Flight Controls Division and especially the Advanced Development Branch, Controls Application Group. A. Finley Barfield has provided much encouragement, enthusiasm and insight and has been an invaluable resource during the program.

I would like to thank the University of Cincinnati, Aerospace Engineering Department and, in particular, my advisor Dr. Bruce Walker and Dr. Gary Slater for their guidance, help and advice.

I. INTRODUCTION

A Large Flexible Space Structure (LFSS) is a space structure characterized by low inherent damping on the order of 1%, low and closely spaced frequencies, and an infinite number of modes required to completely describe the motion of the system. This class of structures includes the space station, large antennas, solar sails, solar power satellites, space telescopes as shown in Figure 1, and other structures which may apply. As a result of low damping inherent in LFSS, it is necessary to suppress unwanted vibrations caused by disturbances or motion of the LFSS -- disturbances may include solar wind or debris while motion of the LFSS may result from pointing or docking maneuvers. Modal control, or the damping of selected modes, is one way to achieve vibration suppression. It is then necessary to formulate the problem in modal form as given in [Ref 1].

The basic equations of motion for a structure are

$$[M]\ddot{\underline{q}} + [C]\dot{\underline{q}} + [K]\underline{q} = \underline{Q} \qquad \text{(eq 1)}$$

where [M], [C] and [K] are the mass, damping and stiffness matrices, and $\underline{Q}$ is the force vector acting upon the structure. Since LFSS generally have very low damping, an assumption of [C] = 0 is valid; a small damping term will be added at a later time. To decouple (eq 1), introduce the linear transformation

$$\underline{q}(t) = [U]\,\underline{\eta}(t) \qquad \text{(eq 2)}$$

where [U] is the modal matrix and $\underline{\eta}(t)$ is a generalized coordinate. (Eq 1) then becomes

$$[M]\,[U]\,\ddot{\underline{n}} + [K]\,[U]\,\underline{n} = \underline{0} \; . \qquad \text{(eq 3)}$$

Premultiplying (eq 3) by $[U]^T$ and normalizing [U] such that its amplitude is no longer arbitrary via

$$[U]^T[M]\,[U] = [I] \qquad \text{(eq 4a)}$$

$$[U]^T[K]\,[U] = [-w^2-] \; , \qquad \text{(eq 4b)}$$

where $[-w^2-]$ is a diagonal matrix of the squares of the eigenvalues, and $[U]^T\underline{Q} = \underline{N}$, yields

$$\ddot{\underline{n}} + [-w^2-]\,\underline{n} = \underline{N} \; . \qquad \text{(eq 5)}$$

For simplicity, a pinned-pinned beam structure will be presented as an example. The fourth order equation for a beam, as cited in [Ref 1], is

$$m\frac{\partial^2 y(x,t)}{\partial t^2} - EI\,\frac{\partial^4 y(x,t)}{\partial x^4} = f(x,t) \qquad \text{(eq 6)}$$

where EI is the stiffness, y(x,t) is the displacement of the beam and f(x,t) is the force distribution applied to the beam. Assuming that free vibration occurs, i.e. f(x,t)=0, and that y(x,t) is separable in time and space as

$$y(x,t) = q(t)\,U(x) \quad , \qquad \text{(eq 7)}$$

then the solutions to (eq 6) obey

$$\ddot{q} + w^2 = 0 \qquad \text{(eq 8)}$$

and

$$U^{(4)} + (m\,w^2/EI)\,U = 0 \; . \qquad \text{(eq 9)}$$

Solving this pinned-pinned beam problem (eq 9) for the natural frequencies, w_n, and the mode shapes, U_n, yields the values

$$w_n = (n\pi)^2\sqrt{EI/(mL^4)} \quad , \; n=1,2,\ldots,\infty \qquad \text{(eq 10a)}$$

$$U_n(x) = A_n \sin(n\pi x/L) \; . \qquad \text{(eq 10b)}$$

The mode shapes are arbitrary in amplitude, A_n. Normalizing such that

$$\int_0^L m\, U_n^2(x)\, dx = 1 \qquad \text{(eq 11)}$$

gives

$$U_n(x) = \sqrt{2/mL}\, \sin(n\pi x/L) \; . \qquad \text{(eq 12)}$$

The total displacement and velocity of the beam can then be represented as the sum of the mode shapes multiplied by the generalized coordinates:

$$y(x,t) = \sum_{n=1}^{\infty} U_n(x)\eta_n(t) \qquad \text{(eq 13a)}$$

$$\dot{y}(x,t) = \sum_{n=1}^{\infty} U_n(x)\dot{\eta}_n(t) \qquad \text{(eq 13b)}$$

The simple beam example used throughout this study is a pinned-pinned beam with an arbitrary impulse force applied as shown in Figure 2. Let the state, $\underline{x}$, be defined as

$$\underline{x} = [\eta_1 \; \dot{\eta}_1 \; : \; \eta_2 \; \dot{\eta}_2 \; : \; \ldots \; : \; \eta_n \; \dot{\eta}_n]^T \qquad \text{(eq 14)}$$

where η_i and $\dot{\eta}_i$ are the i^{th} modal position and velocity, respectively. The state space formulation then becomes

$$\dot{\underline{x}} = A\,\underline{x} + B\,\underline{u} \qquad \text{(eq 15a)}$$

$$\underline{y} = C\,\underline{x} \qquad \text{(eq 15b)}$$

with $$A = \begin{bmatrix} A_1 & & & 0 \\ & A_2 & & \\ & & \ddots & \\ 0 & & & A_n \end{bmatrix}, \quad A_i = \begin{bmatrix} 0 & 1 \\ -w_i^2 & -2\zeta_i w_i \end{bmatrix} \text{ and}$$

$$C = [0 \;\; C_1 \; : \; 0 \;\; C_2 \; : \; \ldots \; : \; 0 \;\; C_n] \; .$$

The matrix C takes the above form for a velocity sensor and, with the assumption that the actuators and the sensors for the LFSS are collocated, $B=C^T$. The damping term ζ_i is included in the dynamics matrix A here to

represent the slight damping inherent in the structure without destroying the decoupled form of the equations.

The basic estimator equation is given by

$$\dot{\underline{x}} = A\,\underline{x} + B\,\underline{u} + K_F\,(\underline{y} - C\,\hat{\underline{x}}) \qquad \text{(eq 16)}$$

where $\hat{\underline{x}}$ is the estimated state and K_F is the filter gain determined by the standard gain matrix and Riccati equations, as given in [Ref 2]. For optimal estimation, the following occur: $\hat{\underline{x}}$ is the complete state of the system; all of the information is processed centrally in an optimal manner; and the best possible estimate of the system for the given set of parameters is obtained [Ref 2]. This is central estimation and will henceforth be referred to as Linear Quadratic Estimation (LQE). Decentralized estimation, on the other hand, processes information locally -- a decentralized estimator's output depends only on information from the corresponding sensor or group of sensors and each actuator/sensor pair, or group of pairs, uses only information contained within that subsystem. From a performance point of view, assuming perfect information of the system parameters, centralized estimation is preferable since it provides the optimal solution. However, if central processing is not desirable or possible, or if computation is an important factor, decentralized estimation may be a better choice. Results from previous work done by the author [Ref 3] indicating performances of central and decentral estimation with perfect modal information is given in Figure 3. The decentral estimation does contain error amplitude shaping as outlined in [Ref 3].

I. OBJECTIVES OF RESEARCH EFFORT

In reality, perfect information is not known since adequate testing cannot be done on earth. Also, the dynamics of the system may actually change after the initial deployment of the LFSS. It is then of utmost importance to evaluate the robustness with respect to parameter variations of a LQE filter and a suboptimal filter. Decentralization is a subset of the latter. Defining robustness as global asymptotic stability under the presence of modeling errors, it is of interest to investigate "phase-shaping" to achieve this guaranteed stability. Since this is a rather strict constraint on the suboptimal estimator, a qualitative sensitivity analysis is also introduced. Finally, a method for obtaining some performance criteria to compare optimal and suboptimal filters is proposed.

III. ROBUSTNESS AND PHASE-SHAPING

Since perfect knowledge of system parameters is not attainable, it is necessary to account for variations in these parameters and to attempt to design a suboptimal filter which is robust under these circumstances. As a starting point, structural frequency errors up to 20% will be investigated. Referring to the block diagram of Figure 4, [Ref 4] states that given the transfer matrices G(s) and H(s), the system is asymptotically stable if at least one of the transfer matrices is positive real and the other is strictly positive real. For a LFSS with collocated actuators and sensors, it can be shown that G(s) is positive real [Ref 5]. Then H(s), which is the combined transfer matrix of the estimator and controller, must be strictly positive real for guaranteed stability. The purpose of the study at hand is to focus on the performance and robustness of estimators. It would then be desirable to be able to first choose filter gains satisfying strictly

positive real requirements and then to choose controller gains without violating these restrictions.

One conservative approach toward solving this problem would be to look at the phase shift caused by closing an estimator in the loop. If the total estimator phase change lies within $\pm 90^{\circ}$, then this portion of the feedback loop is strictly positive real. Looking at the simplest case of a reduced-order 1-mode estimator estimating the first mode, the best result obtained is a phase shift of -90° under certain conditions. This may indicate positive realness rather than strict positive realness. The gains $[K_1 \quad K_2]^T$ for this case were chosen to decrease the sensitivity to changes in the structural frequency. This was done by evaluating the transfer matrix $\hat{\underline{x}} / \underline{x}$:

$$\frac{\hat{\eta}_1}{\eta_1} = \frac{s^2 + (2\zeta_1 w_1 + K_2 C)\, s + \bar{w}_1^2 (1 - K_1 C)}{s^2 + (2\zeta_1 w_1 + K_2 C)\, s + w_1^2 (1 - K_1 C)} \quad \text{(eq 17a)}$$

$$\frac{\hat{\eta}_1}{\dot{\eta}_1} = \frac{2\,\zeta_1 (K_1 C - 1)(w_1 - \bar{w}_1)}{s^2 + (2\zeta_1 w_1 + K_2 C)\, s + w_1^2 (1 - K_1 C)} \quad \text{(eq 17b)}$$

$$\frac{\dot{\hat{\eta}}_1}{\eta_1} = \frac{s\,(\bar{w}_1^2 - w_1^2)}{s^2 + (2\zeta_1 w_1 + K_2 C)\, s + w_1^2 (1 - K_1 C)} \quad \text{(eq 17c)}$$

$$\frac{\dot{\hat{\eta}}_1}{\dot{\eta}_1} = \frac{s^2 + (2\zeta_1 \bar{w}_1 + K_2 C)\, s + w_1^2 (1 - K_1 C)}{s^2 + (2\zeta_1 w_1 + K_2 C)\, s + w_1^2 (1 - K_1 C)} \quad \text{(eq 17d)}$$

where w_1 is the first modeled structural frequency and $\bar{w}_1$ is the actual first structural frequency. These two values may differ by 20%. In an attempt to drive the off-diagonal terms (eqs 17b&c) to zero and the diagonal terms (eqs 17a&d) to one, $K_1 = 1/C$ is chosen and (eq 17) becomes

$$\hat{\eta}_1 / \eta_1 = 1 \qquad \text{(eq 18a)}$$

$$\hat{\eta}_1 / \dot{\eta}_1 = 0 \qquad \text{(eq 18b)}$$

$$\hat{\eta}_1 / \eta_1 = \frac{s\,(\bar{w}_i^{\,2} - w_i^{\,2})}{s\,(s + 2\zeta_i w_i + K_2 C)} \qquad \text{(eq 18c)}$$

$$\hat{\eta}_1 / \dot{\eta}_1 = \frac{s\,(s + 2\zeta_i \bar{w}_i + K_2 C)}{s\,(s + 2\zeta_i w_i + K_2 C)} \qquad \text{(eq 18d)}$$

Choosing a value for K_2 which shifts the pole $-2\zeta_i w_i + K_2 C$ sufficiently to the left will ensure that the response due to that pole dies out quickly. (Eq 18c) then approaches the value of 0 and (eq 18d) approaches the value of 1. The time response of this case is shown, along with LQE results, in Figure 5. The above method works quite well for the pinned-pinned beam example. However, problems may arise if the actual LFSS is not dominated by a single known mode. These results may also depend upon sensor position. It is necessary to evaluate an actual LFSS in order to determine how strongly these dependencies upon circumstances affect the problem at hand.

IV. QUALITATIVE SENSITIVITY ANALYSIS

Since the above phase-shaping results are restrictive, a qualitative sensitivity analysis is in order. Since optimal filters are designed to be

optimal at a specified point, it is not suprising that they are quite sensitive to variations about the specified point. Suboptimal filters -- which include reduced order filters, decentralized filters, etc. -- are not as sensitive [Ref 6] which is in this case an advantage of suboptimal filters. See Figure 6 for an indication of optimal versus suboptimal filter sensitivity. It is obvious that there is a tradeoff here between sensitivity and performance and it is up to the designer to decide where that line should be drawn.

V. PERFORMANCE CRITERIA

Since many times suboptimal/decentralized filters may be numerous and of different orders than LQE filters, some performance criteria to compare the types of estimators must be determined. It is proposed to use the modal sum of the error covariances of each filter as a basis. For those suboptimal filters which are combining modal information, the total error covariances may be obtained via any sufficient type of estimation algorithm [Ref 7] such as Mean Square Error estimate (MSE), Maximum APriori estimate (MAP), or Maximum Likelihood estimate (MLE). In this way, a scalar performance value for each filter may be used for performance comparisons. As far as computations are concerned, it is clear that the lower order the filter, the less computations required. Hardware cost may also be considered due to the fact that decentralized estimation and control rely upon a larger number of actuators and sensors being present.

VI. RECOMMENDATIONS

The robustness and sensitivity of suboptimal and optimal filters have been investigated and, although a degradation in performance occurs, suboptimal filters appear to be more favorable under uncertain parameter conditions. A more in depth sensitivity analysis should be done on the estimators to determine the range of variation in parameters each filter can withstand. Also, variations in mode shapes exist in reality and, upon obtaining satisfactory results for variations in frequencies, this problem should be addressed. The results for the phase-shaping for robustness here are quite limited due to contradicting restrictions on gains. Perhaps a different approach would be to close the loop with a controller and estimator and combine the controller and estimator performance analysis. This seems to contradict the desire to primarily investigate the performance of filters, but it may lead to an improvement in the closed-loop results. It would be valuable to apply the suboptimal results to an actual LFSS such as a truss to reinforce the validity of the proposed methods. Finally, it would be worthwhile to undertake a study of the stated estimation schemes, under various circumstances, to yield the "best" scalar performance value.

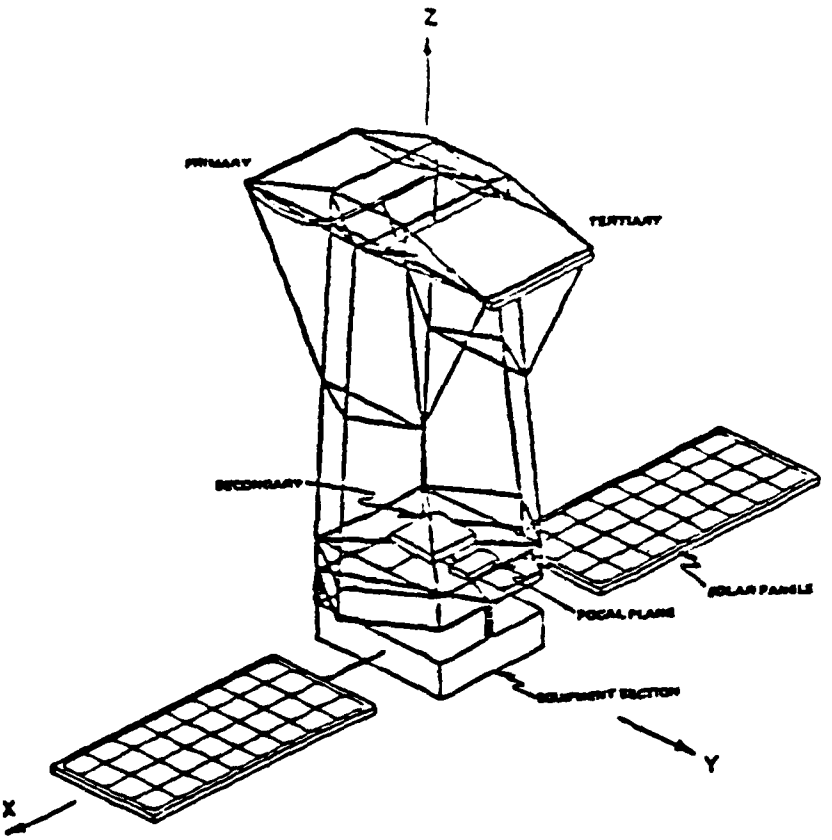

FIGURE 1: The DRAPER II Space Telescope Structure

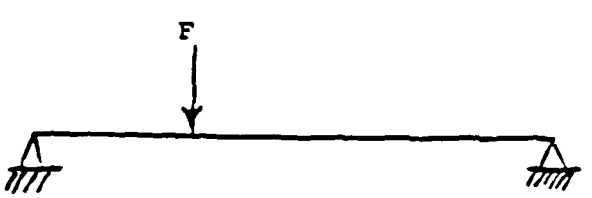

FIGURE 2: Pinned-Pinned beam with impulse force applied as shown.

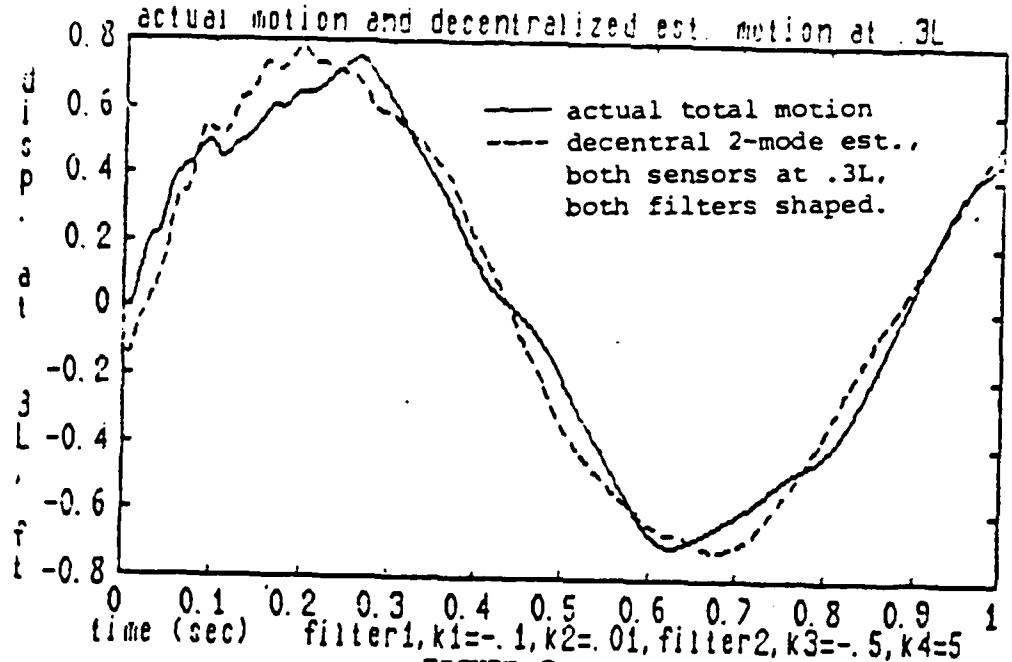

FIGURE 3.a

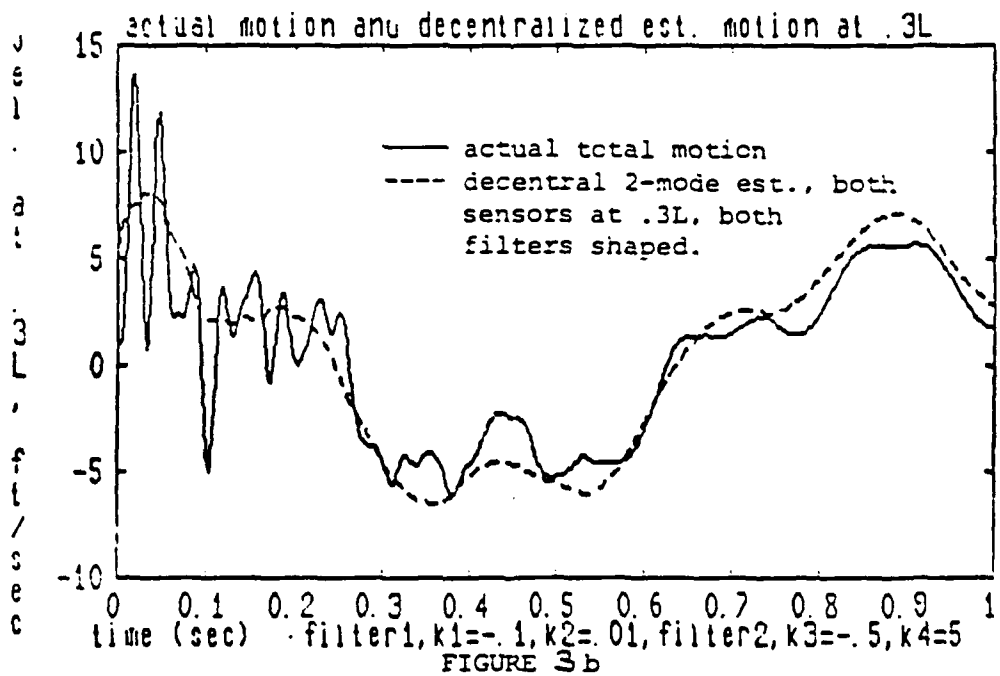

FIGURE 3.b

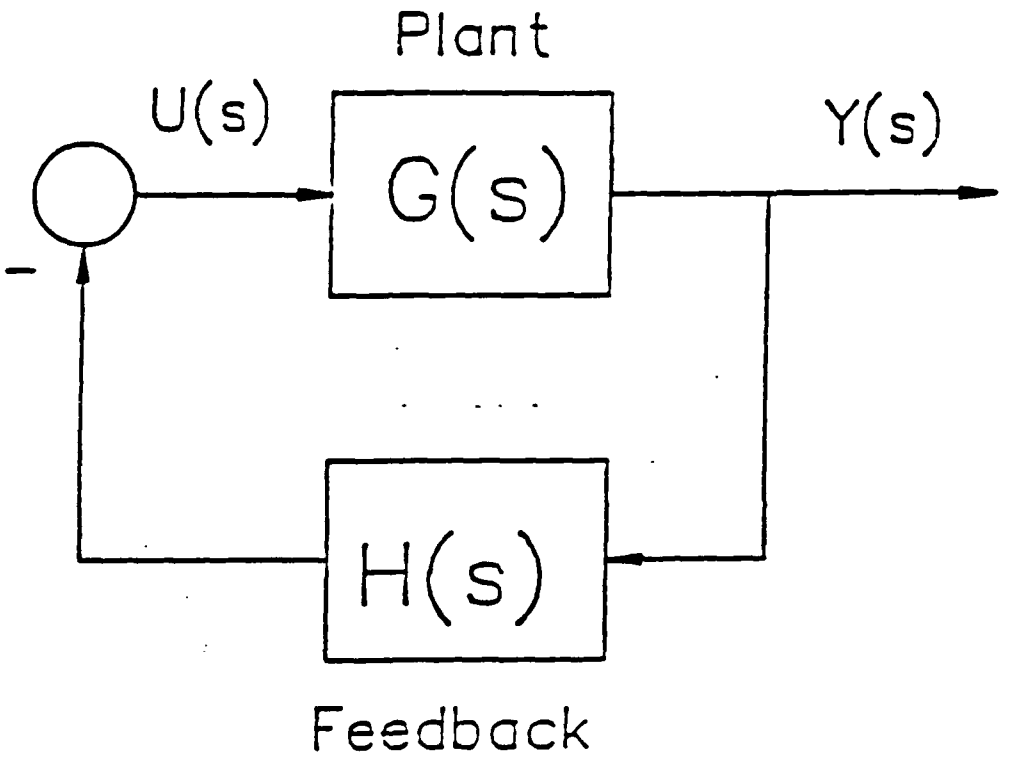

FIGURE 4: General Feedback Control Concept

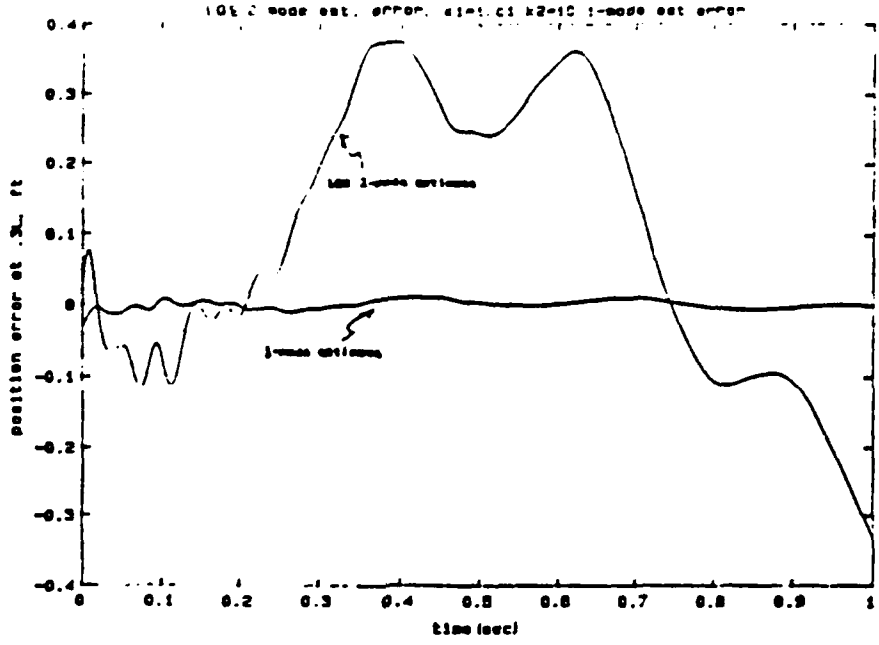
position error at .3L, ft
time (sec)

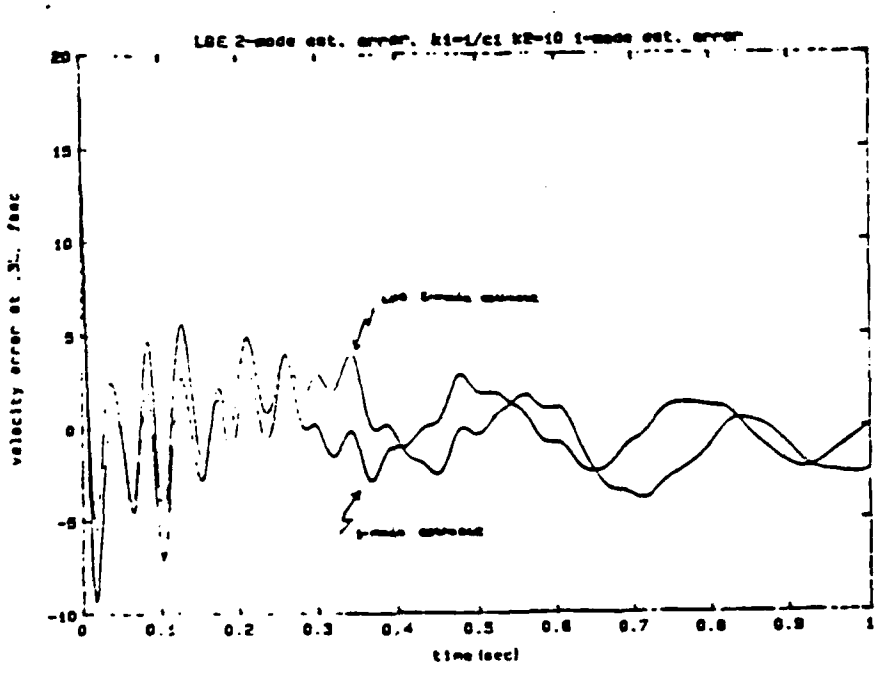
velocity error at .3L, fps
time (sec)

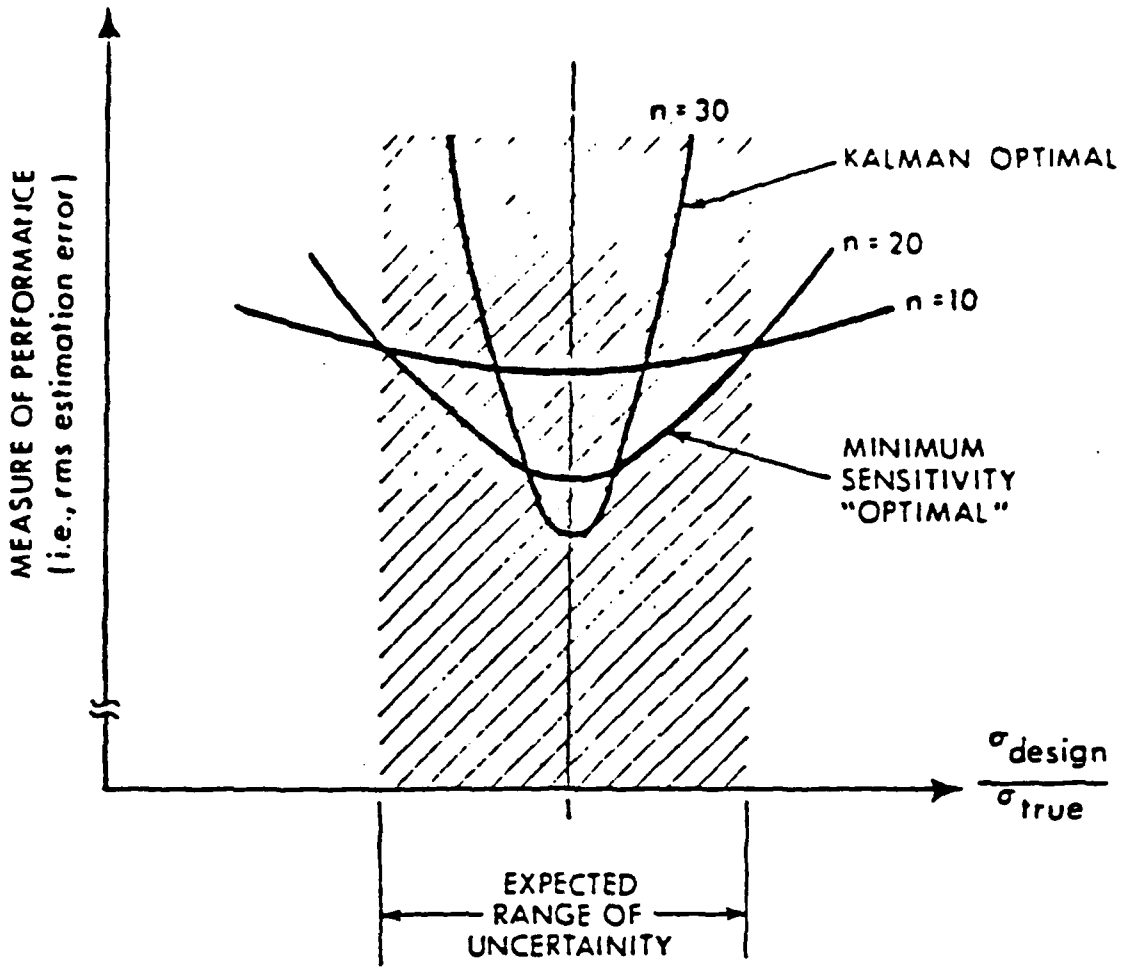

Figure 6 Conceptual Example of Designing for Minimum Sensitivity (σ_{true} held constant, σ_{design} is varied)

REFERENCES

[1] Meirovitch, L., Analytical Methods in Vibrations, The Macmillan Company, New York, 1967.

[2] Kwakernaak, H. and R. Sivan, Linear Optimal Control Systems, John Wiley and Sons, Inc., New York, 1972.

[3] Dumbacher, S.M., "Preliminary Applications of Decentralized Estimation", 1987 Final Report to UES, sponsored by AFOSR, contract F49620-85-C-0013.

[4] Anderson, B.D.O., "A Simplified Viewpoint of Hyperstability", IEEE Trans. on Auto. Control, June 1964, pp 292-294.

[5] Joshi, S.M., "Robustness Properties of Collocated Controllers for Flexible Spacecraft", Journal of Guidance, Vol.9, No.1, Jan.-Feb., 1986, pp 85-91.

[6] Gelb, A., Applied Optimal Estimation, MIT Press, Cambridge, Mass., 1974.

[7] Anderson, B.D.O. and J.B. Moore, Optimal Filtering, Prentice-Hall, Inc., Englewood Cliffs, New Jersey, 1979.

MR. BRYAN FOOS

FINAL REPORT NUMBER 53

NO REPORT SUBMITTED

1988 USAF-UES SUMMER FACULTY RESEARCH PROGRAM/

GRADUATE STUDENT RESEARCH PROGRAM

Sponsored by the

AIR FORCE OFFICE OF SCIENTIFIC RESEARCH

Conducted by the

Universal Energy Systems, Inc.

FINAL REPORT

DEVELOPMENT OF AN AIRCRAFT TIRE-WHEEL INTERFACE MODEL FOR FLANGE/BEADSEAT CONTACT LOADS

Prepared by:	James A. Sherwood, Ph.D.
Academic Rank:	Assistant Professor
Prepared by:	N. Christopher Holmes
Academic Rank:	Graduate Student
Department and University:	Mechanical Engineering University of New Hampshire
Research Location:	AFWAL/FIEMA Wright-Patterson AFB, OH 45433
USAF Researcher:	Monika K. Hilb
Date:	29 Aug 88
Contract No:	F49620-87-R-0004

SAME REPORT AS
PROF. JAMES SHERWOOD
FLIGHT DYNAMICS LABORATORY # 92

1988 USAF-UES SUMMER FACULTY RESEARCH PROGRAM

GRADUATE STUDENT RESEARCH PROGRAM

Sponsored by the

AIR FORCE OFFICE OF SCIENTIFIC RESEARCH

Conducted by the

Universal Energy Systems, Inc.

FINAL REPORT

A FLIGHT CONTROL RECONFIGURATION STUDY USING MODEL REFERENCE ADAPTIVE CONTROL

Prepared by:	William D. Morse
Academic Rank:	BSE
Department and	Department of Electrical Engineering
University:	The Ohio State University
Research Location:	WPAFB/AFWAL
	FIGL/A
	Dayton, OH
USAF Researcher:	Duane Rubertus and Robert Lemble
Date:	19 Sept. 1988
Contract No:	F49620-88-C-0053

A FLIGHT CONTROL RECONFIGURATION STUDY USING MODEL REFERENCE ADAPTIVE CONTROL

by

William D. Morse

The Ohio State University

Department of Electrical Engineering

Columbus, OH 43210

ABSTRACT

A simplified multivariable model reference adaptive control (MRAC) is shown to provide control reconfiguration for the AFTI/F16 during single, double, triple, and quadruple control surface failures. The simplified MRAC is unique in that it may employ a reduced order model and is applicable to unstable nonminimum phase plants. The MRAC is capable of implicitly redistributing the control effort among the aircrafts effective surfaces without explicit knowledge of the failure. The resulting control reconfiguration forces the aircraft to approximate the reference model trajectories. The AFTI/F16 model used for simulations incorporated the nonlinear rate and saturation limited servo dynamics.

Acknowledgements

I wish to express my sincere gratitude to the Flight Dynamics Lab and the Air Force Office of Scientific Research for their sponsorship in this research. Special thanks are extended to Duane Rubertus and Robert Lemble who provided me the opportunity to challenge the difficult problem of control reconfiguration. This research effort would not have been a success without the many valuable discussions with Kurt Newmann, Tom Kobylarz, and Darrell Hammond of the Air Force Institue of Technology, and Curt Clark of the Flight Dynamics Lab.

1. Introduction

Air Force objectives for the future generation of advanced tactical fighters (ATF) include substantially improving their survivability, maintainability, reliability, and life cycle cost. The Self-Repairing Flight Control System Program at the Flight Dynamics Lab (FDL), Wright-Patterson Air Force Base (WPAFB) is an outgrowth of this objective [1]. One component of this effort is to develop a dynamically reconfigurable aircraft controller. A reconfigurable controller possesses the capability during a control system failure to redistribute and coordinate the control effort amongst the aircrafts remaining effective control surfaces such that satisfactory flight performance is retained. Actuator failure and control surface battle damage are prime examples of possible control system failures. By having a reconfigurable flight control system coupled with redundant aerodynamic control surfaces the impact of many control failures is drastically reduced. This accordingly increases aircraft combat survivability. The Vietnam experience revealed an estimated 20 % of the aircraft losses were due to control system failures [2]. Another benefit that the reconfiguration capability provides is the possible elimination of redundant actuators and supporting systems without degradation of pilot safety. Component reduction leads directly to both improved maintainability and cost requirements. With the motivation for control reconfiguration established the problem statement will first be examined. All tables are contained in Appendix A and all figures are contained in Appendix B.

2. Research Objective

The research objective as posed by the FDL, WPAFB [3], is to develop a self-repairing reconfigurable flight control system for the AFTI/F-16 such that it can sustain and recover from the following failure conditions:

- Single surface failures
  - single horizontal tail failure
  - rudder failure

- flaperon failure [1]

- Double surface failures
  - double flaperon failure
  - rudder and canard failure
  - double horizontal tail failure [1]
  - same side flaperon and horizontal tail failure [1]
  - opposite sides flaperon and horizontal tail failure [1]

- Triple surface failures
  - double flaperon and rudder failure
  - double flaperon and canard failure
  - rudder and same side flaperon and horizontal tail failure [1]

- Quadruple Failures [1]
  - rudder, canard, and double flaperon failure [1]
  - rudder, canard, and same side flaperon and horizontal tail failure [1]

The flight envelope of interest for control reconfiguration evaluation is from Mach 0.9 at 20,000 ft. to Mach 0.6 at 30,000 ft. The AFTI/F16 is in the combat flight control mode. The primary states of interest are: (1) pitch rate, (2) roll rate, and (3) yaw rate. The reconfiguration strategy to accomplish these goals is now examined.

[1] An additional failure condition which was considered by the author.

3. Model Reference Adaptive Control as a Reconfiguration Strategy

The general approach presently being used to address the control reconfiguration problem is a combination of a robust baseline controller used in conjunction with a Fault Detection and Isolation (FDI) scheme. The baseline controller is used to maintain stability during the initial moments of a failure while the FDI system locates and isolates the fault. Without the baseline controller the aircraft could in many instances exceed its structural limitations during the FDI time interval. Once the failure is isolated an appropriate control is employed to optimize the remaining effective control surfaces. The primary challenges facing this approach are: (1) developing design techniques and CAD tools such that a sufficiently robust controller for all failure possibilities can feasibly be designed (Quantitative Feedback Theory (QFT) appears to be promising [4]), and (2) perfecting FDI designs such that the probability of a false detection is all but eliminated.

In this effort an alternative method is explored in addressing the reconfiguration problem. The method to be used is a multivariable Model Reference Adaptive Controller (MRAC) developed by I. Bar-Kana and H. Kaufman [5], [6]. The MRAC is capable of implicitly redistributing the control effort among the effective surfaces without explicit knowledge of the failure. Because the MRAC does not use explicit knowledge of the failure for reconfiguration the incorporation of a FDI scheme is not needed. The removal of the FDI scheme from the reconfiguration process eliminates (1) the possibility of false failure detections giving rise to inappropriate possibly catastrophic reconfigurations, and (2) the necessity for a baseline controller because of the associated FDI time delays. In essence, the MRAC is a nonlinear controller which adjusts its controller gains in real time to force the controlled plant to follow the trajectories of a desired model. The variable controller gains are adjusted by a tracking error generated by the comparison of model and plant trajectories. In [5], many of the difficulties and limitations often associated with MRAC controllers are over come. For example:

- Exact knowledge of the plant's relative degree is not required
- The plant can be nonminimum phase
- The plant can be statically unstable
- The model order can be less than or equal to the plant order

The MRAC is proven to guarantee global stability with the nonrestrictive assumption that the plant can be stabilized by a constant gain output feedback. This contribution is significant since MRAC can now be applied to a class of unstable nonminimum phase control problems that originally could not be addressed. The AFTI/F16 is an example of such a plant. It is nonminimum phase, unstable, infinite dimensional, and has significant parameter changes. Additional advantages of a MRAC approach to those already mentioned are:

- Explicit identification of the plant is not required
- Plant parameters are not restricted in the rate of their change
- A sufficiently rich persistently exciting input is not required
- Algorithm is computationally nonintensive

A brief development of the control law is now presented.

3.1 Control Law Development

The desired model represented in state space form is given by

$$\begin{aligned} \dot{\mathbf{x}}_M(t) &= A_M \mathbf{x}_M(t) + B_M \mathbf{u}_M(t) \\ \mathbf{y}_M(t) &= C_M \mathbf{x}_M(t) \end{aligned} \tag{3.1}$$

where $A_M \in R^{r\times r}, B_M \in R^{r\times s}, \mathbf{x}_M(t) \in R^{r\times 1}$, and $\mathbf{u}_M(t) \in R^{s\times 1}$. The plant to be controlled is represented in state space form as

$$\begin{aligned} \dot{\mathbf{x}}_P(t) &= A_P \mathbf{x}_P(t) + B_P \mathbf{u}_P(t) \\ \mathbf{y}_P(t) &= C_P \mathbf{x}_P(t) \end{aligned} \tag{3.2}$$

where $A_P \in R^{n\times n}, B_P \in R^{n\times m}, \mathbf{x}_P(t) \in R^{n\times 1}$, and $\mathbf{u}_P(t) \in R^{m\times 1}$. It is assumed that $r \leq n$ and $s \leq m$. The adaptive control input is given by

$$\begin{aligned} \mathbf{u}_P(t) &= K_x \mathbf{x}_M(t) + K_u \mathbf{u}_M(t) + K_e(t)(\mathbf{y}_M(t) - \mathbf{y}_P(t) \\ &= \begin{bmatrix} K_e(t) & K_x(t) & K_u(t) \end{bmatrix} \begin{bmatrix} \mathbf{y}_M(t) - \mathbf{y}_P(t) \\ \mathbf{x}_M(t) \\ \mathbf{u}_M(t) \end{bmatrix} \\ &= K(t)\mathbf{r}(t) \end{aligned} \tag{3.3}$$

where

$$K(t) = K_P(t) + K_I(t) \tag{3.4}$$

$$K_P(t) = \mathbf{e}_y(t)\mathbf{r}^T(t)\hat{T} \tag{3.5}$$

$$\dot{K}_I(t) = \sigma K_I(t) + \mathbf{e}_y(t)\mathbf{r}^T T \tag{3.6}$$

T and $\hat{T}$ are positive definite weighting matrices and $\mathbf{e}_y(t) = \mathbf{y}_M(t) - \mathbf{y}_P(t)$. Global stability and asymptotically perfect tracking is guaranteed if the plant is Almost Strictly Positive Real (ASPR). A plant is ASPR if there exists a constant gain feedback such that the resulting closed loop system is Strictly Positive Real (SPR). For this to be possible the plant must be minimum phase.

Gauranteed global stability is extended to nonminimum phase plants which can be augmented by a feed forward nonsingular gain matrix, D, such that the resulting augmented plant is minimum phase and ASPR. For this class of plants a bounded tracking error is gauranteed rather than asymptotically perfect tracking. The feed forward gain matrix, D, is further modified to include fast first order dynamics. This is to eliminate the effects of the direct feed forward in conjunction with direct feedback in the augmented plant. The block diagram of this adaptive scheme is shown in Fig 8.7.

4. The AFTI/F16 Aircraft

Provided by the FDL [3], the state space model for the AFTI/F16 is given by

$$\begin{bmatrix} \dot{\theta} \\ \dot{u} \\ \dot{\alpha} \\ \dot{q} \\ \dot{\phi} \\ \dot{\beta} \\ \dot{p} \\ \dot{r} \end{bmatrix} = \begin{bmatrix} 0 & 0 & 0 & 1 & 0 & 0 & 0 & 0 \\ X_\theta & X_u & X_\alpha & X_q & 0 & 0 & 0 & 0 \\ Z_\theta & Z_u & Z_\alpha & Z_q & 0 & 0 & 0 & 0 \\ M_\theta & M_u & M_\alpha & M_q & 0 & 0 & 0 & 0 \\ 0 & 0 & 0 & 0 & 0 & 0 & 1 & 0 \\ 0 & 0 & 0 & 0 & Y_\phi & Y_\beta & Y_p & Y_r \\ 0 & 0 & 0 & 0 & 0 & L_\beta & L_p & L_r \\ 0 & 0 & 0 & 0 & 0 & N_\beta & N_p & N_r \end{bmatrix} \begin{bmatrix} \theta \\ u \\ \alpha \\ q \\ \phi \\ \beta \\ p \\ r \end{bmatrix}$$

$$+ \begin{bmatrix} 0 & 0 & 0 & 0 & 0 & 0 \\ 0.5X_{\delta_e} & 0.5X_{\delta_e} & 0.5X_{\delta_f} & 0.5X_{\delta_f} & 0 & 0 \\ 0.5Z_{\delta_e} & 0.5Z_{\delta_e} & 0.5Z_{\delta_f} & 0.5Z_{\delta_f} & 0 & 0 \\ 0.5M_{\delta_e} & 0.5M_{\delta_e} & 0.5M_{\delta_f} & 0.5M_{\delta_f} & 0 & 0 \\ 0 & 0 & 0 & 0 & 0 & 0 \\ 0.5Y_{\delta_{DT}} & -0.5Y_{\delta_{DT}} & 0.5Y_{\delta_a} & -0.5Y_{\delta_a} & Y_{\delta_c} & Y_{\delta_r} \\ 0.5L_{\delta_{DT}} & -0.5L_{\delta_{DT}} & 0.5L_{\delta_a} & -0.5L_{\delta_a} & L_{\delta_c} & L_{\delta_r} \\ 0.5N_{\delta_{DT}} & -0.5N_{\delta_{DT}} & 0.5N_{\delta_a} & -0.5N_{\delta_a} & N_{\delta_c} & N_{\delta_r} \end{bmatrix} \begin{bmatrix} \delta_{e_R} \\ \delta_{e_L} \\ \delta_{f_R} \\ \delta_{f_L} \\ \delta_c \\ \delta_r \end{bmatrix} \tag{4.1}$$

where the states are

θ = pitch angle (rad)

u = forward velocity (ft/sec)

α = angle-of-attack (rad)

q = pitch rate (rad/sec)

ϕ = bank angle (rad)

β = sideslip angle (rad)

p = roll rate (rad/sec)

r = yaw rate (rad/sec)

and the inputs are

δ_{e_R} = right horizontal tail (rad)

δ_{e_L} = left horizontal tail (rad)

δ_{f_R} = right flaperon (rad)

δ_{f_L} = left flaperon (rad)

δ_c = canards (rad)

δ_r = rudder (rad

The flight parameters for flight condition 2 at M.6, 30,000 ft., and flight condition 3 at M.9, 20,000 ft. are contained in table 7.2. The matrix elements for flight conditions 2 and 3 are contained in table 7.3. The following assumptions are made concerning the plant:

1. All of the plant states, θ, u, α, q, ϕ, β, p, and r are available for control use.
2. The aircraft has a supplemental feedback loop to vary thrust such that the effect of the perturbation velocity can be ignored.
3. The aircraft is a rigid body and of constant mass.
4. The aerodynamics are fixed for mach and altitude.
5. The left and right canards act symmetrically together.

The AFTI/F16 servo power actuator dynamics [10] were incorporated into the AFTI/F16 simulation model. The transfer function of the power actuator is

$$P(s) = \frac{20}{s+20} \tag{4.2}$$

The servo rates and mechanical limits were also included for realistic nonlinear modeling. The rate and mechanical limits for the different control surfaces are given in table 7.1.

4.1 Design

The design work centers around the selection of the weighting matrices, T, and $\hat{T}$, the output matrices C_P, and C_M, and the feed forward gain matrix D. Unfortunately, there is no step by step procedure one can follow when selecting the elements within these matrices. Some very rough and general guidelines though are:

1. C_P must provide stabilizing feedback. Ideally, this feedback configuration should remain stabilizing at high gains.
2. $C_M = C_P$
3. The feedback gain matrix, D, can be found indirectly by first finding a scaled identity matrix, I_s, such that the eigenvalues of

   $$A_{CL} = A_P - B_P I_s C_P \tag{4.3}$$

   are in the left half plane. It is shown in [7] that the zeros of an open loop system with feed forward gains are the eigenvalues of

   $$A_{OL} = A_P - B_P D^{-1} C_P \tag{4.4}$$

   From (4.3) D follows immediately as

   $$D = I_s^{-1} \tag{4.5}$$

   By having a high gain stabilizing feedback, the element magnitudes within D can be minimized which inturn minimizes the effect of the feed forward.
4. T and $\hat{T}$ are found strictly by trial and error so long as they remain positive definite.

For the AFTI/F16 model the final C_P matrix arrived at was

$$C_P = \begin{bmatrix} -1.8484 & 0.0007 & -0.1587 & -70.4253 & -1 & 0 & -1000 & 0 \\ -1.8484 & 0.0007 & -0.1587 & -70.4253 & 1 & 0 & 1000 & 0 \\ -0.0184 & 0 & -0.0016 & -0.7043 & -1 & 0 & -1000 & 0 \\ -0.0184 & 0 & -0.0016 & -0.7043 & 1 & 0 & 1000 & 0 \\ 0 & 0 & 0 & 0 & 0 & -0.1 & 0 & 10 \\ 0 & 0 & 0 & 0 & 0 & 0.1 & 0 & -10 \end{bmatrix} \tag{4.6}$$

The feed forward matrix D was

$$D^{-1} = (10,000)I_{6\times 6} \tag{4.7}$$

The modified feed forward term was

$$D_m(s) = \frac{D}{s+500} \tag{4.8}$$

The weighting matrices $\hat{T}$ and T are

$$\hat{T} = T = (10)I_{20\times 20} \tag{4.9}$$

Most of the design effort and skill centered around the proper element selections for C_P. This was nontrivial since it had to provide stabilizing feedback for not only the case when six healthy control surfaces were available but also for failure combinations of extreme magnitude. Because of the many considerations and complexity in arriving at the final C_P the reader is referred to [9] for complete details.

5. Control Surface Failure Simulations and Results

Control surface failures were simulated by zeroing out the surface command input column vector within the plant's input B matrix. The aircraft maneuver used to test control reconfiguration capabilities was a hard banking right turn. This difficult control maneuver, composed of superimposed longitudinal and lateral command inputs, was selected to thoroughly test the controller's ability to cope with control surface failures. The pilot command sequence is as follows:

Time 0-1 sec: Steady state level flight

Time 1 sec: A 11.5 deg/sec roll rate command is applied

Time 2 sec: A 23 deg/sec pitch rate command is applied

Time 3 sec: Pitch rate command is removed

Time 5 sec: Roll rate command is removed

Time 5-10 sec: Aircraft remains in a banked coordinated turn

The adaptive control was built for simulation using the MATRIX$_X$ SYSTEM-BUILD capability [8]. The simulations were carried out using the variable step Kutta-Mearson method. The eight state model used was linear in the longitudinal mode but nonlinear in the lateral mode. The model's lateral mode provided appropriate roll and yaw to produce a coordinated turn for a given altitude and speed. Simulation results of the double flaperon and rudder failure, and the right flaperon, right horizontal tail, rudder, and canard failure ,both at Mach 0.9, 20,000 ft., were chosen to be representative examples of the 26 failure scenarios tested. The tracking errors for the two failure conditions are shown in Figs. 8.1, and 8.4. The AFTI/F16 states superimposed upon the ideal model trajectories are shown in Figs. 8.2, and 8.5. The control surface commands are shown in Figs. 8.3, and 8.6

The adaptive controller was impressively successful in maintaining coordinated flight for all tested failure combinations except the double horizontal tail failure. The controller's capability to maintain sideslip less then two degrees during catastrophic quadruple failures is quite remarkable.

Figs. 8.1, 8.2, and 8.3 illustrate the controller's response during the triple failure of both flaperons and rudder. The tracking of the plant is very close to that of the model. In Fig. 8.3 the horizontal tail can be seen injecting the superimposed roll and the pitching moments while the canards handle the yawing moment.

Figs. 8.4, 8.5, and 8.6 illustrate the controller's response during the quadruple failure of the right flaperon, right horizontal tail, rudder, and canard. Close examination of Fig. 8.6 reveals the control coordination being exercised between the left flaperon and horizontal tail to achieve the coordinated turn. In Fig. 8.5 it is seen that the aircraft closely tracks the model's pitch and roll rates. Sideslip is oscillatory but damps out as the roll rate command is removed. Ideally, sideslip should remain less then one degree, but given the extent of the control damage the controller is behaving superbly.

The double horizontal tail failure resulted in an uncontrolled aircraft at Mach 0.9, 20,000 ft. The aircraft physically can not accomplish this maneuver because of the small effect the flaperons have in the pitching moment. In simulations the flaperons reached both rate and mechanical limits. However, at higher altitudes and high speeds, e.g. Mach 0.6, 30,000 ft., the aircraft is capable of this maneuver. It is important to note that this is due to structural capabilities and limitations rather then due to controller reconfiguration performance.

6. Conclusions and Recommendations

A successful reconfigurable flight controller was designed using MRAC. Without explicit knowledge of a given failure condition the controller was capable of redistributing the control effort amongst the effective control surfaces to maintain satisfactory flight performance. The controller's capability to withstand quadruple control surfaces failures was outstanding and is illustrative of its potential power.

It is strongly recommended that research in the application of MRAC to flight control reconfiguration be continued for the following reasons:

1. MRAC theory has been advanced such that it is now possible to employ such techniques to unstable nonminimum phase aircraft.
2. Using a MRAC approach to flight control reconfiguration eradicates the need for explicit knowledge of the failure. Accordingly, the open loop FDI process, with its associated probability of false failure detections, can be eliminated.
3. Furthermore, because MRAC does not activity incorporate a FDI scheme there is no associated time delay between the failure occurrence and when the controller begins to compensate by reconfiguration. This eliminates the necessity to have a robust baseline controller for the initial moments into a failure scenario.
4. The MRAC inherently possesses the capability to redistribute the control effort amongst the effective surfaces without the incorporation of special or complicated control mixing techniques.

5. The MRAC is computationally nonintensive.

Follow up research is encouraged to further develop and demonstrate MRAC reconfiguration capabilities. Issues to be addressed in future research are:

1. A reconfigurable MRAC design for the Combat Reconfigurable Controlled Aircraft (CRCA).
2. Studies involving the adaptive controller's response to battle damaged, and partially failed surfaces.
3. Discretizing the adaptive control law and the effects of different sampling periods.
4. Effects and elimination of measurement noise problems.
5. Examination of the adaptive controller's capability to handle the complete nonlinear aircraft model.
6. Determination of absolute controller and plant performance bounds for various failures scenarios.
7. Incorporation of the pilot into the control loop.

This is an exciting area of control research which is only in its infancy. It promises to yield tremendous results and insights beyond the immediate application to fighter aircraft.

7. Appendix A

Surface	Rate Limit	Lower Mechanical Stop	Upper Mechanical Stop
Horizontal Tail	60 deg/sec	-25°	$+25^{\circ}$
Flaperon	52 deg/sec	-23°	$+20^{\circ}$
Canards	108 deg/sec	-27°	$+27^{\circ}$
Rudder	120 deg/sec	-30°	$+30^{\circ}$

Table 7.1: AFTI/F16 Power Actuator Limits.

Parameters	Flight Condition 2	Flight Condition 3
Mach Number	0.6	0.9
Elevation	30,000 ft.	20,00 ft
Dynamic Pressure	158.81 lb/ft^2	552.113 lb/ft^2
Trim Velocity	596.91 ft/sec	933.23 ft/sec
Trim Angle of Attack	4.705 degrees	1.86 degrees

Table 7.2: AFTI/F16 Flight Parameters

Dimensionalized Body Axis Aerodynamic Stability Derivative Elements					
Lateral Direction			Longitudinal Direction		
Element	Flgt Cond 2	Flgt Cond 3	Element	Flgt Cond 2	Flgt Cond 3
$\dot{Y}_\phi$	0.05376	0.03449	$\dot{X}_\theta$	-32.0915	-32.183
$\dot{Y}_\beta$	-0.154099	-0.343554	$\dot{X}_u$	0.005142	0.012075
$\dot{Y}_p$	0.082387	0.032636	$\dot{X}_\alpha$	23.0402	38.2906
$\dot{Y}_r$	-0.998322	-0.997556	$\dot{X}_q$	-48.8785	-30.1376
$\dot{L}_\beta$	-19.2246	-55.2526	$\dot{Z}_\theta$	-0.004425	-0.00112
$\dot{L}_p$	-0.893601	-2.80004	$\dot{Z}_u$	-0.000109	-0.000022
$\dot{L}_r$	0.318845	0.145674	$\dot{Z}_\alpha$	-0.526422	-1.48446
$\dot{N}_\beta$	2.29583	7.237	$\dot{Z}_q$	0.997184	0.994789
$\dot{N}_p$	-0.000888	-0.023184	$\dot{M}_\theta$	0.000313	-0.000309
$\dot{N}_r$	-0.278676	-0.36253	$\dot{M}_u$	-0.000337	-0.00013
$\dot{Y}_{\delta_{DT}}$	0.014398	0.026609	$\dot{M}_\alpha$	2.52708	4.27171
$\dot{Y}_{\delta_a}$	0.000357	-0.001371	$\dot{M}_q$	-0.341902	-0.777221
$\dot{Y}_{\delta_e}$	0.007335	0.026734	$\dot{X}_{\delta_e}$	3.17035	2.00593
$\dot{Y}_{\delta_r}$	0.021165	0.037032	$\dot{X}_{\delta_f}$	-2.09855	2.31681
$\dot{L}_{\delta_{DT}}$	-13.5832	-50.729	$\dot{Z}_{\delta_e}$	-0.066156	-0.149227
$\dot{L}_{\delta_a}$	-17.4468	-51.0502	$\dot{Z}_{\delta_f}$	-0.111711	-0.244924
$\dot{L}_{\delta_e}$	0.414519	5.53185	$\dot{M}_{\delta_e}$	-5.86214	-24.0581
$\dot{L}_{\delta_r}$	3.92325	10.3955	$\dot{M}_{\delta_f}$	-0.211773	-6.47269
$\dot{N}_{\delta_{DT}}$	-1.50547	-5.1371			
$\dot{N}_{\delta_a}$	-0.268403	-1.25006			
$\dot{N}_{\delta_e}$	1.51008	5.89254			
$\dot{N}_{\delta_r}$	-1.96651	-5.8089			

Table 7.3: AFTI/F16 Dimensional Derivative Elements

8. Appendix B

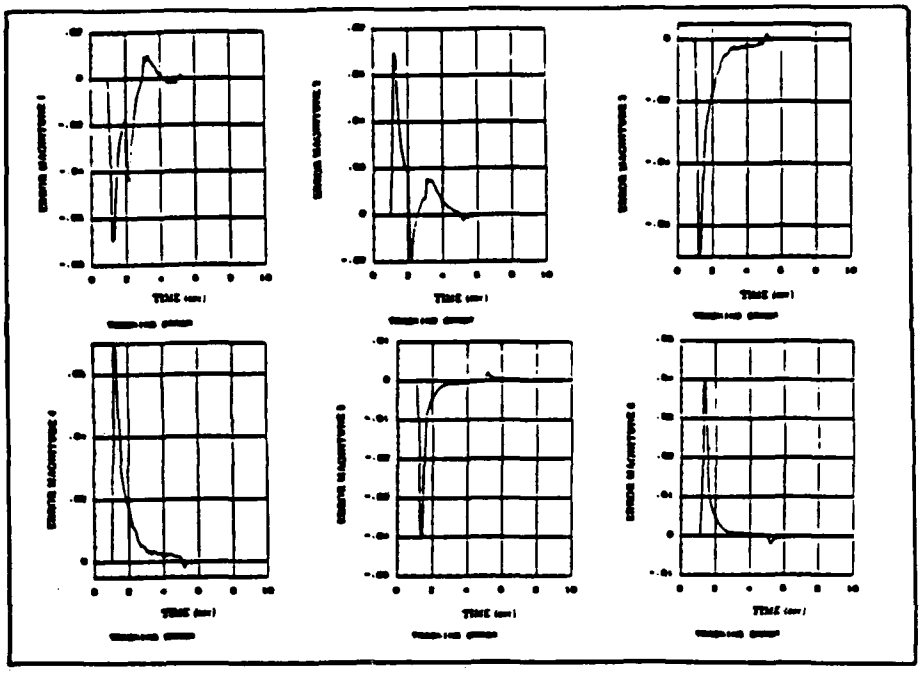

Figure 8.1: Tracking Error
Flaperon and Rudder Failure

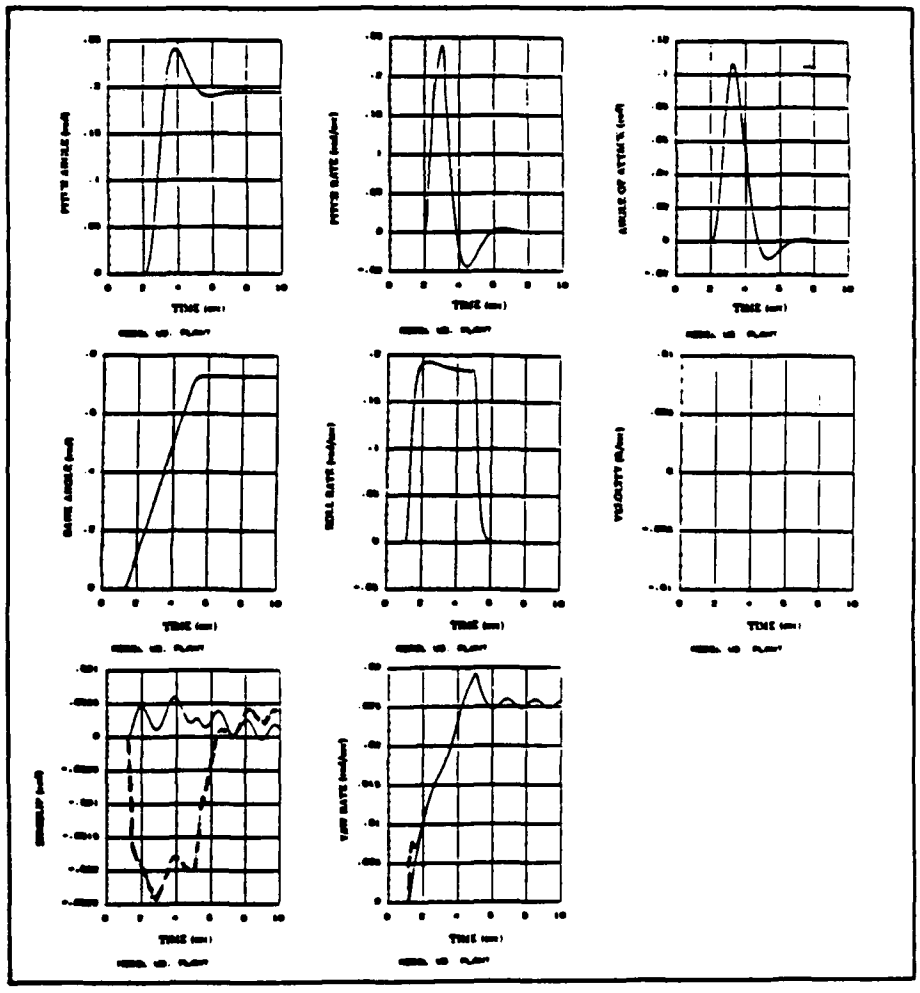

Figure 8.2: Plant and Model Trajectories Superimposed
Double Flaperon and Rudder Failure

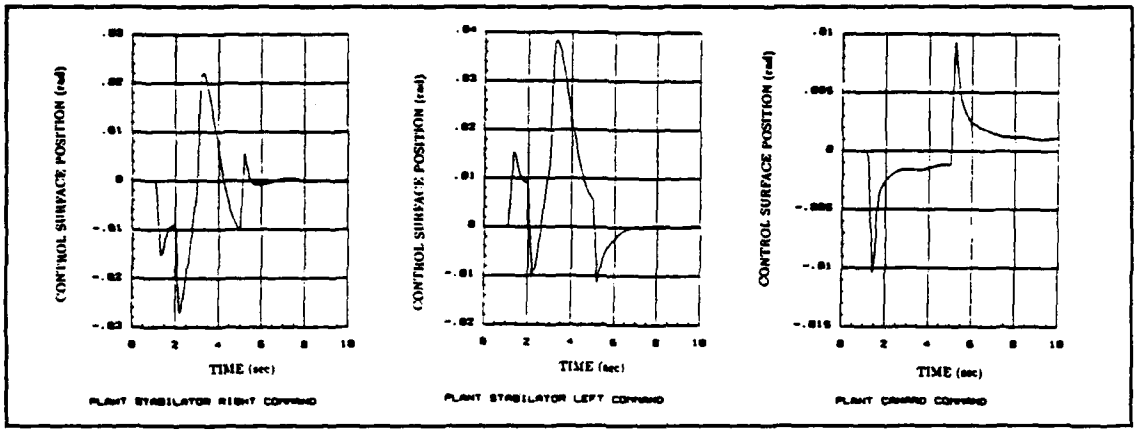

Figure 8.3: Plant Control Surface Positions
Double Flaperon and Rudder Failure

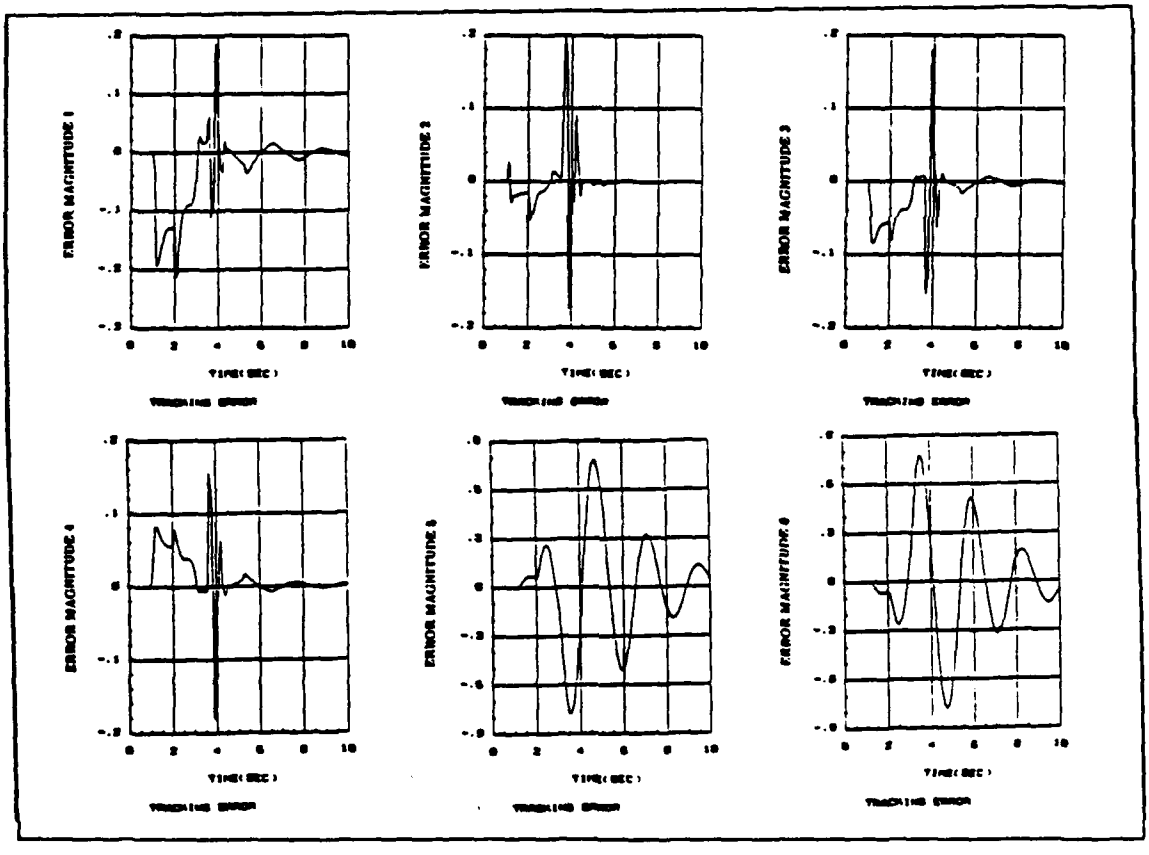

Figure 8.4: Tracking Error Right Flaperon, Right Horizontal Tail,
Rudder and Canard Failure

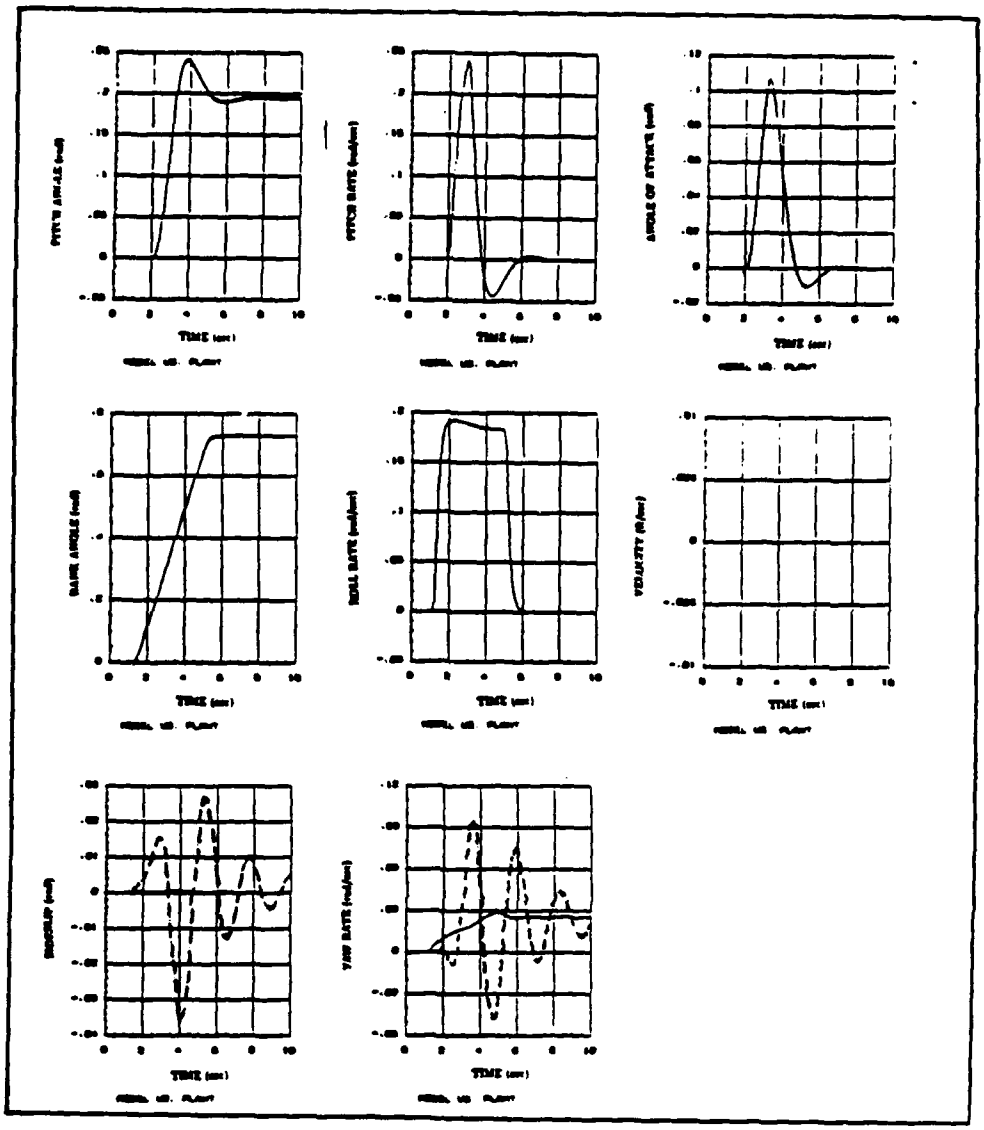

Figure 8.5: Plant and Model Trajectories Superimposed Right Flaperon, Right Horizontal Tail, Rudder and Canard Failure

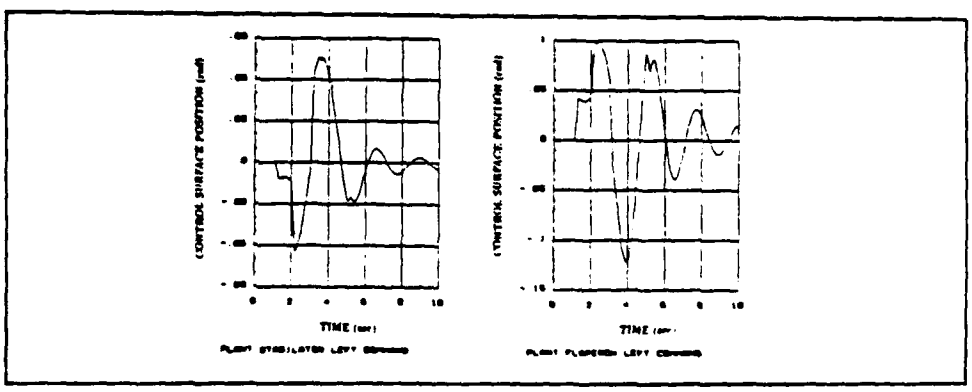

Figure 8.6: Plant Control Surface Positions Right Flaperon, Right Horizontal Tail, Rudder and Canard Failure

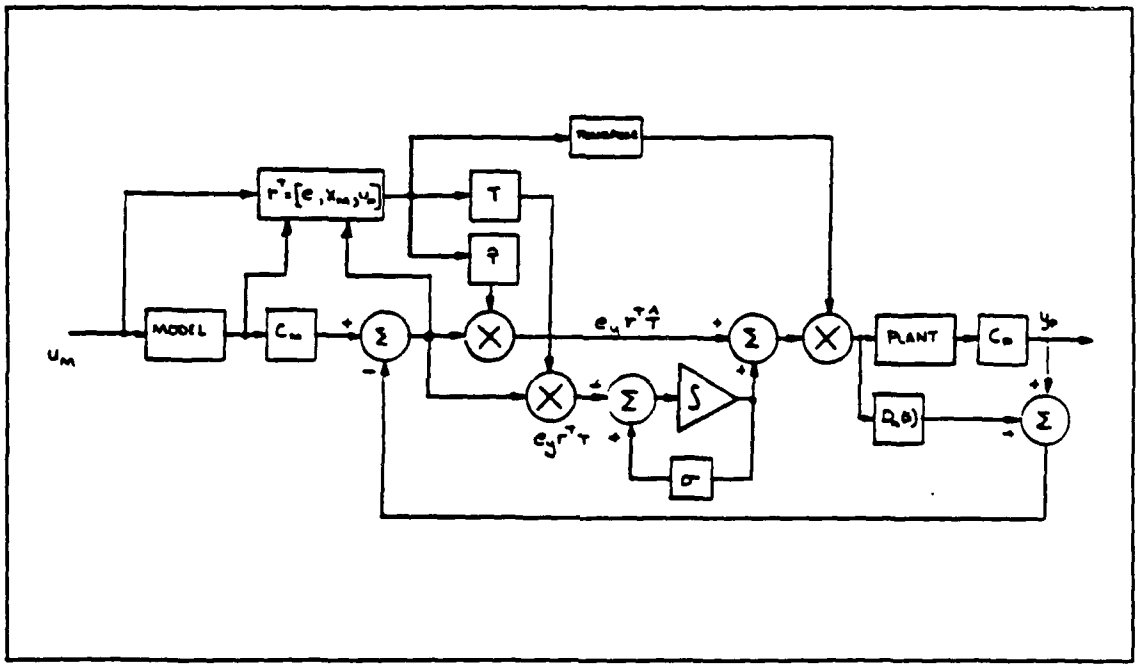

Figure 8.7: MRAC

Bibliography

[1] R.A.Eslinger, and P.R.Chandler, "Self-Repairing Flight Control System Program Overview," Proceedings of the National Aerospace and Electronics Conference, Dayton, OH, May 1988, pp.504-511.

[2] J.Anderson, C.Clark, P.Madsen, and F.Unfried, "USAF AFTI/F16 Self-Repairing Flight Control System (SRFCS) Simulation," Paper presented at the National Aerospace and Electronics Conference, Dayton, OH, May 1987.

[3] D.Rubertus, and R.Lemble, "AFTI/F16 Self-Repairing Flight Control Problem Statement Correspondence," Wright-Patterson AFB, Dayton, OH, Dec. 1987.

[4] Lear Siegler Inc., Reconfiguration Strategies for the Aircraft with Flight Control Systems Subjected to Actuator Failure/Surface Damage, AFWAL-TR-86-3110, Flight Dynamics Lab, Wright-Patterson AFB, Dayton, OH, 1986.

[5] I. Bar-Kana, and H.Kaufman, " Global Stability and Performance of a Simplified Adaptive Algorithm," International Journal of Control, 1985, vol.46, no.6, pp.1491-1505.

[6] I.Bar-Kana, "Adaptive Control: A Simplified Approach," Control and Dynamic Systems: Advances in Theory and Applications, 1987, vol.25, pp.187-235.

[7] A.G.J.MacFarlane, "Frequency Response Methods in Multivariable Control," Proceedings of the American Control Conference, 1980, Plenary II.

[8] Integrated Systems Inc., $MATRIX_X$ User's Guide, Palo Alto, Cal., 1982.

[9] W.D.Morse, "Self-Repairing Reconfigurable Flight Control Using Model Reference Adaptive Control," MS Thesis, The Ohio State University, Columbus, OH, Dec. 1988.

[10] General Dynamics, AFTI/F16 Development and Integration Program, AFWAL-TR-84-3008, Flight Dynamics Lab, Wright-Patterson AFB, Dayton, OH, 1984.

1988 USAF-UES SUMMER FACULTY RESEARCH PROGRAM/

GRADUATE STUDENT SUMMER SUPPORT PROGRAM

Sponsored by the

AIR FORCE OFFICE OF SCIENTIFIC RESEARCH

Conducted by the

Universal Energy Systems, Inc.

FINAL REPORT

DAMAGE IN GRAPHITE/EPOXY PLATES SUBJECTED TO LOW VELOCITY IMPACT

Prepared by:	William E. Wolfe, Ph.D. and Greg Schoeppner
Academic Rank:	Associate Professor , Graduate Student
Department and University:	Civil Engineering Department The Ohio State University
Research Location:	AFWAL/FIBCA Wright Patterson AFB OH 45433
USAF Researcher:	Dr. R. S. Sandhu

Date:	30 Sep 88
Contract No:	F49620-87-R-0004

SAME REPORT AS
PROF. WILLIAM WOLFE
FLIGHT DYNAMICS LABORATORY # 95

1988 USAF SUMMER FACULTY RESEARCH PROGRAM

GRADUATE STUDENT RESEARCH PROGRAM

Sponsored by the

AIR FORCE OFFICE OF SCIENTIFIC RESEARCH

Conducted by the

Universal Energy Systems, Inc.

FINAL REPORT

FINITE ELEMENT ANALYSIS FOR PRELIMINARY STRUCTURAL DESIGN/OPTIMIZATION

Prepared by:	Richard A. Swift
Academic Rank:	Graduate Student (M.S.)
Department and	Aerospace and Mechanical Engineering
University:	University of Notre Dame
Research Location:	AFWAL/FIBRA
	Wright-Patterson AFB OH 45433-6553
USAF Researcher:	Captain R. A. Canfield
Date:	August 17, 1988
Contract No:	F49620-88-C-0053

FINITE ELEMENT ANALYSIS FOR PRELIMINARY STRUCTURAL DESIGN/OPTIMIZATION

by

Richard A. Swift

ABSTRACT

Finite element analysis for use in structural design has advanced to the point where multidisciplinary analysis and design capabilities are well supported by a number of programs. These codes offer unique possibilities in terms of minimizing the time required at the preliminary design stage. Investigations into the theoretical and operational aspects of ASTROS (the Automated STRuctural Optimization System) for its use in preliminary design have supported proposed research into this area at the University of Notre Dame.

I. Introduction

ASTROS represents the most recent generation of a family of finite element codes developed for structural analysis/optimization. The use of such codes for effective preliminary design may aid in reducing the current loads, design, and aeroelastic analysis requirements at this stage of the design process.

My research interests deal with the effective use of finite element analysis for design and optimization at this preliminary design level. Is it possible to generate an optimum flight vehicle configuration in concert with a sophisticated multidisciplinary structural analysis? I believe so. Lockheed has approached this capability with PADS[1,2] (Preliminary Aeroelastic Design of Structures). Such codes will form the basis for the next generation of finite element analysis/optimization programs.

II. Objectives

The main objectives of this summers research are to gain familiarity with ASTROS and to determine which aspects of the code may be applicable to the goal presented previously dealing with preliminary design. The following is a complete list of the objectives identified at the beginning of this research period.

1. A number of short-term objectives (within the 10 week period) have been identified by current Air Force researchers working on ASTROS. The majority of these goals either coincide or fit well within the scope of my own objectives. My objectives this summer are:

a. To develope a background of knowledge involving the NASTRAN and ASTROS codes, both in terms of their theoretical nature and operation.

b. To identify, in conjunction with current personnel, possible avenues of research which might be applicable to continued research at Notre Dame. Of particular interest is the possibility of identifying techniques conducive to geometric optimization in concert with structural optimization. The ultimate goal of such optimization is to yield the most efficient design for given loading and constraint conditions. Also important at the preliminary design stage would be the trends or sensitivities encountered during the geometrical optimization.

2. The short-term goals presented by Captain Canfield include the following:

a. A swept wing optimization problem has been formulated by Northrop and the results have been published. It is desired to match the Northrop results with those obtained from the FDL ASTROS program.

b. Complete four other ASTROS User Training Workshop (UTW) problems, and prepare to assist as an instructor at the UTW.

c. Lockheed has supplied information regarding the finite element modeling of an L1011 wing. It is desired to optimize this structure using ASTROS. A number of goals have been identified for this optimization involving model verification, analysis verification, strength optimization, and air loads. A preliminary schedule for the L1011 problem is as follows:

(1) June 27-July 1 - Identify the modeling problems that are linked to the Multi-Point Constraints (MPCs) and any associated stiffness problems with the model (possible fuselage effects).

(2) July 5-15 - Resolve the MPC problems.

(3) July 18-25 - Resolve the stiffness problem.

(4) July 25-29 - Present final results.

III.

a. Current research at the University of Notre Dame involving finite element analysis at the conceptual/preliminary design stage will require the use of varied optimization and analysis technicues to satisfy a number of current goals.

After reviewing the Theoretical Manual, an investigation into the actual operation of the code itself was performed. This involved completing the workshop problems (several times, as it turned out). These problems were designed specifically so that the workshop participants could gain maximum understanding of the "more important" capabilities of ASTROS. Subjects involved multiconstraint optimization (displacements, natural frequencies, weight), modal and flutter analysis, and static analysis. A complete outline of the workshop problem descriptions is given below.

Problem Set Definition

Problem Set #1: Space Truss
1-1: Modal analysis using Guyan Reduction and Generalized Dynamic Reduction
1-2: Optimization for the first two natural frequencies

Problem Set #2: Rectangular Wing
2-1: Static analysis for tip load
2-2: Optimization for stress constraints
2-3: Optimization for stress constraints with shape functions
2-4: Static analysis with inertia relief
2-5: Aeroelastic trim for wing in straight, level flight

Problem Set #3: Cantilevered Plate
3-1: Static and modal Analysis
3-2: Transient analysis
3-3: Subsonic and supersonic flutter analysis

Problem Set #4: Swept Wing
4-1: Static analysis for gravity load
4-2: Modal analysis
4-3: Optimization for stress and frequency constraints

Problem Set #5: Plane Frame
5-1: Optimization for displacement constraints

During the workshop (20-24 June) the author gave a preliminary presentation of problem set #1 and participated as an instructor. Problem set #1 involved the Active Control Of Space Structures (ACOSS) model, developed by the Charles Stark Draper Laboratory. The finite element model has 33 nodes (90 degrees of freedom), 18 concentrated masses, and 113 rod elements. The material used for all elements was graphite epoxy (E=18.5 Mpsi, density= .055lb/in^3). For this problem, as in all five of the workshop problems, the participants were supplied with the finite element models (nodal coordinates, elements and connectivities, properties, etc.). What is required of the participants? They must create the necessary MAPOL solution set for proper ASTROS execution, and insert any associated "cards" into the bulk data set provided. As an example, the problem statement and the MAPOL solution set for problem #1 are given below.

Problem statement

For this initial design the first three frequencies of the modified ACOSS II truss are: 1.21,2.71, and 4.21 hz.

a) Verify the first three frequencies. Use Guyan reduction or Generalized Dynamic Reduction (GDR) to eliminate the singularites in the mass matrix.

b) Design the truss for minimum weight while raising the fundamental frequency to 2.0 hz and maintaining a separation of at least 1 hz from the remaing modes.

Solution set

```
TITLE=ASTROS USER TRAINING WORKSHOP PROBLEM SET #1
 SUBTITLE=MODAL ANALYSIS FOR PART 1 IS PRINTED FOR FIRST
          OPTIMIZATION PASS
 OPTIMIZE STRATEGY=57
   BOUNDARY METHOD=1,SPC=18,DYNRED=1
   MODES(DCONSTRAINT=2)
  PRINT DESIGN, ROOT=ALL
END
```

This solution set requires the addition of several types of cards to the bulk data set. The fact that this is an optimization requires that design variables be declared, in this case through DESELM cards. Each DESELM card corresponds to a single design element, thus 113 cards are required. Many participants created simple FORTRAN programs to produce these cards, while others used the programable keys of the DEC terminals. METHOD, which is called in the BOUNDARY line, requires the insertion of an EIGR

card for calculation of the natural frequencies. SPC calls associated Single Point Constrain (SPC) cards, while DYNRED calls an associated DYNRED card to specify the frequency range of interest for Generalized Dynamic Reduction. DCONSTRAINT calls associated DCONFRQ cards (in this case) to specify the frequency constraints provided in the problem description. It is interesting to note that a print statement is required. Because of the voluminous data generated during an ASTROS run, the user specifies only those quantities of interest (in this case, the final design areas and frequencies).

Optimization of the structure occurs in twelve iterations.

A recent paper by RAO[3] was identified as a possible avenue of continued research at Notre Dame. Rao has described a method for applying fuzzy set theory to structural optimization; the use of such techniques for preliminary design may prove promising.

IV.

a. NASA[4] and Lockheed[1,2] have performed finite element analysis and optimization an L1011 wing/fuselage model. This model consists of 641 nodes and 1733 elements. There are 170 beam elements for the fuselage rings, fuselage beams, tail, landing gear, and control surface actuators. There are 775 rod elements used to model the spar and rib caps and the stiffeners on the lower fuselage shell. Two spring elements are

incorporated as actuator springs for the control surfaces. The remaining elements are 786 quadrilateral membrane elements used to model the wing and fuselage skins as well as the wing rib and spar shear webs. The current model has been run through a static NASTRAN analysis, but the results show poor correspondance to published NASA results (20% error). Modeling discrepancies are involved.

b. The original finite element model had been reworked heavily by a previous researcher, but a number of problems remained. The most noteable of these was at the wing/fuselage interface. The wing coordinate system was incorrectly described relative to the global system, resulting in the wing having a negative dihedral angle. Surprisingly, this went unnoticed. The wing coordinate system was modified to eliminate this discrepancy by altering the required CORD2R card in the NASTRAN bulk data. The original model also had two suspicious beam elements connecting the coordinate system origin to the engine pylon. No meaning for these elements could be found, so they were deleted.

After performing these alterations, a static analysis was performed using ASTROS, but singularities in the stiffness matrix prevented execution. In order to locate these singularities, the standard MAPOL sequence was altered so that detailed information on the stiffness matrix would be routed to the output file. This information consisted of a listing of the stiffness matrix in terms of nodal points and associated degrees of

freedom. Thus, the associated singularity listed in the output file could be traced to a specific nodal degree of freedom.

The MAPOL solution set with the modification was as follows:

```
EDIT NOLIST;
REPLACE 191;
  CALL IFP(GSIZE,,1)
INSERT 497;
   CALL USETPRT(1);
END;
 SOLUTION
 ANALYZE
     BOUNDARY MPC=131,SPC=121
     STATICS(MECH=1)
     PRINT DISP=ALL
END
```

EDIT NOLIST and CALL IFP(GSIZE,,1) specify that the MAPOL sequence and bulk data , respectively, should not be echoed to the output file. CALL USETPRT(1) specifies the modified stiffness matrix output. Note that all MAPOL edit commands are followed by a semicolon.

A number of nodal degrees of freedom were thus identified as possible

singularities, and these potential singularities were eliminated. The ASTROS run would still not execute fully. A NASTRAN run was then performed using the PARAM, AUTO SPC card in the bulk data to identify any remaining singularities. The NASTRAN run executed fully, and the SPC cards that were generated were employed in the ASTROS run. Execution was still not successful. The most recent error is logic error 1320, occurring in SDCOMP. Additional investigation would be required to locate the cause of this error. The author's NASTRAN results were excellent; nodal displacements for the two loading cases investigated were within 6% of the published NASA EAL results.

V. Recommendations

a. Since the major results of this summers work may be termed as educational, implementation of the results of this research will materialize in the research to be performed in preliminary design within my department. The experience that the author has gained will be invaluable in this respect.

With regard to the progress on the L1011 model, it is hoped that future personnel will be able to continue the ASTROS analysis through optimization aided by the work of the author.

b. At the heart of this summer's work is the hope for follow on research. The author's Masters thesis will involve methods investigated during this research period. The background of information that has been gained this summer, as well as the general experience, have both been extremely rewarding.

Acknowledgements

I wish to thank the Air Force Office of Scientific Research and the Air Force Wright Aeronautical Laboratory for sponsorship of this research. Of course, the involvement of Universal Energy Systems must also be commended.

I would personally like to thank Dr. V. Venkayya, Captain R. Canfield, V. Tishler, and R. Kolonay for their assistance. They helped to make this summer both educational and enjoyable.

References

[1]Radovich, N.A., Preliminary Aeroelastic Design of Structures (PADS) Methods Development and Application, Advanced Flutter and Dynamics Methods, Lockheed-California, Co. April 1983.

[2]Radovich, N.A., Some Experiences in Aircraft Aeroelastic Design Using Preliminary Aeroelastic Design of Structures (PADS), NASA Symposium on Recent Experiences in Multidisciplinary Analysis and Optimization, April 24-26 1984.

[3]Rao, S.S., Optimum Design of Structures in a Fuzzy Environment, AIAA Journal, Vol. 25, No. 12, pp 1633-1636.

[4]Walsh, J.L., Application of Mathematical Optimization Procedures to a Structural Model of a Large Finite-Element Wing, NASA Technical Memorandum 87597, January 1986

1988 USAF-UES Summer Faculty Research Program
Graduate Student Research Program

Sponsored by the
AIR FORCE OFFICE OF SCIENTIFIC RESEARCH
Conducted by the
Universal Energy Systems, Inc.

FINAL REPORT

Prepared by:	David F. Thompson
Academic Rank:	Ph.D. Student
Department and University:	School of Mechanical Engineering Purdue University
Research Location:	AFWAL/FIGL Wright-Patterson AFB, OH 45433-6553
USAF Researcher:	Duane P. Rubertus
Date:	31 Aug 88
Contract No.:	F49620-88-C-0053

Optimal and Sub-Optimal Loop Shaping

in

Quantitative Feedback Theory

by

David F. Thompson

ABSTRACT

The motivation for the development of loop shaping algorithms in the Quantitative Feedback Theory (QFT) method for control system design is discussed, and the conclusions of preliminary research is presented. After a brief introduction and problem statement, basic issues critical to the successful implementation of the QFT method are outlined, followed by a discussion of the benefits an automated loop shaping procedure would afford. Specific results of investigations during the summer research period are presented, and criteria for the evaluation of candidate algorithms to be developed in subsequent work are discussed.

Acknowledgements

I would like to thank the Air Force Systems Command and the Air Force Office of Scientific Research for their sponsorship of this research, and I would also like to thank the personnel of Universal Energy Systems for their patient assistance in handling many of the administrative details of my research program.

I would especially like to thank Mr. Duane P. Rubertus and Prof. C. Houpis for their invaluable assistance in my research effort, both in bringing me to AFWAL/FIGL and in providing an intersting and stimulating working environment. Special thanks go to Prof. I. Horowitz, without whose help much of my recent progress would not have been possible.

I. Introduction:

The development of Quantitative Feedback Theory (QFT), a robust control system design method introduced by Prof I. Horowitz and his colleagues[1]-[4], has received increasing attention over the past few years from control theorists and practitioners alike. The method is advantageous in many cases of multi-input, multi-output (MIMO) control system design since it incorporates many features which are not inherent in other well-known MIMO design methods[5]-[7]. One of the most prominent of these features is the capability for *direct* design to specifications, namely closed loop specifications on the transient or frequency response.

It is these such advantages that the Flight Control Development Branch of the Air Force Wright Aeronautical Labs (AFWAL/FIGL), Wright-Patterson AFB, OH, finds particularly attractive. Projects with potential QFT application are currently underway by FIGL researchers and by AFIT MS students in numerous areas of flight control including reconfigurable and self-repairing control systems.

My research interests lie in refining some of the computational aspects of the QFT design procedure in order to make the method more tractable and thus easier for the control systems engineer to learn and use. Although portions of the design process have been successfully implemented in a computer program[8], the most computationally demanding step in the procedure is still carried out by hand, off line, due to the lack of a satisfactory design algorithm. The goal is to reduce much of this need for *required* interaction by an experienced designer by developing such an algorithm, suitable for interactive programming, which incorporates a mathematical basis for many of the "rules of thumb" used. This would permit a full computer-aided implementation of the method, making it more accessible to the control engineer.

Such an effort is not intended to remove interaction from the design process but rather to gain additional insight into the problem, information which would be critical in analyzing tradeoffs during the course of a design. By doing this, as well as by removing much of the computational burden from the designer, it is believed that a much more flexible and useful CAD package can be developed.

II. Objectives of the Research Effort:

As suggested in the Introduction, the ultimate goal of this research program is to develop algorithms which allow the QFT method to be implemented in a fully automated CAD package. This will require the development of additional theory which has not yet been studied in the context of the QFT problem. After a brief introduction to the QFT design method and a statement of the particular sub-problem being studied, a discussion of the specific accomplishments of the summer research program will be given.

II.1 The QFT Problem:

For the single-input, single-output (SISO) system, the QFT method assumes given a linear time-invariant (LTI) plant P(s) with forward loop compensator G(s) and prefilter F(s) (both also LTI) free to be chosen (Fig. 1). Allowing bounded parametric plant uncertainty, closed loop performance bounds, stated in terms of upper and lower bounds on the closed loop transfer function $T(j\omega)$ $\forall \omega \in [0,\infty)$ (Fig. 2), are translated into corresponding bounds on the open loop transfer function (loop transmission function) $L(j\omega) = P(j\omega)\, G(j\omega)$ $\forall \omega \in [0,\infty)$. The transformation between closed loop and open loop bounds may be accomplished via the Nichols Chart (Fig. 3). Here for a typical design problem[9] the open loop bounds, denoted $B(\omega)$, are illustrated for the discrete set of frequencies $\omega \in \{\omega_1,\ldots\omega_{nf}\}$.

The $B(\omega)$ is actually a set of contours in the logarithmic complex plane which, at each frequency, define allowable regions in which the open loop $L(j\omega)$ must lie in order to satisfy the closed loop performance bounds. It then becomes necessary to develop criteria for choosing $G(j\omega)$. For reasons of economy of bandwidth, it is desirable to choose from among all $G(j\omega)$ yielding feasible $L(j\omega)$ that $G(j\omega)$ having the smallest high frequency gain. This is referred to as the "loop shaping" portion of the QFT design process.

II.2 Optimal and Sub-Optimal Loop Shaping

Horowitz has shown[3] that the ideal optimal (minimum bandwidth) $L(j\omega)$, denoted $L^*(j\omega)$, satisfies the following necessary condition:

(NC.1) $L^*(j\omega)$ lies *on* the boundary $B(\omega)\ \forall\ \omega \in [0,\infty)$

Furthermore, $L^*(j\omega)$ is unique. However, there exists no computational means for finding it or, more practically speaking, no constructive means for approximating it closely.

This yet unsolved problem may be described more specifically as follows. The QFT existence and uniqueness theories[3] state that given $B(\omega)\ \forall\ \omega \in [0,\infty)$, there exists one and only one $L(j\omega)$ lying *on* $B(\omega)\ \forall\ \omega \in [0,\infty)$, and an $L(j\omega)$ having such property is the unique optimal $L^*(j\omega)$. In other words, knowledge of $B(\omega)\ \forall\ \omega \in [0,\infty)$ *completely determines* $L^*(j\omega)$, and no additional design freedom exists.

In the practical computational case this is not so. One may compute the bounds $B(\omega)$ only at a discrete number of frequencies $\omega \in \{\omega_1,...,\omega_{nf}\}$ and, in this case, the uniqueness property is lost; i.e., an $L(j\omega)$ function lying on the boundaries $B(\omega)$, $\omega \in \{\omega_1,...,\omega_{nf}\}$ is *not* unique. An additional design degree of freedom, the *location* of $L(j\omega_i)$ on $B(\omega_i)$, exists at each frequency ω_i.

By specifying $B(\omega)$ only at the discrete set of frequencies $\omega \in \{\omega_1,...,\omega_{nf}\}$ we have perforce accepted that our design will be sub-optimal. However, by exploiting these additional design degrees of freedom (which have heretofore not been considered explicitly), we hope to develop a means for obtaining the "best" sub-optimal controller for a given set of design frequencies $\{\omega_1,...,\omega_{nf}\}$.

II.3 Review of Existing Research:

Software has been developed by Yaniv[8] for computing loop transmission bounds $B(\omega)$ and for carrying out final stages of the QFT design process. This package has come into wide usage within the QFT community, particularly at AFWAL/FIGL, where the software has been applied in numerous practical problems. However, as mentioned, use of the software requires that the designer carry out the loop shaping portion of the process by hand, off line. This requirement places such a burden upon the designer that many MIMO design problems are rendered computationally intractable. Even for single loop (SISO) designs, the computational effort required on the part of the designer, coupled

with the lack of a definitive loop shaping algorithm, can make the method unattractive and even impractical.

Designers are generally unable to cope with the question of bandwidth minimization within the context of the loop shaping problem. Many candidate loop shaping designs which are deemed "acceptable" (largely on the basis of computational tradeoffs) may fall well short of the optimal, minimum bandwidth system. Designers generally can only satisfy the necessary condition (NC.1) at the design frequencies $\{\omega_1, \ldots, \omega_{nf}\}$ and the additional design freedom available is either ignored entirely or, at best, used implicitly through rules of thumb. A practical methodology for iterative refinement of the design to achieve further bandwidth reduction has not been demonstrated.

A non-interactive computer program for SISO QFT design was developed by Horowitz and Rosenbaum[10](1975). Although the program incorporated an early form of loop shaping, the algorithm used was based only upon the satisfaction of the necessary condition (NC.1) at a discrete number of frequencies and, as in the case of hand calculation, bandwidth minimization could not be explicitly considered. Due to the high computational demand of the program and due to its non-interactive nature (which did not allow for tradeoff analyses by the designer), further research in this direction was, at the time, deemed unjustified.

More recently, Gera and Horowitz[11](1980) presented an alternative method for obtaining the optimal $L^*(j\omega)$ using equations involving Bode integrals[12]. It is believed that these equations, suitably modified, may form the basis of a candidate loop shaping algorithm. With recent advances in computer graphics and with increased computing power available to facilitate interactive programming, study of the method of [11], as well as study of other candidate loop shaping algorithms[13] is now of great practical importance.

III. Accomplishments of the Summer Research Program:

The two primary objectives of the summer research program were to study the structure and usage of existing QFT design software and to carry out discussions on specific aspects of the QFT loop shaping problem with Prof. I. Horowitz who was on site

as a consultant to AFWAL/FIGL. Additional technical discussions were held with Prof. C. Houpis, Dept. of Electrical Engineering, Air Force Institute of Technology, who was also on site as a co-supervisor of the summer research program.

III.1 Enhancement of Existing QFT Software:

Development and enhancement of existing QFT design software was undertaken with both short and long-term benefits in mind. Study and improvement of the existing QFT design package furnished by Yaniv[8] provided immediate benefit to FIGL researchers and AFIT MS students who found the improved documentation and expanded technical information obtained through this effort to be of great value. It is also anticipated that this improved documentation will be of further benefit as it will be used in a QFT workshop at the 1989 NAECON Conference.

Detailed study of this software package is also of great long-term value inasmuch as many of its central features will form the basis of an expanded package for QFT design, one which will eventually incorporate one or more of the candidate loop shaping procedures to be developed.

III.2 Development of Transfer Function Approximation:

In addition to the study of the existing QFT design software, effort was directed toward the further development of a program for least-squares approximation of transfer functions (TRANFIT[14]) based upon an algorithm developed initially by Levy[15]. An attempt was made to redevelop the algorithm, originally intended for continuous-time magnitude and phase data (assuming $s = j\omega$), to adapt the program to accept data for discrete time systems ($z = e^{j\omega T}$). This effort is still on-going, and the results should be of immediate benefit in a number of QFT applications involving design for discrete data systems[16].

Development of such a rational function approximation algorithm is also expected to be of further, long-range benefit since such an algorithm is an essential component of the candidate loop shaping method based upon[11].

III.3 Technical Discussions with Prof. I. Horowitz:

Based upon discussions held with Prof. Horowitz over the course of the research period, it was agreed upon that the development of a loop shaping algorithm was a realizable goal and, if suitably implemented in an interactive computing environment, that it would represent a valuable contribution, increasing the overall utility of the QFT method.

The method of Gera and Horowitz[11], as well as a nonlinear programming approach suggested by Polak et al.[13] were discussed as excellent candidates for a comparative study, the goal of such an effort being to determine their viability as potential loop shaping algorithms. The most prominent criteria suggested for evaluating these candidate methods were ease of implementation, computational effort required, and the relative adaptability of each method to tradeoff analyses.

A typical tradeoff analysis in the loop shaping portion of a QFT design problem would involve the assessment of the relative merits of bandwidth reduction (achieved by additional design iterations) versus the relative cost of computational overhead and increased controller complexity. It was felt that the ability to make these considerations during the course of a design was of the utmost practical importance, and the development of an automated design methodology capable of allowing the engineer to do so represented the greatest potential contribution in this area of QFT research.

IV. Recommendations:

The potential value of a loop shaping algorithm that may be incorporated into a CAD package for QFT design has been enunciated, and the desirable features of such a package have been outlined. The research directions to be followed in order to realize these goals will now be discussed.

IV.1 Software Development:

Interactive software must be developed which incorporates all aspects of the QFT design formulation and which allows for the implementation of various candidate loop shaping algorithms. In addition to interactive graphical displays of the pertinent QFT

design data, additional analysis tools must be developed in order to assess the relative effectiveness and desirability of various loop shaping methods.

IV.2 Analytical Development:

Additional theoretical work must be undertaken, not only to adapt the theoretical developments of Gera and Horowitz[11] and of Polak et al.[13] to implementable loop shaping algorithms, but also to develop the analytical tools needed in order to assess the relative merits of each. Such issues have not yet been developed in this context.

In particular, the method of [13] is used for solving nonlinear programming problems similar, but not identical to those obtained by the QFT formulation. A number of subtle mathematical issues must be resolved in order to adapt this methodology to the QFT problem.

It is felt that the resolution of these questions and the ultimate development of a suitable loop shaping algorithm would represent a significant achievement and would be a great enhancement to the QFT design method.

References

[1] Horowitz, I.M., *Synthesis of Feedback Systems*. New York: Academic (1963).

[2] Horowitz, I.M., and M. Sidi, "Synthesis of Feedback Systems with Large Plant Ignorance for Prescribed Time Domain Tolerances," Int. J. Control, V. 16, No. 2 (1972).

[3] Horowitz, I.M., "Optimum Loop Transfer Function in Single Loop Minimum Phase Feedback Systems," Int. J. Control, V. 18, No. 1 (1973).

[4] Horowitz, I.M., and M. Sidi, "Optimum Synthesis of Non-minimum Phase Feedback Systems with Plant Uncertainty," Int. J. Control, V. 27, No. 3 (1978).

[5] Doyle, J.C., and G. Stein, "Multivariable Feedback Design: Concepts for a Classical/Modern Synthesis," IEEE Trans. Auto. Control, V. AC-26, No. 1 (1981).

[6] Kwakernaak, H., and R. Sivan, *Linear Optimal Control Systems*. New York: Wiley-Interscience (1972).

[7] Francis, B.A., and J.C. Doyle, "Linear Control Theory with an H^{∞} Optimality Criterion," SIAM J. Control and Optimization, V. 25, No. 4 (1987).

[8] Yaniv, O., computer program for QFT design, Dept. of Electrical Engineering, Tel-Aviv University, Israel.

[9] Houpis, C., "Quantitative Feedback Theory (QFT)-Technique for Designing Multivariable Control Systems," AFWAL-TR-863107, Air Force Wright Aeronautical Labs, Wright-Patterson AFB, OH (1987).

[10] "Computer Automation for Feedback System Design," Semi-annual Report, NASA-CR-146638, NASA Langley Research Center, Hampton, VA (1975).

[11] Gera, A., and I. Horowitz, "Optimization of the Loop Transmission Function," Int. J. Control, V. 31, No. 2 (1980).

[12] Bode, H.W., *Network Analysis and Feedback Amplifier Design*. New York: Van Nostrand (1945).

[13] Polak, E., D.Q. Mayne, and D.M. Stimler, "Control System Design via Semi-Infinite Optimization: A Review," Proc. IEEE, V. 72, No. 12 (1984).

[14] Lisowski, R., Capt., TRANFIT.FOR program, U.S. Air Force Academy.

[15] Levy, E.C., "Complex Curve Fitting," IRE Trans. Auto. Control, May (1959).

[16] Neumann, K., MS Thesis, Dept. of Electrical Engineering, Air Force Institute of Technology, Wright-Patterson AFB, OH (to appear).

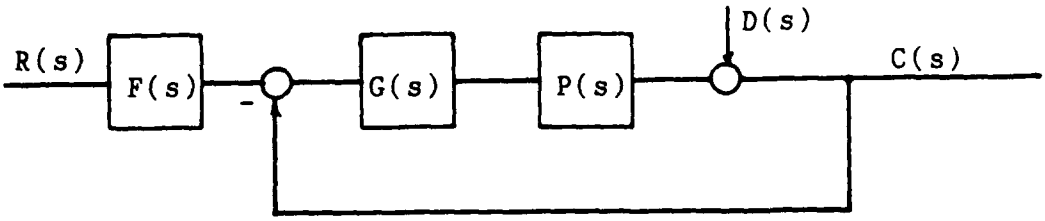

$$L(s) = P(s)G(s) \qquad T(s) = F(s)\,\frac{L(s)}{1 + L(s)}$$

Fig. 1

Assumed QFT Feedback Configuration

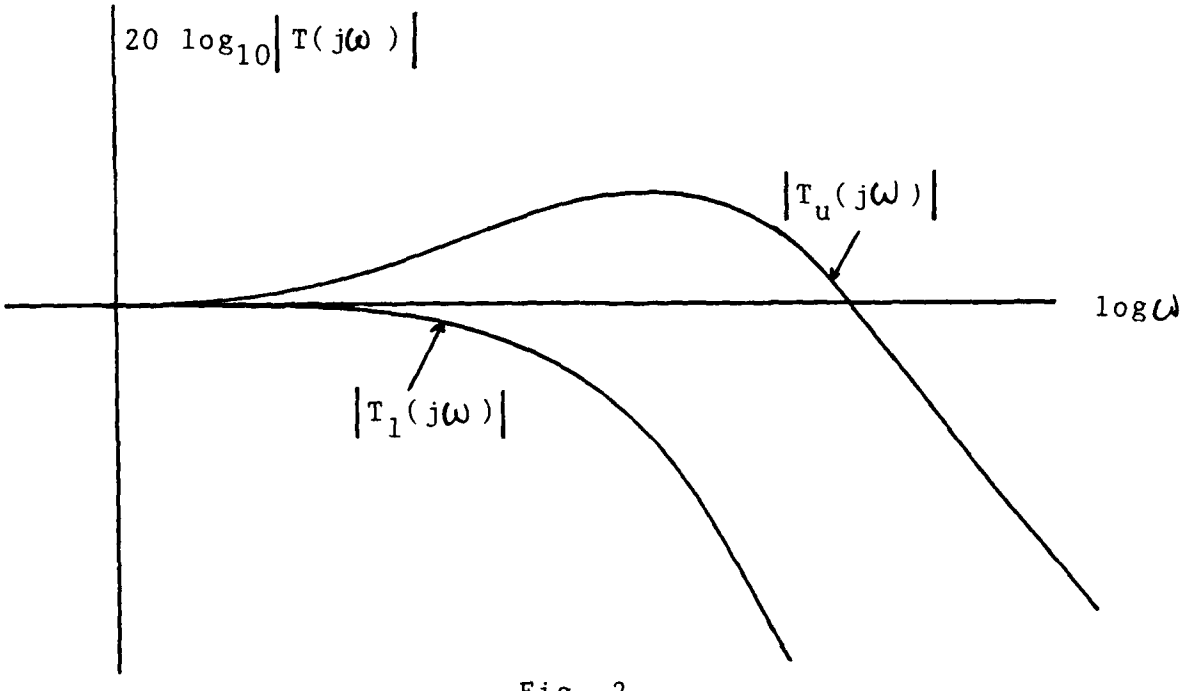

Fig. 2

Upper and Lower Bounds on Closed Loop Transfer Function

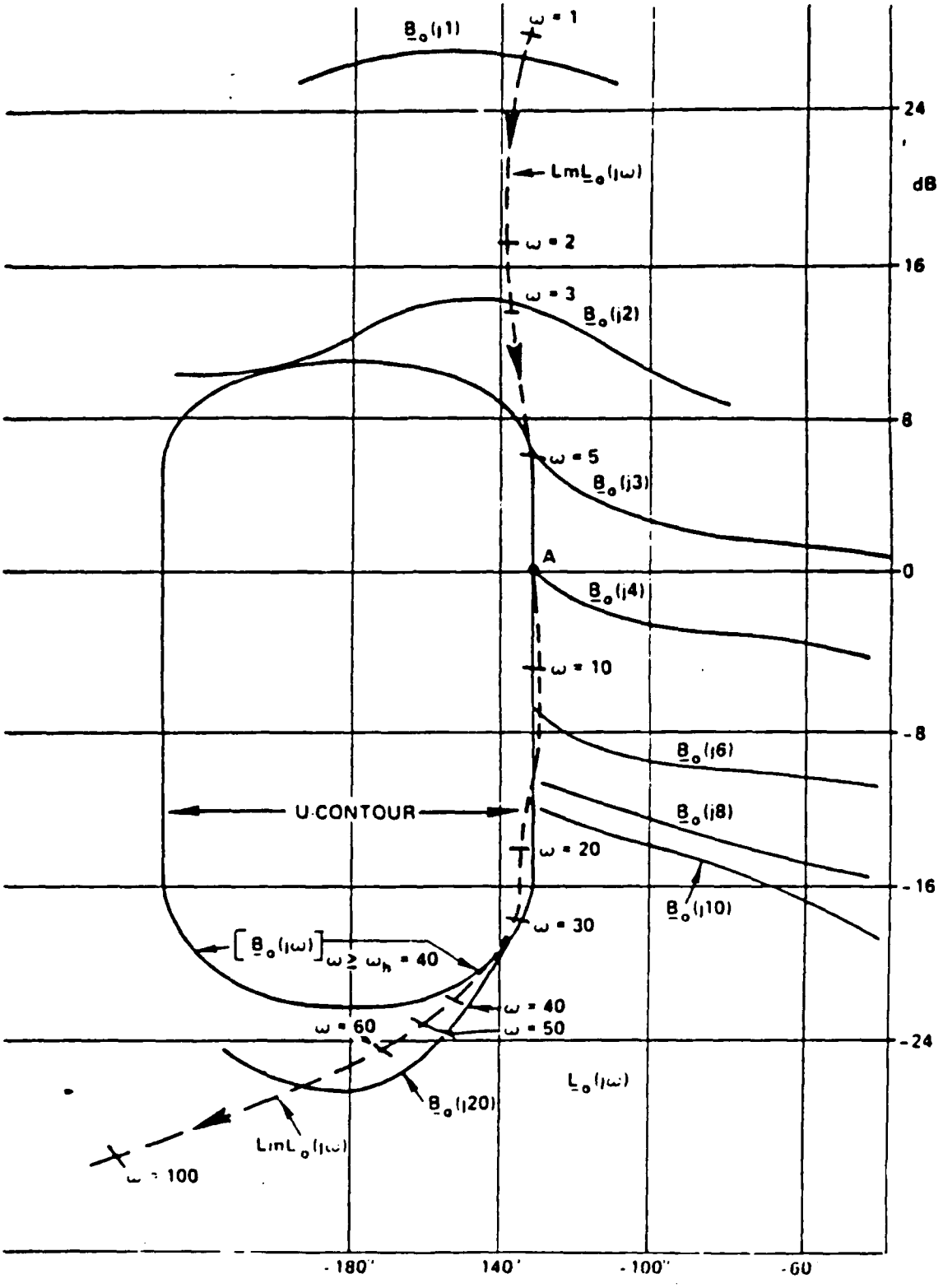

Fig. 3

Illustration of design bounds and loop transmission function for example design problem [9].

1988 USAF-UES FACULTY RESEARCH PROGRAM/

GRADUATE STUDENT RESEARCH PROGRAM

Sponsored by the

AIR FORCE OFFICE OF SCIENTIFIC RESEARCH

Conducted by the

Universal Energy Systems, Inc.

FINAL REPORT

PHOTOREFLECTANCE AS A CHARACTERIZATION TOOL FOR GALLIUM ARSINIDE AND ALUMINUM GALLIUM ARSINIDE MATERIALS

Prepared by:	James E. Angelo
Academic Rank:	B.S.
Department and	Physics Dept.
University:	Univ. of Mn. Duluth
Research Location:	AFWAL/MLPO
	Wright-Patterson AFB
	Dayton Ohio 45433
USAF Researcher:	William Mitchel
Date:	26 Aug 88
Contract No:	F49620-88-C-0053

PHOTOREFLECTANCE AS A CHARACTERIZATION TOOL FOR GALLIUM ARSINIDE AND ALUMINUM GALLIUM ARSINIDE MATERIALS

by

James E. Angelo

ABSTRACT

Modulation Spectroscopy[1,2] and Electroreflectance (ER) in particular have been used extensively to characterize semiconducting materials. Photoreflectance (PR), a contactless form of ER, is being realized as a method of characterizing semiconductors nondestructively. This paper shows that PR allows for quick determination of the band gap energy, and doping level in Gallium Arsinide (GaAs). It also allows for the determination of alloy composition of GaAs/Aluminum Gallium Arsinide ($Al_xGa_{1-x}As$) quantum wells.

ACKNOWLEDGEMENTS

I wish to thank the Air Force Systems Command and the Air Force Office of Scientific Research for sponsorship of this research. I would also like to thank the Materials Laboratory for allowing me to use their facilities for my research. Universal Energy Systems also deserves mention for their help with the administrative aspects of the program.

Many people helped to make my summer a rewarding experience, these include Lt. Kevin Schoen, Ron Perrin, Dr. P.M. Hemenger, and Dr. W. Mitchel. I would like to thank Dr. D. Gaskill and Dr. W. Theis for their help with the theoretical background of this report. I would especially like to thank Dr. Mike Sydor who provided me with a wealth of knowledge and experience.

I. INTRODUCTION:

GaAs has been an important semiconductor for use in many high technology devices. Recently there has been a desire to grow alternating layers of GaAs and AlGaAs to produce quantum well structures. These structures have the potential for being used in infrared (IR) detectors.

The Materials Laboratory of the Air Force Wright Aeronautical Laboratory at Wright-Patterson Air Force Base is particulariy interested in characterizing both GaAs and GaAs/AlGaAs structures grown by Molecular Beam Epitaxy (MBE). There is a need to improve the samples grown, and to be able reproduce the high quality samples.

My research interests are in the area of the growth and characterization of various semiconducting structures. By working with the Materials Laboratory, I have gained a knowledge of how to characterize GaAs and AlGaAs samples using PR.

II. OBJECTIVES OF THE RESEARCH EFFORT:

Currently, the samples grown by the MBE group are characterized by Hall measurements, which determine the doping levels, and Photoluminescence (PL), which determines the band gap energy. Another method of characterizing the samples is desired since both methods require cryogenic temperatures, which is cumbersome. The Hall measurements also require the anodization of leads to the sample, thus destroying it.

My assignment as a participant in the 1988 Graduate Student Research Program (GSRP) was to assist Professor Mike Sydor in the construction of a PR station. Once completed, various samples, grown by the MBE group, were studied. I then analyzed the data, on a Vax microcomputer, to see if PR could be used as a characterization tool.

III.

a. The PR signals for the samples can be classified into two categories according to the magnitude of the surface electric field, E_S. The first is the high field region where the surface field is large. This is usually the case for doped samples. The second is called the low field region. This is usually the case for undoped samples. Aspnes[3] showed that the PR signal is in the low field limit when:

$$\hbar\Omega < \Gamma/3 \tag{1}$$

$\hbar\Omega$ is a characteristic energy associated with the critical point. It is related to E_S by:

$$\hbar\Omega=(e^2E_S^2\hbar^2/8\mu)^{1/3} \tag{2}$$

Where μ is the interband reduced mass. Γ is a broadening parameter for the critical point energy, E_{cp}. Aspnes[3] derived a quick rule of thumb, that if the PR signal is such that:

$$\Delta R/R<10^{-4} \tag{3}$$

then the signal is in the low field limit.

b. In the low field region the line shape is given by[3]:

$$\Delta R/R=Re\{Ce^{i\theta}(\hbar\omega-E_{cp}+i\Gamma)^{-n}\} \tag{4}$$

Where $\hbar\omega$ is the energy of the probe beam, C and θ are an amplitude and phase factor that vary slowly with $\hbar\omega$. n refers to the type of critical point in question. n=2, 2.5, 3 for an exciton, a three dimensional band to band, and a two dimensional band to band transition respectively.

An undoped GaAs signal is shown in figure 1. The structure is broad and the signal is small so that the low field limit is applicable. The curve was fitted using an excitonic transition of the third derivative form (TDF) given by Eqn(1). The fit was good as can be seen by the smoothed curve of fig. 1.The fit showed an excitonic structure at 1.415 eV. It is believed that the signal also includes a band to band structure, which is masked by the excitonic transition.

A highly In and Si doped GaAs bulk PR line shape is shown in fig. 2. It has been argued[4] that extremely highly doped samples exhibit a flat band condition, and can thus be fitted using TDF. The curve was fitted using a sum of an exciton and a three dimensional band to band transition of the TDF. Again the fit was good as can be seen from the smoothed curve of fig. 2. The fit gives the value of the band gap energy at 1.421 eV. This agrees well with the value determined from other optical methods.

c. In the high field limit, the PR signal is proportional to the product of airy functions and their derivatives. These take the asymptotic form[5]:

$$\Delta R/R \cong \cos\{(2/3)[(\hbar\omega - E_{cp})/\hbar\Omega]^{3/2} + \pi(d-1)/4\} \qquad (5)$$

Where d is the dimensionality of the critical point. For GaAs, with a direct transition, d=3. This line shape has an oscillatory nature, where the oscillations are termed Franz-Keldysh Oscillations (FKO). Fig. 3 shows the PR trace for a moderately Si doped GaAs sample. The extrema for the FKO are given by[6]:

$$[\hbar\omega]_j=\hbar\Omega(F_j)+E_g \qquad j=0,1,2,... \tag{6A}$$

$$F_j=[3\pi(j+1/2)/2]^{2/3} \tag{6B}$$

As indicated by Eqn(6), a plot of $[\hbar\omega]_j$ vs F_j is a straight line with slope $\hbar\Omega$, and intercept E_g, the band gap energy. This plot, shown in fig. 4, uses the FKO extrema marked 1,2,3 in fig. 2. It gives a band gap energy of E_g= 1.420 eV. This again agrees well with the value determined by other optical techniques. Now $\hbar\Omega$ is related to E_s by Eqn(1). By assuming a reduced mass[6] $\mu=.057m_e$ the surface electric field can be determined.

Bottka et al[7] have shown that the field so determined is related to the carrier concentration, N, and the built-in potential, V_b, by the generalized Schottky equation:

$$E_s=[2eN(V_b-V_p-kT/e)/\kappa\varepsilon]^{1/2} \tag{7}$$

V_p is the quasi-equilibrium photovoltage of the laser, kT/e is a thermal term, and $\kappa\varepsilon$ is the dielectric constant times the permitivity of free space. Because of pinning at the surface V_b=.73 volts[8] and κ=13.18 for GaAs[7]. V_p was determined from Eqn(7) using calibrated samples where N was known.

Using the calibrated samples a curve of (E_2-E_1), where E_2 and E_1 refer to the energies of the second and first FKO respectively, vs N was plotted. This curve is shown in fig. 5. The samples grown by the MBE group are also shown on the graph. They fall reasonably well along the curve. For comparison, some of the Hall and PR values, determined by the FKO, of carrier concentrations are listed in Table 1.

d. PR can also be used to determine the alloy composition in GaAs/$Al_xGa_{1-x}As$ quantum wells. The energy position of the $Al_xGa_{1-x}As$ line shape structure is related to the mole fraction, x, of aluminum by[9]:

$$E(x)=1.424+1.247x \qquad (8)$$

A PR trace for a GaAs/$Al_xGa_{1-x}As$ structure grown by the MBE group is shown in fig. 6. From the energy position, E(x)=1.733 eV, the mole fraction was determined to be x=.25. This is in good agreement with the value, x=.21, determined by Reflection High Energy Electron Diffraction (RHEED).

IV. RECOMMENDATIONS:

a. PR has been shown to be a viable method for quick characterization of samples. It can be used to help improve the quality of the samples grown by the MBE group.

b. The possibility of using PR in situ, in the MBE machine, should be considered. It has the possibility of allowing even better quality control of grown samples.

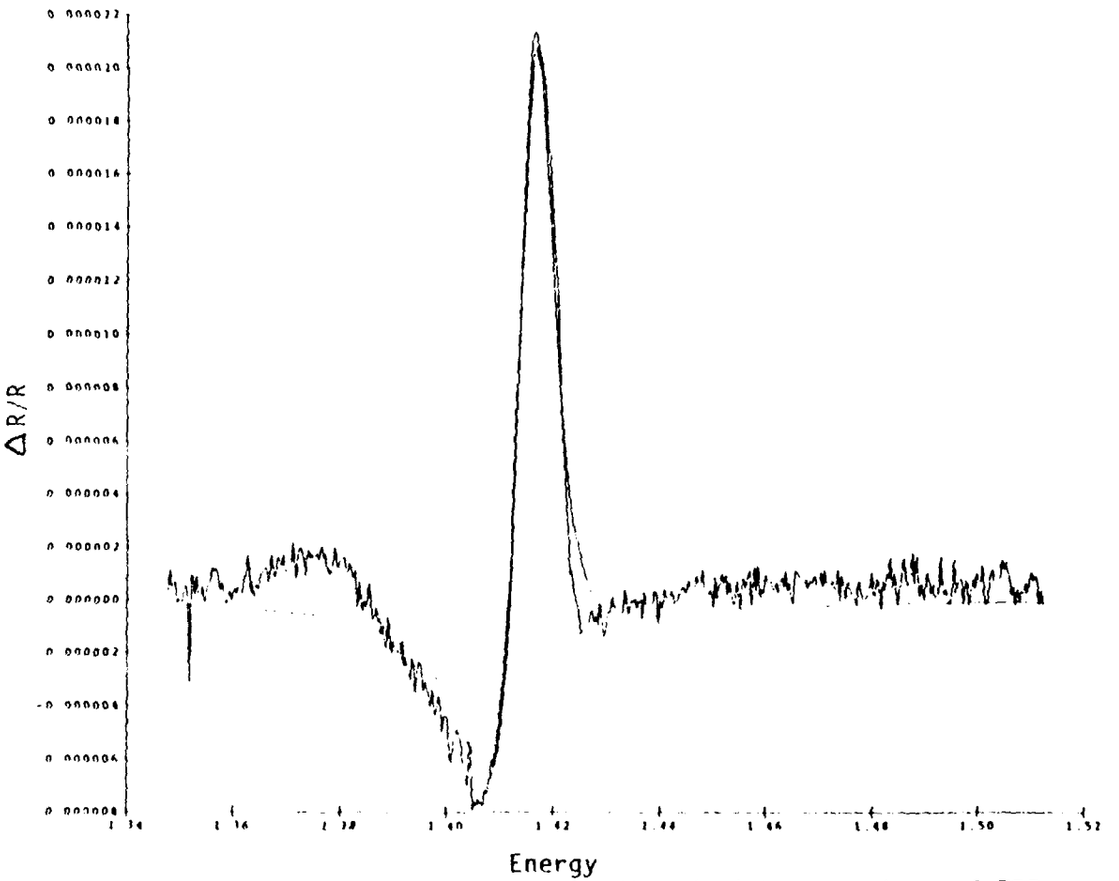

Figure 1: An undoped GaAs sample fitted with an exciton of TDF.

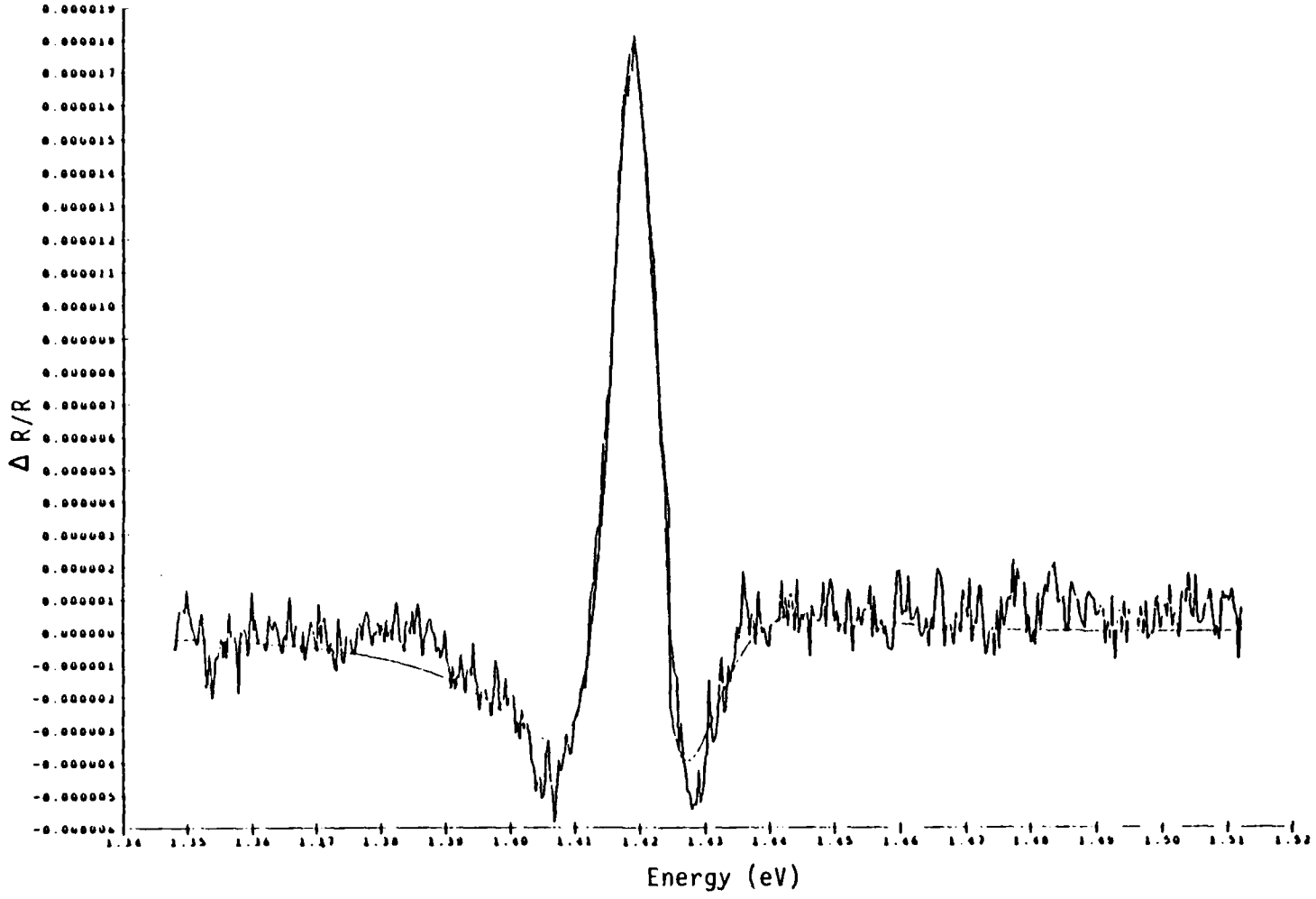

Figure 2: A heavily In and Si doped GaAs sample fit with an exciton and three dimensional band to band transition of TDF.

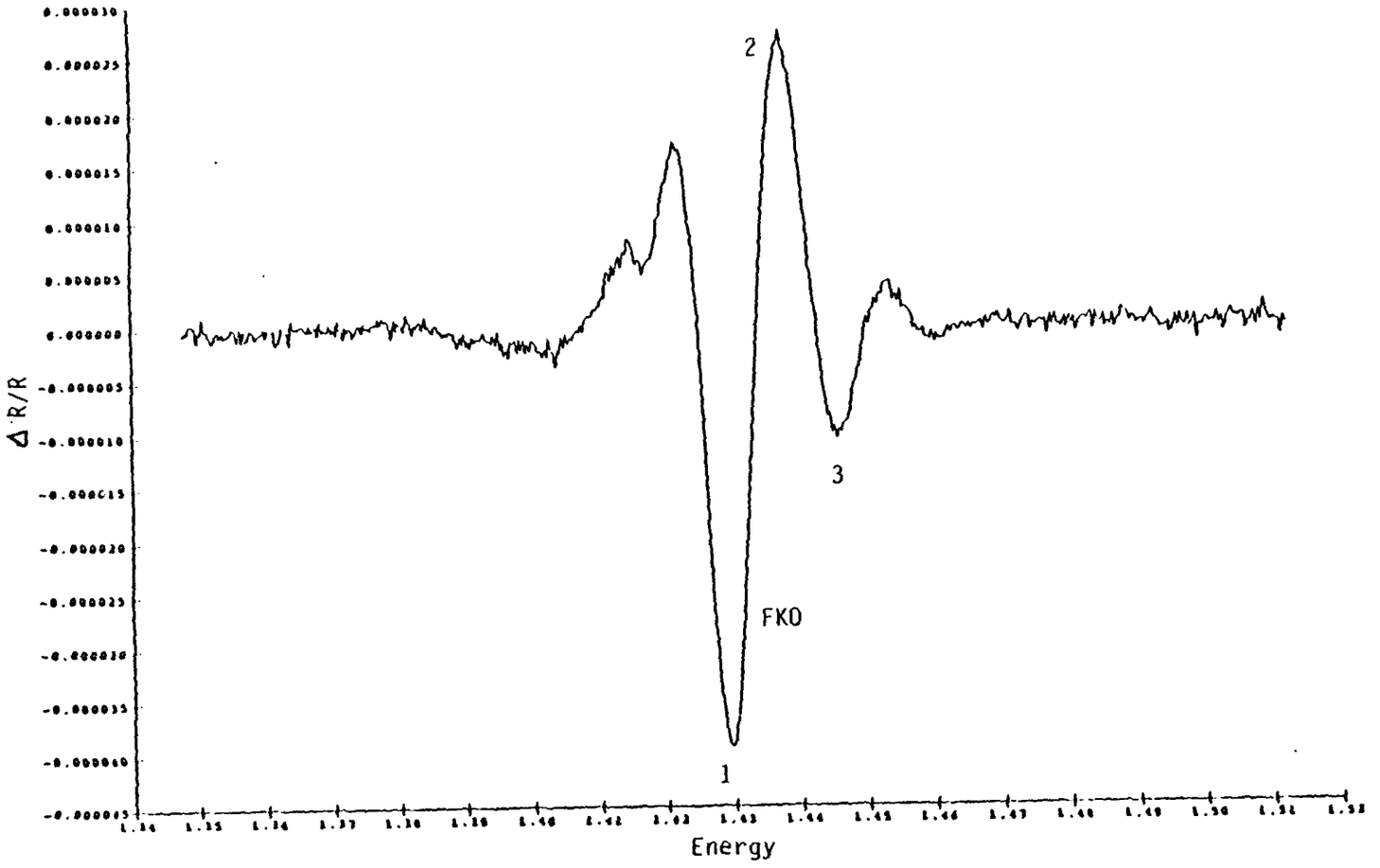

Figure 3: A moderately Si doped GaAs sample displaying FKO.

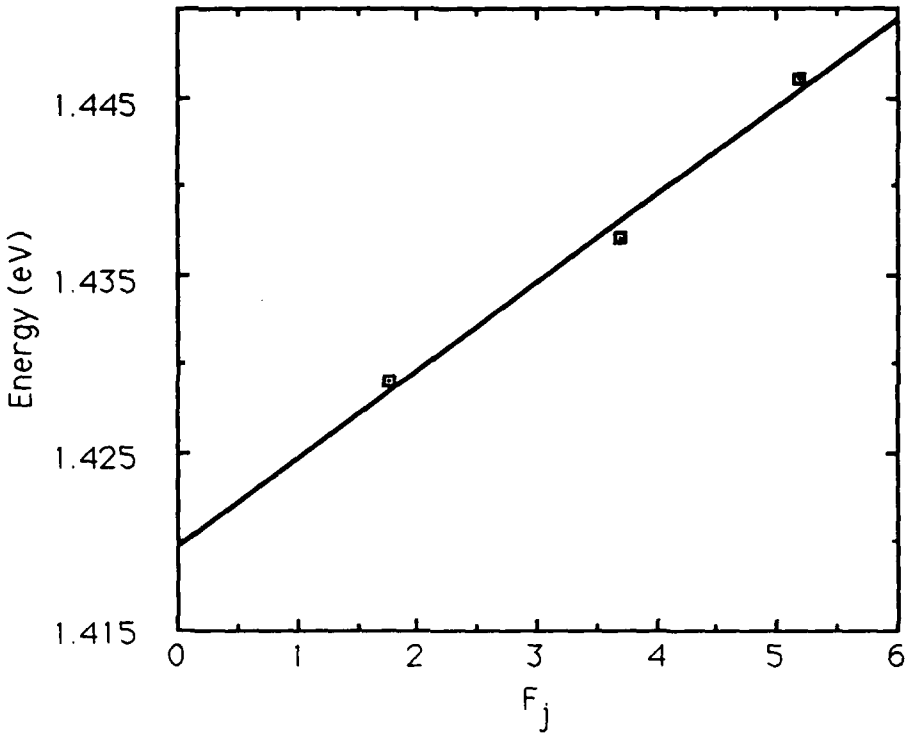

Fitted Line is: Energy=4.95e-3*F_j+1.42

Figure 4: A plot of FKO energy vs F_j

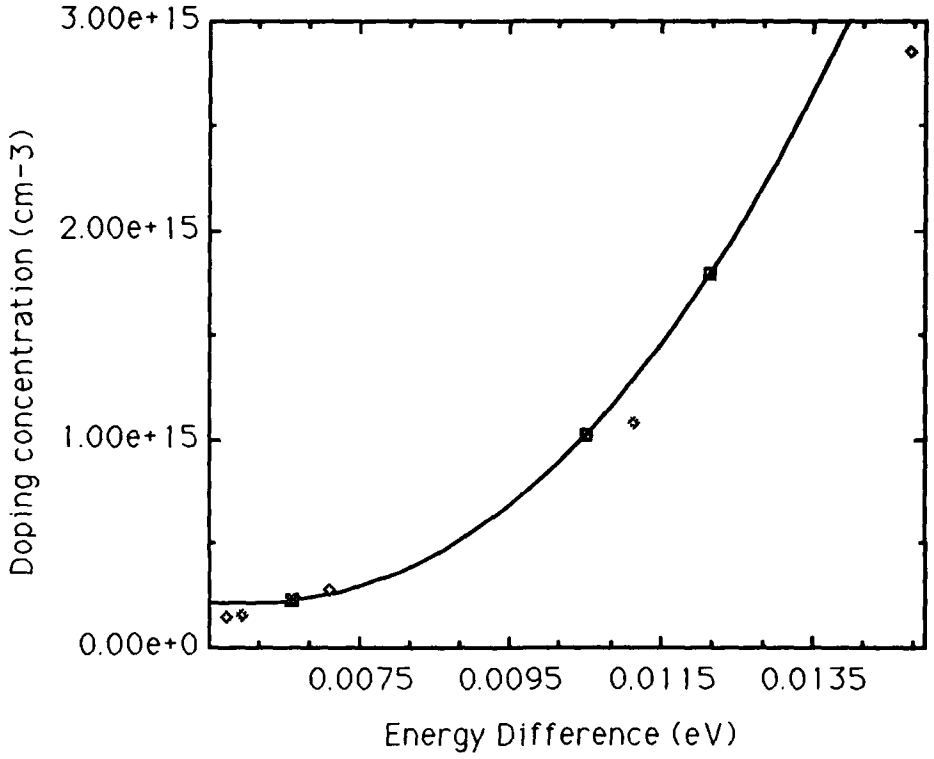

Fitted Line is: N=1.17e15-2.79e17*(E2-E1)+ 1.21e19 *(E2-E1)**2+1.23e21*(E2-E1)**3

Figure 5. Doping Concentration vs Energy Difference in FKO Extrema

Sample	Hall Value	PR Value
Yen12	2.1×10^{14}	1.5×10^{14}
Yen13	1.5×10^{14}	2.7×10^{14}
Yen14	2.1×10^{14}	1.6×10^{14}
Yen16	4.2×10^{14}	2.2×10^{14}
Mo5-128	1.8×10^{15}	1.8×10^{15}

Table 1: A comparison of Hall and PR determined values of carrier concentration for selected samples

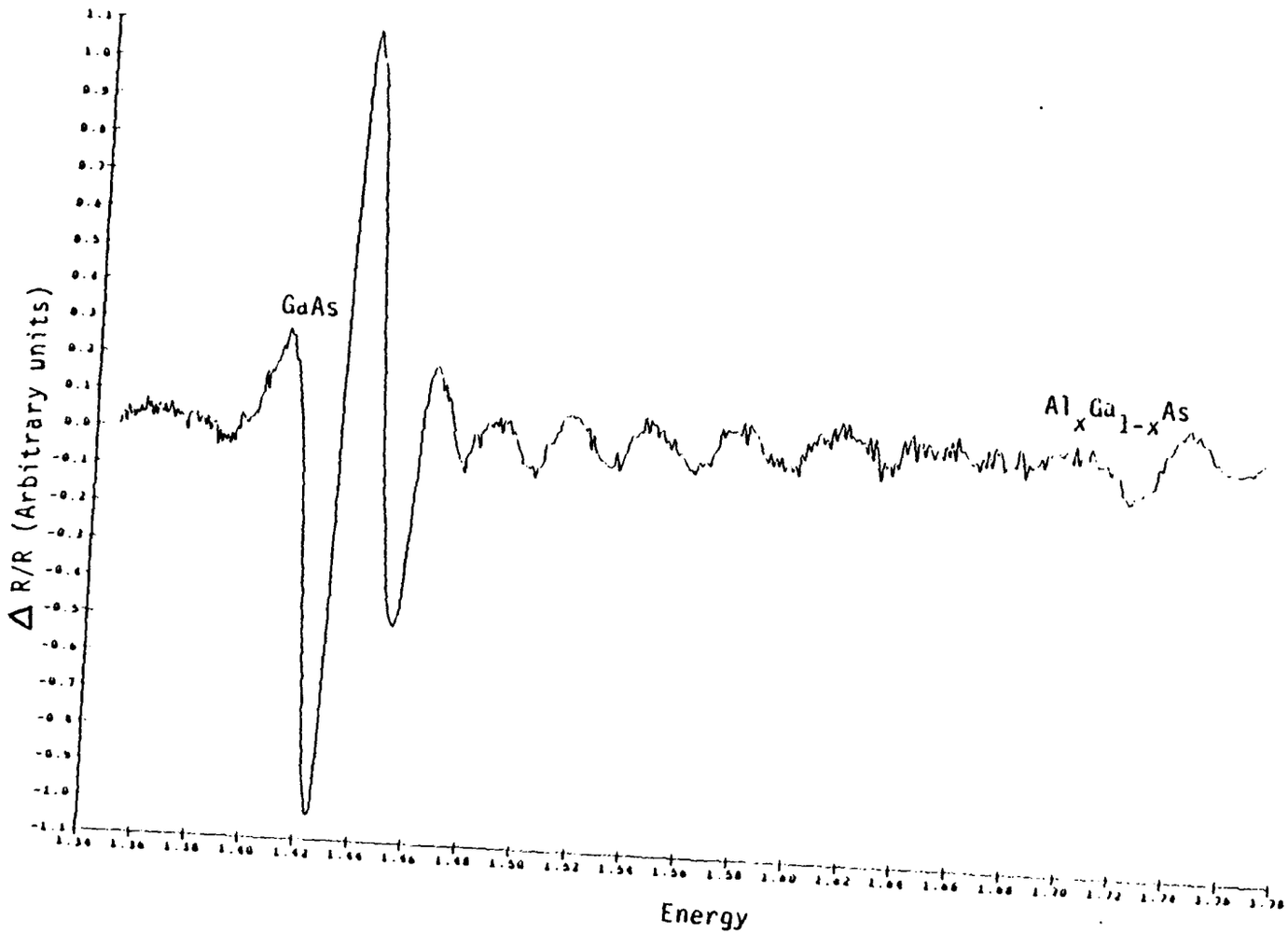

Figure 6: A GaAs/$Al_xGa_{1-x}As$ quantum well structure with x=.25

REFERENCES

1. Cardona, M. in Modulation Spectroscopy, New York, N.Y., Academic Press, 1969.

2. Semiconductors and Semimetals Vol. 9, edited by R.L. Willardson and A.C. Beer, New York, N.Y., Academic Press, 1972.

3. Aspnes, D.E. Surf. Science 37 (1973),p.418.

4. Peters, L. L. Phaneuf, L.W. Kapitan, and W.M. Theis. J. Appl. Phys. 62(11) (1987), p.4558.

5. Aspnes, D.E., and A.A. Studina. Phys. Rev. B7 (1973), p.4605.

6. Bottka, N., D.K. Gaskill, R.J.M. Griffiths, R.R. Bradley, T.B. Joyce, C. Ito, and D. McIntyre. To be published in J. of Crystal Growth.

7. Bottka, N., D.K. Gaskill, R.S. Sillmon, R. Henry, R. Glosser. J. Electron. Materials 17 (1988), p.161.

8. Spicer, W.E., I. Lindau, P. Skeath, C.Y. Su, and R. Glosser. J. Elect. Mat. 17 (1988), p.420.

9. Casey, J.R., and M.B. Panish in Heterostructure Lasers, Part B: Fundamental Principles, New York, N.Y., Academic Press, 1978.

1988 USAF-UES SUMMER FACULTY RESEARCH PROGRAM/

GRADUATE STUDENT RESEARCH PROGRAM

Sponsored by the

AIR FORCE OFFICE OF SCIENTIFIC RESEARCH

Conducted by

Universal Energy Systems, Inc.

FINAL REPORT

ANALYTICAL AND NUMERICAL SOLUTIONS OF THE NONLINEAR DIFFUSION EQUATION

Prepared by:	Darwin L. Boyd
Academic Rank:	Graduate Student
Department and University:	Physics Department Kent State University
Research Location:	AFWAL/MLPO WPAFB Dayton OH 45433
USAF Researcher:	Dr. Patrick M. Hemenger
Date:	August 09, 1988
Contract No.:	F49620-88-0053

ANALYTICAL AND NUMERICAL SOLUTIONS OF THE NON-LINEAR DIFFUSION EQUATION

by

Darwin L. Boyd

ABSTRACT

Using an approximate analytical solution, zeroth and first order correction terms of dopant concentration profiles were calculated for several special cases of concentration dependence of diffusivity. The three cases of the dependence studied were $D=D_vC^v$, $D=D_e\exp(kC)$, and $D=D_o\sinh^2(kC)$. These were compared with numerical results obtained from a forward time centered space (FTCS) differencing of the nonlinear diffusion equation. Close agreement was obtained for some cases indicating that the analytical approach may be an attractive alternative to the central proccessing unit intensive numerical integration of the dopant diffusion equation.

ACKNOWLEDGEMENTS

I would like to thank the Air Force Systems Command, Air Force Office of Scientific Research, and the Air Force Wright Aeronautical Laboratories / Materials Laboratory where I worked for sponsorship of this research. I would also like to thank Universal Energy Systems for a well run and administered program.

Thanks to Dr. David Uhrich my advisor and the Physics Department of Kent State Univeristy for allowing me the time to complete this work. A special thanks to everyone at the materials laboratory who help me, Dr. Patrick Hemenger for helping in many ways and always making sure I had what I needed, Ron Perrin for all his assistance and expertise with the computers, Kevin Rose for helping me transfer my files to the Macintosh, Tom Kensky for helping me with the Macintosh, and Captain Greg Peisert for help with the Macintosh and for his class on Microsoft Word. Finally a very special thanks to Dr. David Moroi for his help, guidance, and patience throughout this work and for the many times we went fishing together.

I. INTRODUCTION:

Nonlinear diffusion processes play important roles in many areas of engineering and physics. In particular the dopant profile during annealing of ion-implanted semiconductors may display "concentration-enhanced" diffusivity.[1] An understanding of this process is necessary in order to control electrical properties of these ion-implanted semiconductor materials.

The materials laboratory of the Air Force Wright Aeronautical Laboratories at Wright Patterson Air Force Base has studied ion-implanted semiconductors in order to optimize characteristics for infra-red detectors.

My background in solid state physics as well as experience with computers and programming proficiency contributed to my assignment to this project.

II. OBJECTIVES OF THE RESEARCH EFFORT

Direct numerical integration of the nonlinear diffusion equation while simple and straightforward has several drawbacks. Among them the major one being the large amounts of computer time required to obtain the final dopant profiles. An analytical solution could be physically transparent and many times more efficient in calculating profiles.

Recently Moroi and Hemenger[2] have developed such an analytical solution. My assignment as a participant in the 1988 Summer Graduate Student Research Program entailed obtaining dopant profiles from the anlaytical solution and comparing them with profiles obtained from numerical integration of the nonlinear diffusion equation. This work is a continuation and elaboration of the work of Bucey.[3]

An additional objective added during my work was the numerical evaluation of the integral of the Greens function.[4]

III. NUMERICAL INTEGRATION OF NONLINEAR DIFFUSION EQUATION

The one dimensional nonlinear diffusion equation is

$$\frac{\partial C}{\partial t} = \frac{\partial}{\partial z}\left(D \frac{\partial C}{\partial z}\right) \qquad z, t \geq 0 \tag{1}$$

where $C(z,t)$ is the concentration at position z, time t, and $D[C(z,t)]$ is the diffusivity which may be an arbitrary function of the concentration.

Using the FTCS method[5,6] this may be differenced as

$$C(z,t+\Delta t) = C(z,t) + \frac{\Delta t}{2(\Delta z)^2}\{(D[C(z+\Delta z,t)]+D[C(z,t)])(C(z+\Delta z,t)-C(z,t))$$
$$-(D[C(z-\Delta z,t)]+D[C(z,t)])(C(z,t)-C(z-\Delta z,t))\} \tag{2}$$

where Δt is the time step and Δz the space step. This equation allows us to obtain the concentration at a particular grid point with coordinates z and $t+\Delta t$ in terms of the concentration at adjacent grid points $z-\Delta z$, z, and $z+\Delta z$ at time t. Known initial and boundry conditions provide values necssary to start the calculation. The solution will be stable and non-oscillatory for boundry conditions that remain constant with time if[5]

$$D[C(z,t)] \frac{(\Delta t)}{(\Delta x)^2} \leq \frac{1}{4} \tag{3}$$

In practice this was satisfied by choosing Δt such that

$$\Delta t = \frac{(\Delta x)^2}{4\, D_{max}} \tag{4}$$

where D_{max} was the maximum diffusivity. Boundry conditions are[2]

$$\left.\frac{\partial C(z,t)}{\partial z}\right|_{z=0} = 0 \tag{5}$$

$$C(\infty,t) = 0\,. \tag{6}$$

Equation (5) was attained by setting $C(-\Delta z,t) = C(\Delta z,t)$, in effect mirroring about z=0 [7], and Eq. (6) by continuing the calculation to sufficiently large values of z such that the concentration was less than some small value (typically 0.001 C_{max}).

The numerical calculations were computed with program NONLIN (see appendix). At first the initial dopant profile was chosen to be a truncated Gaussian.

$$C_0(z) = C_m \exp\left[-\frac{(z-z_0)^2}{2S_0^2}\right] \tag{7}$$

Later the program was slightly modified to read in an arbitrary initial dopant profile. Ghez, et al.[1] have found that the dopant profile of an ion-implanted silicon wafer is well represented by a truncated Gaussian.

Three different functional dependencies of the diffusivity on concentration were examined.

$$D = D_v C^v \tag{8}$$

$$D = D_e \exp(kC) \tag{9}$$

$$D = D_o \sinh^2(kC) \tag{10}$$

For the cases given by Eqs. (8) and (9) the initial dopant profile was the truncated Gaussian while for the case given by Eq. (10) it was a slightly modified form.

IV. ANALYTICAL SOLUTION

By introducing new variables defined by

$$\zeta = \zeta(z,t) = \int_0^z \varphi[C(z',t)]\, D^{-1}[C(z',t)]\, dz' \tag{11}$$

$$\tau = \tau(z,t) = \int_0^t \varphi^2[C(z,t')]\, D^{-1}[C(z,t')]\, dt' \tag{12}$$

$$\Gamma = \Gamma(\zeta,\tau) = \beta \int_0^{C(z,t)} \varphi(C')\, dC' \tag{13}$$

Moroi and Hemenger have been able to transform Eqs. (1) and (5)-(7) into

$$\frac{\partial \Gamma}{\partial \tau} - \frac{\partial^2 \Gamma}{\partial \zeta^2} = \varepsilon \tag{14}$$

$$\Gamma_0(\zeta) = \Gamma(\zeta,0) = \beta \int_0^{C_0(z)} \varphi(C')\, dC' \tag{15}$$

$$\left.\frac{\partial \Gamma}{\partial \tau}\right|_{\zeta=0} = 0 \tag{16}$$

$$\Gamma(\infty,\tau) = 0 \tag{17}$$

where β is a constant scaling factor and ε is given by

$$\varepsilon = \varepsilon(\zeta,\tau) = \frac{\partial \Gamma}{\partial \tau}\frac{D}{\varphi}\frac{\partial}{\partial z}\left[\frac{D}{\varphi}\frac{\partial \tau}{\partial z}\right] - \frac{\partial \Gamma}{\partial \zeta}\frac{D}{\varphi^2}\frac{\partial \zeta}{\partial t} + 2\frac{\partial^2 \Gamma}{\partial \tau \partial \zeta}\frac{D}{\varphi}\frac{\partial \tau}{\partial z} + \frac{\partial^2 \Gamma}{\partial \tau^2}\left[\frac{D}{\varphi}\frac{\partial \tau}{\partial z}\right]^2. \tag{18}$$

Two different functional forms of $\varphi(C)$ were considered.

$$\varphi = a\sqrt{D} \tag{19}$$

$$\varphi = \alpha D \tag{20}$$

By setting

$$\Gamma = \Gamma^{(0)} + \Gamma^{(1)} \tag{21}$$

they were able to use a standard perturbation method to get an approximate solution to Eq. (14).

In Eq. (21) $\Gamma^{(0)}$ and $\Gamma^{(1)}$ are the zeroth and first order terms in the perturbation and satisfy the following equations

$$\frac{\partial \Gamma^{(0)}}{\partial \tau} - \frac{\partial^2 \Gamma^{(0)}}{\partial \zeta^2} = 0 \tag{22}$$

$$\frac{\partial \Gamma^{(1)}}{\partial \tau} - \frac{\partial^2 \Gamma^{(1)}}{\partial \zeta^2} = \varepsilon^{(0)} \tag{23}$$

with the appropriate initial and boundry conditions. The $\varepsilon^{(0)}$ is given by

$$\varepsilon^{(0)}(\zeta,\tau) = \varepsilon(\zeta,\tau)\big|_{\Gamma \to \Gamma^{(0)}} . \tag{24}$$

The solution to Eq. (22) satisfying the initial and boundry conditions is

$$\Gamma^{(0)}(\zeta,\tau) = \frac{1}{\sqrt{4\pi\tau}} \int_0^\infty \left\{ \exp\left[- \frac{(\zeta-\zeta')^2}{4\tau} \right] + \exp\left[- \frac{(\zeta+\zeta')^2}{4\tau} \right] \right\} \Gamma_0(\zeta') d\zeta' \tag{25}$$

The solution to Eq. (23) satisfying the initial and boundry conditions is

$$\Gamma^{(1)}(\zeta,\tau) = \int_0^\tau \int_0^\infty G(\zeta,\tau \mid \zeta',\tau') \, \varepsilon^{(0)}(\zeta',\tau') \, d\zeta' d\tau' \tag{26}$$

where $G(\zeta,\tau \mid \zeta',\tau')$ is the Greens function and is given by

$$G(\zeta,\tau \mid \zeta',\tau') = \frac{1}{\sqrt{4\pi(\tau - \tau')}} \left\{ \exp\left[- \frac{(\zeta-\zeta')^2}{4(\tau-\tau')} \right] + \exp\left[- \frac{(\zeta+\zeta')^2}{4(\tau-\tau')} \right] \right\} . \tag{27}$$

The concentration in real space time is

$$C(z,t) = C^{(0)}(z,t) + C^{(1)}(z,t) \tag{28}$$

where $C^{(0)}$ and $C^{(1)}$ are determined by Eq. (13).

$$\Gamma^{(0)}(\zeta,\tau) = \beta \int_0^{C^{(0)}(z,t)} \varphi(C^{\prime})dC^{\prime} \tag{29}$$

and

$$\Gamma^{(1)}(\zeta,\tau) = \beta \int_{C^{(0)}(z,t)}^{C(z,t)} \varphi(C^{\prime})\, dC^{\prime} \approx \beta C^{(1)}(z,t)\, \varphi\left[C^{(0)}(z,t)\right] . \tag{30}$$

For the choice of $\varphi = \alpha D$ the special case for the functional form of the diffusivity studied was

$$D = D_v C^v . \tag{8}$$

For this case the initial dopant distribution in real space was a truncated Gaussian.

$$C_0(z) = C_m \exp\left[- \frac{(z-z_0)^2}{2S_0^2} \right] \tag{7}$$

Equations (11)-(13) and (18) become

$$\zeta = \alpha z \tag{31}$$

$$\tau(z,t) = \alpha^2 D_v \int_0^t C^v(z,t^{\prime})\, dt^{\prime} \tag{32}$$

$$\Gamma^{(0)}(\zeta,\tau) = \frac{\alpha\beta D_v}{v+1} C^{(0)(v+1)}(z,t) \tag{33}$$

$$\varepsilon^{(0)}(\zeta,\tau)=\frac{\partial\Gamma^{(0)}}{\partial\tau}\left\{\left[\frac{\Gamma^{(0)}(\zeta,\tau)}{\Gamma^{(0)}(\zeta,0)}\right]^{\left[\frac{\nu}{\nu+1}\right]}-1-\left(\frac{\nu}{\nu+1}\right)\left(\frac{2\nu+1}{\nu+1}\right)\Gamma^{(0)}\left(\frac{\nu}{\nu+1}\right)\int_0^{\tau}\frac{\left[\frac{\partial\Gamma^{(0)'}}{\partial\zeta}\right]^2 d\tau'}{\Gamma^{(0)}\left(\frac{\nu}{\nu+1}+2\right)}\right\}$$

$$+2\left[\frac{\partial^2\Gamma^{(0)}}{\partial\tau\partial\zeta}+\left(\frac{\nu}{\nu+1}\right)\frac{\partial\Gamma^{(0)}}{\partial\tau}\frac{\left(\frac{\partial\Gamma^{(0)}}{\partial\zeta}\right)}{\Gamma^{(0)}}\right]\frac{\partial\tau}{\partial\zeta}+\left[\frac{\partial^2\Gamma^{(0)}}{\partial\tau^2}+\left(\frac{\nu}{\nu+1}\right)\frac{\left(\frac{\partial\Gamma^{(0)}}{\partial\tau}\right)^2}{\Gamma^{(0)}}\right]\left(\frac{\partial\tau}{\partial\zeta}\right)^2 \quad (34)$$

with

$$\Gamma^{(0)'}\equiv\Gamma^{(0)}(\zeta,\tau') \quad (35)$$

and

$$\frac{\partial\tau}{\partial\zeta}=\left(\frac{\nu}{\nu+1}\right)\Gamma^{(0)}\left(\frac{\nu}{\nu+1}\right)\int_0^{\tau}\frac{\partial\Gamma^{(0)'}}{\partial\zeta}\left[\Gamma^{(0)'}\right]^{-\left(\frac{\nu}{\nu+1}+1\right)}d\tau' \quad (36)$$

The initial distribution in the new space is given by

$$\Gamma_0(\zeta)=\Gamma_m\exp\left[-(\zeta-\zeta_0)^2\right] \quad (37)$$

where

$$\Gamma_m=\frac{\alpha\beta D_\nu}{\nu+1}C_m{}^{\nu+1} \quad (38)$$

$$\alpha=\frac{\sqrt{\frac{\nu+1}{2}}}{s_0}. \quad (39)$$

The LHS of Eq. (33) is obtained by substituting Eq. (37) into Eq. (25) and integrating over ζ':

$$\Gamma^{(0)}(\zeta,\tau) = \frac{\Gamma_m}{2\sqrt{4\tau+1}}\left\{ \exp(-w^{(+)})\mathrm{erfc}(\xi^{(+)})+\exp(-w^{(-)})\mathrm{erfc}(\xi^{(-)}) \right\} \qquad (40)$$

where

$$w^{(\pm)} = \frac{(\zeta\pm\zeta_0)^2}{(4\tau+1)} \qquad (41)$$

$$\xi^{(\pm)} = \frac{\pm\zeta-4\zeta_0\tau}{\sqrt{4\tau(4\tau+1)}} \qquad (42)$$

and erfc(ξ) is defined by[8]

$$\mathrm{erfc}(\xi) = \frac{2}{\sqrt{\pi}}\int_{\xi}^{\infty}\exp(-x^2)dx\ . \qquad (43)$$

In practice erfc(ξ) was evaluated by[6]

$$\mathrm{erfc}(\xi) = t\exp\left(-z^2 + \sum_{i=0}^{9} a_i\, t^i\right) \qquad \xi \geq 0$$

$$\mathrm{erfc}(\xi) = 2 - t\exp\left(-z^2 + \sum_{i=0}^{9} a_i\, t^i\right) \qquad \xi < 0 \qquad (44)$$

where

$$z = |\xi|$$

$$t = \frac{1}{\left(1+\frac{z}{2}\right)}$$

$a_0 = -1.26551223$ $a_1 = 1.00002368$ $a_2 = 0.37409196$ $a_3 = 0.09678418$

$a_4 = -0.18628806$ $a_5 = 0.27886807$ $a_6 = -1.13520398$ $a_7 = 1.48851587$

$a_8 = -0.82215223$ $a_9 = 0.17087277$

For the choice of $\alpha = a\sqrt{D}$ the special case for the functional form of the diffusivity studied was

$$D = D_0 \sinh^2(kC) . \tag{10}$$

For this case the initial dopant distribution is a truncated Gaussian in the transformed variables.

$$\Gamma_0(\zeta) = \Gamma_m \exp\left[-(\zeta-\zeta_0)^2\right] \tag{37}$$

Equations (11)-(13) and (18) now become

$$\zeta(z,t) = \frac{a}{\sqrt{D_0}} \int_0^z \frac{dz'}{\sinh(kC(z',t))} \tag{45}$$

$$\tau = a^2 t \tag{46}$$

$$\Gamma^{(0)}(\zeta,\tau) = A\left[\cosh(kC^{(0)}) - 1\right] \tag{47}$$

$$\varepsilon^{(0)}(\zeta,\tau) = \frac{\dfrac{\partial \Gamma^{(0)}}{\partial \zeta}}{\sqrt{\Gamma^{(0)}(\Gamma^{(0)}+2A)}} \int_0^\zeta \frac{\left[\Gamma^{(0)'}+A\right]\dfrac{\partial \Gamma^{(0)'}}{\partial \tau}}{\sqrt{\Gamma^{(0)'}(\Gamma^{(0)'}+2A)}} d\zeta' \tag{48}$$

with

$$A = \frac{a\beta\sqrt{D_0}}{k} . \tag{49}$$

From Eq. (47) we obtain Γ_m in terms of C_m.

$$\Gamma_m = A[\cosh(kC_m) - 1] \tag{50}$$

The LHS of Eq. (47) is given by Eq. (40).

Note that because of the relationship between ζ and z in Eq. (45) the initial dopant distribution in real space is not a truncated Gaussian.

The two choices for φ, $\varphi = \alpha D$ and $\varphi = a\sqrt{D}$ were implemented in the programs FIRSTO and CA respectively (see appendix). Results are plotted in Figs. 1-13.

For the case $\varphi = \alpha D$ numerical problems were encountered in evaluating $\varepsilon^{(0)}$. It was determined that for some values of the variables certain terms with different signs in Eq. (34) increased towords infinity. An attempt was made to rewrite Eq. (34) in a form more suitable for computation. This attempt was not completely successful. However the program FIRSTO did produce zereoth order results since the zereoth order term does not depend on $\varepsilon^{(0)}$.

For the case in which $\varphi = a\sqrt{D}$ the expression for $\varepsilon^{(0)}$ is much simpler and good agreement between the analytical and numerical results was obtained for several values of the parameter k (see Figs. 5-13).

V. RECOMENDATIONS

The programs presented in the appendix are documented to provide guidance for their use and modification. All are written in FORTRAN77 and were run on a Microvax III.

More work on the case where $\varphi = \alpha D$ may lead to a form of $\varepsilon^{(0)}$ that is suitable for numerical calculation. This case is attractive because the initial dopant profile in real space is a truncated Gaussian which has been found to accurately fit experimental dopant profiles. For the case where $\varphi = a\sqrt{D}$, although the initial dopant profile is not a truncated Gaussian it differs primarily in the tail regions at low concentrations. Therefore it may describe the profile adequetly in the region of interest. An analysis of how well experimental dopant

profiles could be fit with this functional form could help determine the usefulness of this case.

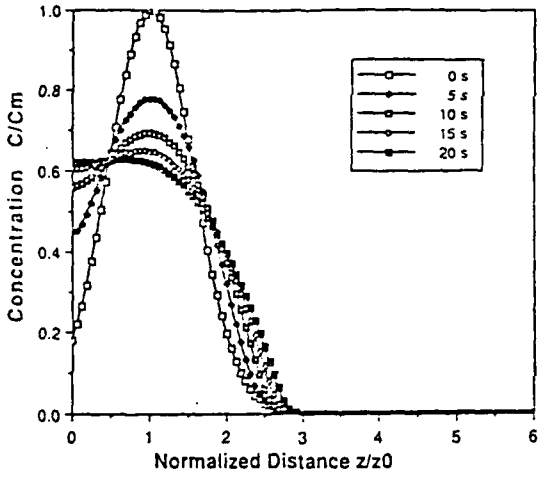

Figure 1. Numerical dopant profiles. $D=D_vC^v$. $v=1$.

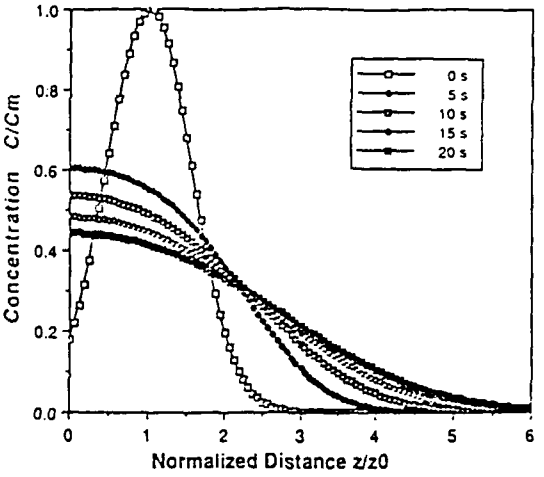

Figure 2. Numerical dopant profiles. $D=D_e\exp(kC)$. $k=1$.

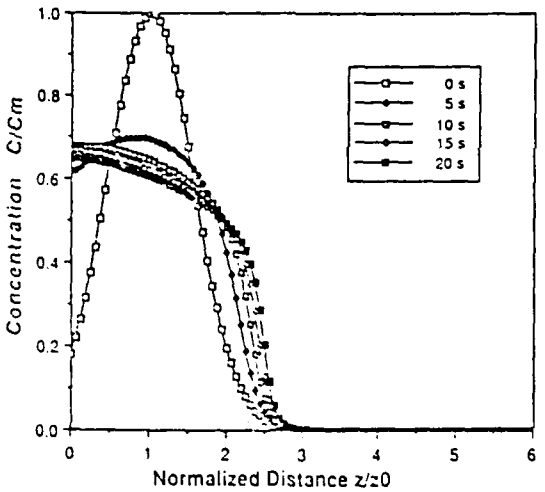

Figure 3. Zeroth order analytical dopant profiles. $D=D_vC^v$. $v=1$.

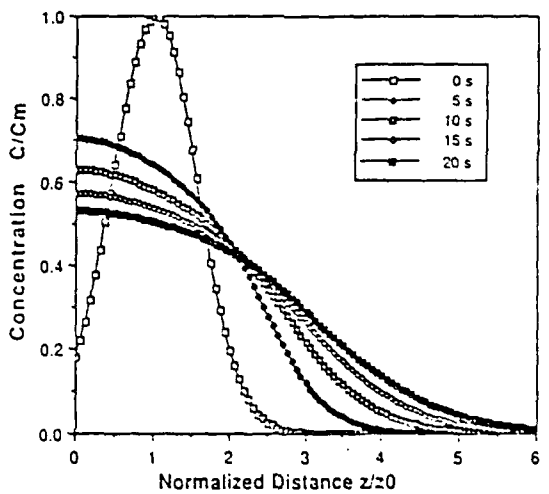

Figure 4. Zeroth order analytical dopant profiles. $D=D_e\exp(kC)$. $k=1$.

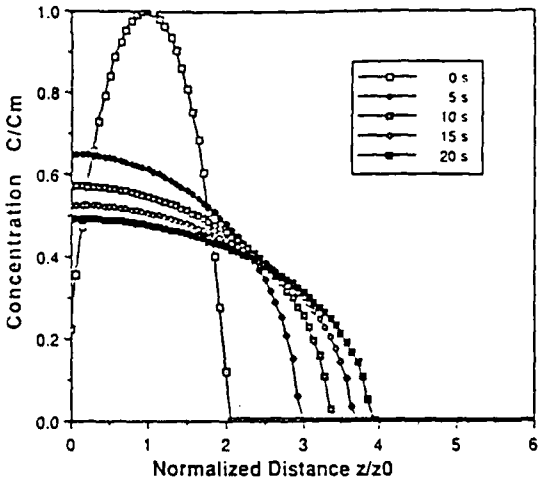

Figure 5. Numerical dopant profiles. $D=D_0\sinh^2(kC)$. $k=\frac{1}{2}$.

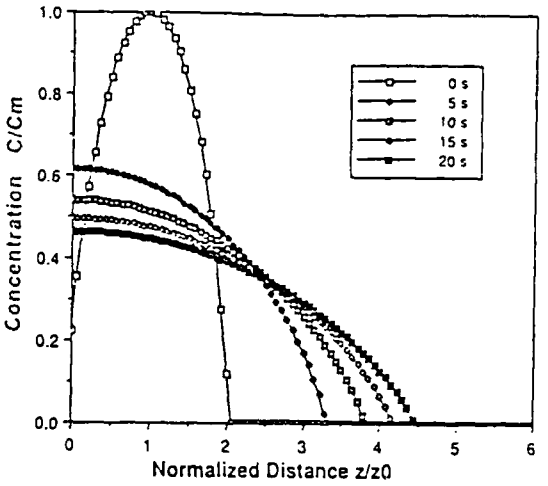

Figure 6. Zeroth order analytical dopant profiles. $D=D_0\sinh^2(kC)$. $k=\frac{1}{2}$.

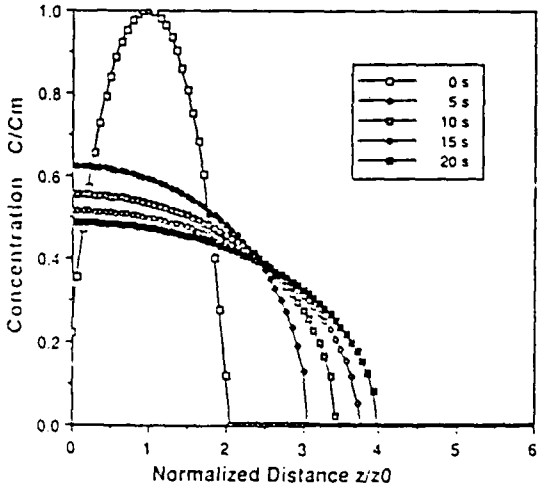

Figure 7. First order corrected analytical dopant profiles. $D=D_0\sinh^2(kC)$. $k=\frac{1}{2}$.

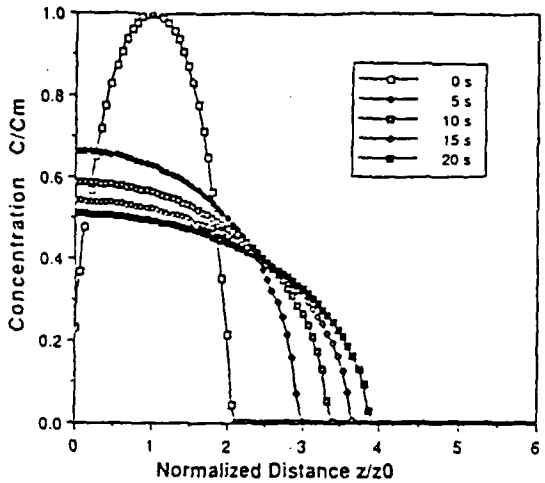

Figure 8. Numerical dopant profiles. $D=D_0\sinh^2(kC)$. k=1.

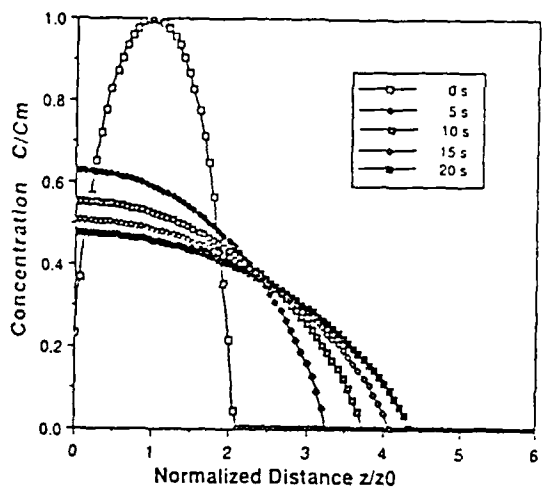

Figure 9. Zeroth order analytical dopant profiles. $D=D_0\sinh^2(kC)$. k=1.

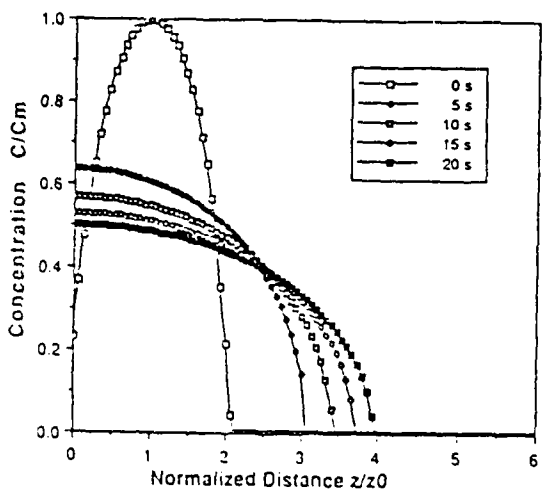

Figure 10. First order corrected analytical dopant profiles. $D=D_0\sinh^2(kC)$. k=1.

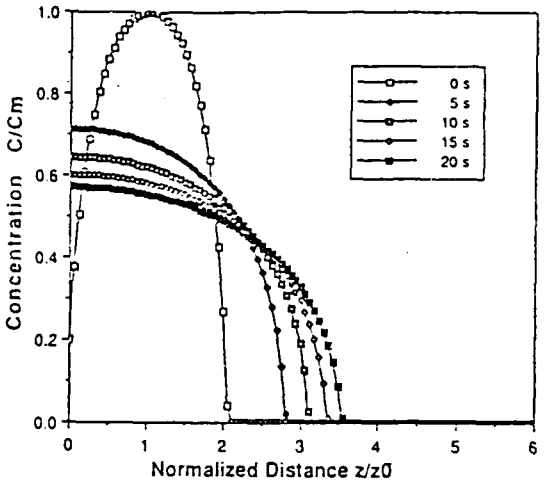

Figure 11. Numerical dopant profiles. $D=D_o\sinh^2(kC)$. k=2.

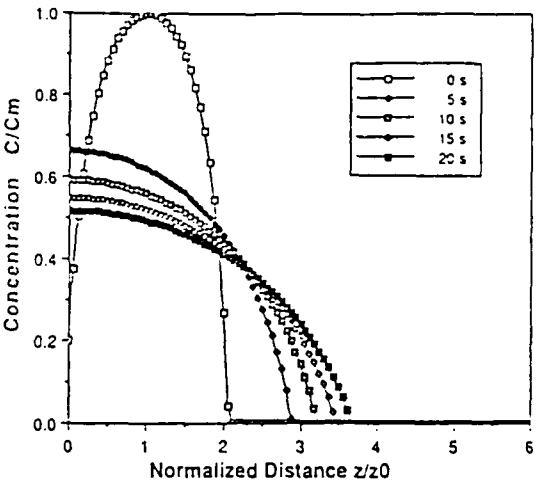

Figure 12. Zeroth order analytical dopant profiles. $D=D_o\sinh^2(kC)$. k=2.

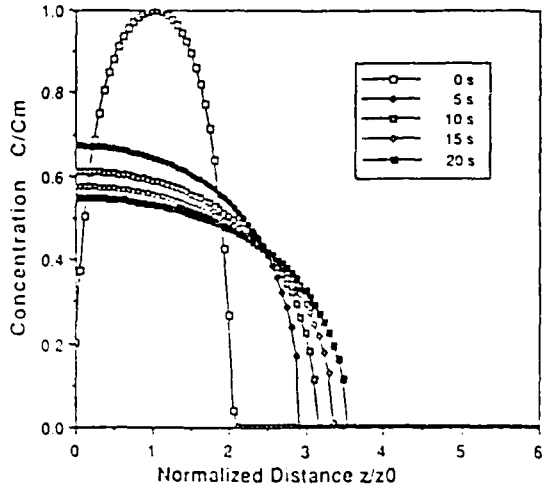

Figure 13. First order corrected analytical dopant profiles. $D=D_o\sinh^2(kC)$. k=2.

REFRENCES

[1]R. Ghez, G. S. Oehrlein, T. O. Sedgwick, F. F. Morehead, and Y. H. Lee, "Exact Description and Data Fitting of Ion-implanted Dopant Profile Evolution During Annealing", Applied Physics Letters 45, 881 (1984).

[2]D. S. Moroi and P. M. Hemenger, "Perturbation Method for Solution to Nonlinear Diffusion Equation", to be published.

[3]S. W. Bucey, "Computer Evaluation of Ion-implanted Dopant Profile Evolution During Annealing", final report to USAF-UES summer faculty research program/graduate student research program, 1987.

[4]The integral evaluated was $\int_0^\tau \int_0^\infty G(\zeta,\tau \mid \zeta',\tau')\, d\zeta' d\tau'$ which was found to equal τ in agreement with the analytical result of Dr. Moroi.

[5]M. L. James, G. M. Smith, and J. C. Wolford, Applied Numerical Methods for Digital Computation with FORTRAN and CSMP, second edition, New York, Harper and Row, 1977.

[6]W. H. Press, B. P. Flannery, S. A. Teukolsky, and W. T. Vettering, Numerical Recipes : The Art of Scientific Computing, Cambridge, New York, Cambridge University Press, 1986.

[7]G. A. Geist and R. F. Wood "Modeling of Complex Melting and Solidification Behavior in Laser-irradiated Materials, [A Description and Users Guide to the LASER8 Computer Program]", ORNL-6242, Oak Ridge National Laboratory, Oak Ridge, TN, November 1985.

[8]M. Abramowitz and I. A. Stegun, Handbook of Mathematical Functions, Washington D.C., U.S. Dept. of Commerce, NBS, 1970.

APPENDIX MAY BE OBTAINED FROM

UNIVERSAL ENERGY SYSTEMS, INC.

OR AUTHOR

ON REQUEST

1988 USAF-UES SUMMER FACULTY RESEARCH PROGRAM/
GRADUATE STUDENT RESEARCH PROGRAM

Sponsored by the

AIR FORCE OFFICE OF SCIENTIFIC RESEARCH

Conducted by the

Universal Energy Systems, Inc.

FINAL REPORT

QPA Control of the End Milling Process

Prepared by:	Barry Fussell, Ph.D (Doug Gagne)
Academic Rank:	Assistant Professor (Graduate Student)
Department and	Department of Mechanical Engineering
University:	University of New Hampshire
Research Location:	AFWAL/MLTC
USAF Researcher:	Major Steve LeClair Mr. Tom Lagnese

Date:	28 September, 1988
Contract No:	F49620-87-R-0004

SAME REPORT AS
PROF. BARRY FUSSELL
MATERIALS LABORATORY # 100

1988 USAF-UES SUMMER FACULTY RESEARCH PROGRAM/

GRADUATE STUDENT RESEARCH PROGRAM

Sponsored by the

AIR FORCE OFFICE OF SCIENTIFIC RESEARCH

Conducted by the

Universal Energy Systems, Inc.

FINAL REPORT

Can Design For Extruded Powder Metallurgy Materials, and the Effects of Can Geometry and Can Material on the Powder Metallurgy Material Core.

Prepared by:	Robert L. Goetz
Academic Rank:	Graduate Student
Department and University:	Department of Mechanical Engineering, Ohio University
Research Location:	AFWAL/Materials Labratory - MLLM, Wright-Patterson AFB, Ohio 45433-6533
USAF Researcher:	James C. Malas
Date:	August 26, 1988
Contract No:	F49620-88-C-0053

Can Design For Extruded Powder Metallurgy Materials, and the Effects of Can Geometry and Can Material on the Powder Metallurgy Material Core.

by

Robert L. Goetz

ABSTRACT

The objective of this project was to examine the effects of "can" thickness and "can" material on the state of stress and the uniformity of the velocity field for the co-extrusion of a "canned" P/M material. The process was simulated as isothermal using the FEM code MME-ALPID. Three can thicknesses were simulated; 1/8", 1/4", and 1/2". The P/M material used was IN100, and Austenitic Stainless Steel was used for the "can" material. Simulations proceeded to the point where the nose cap was extruded before remeshing was required. Initial results show that the 1/8" can will possibly fracture. The 1/4" can has a more uniform deformation than 1/8" can. No conclusions have been made about the 1/2" can as yet. The stress ratio of $\sigma m/\bar{\sigma}$ in the 1/4" can shows a transition from compressive to tensile stresses near the die exit. It is recommended that, in addition to the present simulation, a non-isothermal simulation using ALPID be made, and that ALPIDP be used for a comparison. These projects would ultimately aid in the "can" design for any P/M material.

ACKNOWLEDGEMENTS

I would like to thank the Air Force Systems Command and the Air Force Office of Scientific Research for sponsorship of this research. I would also like to thank Universal Energy Systems for managing this program and for providing administrative support.

In addition to the Air Force and UES, I would like to thank those individuals whose help I greatly appreciated. First, I would like to thank Jim Malas, Jim Morgan, and Bill O'Hara of the Processing Science Group, because they went out of their way to provide the support that I needed. I would also like to thank Venkat Seetharaman for his advice and help with materials and their behavior. I would like to thank those who provided computer support; Vijay Shinde and Nittin of UES-Columbus, and Siamack Mazdiyasni of the Materials Lab. Finally, I would like to thank Prof. Ken Halliday who brought this program to my attention, and suggested that I apply for it.

I. INTRODUCTION:

One of the goals of the Processing Science In-House Research Group is to develop analytical modeling techniques for manufacturing processes, and it is hoped that this project will provide a better understanding of the co-extrusion of "canned" powder metallurgy (P/M) materials. The results from this project can then be applied to the actual extrusion work being performed at the Experimental Metal Processing Laboratory (EMPL). The objective of this project is to model the co-extrusion of a "Canned" P/M material through a streamlined die using the finite element code MME-ALPID. ALPID stands for "Analysis of Large Plastic Incremental Deformation". ALPID was developed by Battelle's Columbus Laboratories under Air Force contract. MME refers to the Material Modeling Environment developed by Universal Energy Systems-Knowledge Integration Center (UES-KIC).

The process of extruding "canned" P/M materials is similar to the drawing or extruding of bi-metal wire. However, it is different, in that in this case, it is used as a conditioning process for P/M materials. Extrusion is used to compact the P/M material to as close to 100% density as possible while completely deforming the material in a uniform manner. Other methods of compaction, like forging, do not offer the uniform deformation that extrusion using streamlined dies does. Processes like forging cause tensile stresses, which lead to defects, whereas extrusion usually doesn't. The "can" has several functions. First, it acts as the container for the powdered material. Secondly, it acts as an insulator from the chilling effects of the die. Also, certain high temperature alloys must be processed in an evacuated environment to avoid oxidation. Thus, most cans are evacuated after the can

has been filled with the P/M material. P/M materials, in general, are advantageous because they offer the possibility of a fine grain structure, which usually means high strength and hardness. Also, greater control over an alloy's mixture and purity is possible. Casting of these alloys leads to large voids and defects, which requires further deformation processing. However, the never alloys of interest to the aerospace industry, those that offer large strength to weight ratios, are very hard to deform.

A second reason for doing can extrusions is for the validation of a materials behavior as predicted by the MME processing maps which show the stable/ unstable regions of a material based on strain rate and temperature. These maps are constructed using compression test data generated at various temperatures and strain rates, and observing the effects on actual grain structure. A possible P/M material for this project is Titanium-Aluminide, TiAl. It is currently being extruded at EMPL, but at a temperature of around 1350-1400°C. The processing maps, however, only go to 1350°C due to testing limitations. ALPID simulations of this material at these lower temperatures must be done in conjunction with actual extrusions to validate the maps.

II. OBJECTIVE:

The objective of this project is to examine the effects of can thickness and can material on the state of stress, and the uniformity of the velocity field of the P/M material inside. Figure 1 shows the can dimensions used in the isothermal ALPID simulations . Three can thicknesses have been chosen, and are typical of those used at EMPL. They are; 1/8", 1/4", and 1/2". A typical can material is austenitic stainless steel and for the simulations, IN100 will be used as the P/M core material.

Specifically, it is hoped that the tensile forces at the "can/core" interface will be shown. From Avitzur [2], it is known that the more ductile of the two materials will flow more easily, and depending on the amount of friction at the interface, a tensile force will be applied on the less ductile of the two materials. It is known that to avoid the defect, central bursting, axial tensile stresses must be avoided. Axial tensile stresses occur when the ratio of mean stress, σm, to effective stress, $\bar{\sigma}$, is greater than -2/3 [1]. Thus, central bursting is avoided when $\sigma m/\bar{\sigma} < -2/3$. It is hoped that by changing the can thickness, the ratio of $\sigma m/\bar{\sigma}$ will show the likelihood of central bursting as a function of thickness. The uniformity of the velocity field will be examined using the grid distortion and the strain rate contours as the billet moves through the die. As stated above, the P/M material selected for the project was IN100. It was selected because stress/strain compression data was readily available on the MLLM micro-VAX in the MME database. However, no such data was available in the MME database for any type of stainless steel . Thus, a literature search was required for pertinent data on any suitable stainless steel.

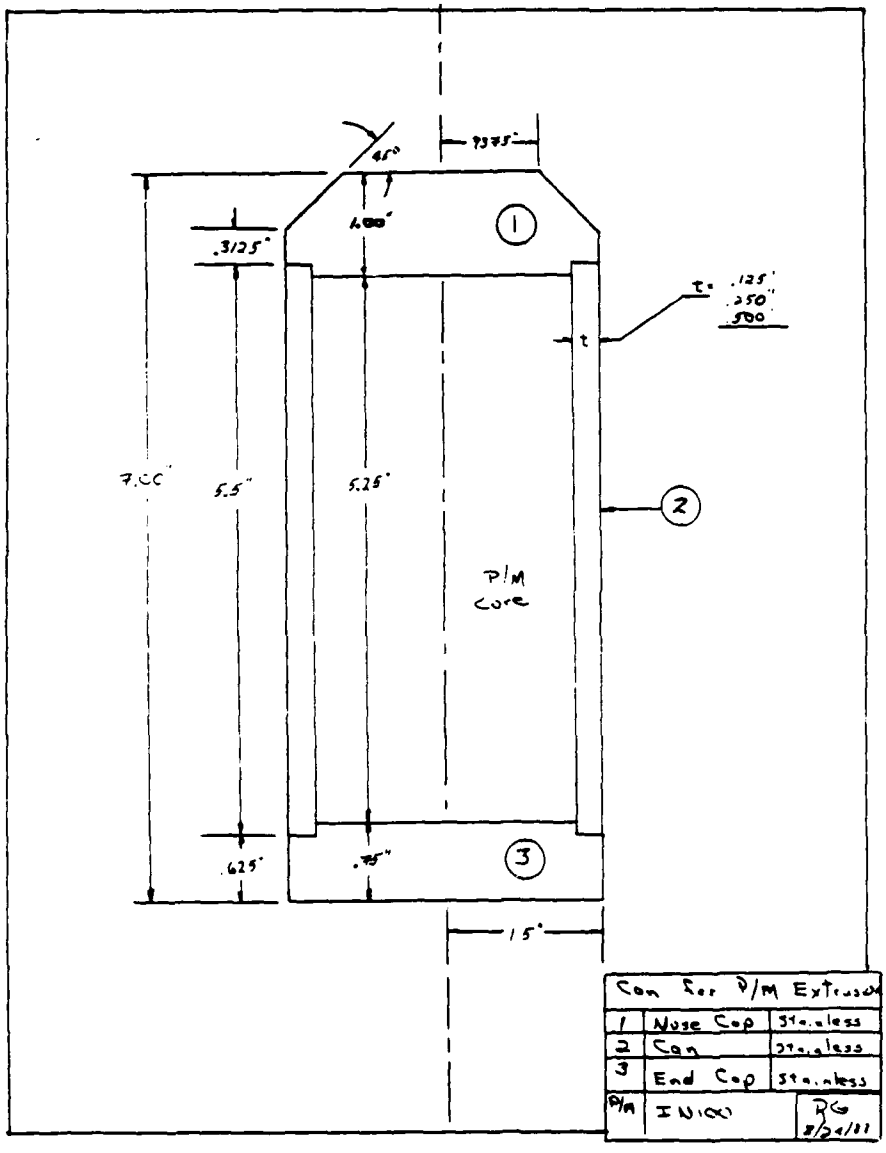
.7375"
45°
.400"
.3125"
1
t= .125"
.250"
.500"
t
7.00"
5.5"
5.25"
2
P/M
Core
.625"
.75"
3
1.5"
Can for P/M Extrusion
1 Nose Cap 304 stainless
2 Can 304 stainless
3 End Cap 304 stainless
P/M INCO
RG
8/24/81

Fig. 1

III. EXTRUSION PARAMETERS:

Relevant extrusion parameters include temperature, ram velocity, coefficient of friction, die geometry, material constitutive values and can geometry. A temperature of 1900°F was chosen for the simulation. At this temperature, the extrusion is well into the plastic region of any stainless steel used for the can, and any work hardening effects can be neglected. This also affects the constitutive equation used by ALPID to calculate flow stresses for the Stainless Steel can. The equation is as follows;

$$\bar{\sigma} = k*(\varepsilon)^{n}*(\dot{\varepsilon})^{m} \qquad (1)$$

where:
- $\bar{\sigma}$ = flow stress
- ε = true strain
- $\dot{\varepsilon}$ = strain rate
- n = strain hardening factor
- m = strain rate sensitivity factor
- k = flow stress constant

For plastic deformation, the factor, n, equals zero. Thus, equation (1) is reduced to;

$$\bar{\sigma} = k*(\dot{\varepsilon})^{m} \qquad (2)$$

The values of k and m for the can were, k = 30,000 psi, and m = .15. The value of m was chosen based on reference [3]. The value of k was chosen arbitrarily, but proved reasonably close when the data for type 304 stainless steel from reference [4] was located. See section IV. for the determination of k and m from reference [4]. Flow stress values for IN100 were obtained directly from the MME database by ALPID, and eqn. (2) was not used.

A ram velocity of 0.5 in/sec. was used, and the constant shear friction factor, m, was applied. A value of 0.05 was chosen for m. A streamlined die of 6.2:1 area reduction ratio was used, with the profile defined by the cubic equation given on the following page.

$$R(x) = A + B*x + C*x^2 + D*x^3 \quad (3)$$

where $R(x)$ = radius as a function of the axial length from the extrance

x = axial length from the extrance

A, B, C, D = variables dependent on entry & exit radii, and the die length.

For a streamlined die, the slope of the die profile is zero at both the entry and the exit. Thus, knowing this, the entry & exit radii, and the die length, the values of A, B, C, and D can be found using the following relations;

$$A = Ri \quad (4)$$

$$B = 0.0 \quad (5)$$

$$C = \frac{3*(Ro - Ri)}{L^2} \quad (6)$$

$$D = \frac{-2*(Ro - Ri)}{L^3} \quad (7)$$

where: Ro = exit radius
Ri = entry radius
L = die length

An entry radius of 1.5 inches was used as that is the radius used at EMPL. Die length was set at 3.0 inches. From the reduction ratio, the exit radius was calculated to be .6024 inches. The can geometry is shown in Fig. 1. All dimensions were held constant, except the thickness, which was varied between 1/8", 1/4", and 1/2" as part of the project.

IV. Stress & Strain Rate Data for Type 304 Stainless Steel:

This section deals with the Flow Stress-Strain Rate data for Type 304 stainless steel found in Dadras [4]. Type 304 Stainless Steel is a possible "can" material. The data found in reference [4] was in the form of Stress-Strain curves at various strain rates and at 900°C & 1200°C. Stresses were taken from these curves at a strain of 0.5 for the various strain rates. See Tables 1 & 2. The data was then fitted to equation (2) by plotting $\log(\bar{\sigma})$ vs. $\log(\dot{\epsilon})$. These plots are shown in Figures 2 and 3. Using these plots, values of m & k were found using a least squares linear curve fit. For 1037°C (1900°F), m & k were interpolated using the values found at 900°C and 1200°C, and are shown in Table 3. These results, however, were not used because reference [4] was located after too much C.P.U. time had been consumed using values of: m=.15 ; k=30 kpsi. They will be used in later simulations to study the effects of material choice.

TABLE 1.
TYPE 304 STAINLESS STEEL
@ 1200°C , @ ε = 0.5

$\dot{\varepsilon}$ (1/sec.)	log($\dot{\varepsilon}$)	$\bar{\sigma}$ (MPa)	log($\bar{\sigma}$)
0.2	-.6989	84.4	1.9260
0.8	-.0969	95.3	1.9790
3.5	.5441	107.8	2.0326
10.0	1.0000	118.8	2.0748
30.0	1.4770	128.1	2.1080
100.0	2.0000	140.6	2.1480

TABLE 2.
TYPE 304 STAINLESS STEEL
@ 900°C , @ ε = 0.5

$\dot{\varepsilon}$ (1/sec.)	log($\dot{\varepsilon}$)	$\bar{\sigma}$ (MPa)	log($\bar{\sigma}$)
1.5	0.1761	250.0	2.3980
8.0	0.9031	278.0	2.4440
40.0	1.6021	306.8	2.4870
100.0	2.0000	318.2	2.5030

TABLE 3.
Values of m, and k for
Type 304 Stainless Steel

Temp. (°C)	m	k (psi)
900.0	0.0585	35,562
1037.7 *	0.0696	25,694
1200.0	0.0826	14,062

* - interpolated from 900°C & 1200°C data.

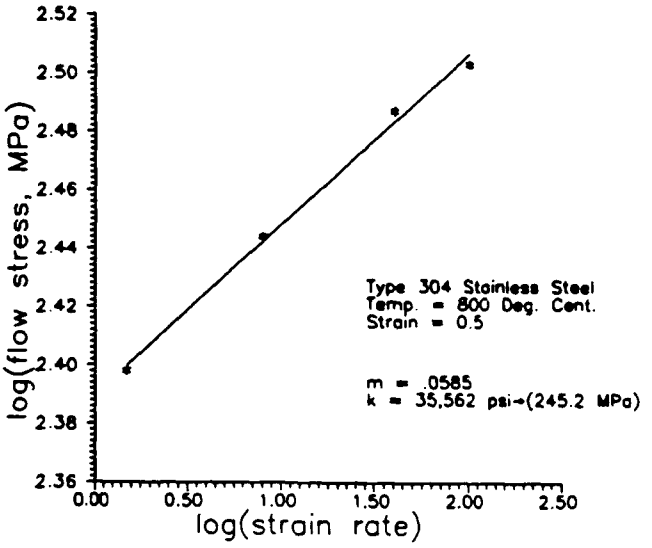
2.52
2.50
2.48
2.46
2.44
2.42
2.40
2.38
2.36
log(flow stress, MPa)
0.00
0.50
1.00
1.50
2.00
2.50
log(strain rate)
Type 304 Stainless Steel
Temp. = 800 Deg. Cent.
Strain = 0.5
m = .0585
k = 35,562 psi→(245.2 MPa)

Fig. 2

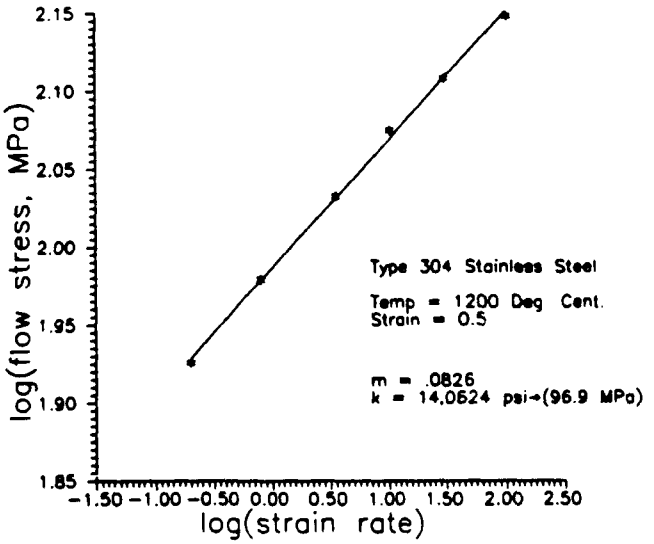
2.15
2.10
2.05
2.00
1.95
1.90
1.85
log(flow stress, MPa)
−1.50 −1.00 −0.50 0.00 0.50 1.00 1.50 2.00 2.50
log(strain rate)
Type 304 Stainless Steel
Temp = 1200 Deg Cent.
Strain = 0.5
m = .0826
k = 14,0624 psi→(96.9 MPa)

Fig. 3

V. AlPID Simulations:

ALPID simulations for the 1/8", 1/4", and 1/2" cans have not been completed, and are continuing. Figure 4 shows the initial mesh used for the 3 can sizes, and figures 5, 6, & 7 show the progress made for the 1/8" and 1/4" cans. At this point, remeshing is required for both cans so that the simulations may continue, and it is currently under way. The simulation for the 1/2" can has proceeded to the point where the can is just emerging from the die exit. Approximately 24 hrs. of C.P.U. time were required for both the 1/8" and the 1/4" simulations to reach their present states. It should be noted that when both the 1/8" and the 1/4" cans reached the point where the can was emerging from the die exit, the maximum time allowed per step had to be reduced. This is believed to be related to the implicit/explicit integration used by ALPID. It is known that the accuracy of these methods is dependent on the size of the integration step. An examination of figure 5, which shows the grid distortion of the 1/8" can, would seem to indicate that the can is about to be fractured as the P/M core is entering the region of maximum reduction. The shadowed area highlights the "can" material. Figure 6 shows the 1/4" can in approximately the same phase, but with a more uniform deformation than the 1/8" can. This is typical of a can that is too thin, resulting in the nose cap and can seperating, punching the core through without the can.

Figure 8 shows the strain rate contours of the 1/4" can at step 70 . The minimum is .125 (1/sec.) and the maximum is 1.624 (1/sec.). These strain rates are well within the stable processing region for IN100 at 1900°F (1037°C) as shown by figure 9.

Even though the simulation has not reached steady state, where both the core and can are exiting the die, it is expected that strain rate values will remain in range between 0.0 (1/sec.) and 1.6 (1/sec.).

Figures 10 and 11 show the grid distortion and the stress ratio of $\sigma m/\bar{\sigma}$ for the 1/4" can at step 74. The stress ratio plot shows the transition of $\sigma m/\bar{\sigma}$ from -.99 to -.33. This represents the transition from compressive to tensile axial stresses. This is also shown in plots of earlier steps that were not included in this report. Further simulations will show if this persists as steady state is reached with the core exiting the die. The cross-hatched area highlights the elements representing IN100.

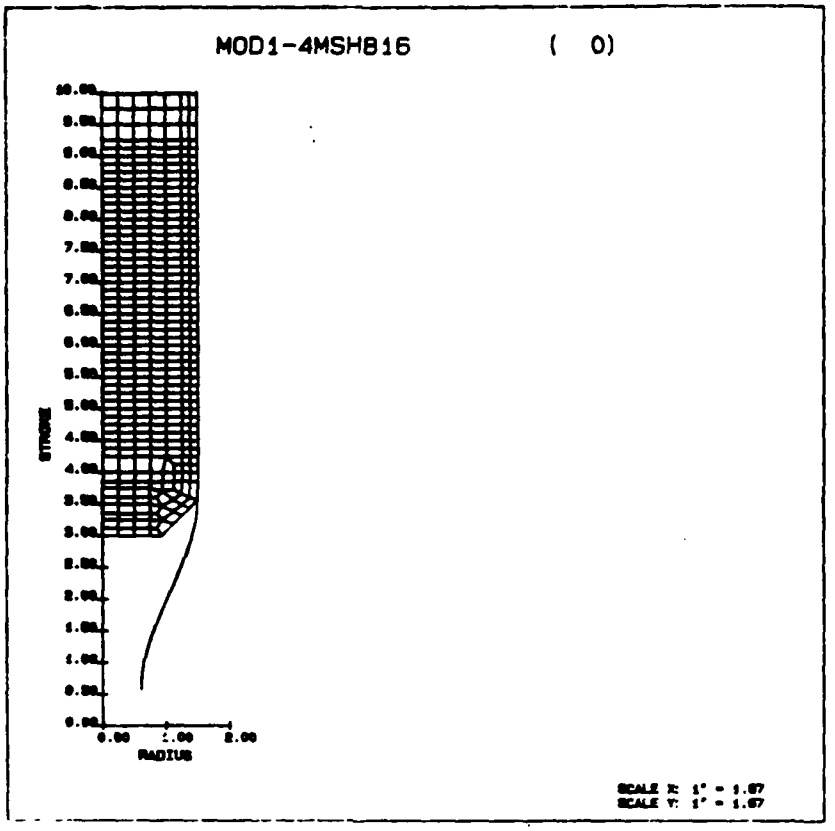
MOD1-4MSH816 (0)
STROKE
RADIUS

Fig. 4

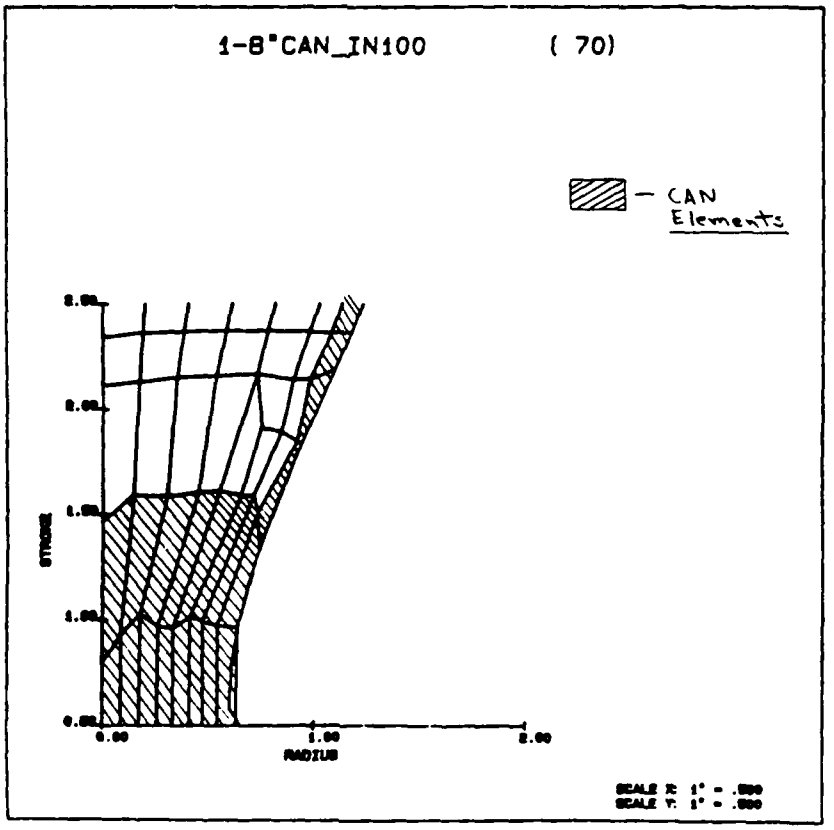
1-8"CAN_IN100 (70)
CAN Elements
STROKE
RADIUS

Fig. 5

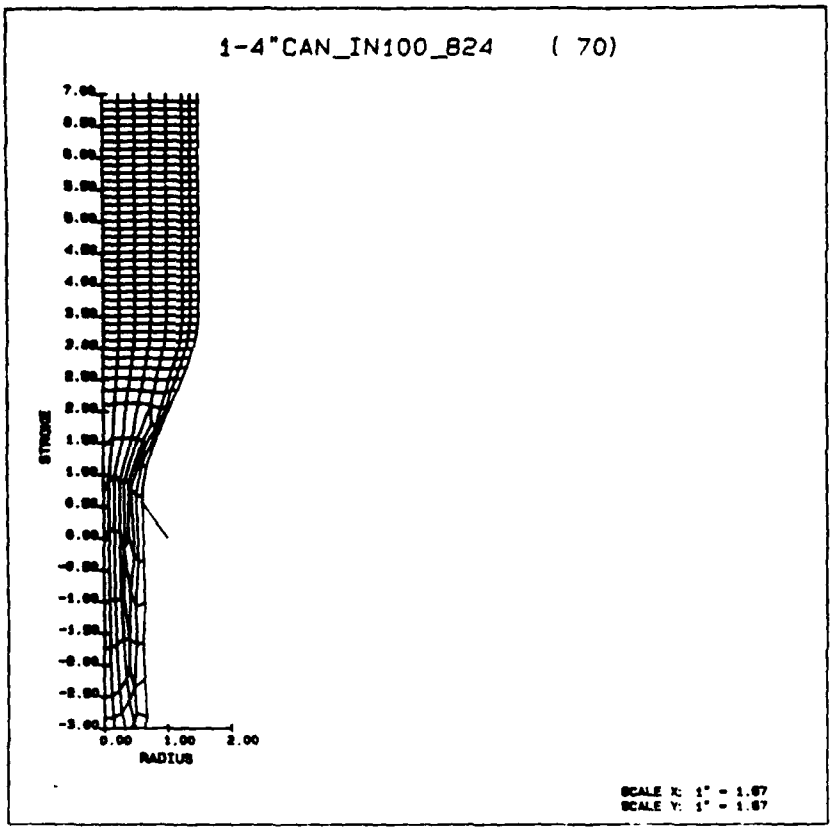
1-4"CAN_IN100_824 (70)
STROKE
RADIUS
0.00
1.00
2.00

Fig. 6

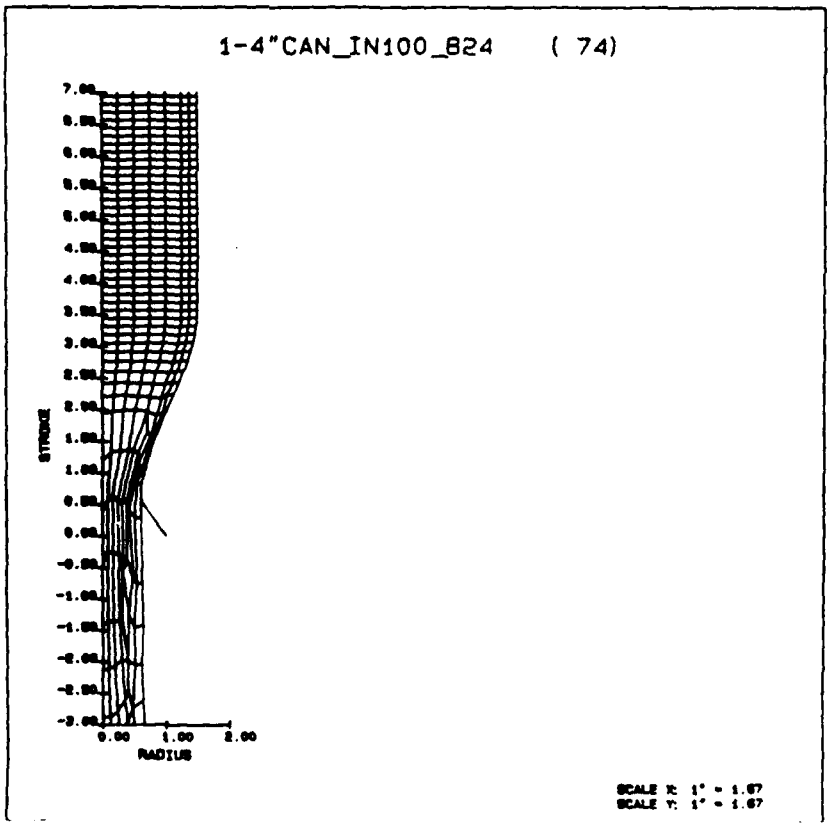
1-4"CAN_IN100_824 (74)
STROKE
RADIUS
0.00
1.00
2.00

 Fig. 7

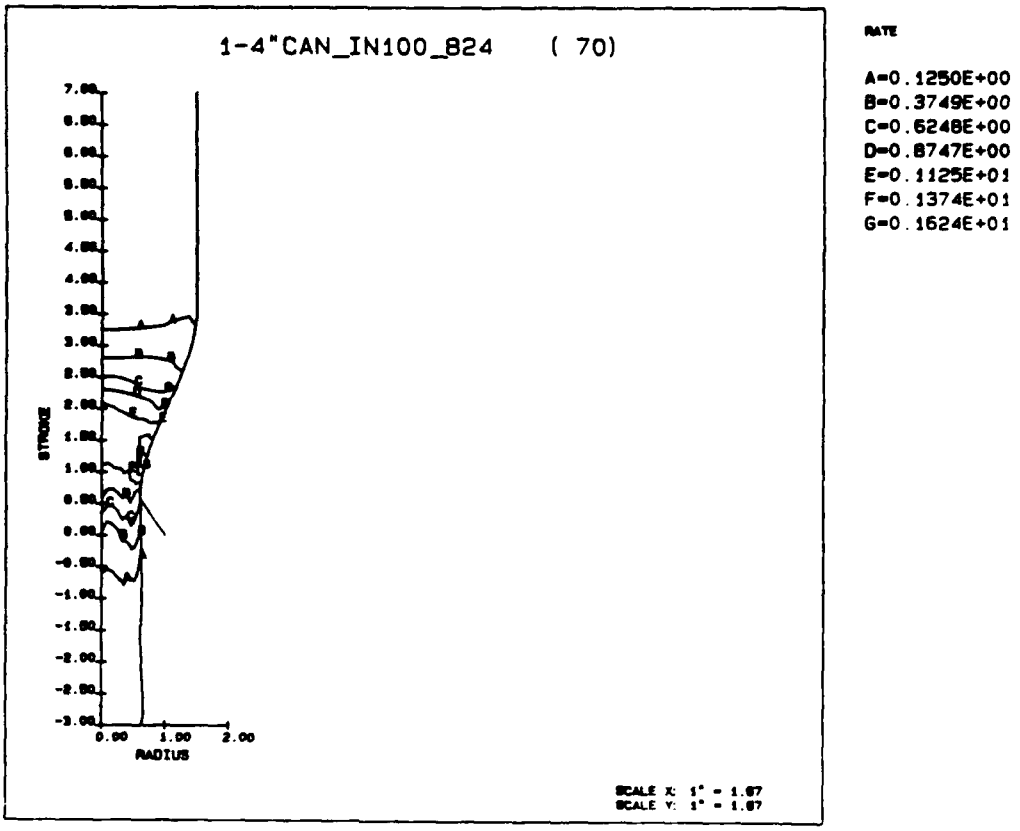
1-4"CAN_IN100_824 (70)
RATE
A=0.1250E+00
B=0.3749E+00
C=0.6248E+00
D=0.8747E+00
E=0.1125E+01
F=0.1374E+01
G=0.1624E+01
STROKE
RADIUS
0.00
1.00
2.00
SCALE X: 1" = 1.67
SCALE Y: 1" = 1.67

Fig. 8

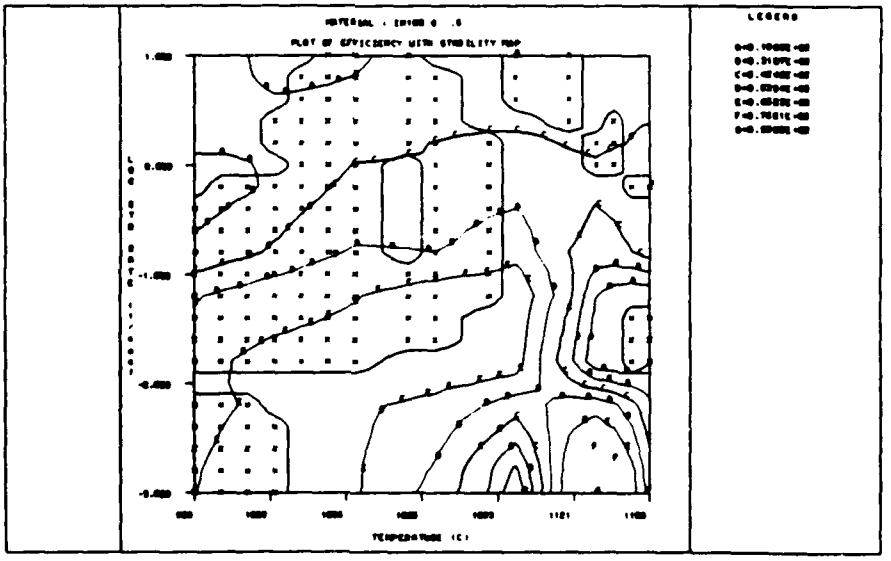

Fig. 9

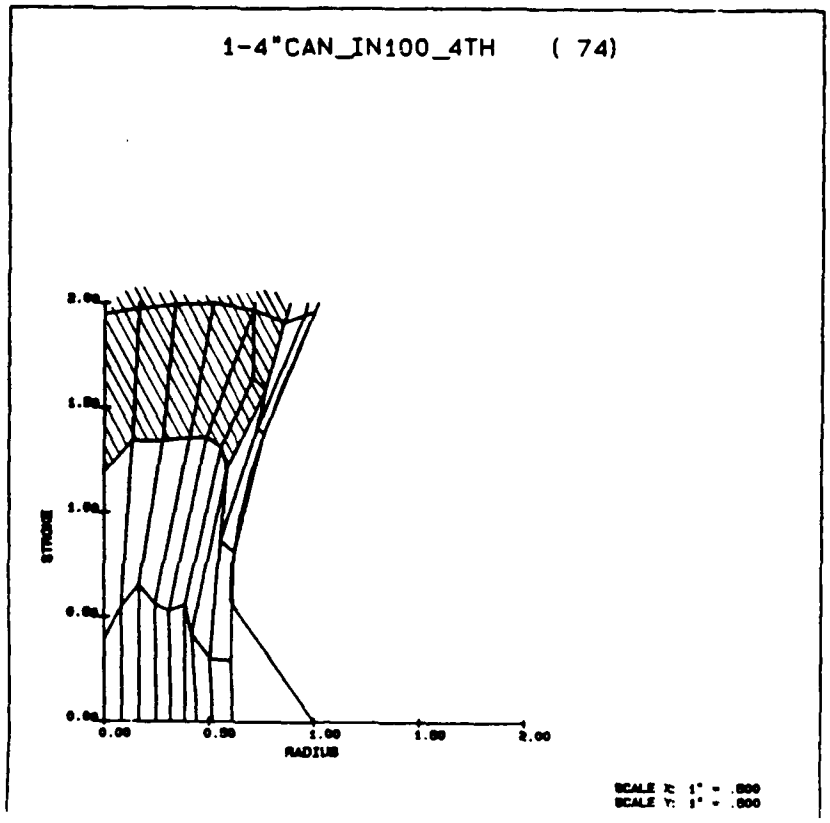
1-4"CAN_IN100_4TH (74)
STROKE
RADIUS
0.00
0.50
1.00
1.50
2.00

Fig. 10

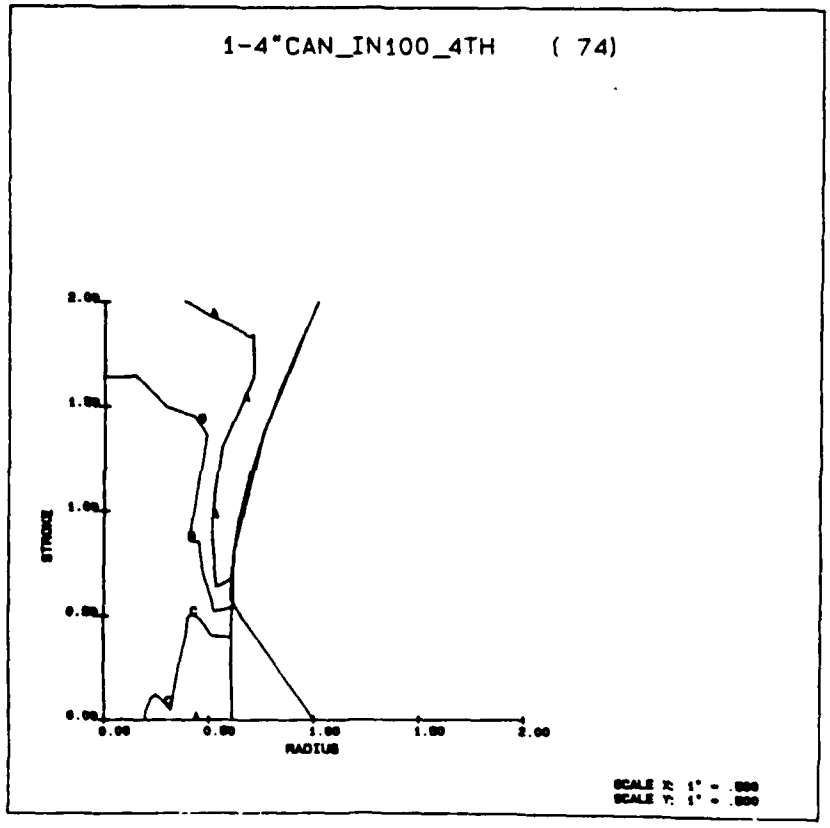
1-4"CAN_IN100_4TH (74)
STROKE
RADIUS
0.00
0.50
1.00
1.50
2.00
STRESS RATIO
A=-.9900E+00
B=-.6600E+00
C=-.3300E+00
D=0.0000E+00

Fig. 11

VI. Recommendations:

From the work completed to this time, it is believed that further work will prove helpful in the area of can design. At the very least, further work will prove helpful in the extrusion of IN100. It is recommended that work also be done in the area of non-isothermal ALPID simulations of "canned" extrusion. A study of only one can design would show the temperature distributions between the can and die, and within the can itself. The results from the isothermal and non-isothermal simulations would then give a more complete understanding of "canned" P/M material extrusions. To finally complete the investigation of "canned" P/M extrusions, the P/M version of ALPID, ALPIDP, could be used to simulate the process. However, the use of ALPIDP requires more than the relation, $\bar{\sigma} = f(temp,\varepsilon,\dot{\varepsilon})$. Density also becomes a factor, making flow stress a very complex function of; $\bar{\sigma} = f(temp,\varepsilon,\dot{\varepsilon},rho)$. This calls for more extensive experimental material modeling.

References:

(1) Gegel, H.L., et al., "Billet Conditioning Technique for Manufacturing Powder Metallurgy Preforms," AF Inv 16758.

(2) Avitzur, B., Wu, R., et al., "Criterion for the Prevention of Core Fracture During Extrusion of Bimetal Rods," Journal of Engineering for Industry, Aug. 1982, Vol. 104/293.

(3) Kassner, M.E., "Variation of the Yield Strength and Strain Rate Sensitivity Exponent of Type 21-6-9 Stainless Steel Over a Wide Temperature Range," UCID - 19597, Lawrence Livermore Laboratories, 1982.

(4) Dadras, P., "Flow Stress Equations for Type 304 Stainless and AISI 1055 Steels," Journal of Eng. Mat. and Techn., Vol. 107, April 1985, pp. 97-100.

1988 USAF-UES SUMMER FACULTY RESEARCH PROGRAM/

GRADUATE STUDENT RESEARCH PROGRAM

Sponsored by the

AIR FORCE OFFICE OF SCIENTIFIC RESEARCH

Conducted by the

Universal Energy Systems, Inc.

FINAL REPORT

INTERFACE RESISTIVITY MODELLING OF THE HOT ROLLING OF Ti-48Al-1V

Prepared by:	Andrew E. Hensley
Academic Rank:	Graduate student
Department and	Mechanical Engineering Department
University:	University of Detroit
Research Location:	AFWAL/MLLM Wright-Patterson AFB Ohio 45433-6533
USAF Researcher:	W. T. O'Hara and L. E. Matson

Date:	19 Aug 88
Contract No:	F49620-88-C-0053

INTERFACE RESISTIVITY MODELLING OF THE HOT ROLLING OF Ti-48Al-1V

by

Andrew E. Hensley

ABSTRACT

In order to obtain computer simulations of the gamma titanium aluminide hot rolling process using finite element modelling, it is necessary to gather data on the interface properties between the TiAl workpiece and the TZM molybdenum rolls. One of these interface conditions which needs a great deal of further investigation is the coefficient of electrical resistivity between these two materials. In order to accomplish this, test methods and procedures must be established. Also, there needs to be a great deal of microstructural work done with gamma titanium aluminide in order to gain insight into its characteristics during processing.

ACKNOWLEDGEMENTS

I would like to at this time thank the Air Force Systems Command, the Air Force Office of Scientific Research, AFWAL/MLLM, and Universal Energy Systems for their sponsorship and administration of this research. On a more individual level I would like to thank Dr. Vinod Jain for his instruction in many of the aspects of mechanical engineering, including engineering design. I would like to thank Larry Matson, Bob Lewis, and the entire staff of the metallography lab for providing me with an insight into material microstructures, for putting up with me, and for answering all of my questions (even the dumb ones). I would also like to thank Bill O'Hara for acting as my effort focal point, for providing me with an insight into some of the philosophies of engineering and science, and for providing me with many answers.

I. INTRODUCTION

Presently the Air Force has focused a great deal of interest on titanium aluminide as a potentially viable high temperature material for military applications. Gamma titanium aluminide (Ti-48Al-1V) has favorable strength and density characteristics at high temperatures with a relatively stable crystal structure, but its high degree of brittleness leads to processing difficulties. Since there exists a need to roll gamma titanium aluminide into sheet form for future Air Force utilization, these problems must be resolved. It is therefore necessary to establish the narrow range of rolling conditions in which the necessary material deformation is achievable. It is important to determine various parameters so that the rolling process, which is to be performed by rolling the TiAl between TZM molybdenum rolls that will be resistance heated, can be adequately modelled. My responsibility lies in the modelling of the conditions which exist during this rolling process at the interface between the TiAl sheet and the TZM molybdenum rolls. The conditions of interest are the coefficient of static friction, the heat transfer coefficient, and the electrical resistance at the workpiece and roll interface. Test fixtures to determine the TiAl-TZM interface coefficient of friction and the heat transfer coefficient at this interface are already in advanced stages of development and therefore need only be mentioned here. These two properties are obtained through ring compression testing of TiAl rings between TZM dies at a controlled temperature and atmosphere to determine the frictional coefficient and the fixturing of a TiAl ring between TZM platens at a controlled temperature and atmosphere and measuring the temperature gradient through the

system with thermocouples to determine the coefficient of heat transfer. What most of my time has been spent on is the development of a test fixture to measure the electrical resistance at the interface of the TiAl and TZM test samples. Time has also been spent on looking at the microstructure of forged gamma titanium aluminide.

II. OBJECTIVES OF THE RESEARCH EFFORT

Currently there has not been any successful rolling of gamma titanium aluminide into sheet although there has been some alpha sheet produced. The ultimate goal of this research effort is to provide sufficient data concerning TiAl-TZM interface properties to allow the repeated production of usable lengths of gamma foil with a maximum thickness of 0.050" and a thickness of 0.020" being the most desirable. The immediate objective of my research is the determination of existing conditions at the roll and workpiece interface during this rolling of the gamma material so that constitutive equations can be written for computer simulations using finite element modelling. Although a good deal of time was spent on the design of apparatuses and the establishment of test methods to determine the interface heat transfer coefficient and the interface coefficient of friction, the bulk of my time was spent on the design of a device for testing the electrical resistivity of the roll and workpiece materials and in looking at gamma microstructures.

Even thou[illegible] my part in the attainment of the ultimate goal seems

somewhat trivial by comparison, it is a necessary piece in the solution of the gamma rolling puzzle. In order to be able to model the process with even remote accuracy it is required that each interface property be thoroughly examined and painstakenly measured. In order to obtain a complete answer, it is imperative that all parts of the question are accurately resolved.

III.

Due to the fact that my major objective involves actually designing a test device to be used for measuring interface resistivity, it is necessary to go through some basic steps in the engineering design process as an approach to realizing this objective. The first and most obvious step is to state the need, which is for the establishment of an accurate method to determine the electrical resistivity at the area of contact between the titanium aluminide sheet and the TZM molybdenum rolls. The next step is to state the problem, which is to design a piece of equipment which can accurately duplicate the conditions which exist in the actual gamma rolling procedure and provide a way in which the interface resistivity within this model can be physically measured and applied to the real life situation. Once these early steps are clearly stated and understood, it is then possible to progress further and examine the proposed solution.

The solution which was settled on at this point is illustrated in the back of this report. It is a fairly simple design, but it should be

more functional and accurate than the c-clamp knife edge configuration which was proposed before I began working on the project. The main problem I had with this c-clamp system was the fact that the clamps would have to be positioned by hand, which would impose a certain degree of human error right at the beginning of the experiment. My design, which will be explained in more detail later, has a built-in knife edge system that will provide a more exact and repeatable potential contact spacing, which is extremely important since the electrical resistivity will be calculated using the equation:

$$\rho = \frac{R \cdot As}{\ell p} \quad (\Omega - cm) \qquad (1)$$

where: R = the measured d.c. resistance in ohms

As = the specimen area in cm^2

ℓp = potential contact spacing in cm.

As can easily be seen, a small variance in potential contact spacing can lead to fairly large percentage of error once it is mathematically incorporated into this formula.

This test equipment will have to be contained in an environmental chamber in the same manner as the tests for heat transfer coefficient and frictional coefficient. The reason for this chamber is to reproduce the conditions that will exist during the real life gamma rolling process, which will be temperatures up to 2200°F and an inert environment to prevent roll and workpiece oxidation. A precision Kelvin bridge will have to be utilized for this resistivity test in order to measure the extremely low values of resistance which will exist in our system. The bridge is also used to provide the current needed to find the potential drop between the knife edges and through the interface. We

plan to use a Biddle Instruments DLRO digital low resistance ohmmeter for our bridge.

The device illustrated in this report is a relatively simple one, but is should prove effective in keeping equal spacing between the potential contacts and in keeping these knife edges touching the samples with a reasonable amount of contact force. This force will be provided by a leaf spring constructed from a formed 0.125" piece of high temperature material, possibly Inconel X750, although material determination for the components of this design has not been accomplished to date and will require some testing and interaction with metallurgists. The knife edges will be kept in contact with the samples by sliding the entire fixtured unit along the provided slots and tightening the appropriate bolts and by adjusting the two major bolts between the knife edges. The knife edges will be isolated from each other through insulation with mica or some other nonconductive ceramic. The current from the Kelvin bridge will enter at the base of each sample and the resistance will be measured across the knife edges as indicated. The press will cause intimate contact between the TZM and TiAl samples and therefore eliminate the possibility of reading a misleadingly high constriction resistance due to the surface finishes of the samples. The samples will be square to allow better knife edge contact and will each contain a thermocouple to check for temperature gradient.

The next completely unique objective which I personally worked on was to determine whether there was a consistency of flow units (the largest visible microstructural entities) within an forged billet of gamma titanium aluminide. This determination is an important one due to the fact that any discontinuity of the flow units would require accurate

mapping of where each compression sample came from within the billet. I checked the billet by obtaining a cross sectional slice which was cut from the whole by EDM. From this slice I cut six samples from various locations and mapped these locations as can be seen in the provided diagram. I then mounted, polished, etched using Keller's etch, and photographed each microstructure. As can be seen from the photographs, it appears that there is in fact a consistent flow unit of a lamella structure throughout the billet, therefore compression samples may be taken from virtually any location within the billet with reasonably similar results.

IV. RECOMMENDATIONS

In order to produce a usable prototype of the proposed resistivity testing device, it is first necessary to determine the materials to be used for its component parts. Although oxidation will not be a problem due to the inert environment that will be used, all materials must be able to maintain integrity at high temperatures. For example, the material to be used for the leaf spring must be able to maintain its modulus of elasticity through a wide range of temperatures since deterioration of this modulus would decrease the contact force between the knife edges and the samples and thereby introduce a degree of error into the experiment. As can be expected, my recommendations also include the building and testing of this apparatus. From testing, design changes can be made as appropriate.

Continued work in gathering interface properties is imperative if the rolling of the gamma titanium aluminide is ever to be realized. Without this data computer simulations will not be possible, leaving trial-and-error rolling as the only remaining method of determining processing conditions. Due to the extremely high cost of the gamma material, this is not a truly feasible option. It will be necessary to continue microstructural work for a complete insight into this material system, so this is also recommended.

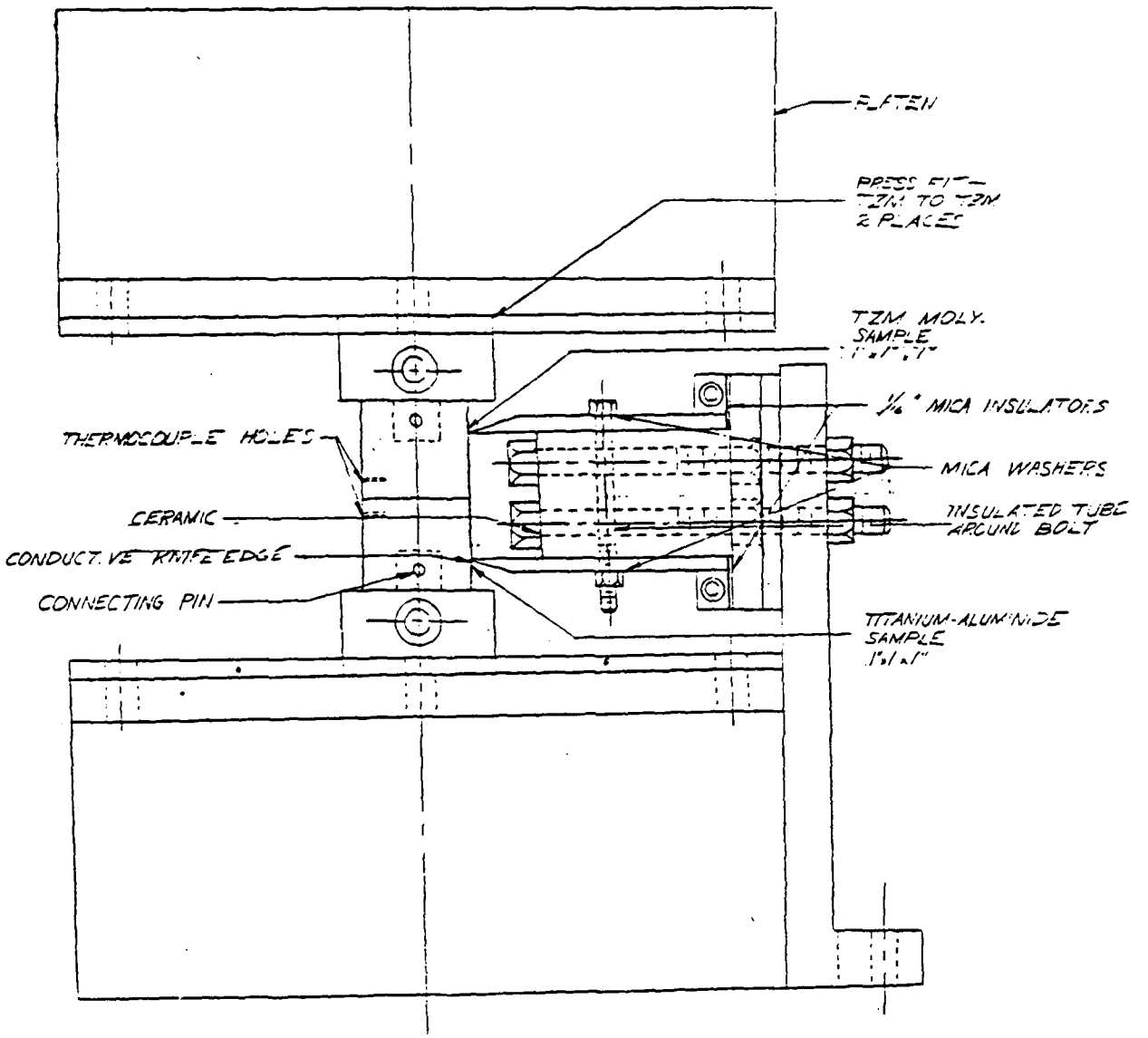

FRONT VIEW

TEST APPARATUS FOR RESISTIVITY

A. HENSLEY
65% REDUCTION

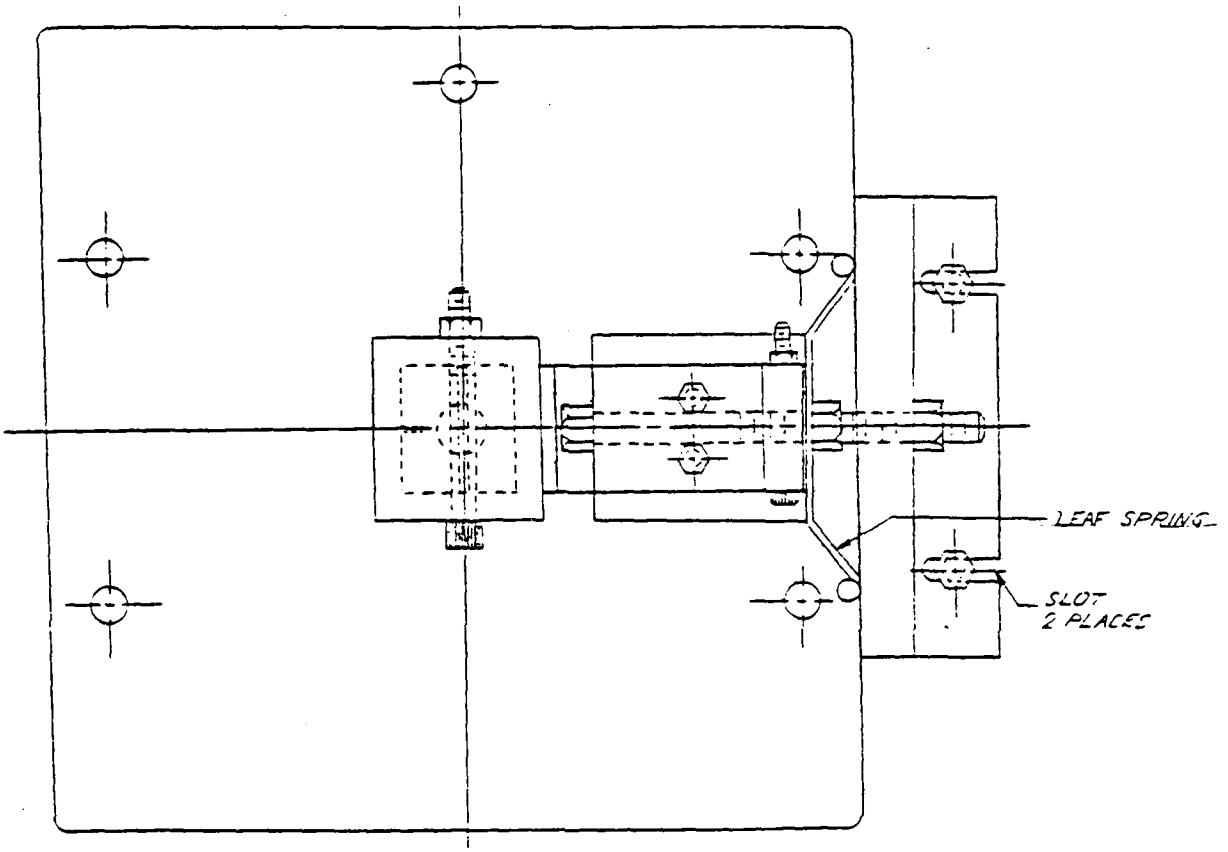

TOP VIEW
TOP PLATEN REMOVED

TEST APPARATUS FOR
RESISTIVITY

A. HENSLEY
65% REDUCTION

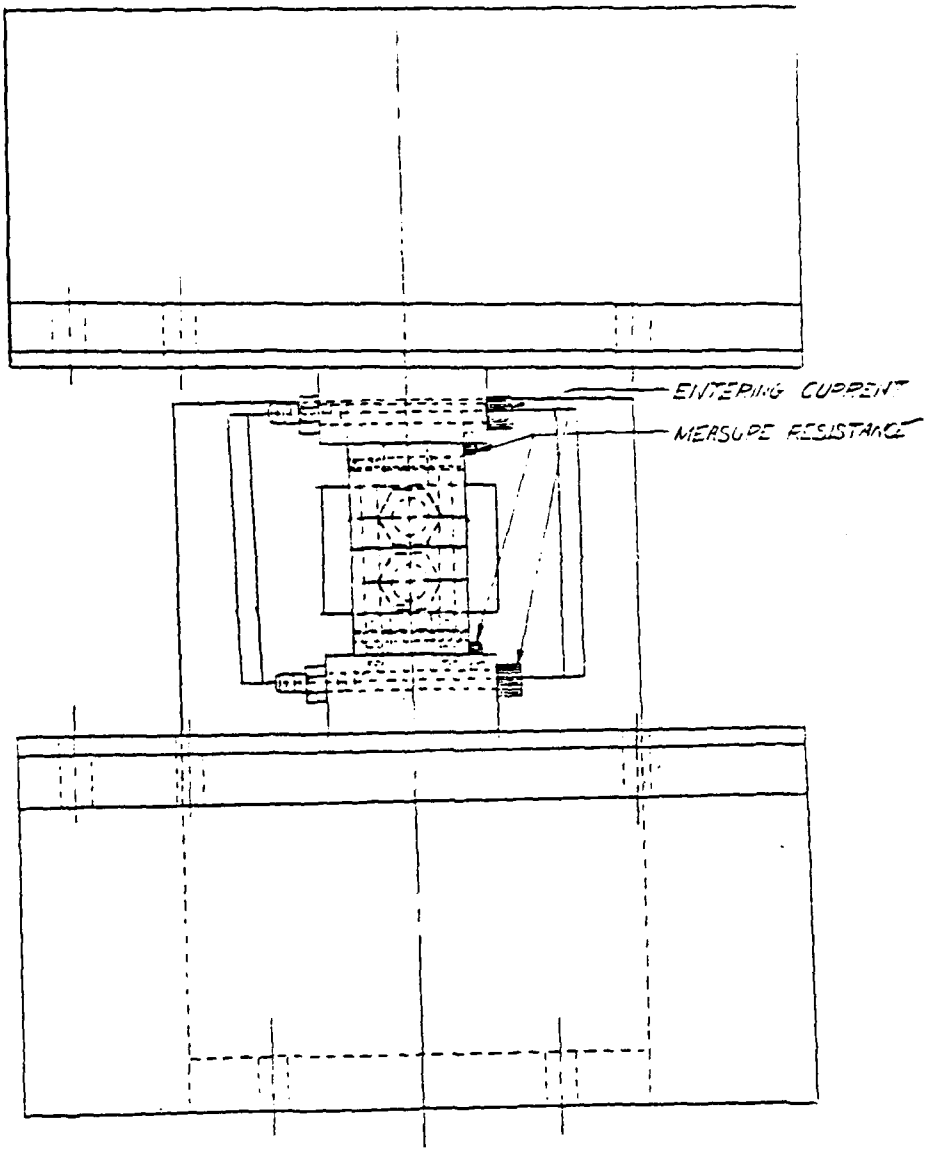

LEFT VIEW

TEST APPARATUS FOR
RESISTIVITY

A. HENSLEY
65% REDUCTION

MAP OF SLICE FROM BILLET

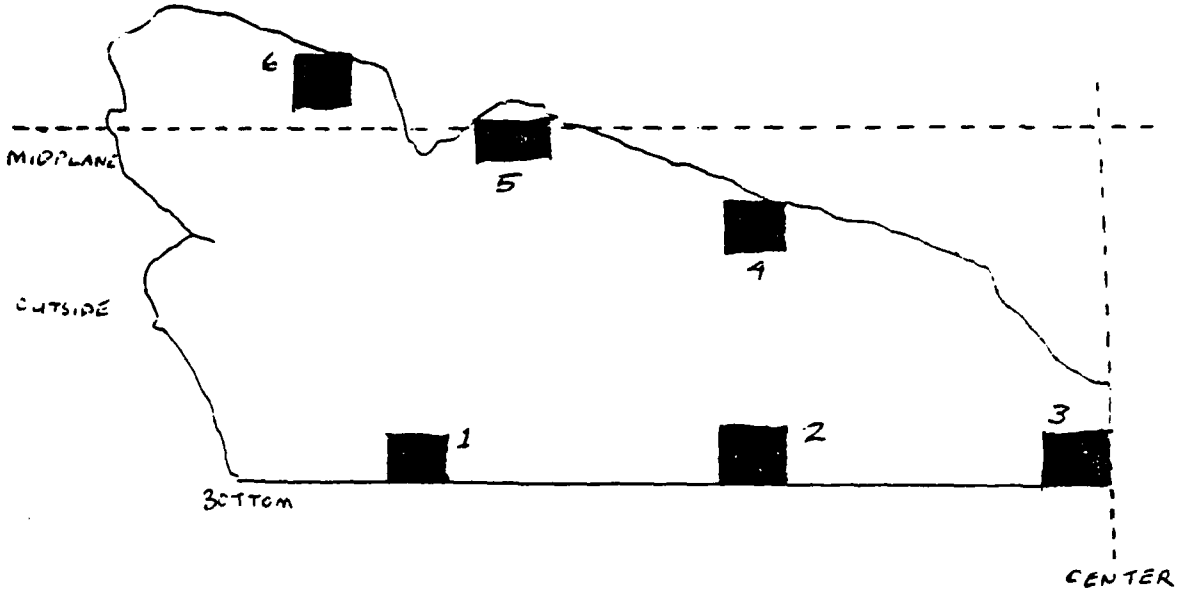

#1 200x

#2 200x

#3 200x

#4 200 x

#5 200x

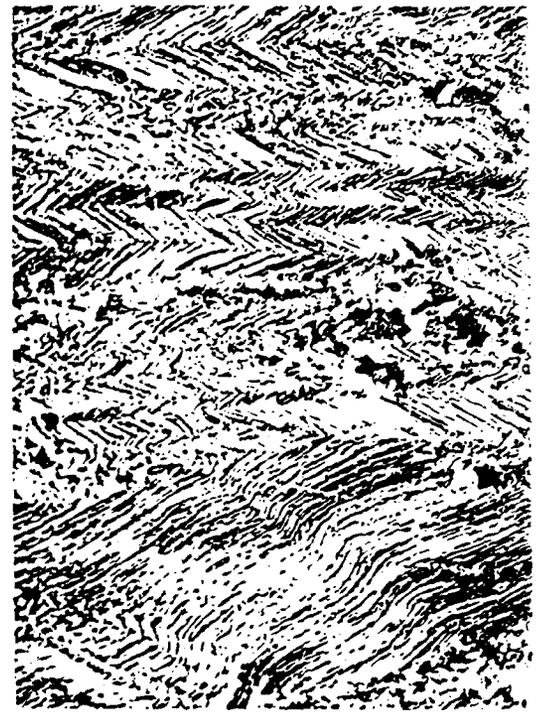

#6 200x

REFERENCES

Holm, Ragnar, Electric Contacts, Theory and Application, New York, New York, Springer-Verlag New York Inc., 1967.

Jain, Vinod, "Technical Proposal for Experimental Determination of Coefficient of Friction, Heat Transfer Coefficient, and Electrical Resistivity", University of Dayton, Dayton, Ohio, March 1986.

1988 USAF-UES SUMMER FACULTY RESEARCH PROGRAM/
GRADUATE STUDENT RESEARCH PROGRAM

Sponsored by the
AIR FORCE OFFICE OF SCIENTIFIC RESEARCH
Conducted by the
Universal Energy Systems, Inc.
FINAL REPORT

Phase Relationships in Al-Nb-X Ternary Alloy Systems

Prepared by:	J.P. Simmons
Academic Rank:	Graduate Student
Department and University:	Department of Metallurgical Engineering and Materials Science Carnegie Mellon University Pittsburgh, PA 15213
Research Location:	AFWAL/MLLM Wright-Patterson Air Force Base Fairborn, OH 45433
USAF Researcher:	D.M. Dimiduk
Date:	September 27, 1988
Contract No:	F49620-88-C-0053

Phase Relationships in Al-Nb-X Ternary Alloy Systems

by

J.P. Simmons

ABSTRACT

Samples of Al-Nb-Mo, Al-Nb-Co, and Al-Nb-Cr were heat treated and examined with microprobe and X-ray diffraction analysis in order to determine whether or not any $L1_2$ compounds form in the ternary systems. It was found that no $L1_2$ ternaries were formed as a result of substitution for the Al by the elements Co and Cr at 1200°C and 1300°C, respectively. Preliminary information indicated this to be the case with Mo at 1400°C as well. From the samples examined, it was not possible to determine whether or not any $L1_2$ phases formed as a result of substitution for Nb. Preliminary evidence of an unreported phase in the Al-Nb-Mo system was found. It was also found that Mo was the only one of these that dissolved to any extent in the DO_{22} phase. Some phase diagram data were generated. Recommendations were made as to completion of work in these systems, procedural changes, and the applicability of the Pettifor scheme as a predictive tool.

Acknowledgements

The author wishes to express appreciation to Dennis Dimiduk and Dan Miracle of AFWAL for their advice and assistance as well as to P.R. Subramanian of Universal Energy Systems (UES), with whom the author worked closely during all phases of this work.

The technical assistance of Tim Campbell and George Cornish of UES in sample preparation was greatly appreciated. Special mention should go to Joe Henry of UES for virtually all of the microprobe measurements made in this study.

This work was sponsored by the Air Force Office of Scientific Research/AFSC under contract #F49620-88-0053 and administered by UES.

I. Introduction

The modern superalloys are based on the Ni-Al system and derive a significant proportion of their strength from the γ' Ni_3Al phase. It is anticipated that the Ni based superalloys will not provide sufficient high temperature stability for gas turbine engine materials needs into the next century. This work is an attempt to identify suitable materials for the development of higher temperature superalloys.

The γ' phase has a cubic, $L1_2$ structure. This phase has the property that its strength increases with increasing temperature.[1] Since other intermetallic compounds with the $L1_2$ structure have been identified with this property,[2,3,4] it is natural to search for high melting point compounds with this structure. Since none of the known binary $L1_2$ compounds have suitable properties, the search has been directed towards ternary compounds that have the $L1_2$ structure.

The Al-Nb system has an intermetallic compound with Al_3Nb stoichiometry that is stable up to about 1600°C,[5] and forms the starting point of this investigation. This compound has a tetragonal DO_{22} structure, which can be viewed as two $L1_2$ unit cells, with the center (001) plane translated by 1/2[1 1 0].

Work by Pettifor[6] and Villars[7,8] give mapping schemes by which, in principle, the structures of binary alloys can be predicted from available information. Within the Pettifor scheme, the observed structures corresponding to a particular combination of elements tend to cluster into regions, or structure fields, when plotted against a parameter referred to as 'the Mendeleev number.' The DO_{22} structure field forms an 'island' within the $L1_2$ structure field. Pettifor[9] suggests a method by which these results may be applied to ternary and quaternary alloys in order to convert one structure to another, by averaging the Mendeleev numbers. This work uses the work of Pettifor as a predictive tool in order to identify suitable ternary additions that will produce ternary compounds with the $L1_2$ structure.

The demands of increasing performance of gas turbines will require structural materials able to withstand higher temperatures than presently available. High temperature materials then comprise a class of materials in which the Air Force is very interested for future aircraft propulsion systems. The study of high temperature intermetallic compounds has been initiated in order to achieve these increased temperature stabilities. The major subject of interest of the author is chemical ordering in solids; he has received a Masters of Engineering in metallurgical engineering at Carnegie Mellon University and is currently

pursuing a PhD in metallurgical engineering at the same school, studying order-disorder reactions.

II. Objectives

This work was part of an ongoing project and had three objectives: (1) to determine whether or not $L1_2$ compounds formed in ternary Al-Nb-X systems, (2) to give a preliminary evaluation of the applicability of the Pettifor scheme for materials design, and (3) to generate reliable phase diagram data in the systems studied, particularly as pertains to the DO_{22} phase fields.

The primary objective of this work was to determine whether or not $L1_2$ compounds are formed in certain ternary Al-Nb-X systems, those containing Mo, Co, and Cr as the ternary element. It was determined that, in the systems examined, no $L1_2$ compounds form as a result of ternary substitution for Al. The alloy compositions examined were too lean in Al content to determine whether or not $L1_2$ compounds formed by ternary substitution for Nb.

Traditionally, investigations of this type have proceeded according to a trial-and-error algorithm. This is a time consuming and costly approach. As a second objective, it was decided to use this work as a preliminary evaluation of the applicability of the Pettifor scheme for materials design. Some suggestions as to application of this approach are made in the Recommendations section.

It was decided to conduct the work with sufficient care so that some useful phase diagram information would be generated as a by-product. This final objective was considered to be independent of those mentioned above. Again, particular attention was paid towards generating reliable data as to the ternary element solubility in the DO_{22} phase.

III. Experimental Procedures

Buttons of five Al-Nb-X alloys that were prepared by arc melting in vacuo were heat treated at various temperatures and examined with both microprobe and X-ray powder diffraction. The compositions of the samples are listed in Table 1. Throughout this work, alloy compositions will be referred to with the notation: x-y elem./T, which is a shorthand notation for Al-x%at.Nb-y%at.elem. heat treated at temperature T. Thus, 20-20 Mo/1400°C designates the sample of nominal composition Al-20%at.Nb-20%at.Mo that was heat treated at 1400°C.

Samples were wrapped in Ta foil and then heat treated in an atmosphere of Ar that was purified by passing over Ti chips at 1000°C. In order to insure that equilibrium was

reached, heat treatment times of at least 100 hours were employed. Usually some weight loss (1-2%) was observed, indicating that some Al volatilization had occurred.

Samples were cut from the buttons with an abrasive disk saw, mounted in resin, and polished for microprobe. Microprobe examinations were made with a 10nA beam with a 20kV accelerating potential. Composition data were measured with the microprobe, using the the ZAF method,[10] and were statistically analyzed in the standard fashion.[11]

Samples were prepared for X-ray analysis by powdering in a mortar and pestle to -360 mesh. Generally, a strain anneal at 1000°C for 1 hour was required in order to produce sharp X-ray peaks. This was done by wrapping in Ta foil and heating either in vacuo or in an atmosphere of Ar. No oxidation was observed, but a small amount of Al generally was deposited on the foil, indicating some Al volatilization had occurred. X-Ray powder patterns were generated with a diffractometer employing Cu Kα radiation produced with an accelerating voltage of 40kV and tube current of 50 - 150 mA.

IV. Results And Discussion

Generally, each sample was within a three phase field, which made it possible to examine large regions of the isothermal phase diagram with a small number of samples. This work did not identify enough three phase triangles to completely characterize the entire diagrams of any of the ternary systems examined, but enough of each diagram was examined to preclude the formation of $L1_2$ compounds by substitution of the ternary element for Al in the Al-Nb-Co and Al-Nb-Cr samples. That is, no compounds with composition $(Al,X)_3Nb$ distinct from the DO_{22} phase were identified in these systems. The results of the Al-Nb-Mo ternaries are regarded as preliminary, but seem to indicate that no $L1_2$ phases form in this system as a result of Al substitution. It was not possible to unambiguously determine whether or not any $Al_3(Nb,X)$ $L1_2$ compounds were formed by Nb substitution.

Al-Nb-Mo

Two samples, 20-20 Mo/1400°C and 25-12.5 Mo/1400°C were examined. The results of these two are contradictory, since all three of the 25-12.5 Mo/1400°C phases lie entirely within the three phase triangle formed by the 20-20 Mo/1400°C sample. These are shown in Figs. 1(a) and 1(b). In all, four phases were identified that were found in these two samples.

Two of the four phases were identified as being DO_{22} $Al_3(Nb,Mo)$ and A15 $Al(Nb,Mo)_3$. Of the other two, one is believed to be the σ phase, while the other has not been identified.

A sample of 20-20 Mo/1300°C was used to identify the DO_{22} and A15 structures. Differential thermal analysis (DTA) was used to show that no reaction occurred between 1300°C and 1400°C. It is believed that the 1300°C results were representative of the 1400°C microstructure, insofar as phase identification is concerned. Sixteen peaks (out of sixteen calculated for DO_{22}) that did not overlap any A15 peaks in a sample of 20-20 Mo/1300°C were identified. The A15 structure was identified in this sample by seven (of eight calculated) peaks that did not overlap those of the DO_{22} structure. The compositions of these phases, along with all of the composition data obtained in this study are listed in Table 2.

The 20-20 Mo/1400°C sample was found to have DO_{22} and A15 plus a third, of composition Al-40%at.Nb-17%at.Mo (approximately the composition of Al_2Nb_2Mo). This phase was also found to be present in the 25-12.5 Mo/1400°C sample (identified by its composition), and is plotted in Fig. 1(a). This could be an extension of the σ phase found in the binary, but it is believed, at this writing to be another, unreported phase.

The composition of the σ phase in the binary is Al-59%at.Nb.[12] In an earlier X-ray study[13] by Hunt and Raman, the σ phase boundary was reported to be at approximately Al-35%at.Nb-35%at.Mo at 1000°C. This composition does not agree with that of the Al_2Nb_2Mo phase, but does agree with one of the phases found in the 25-12.5 Mo/1400°C sample, as shown in Fig. 1(b). The composition of this phase was found to be Al-33%at.Nb-28%at.Mo. For this reason, this phase will be designated σ(?) in this work, since it appears to be the σ phase. It was not possible to obtain a confident fit between the diffraction peaks for this sample and simulations of the σ structure. A sample with a larger volume fraction of this phase would give much more reliable diffraction data.

It is not clear exactly why the σ(?) phase was found in the 25-12.5 Mo/1400°C sample, but not in the other. It is possible that it is stabilized by a small amount (~1%at.) of Ti impurity that was found in the 25-12.5 Mo/1400°C sample with the microprobe. Additional work in this system is recommended in the Recommendations section.

According to the Pettifor scheme, if compounds were to form by substitution for Al, there should be an $L1_2$ phase at a composition corresponding to an average Mendeleev number of 76, which should form at the ideal composition of 25-12.5 Mo. This is

apparently not the case here, although the reproducibility of the above results is not comforting. No conclusion regarding the $L1_2$ phase formation in this system is then made.

Typical microstructures examined are shown in Figs. 3(a) and 3(b), which show the 20-20 Mo/1300°C and 25-12.5 Mo/1400°C microstructures, respectively. The DO_{22} and A15 phases image in Fig. 3(a) as dark and light, respectively. The DO_{22}, σ(?), and Al_2Nb_2Mo phases image in Fig. 3(b) as dark, light, and grey, respectively.

A considerable solubility for Mo was found in the DO_{22} phase, reaching approximately 5%at. This phase field appears to be elongated in the direction of Al_3(Mo,Nb), indicating that the Mo substituted for the Nb atoms. No independent confirmation of this point was made. The maximum solubility of Mo in the DO_{22} phase is probably much higher; it was reported to be about 15%at. at 1000°C by Hunt and Raman.

Al-Nb-Co

Samples of 20-5 Co/1200°C and 25-12.5 Co/1200°C were examined. The ternary diagram for these alloys is shown in Fig. 2. The compositions of the phases found are listed in Table 2. Originally only the 25-12.5 Co/1200°C sample was analyzed with DTA; subsequent work in the 20-5 Co/1200°C alloy showed a reaction at approximately 1170°C. This appears to have been a peritectic melting point of the δ phase of the Al-Co binary.[14]

Four phases were identified between these two samples: DO_{22}, B2, what appears to be the C14 Laves phase, and the remains of the liquid that was present in the 20-5 Co/1200°C alloy. The DO_{22} phase was identified by its diffraction pattern in the 20-5 Co/1200°C sample, as well as by its composition. All others were identified by their compositions by comparison with those available in the literature. No $L1_2$ phases were observed.

The 20-5 Co/1200°C sample was found to contain DO_{22} Al_3Nb, B2 AlCo, and what appears ω be solidified liquid. Twenty-five (of twenty-six calculated) peaks in the DO_{22} structure that did not overlap any of those calculated for B2 were identified in the pattern. Only two peaks were found in addition to those predicted for DO_{22}; one of these matched that of the B2. It is believed that the volume fraction of all but the DO_{22} phase were too small to be reliably detected with X-ray diffraction. The DO_{22} phase was found to have a composition Al-25%at.Nb-0.15%at.Co, in agreement with the ideal stoichiometry as given in the published Al-Nb phase diagram.[15] The B2 alloy was found to have the composition Al-0.04%at.Nb-46.5%at.Co, which agrees with the 46%at.Co solvus boundary for the AlCo (ζ) phase given in the published Al-Co phase diagram.[16] The final mass of material in this phase is thought to be a mixture of γ- and δ- Al-Co phases that formed on furnace

cooling from a liquid. Its composition was found to be Al-0.3%at.Nb-28.1%at.Co, which compares with Al-25%at.Co, for the location of the liquidus at 1200°C reported in the published binary diagram. Obviously, if reliable phase diagram information is desired, this work should be repeated below the liquidus; this result is presented here simply because it shows that no ternary phases form in this three phase field.

The 25-12.5Co/1200°C sample had three phases that were identified as the DO_{22}, B2, and what appears to be the C14 phases. The identifications here were made strictly on the basis of their compositions. The composition of the C14(?) phase was measured to be Al-33%at.Nb-15.4%at.Co. Hunt and Raman[17] report extensive solubility in the C14 Nb-Co binary phase that extended almost to the Al-Nb binary diagram. This determination is regarded as preliminary.

According to the Pettifor scheme, if the Co were to substitute for the Al, there should be an $L1_2$ phase at a composition corresponding to Mendeleev number 76 on the Al sublattice. Thus, at a composition of Al-25%at.Nb-18.8%at.Co, there should be an $L1_2$ compound, according to an Al-substitution scenario within the Pettifor scheme. This composition lies within the 25-15.5 Co/1200°C three phase (solid) triangle, as shown in Fig. 2. No $(Al,Co)_3Nb$ phase was observed.

Typical microstructures of these two alloys are given in Figs. 3(c) and 3(d). In Fig. 3(c), the matrix is the DO_{22} phase, the grey areas are B2, and the black areas are the former liquid. Again, the results for the 20-5 Co/1200°C sample should be viewed as preliminary. In Fig. 3(d), the DO_{22} phase images as grey, the B2 as dark, and the C14 phase images as light.

No appreciable amount of Co was found to dissolve in the DO_{22} phase, being about 0.15 and 0.74%at. in the 20-5 Co/1200°C and 25-12.5 Co/1200°C samples, respectively. Some of the compositional measurements in the binary phases listed in Table 2 had some scatter, giving 95% confidence limits outside of the diagram. Since all of these solubilities were small, it was decided not to be worth pursuing further.

Al-Nb-Cr

Two samples, 25-12.5 Cr/1300°C and 15-25 Cr/1300°C were examined. Both were within the same three phase triangle. The ternary diagram determined by the 15-25 Cr/1300°C sample is given in Fig. 3.

Four phases were found to be in the 25-12.5 Cr/1300°C sample. These phases are likely to be DO_{22}, A2 Cr(+Al) solid solution, σ phase, and C14 (Laves phase), as identified from

their compositions. Obviously, equilibrium had not been attained, since there were four phases. The C14(?) phase appeared in the as cast microstructure, implying that this phase had formed during cooling. All except the C14(?) phase were found in the 15-25 Cr/1300°C sample. Apparently, this phase formed on cooling from the melt, followed by a peritectic-type reaction, requiring dissolution of C14 to form another phase. The kinetics of dissolution of this phase would inhibit its disappearance.

The composition of the DO_{22} phase was found to be Al-24%at.Nb-1%at.Cr in the 25-12.5 Cr/1300°C sample and Al-25.0%at.Nb-1.31%at.Cr in the 15-25 Cr/1300°C sample. The Cr(+Al) solid solution compositions for these two samples were Al-0.7%at.Nb-70.4%at.Cr and Al-0.4%at.Nb-65.8%at.Cr, respectively. These compositions are in agreements with the reported solidus locations as reported in the published binary diagram.[18] Those for the σ(?) phase were Al-49.9%at.Nb-15.9%at.Cr and Al-49.8%at.Nb-17.3%at.Cr in the two samples, respectively. This is additional evidence that the C14(?) phase formed from the melt, but did not completely dissolve at lower temperatures, where the three equilibrium phases formed.

Hunt and Raman[19] reported the phase boundary at 1000°C for the C14 phase to be within the three phase triangle determined here. This is probably in error, since the heat treatments given here were 1300°C for 100 hours, whereas their heat treatments were 1000°C for one week (168 hours). Apparently, the high temperature boundary of the C14(?) phase is within this triangle, but recedes with descending temperatures. Hunt and Raman also reported about 5%at. solubility for Cr at 1000°C. This work gave a much smaller solubility of about 1%at. at 1300°C.

According to the Pettifor scheme, if the $L1_2$ compound formed by substitution of Cr for Al, the average Mendeleev number of 76 would be required. The composition of the expected $L1_2$ phase would have been Al-25%at.Nb-13%at.Cr. This composition is within the three phase field given in Fig. 3. No $L1_2$ compound was formed by Al substitution.

A typical microstructures of the 15-25 Cr/1400°C alloy is given in Fig. 3(e). The DO_{22} phase images as grey, the Cr(+Al) solid solution images as black, and the σ(?) phase images as light.

The compositions of the phases found in the 15-25 Cr/1300°C alloy are listed in Table 2. Those for the 25-12.5 Cr/1300°C alloy are not listed because (1) they did not correspond to an equilibrium microstructure, and (2) about 0.5%at. W contamination was detected in this sample with the microprobe. It is believed that the 15-25 Cr/1300°C sample is representative of the equilibrium phase distribution.

VI. Recommendations

This report makes recommendations of three types: (1) regarding changes in procedures, and (2) regarding unfinished work in these three systems, and (3) regarding future systems to examine. The procedural changes recommended here are largely designed to reduce the amount of work involved in characterizing the phases that form in ternary systems. Additional work in recommended in the Mo,Co, and Cr ternaries. Recommendations of future systems that are likely to conform to the assumptions of the Pettifor scheme are made.

Procedures

Two problems were encountered during this work that increased the time necessary to generate phase diagram information: (1) heat treatments that did not produce microstructures sufficiently coarsened that all of the phases could be analyzed with the microprobe and (2) appearance of four phases in samples even after long heat treatments at elevated temperatures.

It was originally planned to generate isotherms at temperatures that were chosen somewhat arbitrarily at 100-200°C below the lowest temperature reaction observed in DTA on one alloy per ternary system. This was not possible, since heat treatments conducted at these temperatures required excessive heat treatment times to produce acceptable microstructures. Generally, heat treatments at 25-50°C below this reaction were required in order to guarantee that equilibrium would be reached in 100 hours.

It is believed that samples that had four phases contained one phase that formed from the melt that was not an equilibrium phase at the lower temperature. This has been a serious problem, since heat treatments to dissolve one solid phase in order to produce another require an impractical length of heat treatment time. Alloy compositions of this type should be avoided.

In light of these difficulties, the following recommendations are made in order to reduce time required to produce phase diagram information:

(1) Generate DTA scans for all samples. From these, a heat treatment temperature of approximately 25-50°C below the lowest temperature reaction can be chosen.

(2) Heat treat each sample for 100 hours at 25-50°C below the lowest temperature reaction observed in its DTA scan. Obviously, not all samples will be heat treated at the same temperature, by this algorithm. However, the compositional data can be projected

onto one plane, just as cooling curves are in ceramic engineering. This will give the approximate phase boundary locations that will be useful if subsequent isotherm determination is undertaken. This information is sufficient to characterize the ternary system in terms of phase identities.

(3) Chose the initial composition in order to avoid peritectic reactions. Since in all cases, the DO_{22} phase is expected to be in the sample, the starting composition should be chosen close enough to the DO_{22} composition that this phase is the first to form on cooling. In the past, the alloy composition was chosen to correspond to that of the predicted $L1_2$ compound; it is recommended that the alloy composition be about half way between this composition and that of the DO_{22}.

Completion of Mo,Co, and Cr Ternary Work

Some questions remain regarding these three systems. The following recommendations are made in order to clarify these:

(1) Repeat the Mo determination. The irreproducibility of the Al-Nb-Mo data at 1400°C is cause for concern. An additional alloy mixture of a composition lying within the 20-20 Mo/1400°C three phase triangle should be prepared and heat treated at 1400°C for a longer period of time, say 200 hours. It is expected that this will cast a deciding vote in favor of one of the other results previously obtained.

(2) Repeat one Co determination. The 20-5 Co/1200°C sample apparently was heat treated above the liquidus of in the Al-Co binary. A sample of 20-5 Co should be heat treated at about 25°C below the peritectic temperature as determined by DTA and re-examined. It is not expected that this will yield any new information, but it will provide more uniformity of procedures.

(3) Investigate for Nb substitution. All three systems should be investigated further to determine the behavior along the $AL_3(Nb,X)$ compositions. It is expected that the Mo will not convert the DO_{22} to $L1_2$, in agreement with the predictions of the Pettifor scheme and the 1000°C data of Hunt and Raman. It is also expected that neither Cr or Co will dissolve extensively in the DO_{22}. These predictions should be verified, however.

(4) Investigate the Al_2Nb_2Mo phase. The identity of this phase should be made by preparing an alloy close to this composition and generating X-ray diffraction data.

Future Systems

Although no ternary $L1_2$ phases were found to form in these systems, this does not disprove the Pettifor scheme. This scheme is based on existing information and can be summarized as follows: if the ternary $L1_2$ compound forms, then its composition will be within the $L1_2$ structure field. There may be a number of subsidiary conditions that must also be met in order for the ternary $L1_2$ structure to be formed, given that it appears in the $L1_2$ structure field.

In order for an average Mendeleev number to be used for predicting this ternary phase, it is important for the two elements that comprise this average be similar, chemically. That is, they must be interchangeable. One property of two elements of this type is extended miscibility in the binary, since one element can replace the other without upsetting its crystal structure greatly.

This work then predicts that the ternary additions that will behave as Pettifor describes will include those that have extended solubility in either Al or Nb (or both). The elements that exhibit extended solubility in Al should replace the Al in the DO_{22} to produce $(Al,X)_3Nb$, while those that have extended solubility for Nb should form $Al_3(Nb,X)$. This is apparently the case with Mo, which has complete miscibility with Nb and is quite soluble in the DO_{22} phase. The fact that Co and Cr have small solubilities Al seems to agree with the observation that neither dissolves in the DO_{22} to any great extent.

The elements that exhibit solubility in Al in excess of 20%at. and that can be added to Al to move the composition of the alloy into the $L1_2$ structure field are Zn(60%), Ag(20%), and Mg(20%). Those corresponding to Nb are U(100%), Ru(60%), Re(45%), Os(32%), and Rh(23%). The compositions of the $L1_2$ compounds predicted by the Pettifor scheme, along with suggested alloy compositions to be prepared, are listed in Table 3.

VII. Summary

Samples of Al-Nb-Mo, Al-Nb-Co were examined in order to determine whether or not any ternary $L1_2$ compounds formed by substitution for Al by the ternary elements. It was found that this did not occur. It was fourd that Mo was the only element to dissolve to any extent in the DO_{22} Al_3Nb phase. Recommendations were made of procedural changes, future work in these systems, and the ways of applying the Pettifor scheme were made. Predictions as to the applicability of the Pettifor scheme to ternary mixtures were made.

References

1. Stoloff, N.S, "Ordered Alloys For High Temperature Applications," MRS Symposia Proceedings, Boston, MA, November 26-28, 1984, pp. 3 27.
2. Kumar, K.S., and Pickens, J.R., "Compression Behavior of the $L1_2$ Ordered Intermetallic $Al_{22}Fe_3Ti_8$," Scripta Metallurgica, 22, 1988, pp. 1015 1018, (1988).
3. Liang, S.J., and Pope, D.P., "The Yield Stress of $L1_2$ Ordered Alloys," Acta Metall., 25, 1977, pp.485 493.
4. Mishima, Y., Oya, U., and Suzuki, T., "Characteristic Mechanical Properties and Phase Stability of $L1_2$ Intermetallic Compounds," MRS Symposia Proceedings, 39, Boston, MA, November 26-28, 1984, pp. 263 277.
5. Bennett, L.H., ed.,"The Al-Nb System," Bulletin of Alloy Phase Diagrams, 2(1), 1981, pp. 75 81.
6. Pettifor, D.G., "The Structures of Binary Compounds: I. Phenomenological Structure Maps." J. Phys. C: Solid State Phys., 19, 1986, pp. 285 313, (1986).
7. Villars, P., Three-Dimensional Structural Stability Diagrams for 648 Binary AB_3 and 389 Binary A_3B_5 Compounds: III," J. Less-Commons Metals, 102, 1984, pp. 199 211.
8. Villars, P., "A Semiempirical Approach to the Prediction of Compound Formation for 3486 Binary Alloy Systems," J. Less-Common Metals, 109, 1985, pp. 93 115.
9. Pettifor, D.G., Submitted to Mat. Sci. and Tech.
10. Goldstein, J.I., Newbury, D.E., Echlin, P., Joy, D.C., Fiori, C., Lifshin, E., Scanning Electron Microscopy and X-Ray Microanalysis, New York, Plenum Press, 1981, pp. 326 306.
11. Ibid., pp. 430 439.
12. "The Al-Nb System," Bulletin of Alloy Phase Diagrams, 2(1), 1981, pp. 75 81.
13. Hunt, C.R., and Raman, A., "Alloy Chemistry of $\sigma(\beta U)$-Related Phases," Z. Metallkde., 59(9), 1968, pp. 701 707.
14. Massalski, T.B., ed., "Al-Co (Aluminum-Cobalt)," Binary Alloy Phase Diagrams, VI, Metals Park, OH, ASM, 1986, 102 103.
15. "The Al-Nb System," Bulletin of Alloy Phase Diagrams, 2(1), 1981, pp. 75 81.
16. Massalski, T.B., ed., "Al-Co (Aluminum-Cobalt)," Binary Alloy Phase Diagrams, VI, Metals Park, OH, ASM, 1986, 102 103.
17. Hunt, C.R., and Raman, A., Op. Cit.
18. Massalski, T.B., ed., "Al-Cr (Aluminum-Chromium)," Binary Alloy Phase Diagrams, VI, Metals Park, OH, ASM, 1986, 103 104.
19. Hunt, C.R., and Raman, A., Op. Cit.

Table 1. Alloy compositions (atomic %) used in this study.

Nom. Comp.		Al	Nb	Mo	Co	Cr	C	N	O
20-20	Mo	55.2	22.6	21.7	--	—	0.2	0.4	0.0
25-12.5	Mo†	56.9	27.6	13.7	—	—	0.1	1.8	10×10^{-3}
20-5	Co	73.1	20.8	—	5.0	—	0.3	0.7	27×10^{-3}
25-12.5	Co	63.6	24.3	—	11.3	—	0.2	0.6	20×10^{-3}
15-25	Cr	61.0	14.3	—	—	23.8	0.2	0.8	20×10^{-3}

† Approximately 1%at. Ti was found to be present in the 25-12.5 Mo sample with the microprobe.

Table 2. Phase boundary compositions (atomic %) determined in this study.
Error bars are calculated for 95% confidence.

Nom. Comp.		Temp.(°C)	phase	Al	Nb	Mo
20-20	Mo	1300	DO_{22}	75.0±0.2	19.2±0.3	5.8±2.2
			A15	28.4±1.7	14.5±0.4	57.1±1.2
20-20†	Mo	1400	DO_{22}	74.4	21.1	4.5
			A15	26.9	23.6	49.6
			σ?	42.3	40.3	17.4
25-12.5	Mo	1400	DO_{22}	74.4±0.3	21.9±0.4	3.56±0.04
			σ?	38.1±0.3	33.3±0.7	27.9±0.5
			2-2-1?	41.7±0.2	41.4±1.6	15.7±0.3
20-5	Co	1200	Liquid	71.5±1.9	0.3±0.4	28.2±0.1
			B2	53.4±0.7	0.04±0.02	46.5±0.4
			DO_{22}	74.6±0.4	25.3±1.0	0.15±0.02
25-12.5	Co	1200	B2	52.2±0.3	47.5±0.5	0.3±0.4
			C14?	51.4±0.2	33.2±1.5	15.4±0.2
			DO_{22}	74.11±0.04	25.2±1.1	0.74±0.04
15-25	Cr	1300	Cr (+Al)	33.8±0.2	0.4±0.2	65.8±0.2
			σ?	32.9±0.3	49.8±0.7	17.3±1.0
			DO_{22}	73.7±0.2	25.0±0.7	1.31±0.05

† Results for 20-20 Mo/1400C are preliminary.

Table 3. Alloy compositions recommended for further study. The Pettifor scheme was used to predict $L1_2$ $(Al,X)_3Nb$ or $Al_3(Nb,X)$ compounds. The Mendeleev number listed is the average Mendeleev number of the substituted sites.

	X	Mendeleev No.	$L1_2$ Comp.		Alloy Comp.	
Al Substitution						
	Zn	79	25-18.75	Zn	25-9	Zn
	Ag	76	25-33	Ag	25-15	Ag
	Mg	76	25-43	Mg	25-21	Mg
Nb Substitution						
	U	48	9-16	U	17-8	U
	Ru	58	11-14	Ru	18-7	Ru
	Re	55	15-10	Re	20-5	Re
	Os	58	12.5-12.5	Os	18.8-6.2	Os
	Rh	58	14.5-10.5	Rh	19.8-5.2	Rh

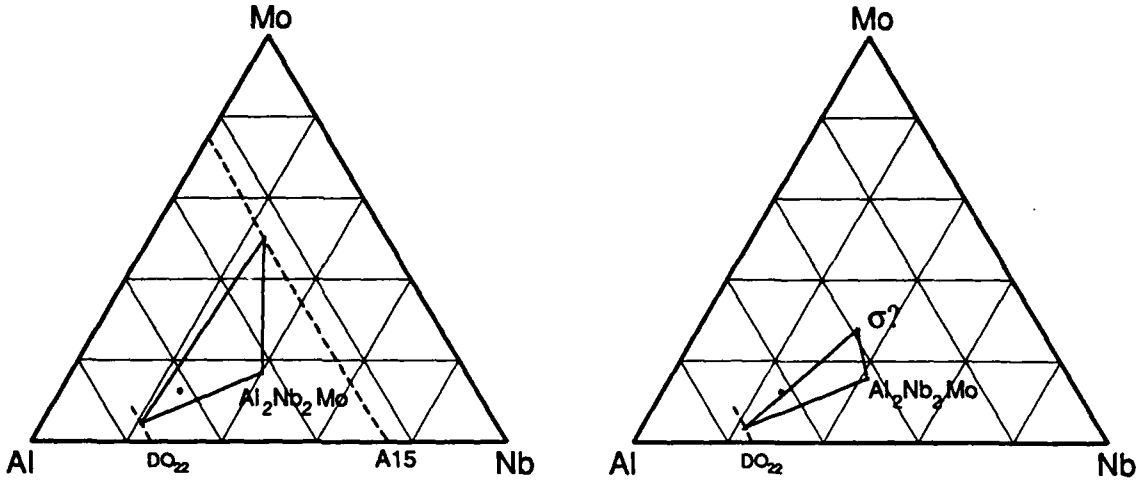

Fig. 1. Al-Nb-Mo 1400 C isotherms determined in this study. (a) 20-20 Mo/1400 C, (b) 25-12.5 Mo/1400 C. The circles represent compositions of ternary L12 phase predicted by the Pettifor scheme.

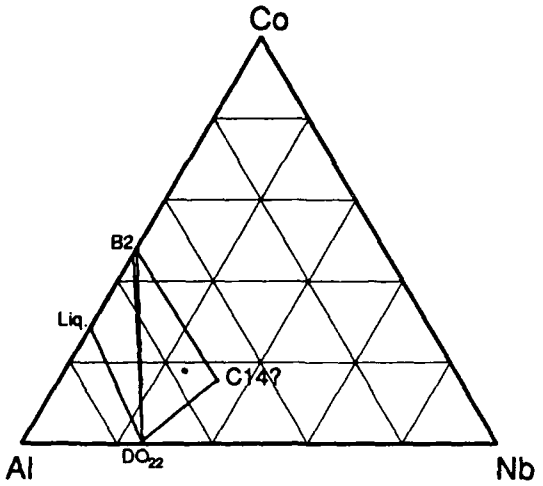

Fig. 2. Al-Nb-Co 1200 C isotherm determined in this study. The circle represents the composition of the L12 phase predicted by the Pettifor scheme.

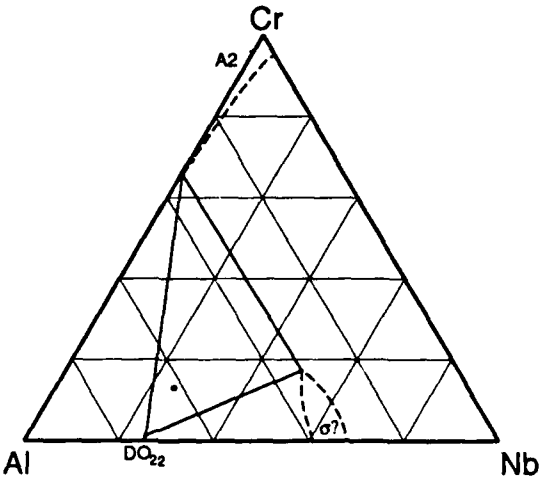

Fig. 3. Al-Nb-Cr 1300 C isotherm determined in this study. The circle represents the composition of the L12 phase predicted by the Pettifor scheme.

(a)

10 μ

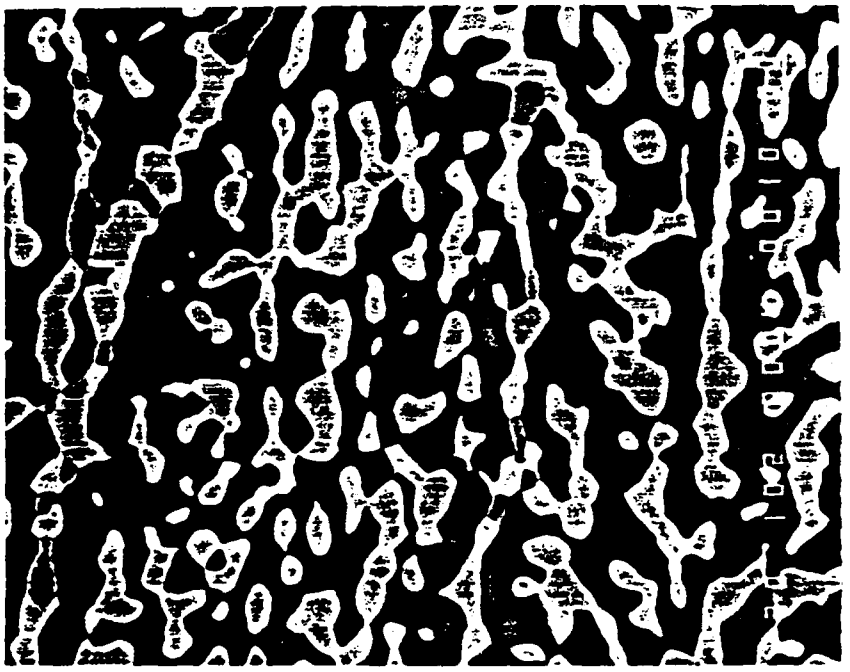

(b)

10μ

Fig. 4. (a) Typical microstructure of 20-20 Mo/1300 C examined in this study. (b) Typical microstructure of 25-12.5 Mo/1400 C examined in this study.

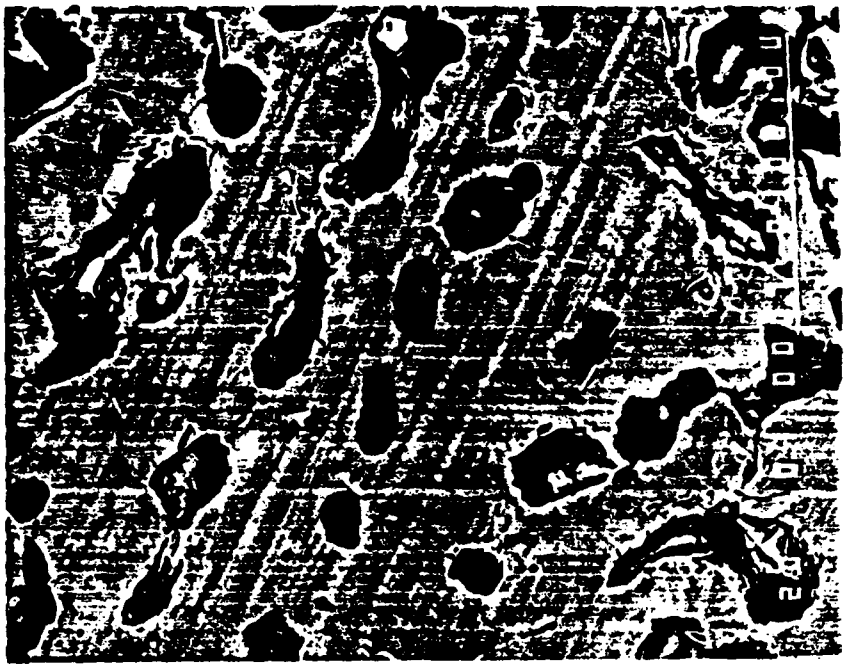

(c)

10 μ

(d)

10 μ

Fig. 4. cont. (c) Typical microstructure of 20-5 Co/1200 C examined in this study. (d) Typical microstructure of 25-12.5 Co/1200 C examined in this study.

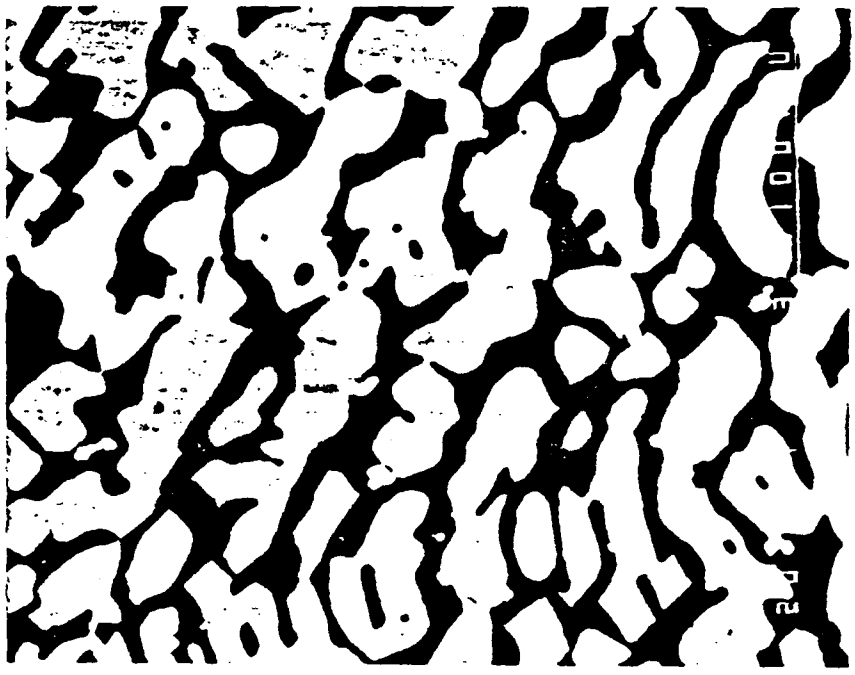

(e)

10 μ

Fig. 4. cont. (e) Typical microstructure of 15-25 Cr/1300 C examined in this study.

1988 USAF-UES SUMMER FACULTY RESEARCH PROGRAM/

GRADUATE STUDENT RESEARCH PROGRAM

Sponsored by the

AIR FORCE OFFICE OF SCIENTIFIC RESEARCH

Conducted by the

Universal Energy Systems, Inc.

FINAL REPORT

Design of mechanical joints and their implications to the implementation of a comprehensive computer aided design package.

Prepared By:	David A. Swick
Academic Rank:	Masters Candidate
Department and	Mechanical Engineering
University:	Ohio University, Athens, Ohio
Research Location:	AFWAL/MLTC, Wright-Patterson AFB, Ohio.
USAF Researcher:	Major Steven R. LeClair, Ph.D.
Date:	August 26, 1988
Contract No:	F49620-88-C-0053

Design of mechanical joints and their implications to the implementation of a comprehensive computer aided design package.

by

David A. Swick

ABSTRACT

The topic of this paper is to determine the kind of knowledge needed to implement a comprehensive computer aided design package. The design is comprehensive in the sense it gives the designer support, from the conceptual through the final stages of product development. The biggest benefit of a comprehensive design package, is it gives the human designer immediate feedback on the choices being made concerning the designed product. It is proposed that a comprehensive computer aided design tool, could help the human designer produce designs that are more cost effective as well as manufacturable.

In order to demonstrate what mechanical engineering knowledge is needed, for a comprehensive design system, a small test program has been written to aid the designer in the selection of joining processes. The program will help the designer in crossing technological domains, that he or she might not otherwise consider as a possible design option. This hesitancy to cross domain boundaries may be due to a lack of familiarity with characteristics involved in an unknown area of expertise.

Acknowledgements

I would like to take this opportunity to thank the Air Force Systems Command and the Air Force Office of Scientific Research for providing the financial support for this research. I am particularly grateful to the people who provided suggestions and motivation for this work. Dr. Kenneth Halliday, who provided the main motivation of this research and Major Steven LeClair for his insight and guidance in my research. Finally I would like to thank UES Inc. for the administrative help which they provided throughout the summer.

I. INTRODUCTION: COMPREHENSIVE COMPUTER AIDED DESIGN

Generally, expertise from several very different disciplines is required to find a solution to a problem or need. This realization of a solution involves two distinct mental processes. The initial step toward a solution is the recognition of a need. This recognition process is the creativity of a visionary who assimilates ideas, thoughts and imagination in order to define a problem statement. It would be considered far to ambitious for this project to try and capture the thought processes of a visionary in a computer program. Next, after the need has been recognized, design, marketing, financial and other types of knowledge can be applied to the problem. As each of these disciplines are applied, the problem is shaped and defined until a conclusion is formed. Figure 1 shows a "problem solving machine" and how each professional discipline effects the development of a problem statement into a solution.

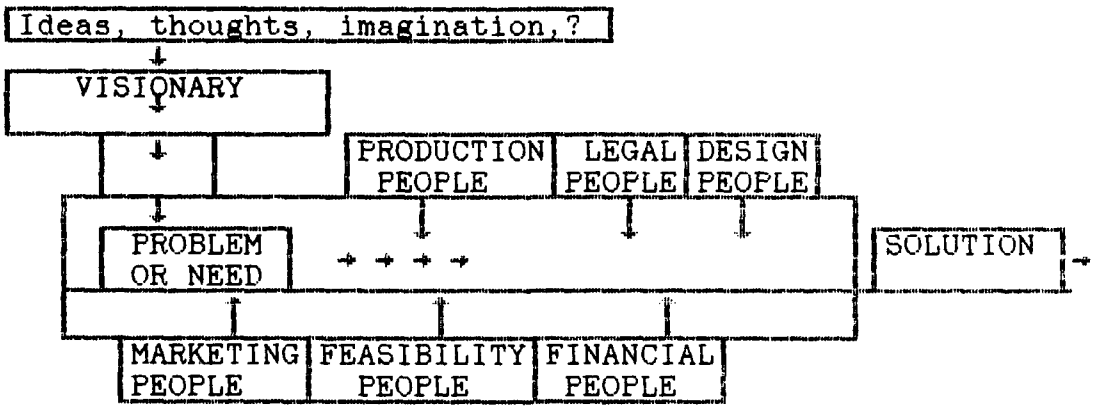

Figure 1: Schematic of the kind of knowledge needed to transform a problem statement or need into a solution.

This figure express the idea that mechanical engineers do not work in a vacuum, and are often forced to conform to constraints applied by other disciplines, suggesting a comprehensive design package will need more than just engineering knowledge. Due to this authors experience in the

mechanical design field, the focus of the paper will show how this knowledge relates to the structure of a comprehensive design system.

II. OBJECTIVE OF RESEARCH EFFORT:

The impetus of this research is to outline the kind of mechanical knowledge that is needed in order to implement a comprehensive computer aided design system. The mechanical knowledge will then be applied to an application program or case study. The goal of the case study is to demonstrate how mechanical engineering knowledge is used in a practical design problem. The case study will deal with the conceptual selection of joining processes. The conceptual design phase is targeted as a fertile research area because extensive work and numerous programs are available for the preliminary and final design stages. The joining domains considered are threaded fasteners, welded and allied processes, adhesives and rivets. The computer program will aid the designer in the conceptual design stages to select the most likely solution or solutions.

III. Mechanical Knowledge Needed for Comprehensive Design

In the domain of mechanical design the product evolves through three distinct stages of development, shown in figure 2.

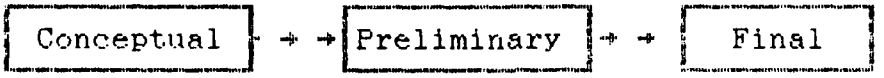

Figure 2: Stages of product development in mechanical design.

The main area of interest for this research is the conceptual design which is the first phase of product development. For the mechanical designer there are two goals or activities involved in the conceptual design. First the definition and clarification of the problem statement. Definition and clarification involves examining the design

constraints and realizing the implications of these constraints on the design solution. The second aspect is the synthesis of mechanical elements into a coherent design solution. This last aspect could be typified by the organization of mechanical elements such as bearings, nuts and bolts, I-beams and other physical elements into one assembly. The organization process is based largely on experience. The more experience with similar types of problems the faster a concept can be realized.

As was stated before, one aspect of the conceptual design is the clarification of the problem statement. Design considerations can be used to help define and clarify the problem and force the human designer to examine the intent of the product. At this point the important factor is the design intent not the architecture of the product. The computer then uses these considerations as pointers in a rule based or associative programing structure. The design considerations will act like a road map to connect the user to the correct knowledge bases. The following are the types of design considerations needed to shape a road map for the computer.

A) RELATIVE FORCE MAGNITUDE: A relatively high force suggests the design must be checked to satisfy the strength of materials theories. Knowing the loading conditions on the design, such as vibrations or cyclic loading, are also beneficial.

B) RELATIVE MOTION: If motion is a requirement for the product then wear, kinematics and dynamics become important to the design.

C) WEIGHT, SIZE OR SHAPE: Physical aspects suggest handling procedures and storage requirements for the product. Spacial concerns often dictate the shape of the product.

D) SERVICE CONDITIONS: Environmental factors such as moisture, temperature and corrosion, will suggest material properties or additional preventative steps to protect against product damage.

E) SAFETY: Product liability is important should catastrophic injury occur. There are specific design domains where codes and regulations apply.

F) REPAIRABILITY: If service to the product is required the design will need to allow for easy access to the parts of the product needing repair.

G) ESTHETICS: Product appearance with respect to codes or requirements that need to be met.

H) JOB SIZE: Job size deals with the size of the production run. Less than 100 parts would be considered a job shop process and greater than a million parts, over a five year period, would be a mass production. This information suggests possible production methods.

I) COST: Generally the design should attempt to maximize the company profit with a desired production cost set before the initiation of the design.

J) CODES AND STANDARDS: Certain domains such as boilers and pressure vessels are specified by production standards that the design has to meet.

K) ASSEMBLY CONDITIONS: The conditions in which the product is to be assembled has a bearing on the types of tools available. In a factory environment, fixtures will be available to hold the product, conversely in the field these devices will not be appropriate.

L) RELIABILITY: The projected life of the product will give an indication to the durability and quality desired.

M) CONTROL: If the product developed is part of a larger system and the function is to regulate a certain aspect of the system, then certain considerations must be made concerning the type of input needed, whether manual or numerical.

N) NOISE: This could also fall under the area of codes and standards or esthetics but often needs to be considered separately because noise is a result of vibration or impact.

To demonstrate what insights the design considerations offer, they will be applied to the problem of joining two plates. A problem statement needs to be defined in order to give the problem a domain.

Case Study Problem statement:

The design problem is to join two plates to form a lap joint for a certain construction application. The joint is to carry a service load of 5ØØ lbs. and target dimensions for the plates that are 5 inches wide and .75 inches thick. The most likely material will be a 1Ø2Ø carbon steel. Due to repair requirements elsewhere in the design, it is desired to disassemble this joint for service to the structure. A sketch of a lap joint is shown in figure 3.

Front View Top View

Figure 3: Test Case of a lap joint for a construction application.

It must be realized that in the context of this problem that a certain degree of conceptual design has already taken place. The materials and physical dimensions of the plates should be specified before the conceptual design of the joining process begins. The following design considerations are important to the solution of the problem statement. There are seven of these design considerations enumerated below and their impacts on the joining processes.

1. RELATIVE FORCE MAGNITUDE: The forces acting on the joint are moderate to small compared to other structural problems such as bridges. The forces do suggest that adhesives will not be a wise joining process selection, due to their inability to support these loads. It is assumed that the rest of the modes of joining can be sized to carry the loads, and at this point in the design, an estimation of the size is required for each process.

2. WEIGHT, SIZE OR SHAPE: The physical dimensions will also help define the joining process that will best solve the problem statement. For example, if the plate width is too narrow to support the fastener size, estimated earlier, then the designer has two options. One, the plate dimensions can be redesigned to support the fastener size, otherwise threaded fasteners are eliminated as a possible option.

3. SERVICE CONDITIONS: The service requirements of the lap joint should be designed to withstand a corrosive atmosphere. Corrosion requires the threaded fasteners to have a protective coating that facilitates ease in removal.

4. SAFETY: Designers are required to follow safety codes in many design applications where human safety is a factor. For the case study there are numerous safety and design suggestions found in the steel construction codes. A typical safety factor may have a value of 4 to 6 for this type problem.

5. JOB SIZE: Only one connection will be made, therefore specialized tools or techniques such as, submerged arc welding, would not be an appropriate solution. Suitable solutions for the case study require techniques using tools characterized as being manual, portable and general purpose.

6. CODES AND STANDARDS: These are design standards and in certain domains will be very specific as to what the design architecture should resemble. For the case study the safety factors are of primary importance because of the problems relationship to the construction industry.

7. ASSEMBLY CONDITIONS: The case study requires the joint be made on sight, meaning standard tools will be used to make the connection.

The second phase of conceptual design was previously defined as the synthesis of architecture and was discovered to be based largely on experience. Typically the development of an architecture forces the designer to work in an abstract environment. Including experience, there are three aspects that will be referred to as conceptual architecture characteristics. These three points will aid in the reduction

of vagueness associated with this stage of development. These three topics are enumerated below with their impact on the case study.

1. **EXPERIENCE**: Experience allows the designer to relate design context to the knowledge required to solve an engineering problem. For the case study of the joining processes, experience will supply the knowledge needed in recognizing the valid bolt patterns, if threaded fasteners are the design option.

2a. **FORCE FLOW**: Force flow is a study of how external loads are transferred from one location in the design space to another. Force flow applies the general principles of statics and strength of materials to suggest a suitable architecture for the design. General principles do not suggest a full blown FEM package only sufficient computational ability to give rough estimations of product sizes.

2b. **FUNCTIONALITY**: Functionality offers the same type of information about the motion of the design as does force flow for its structure. Functionality applies the general principles of dynamics, kinematics, gear sizing and mechanism design.

3. **REPAIRABILITY - RELIABILITY**: These topics are often at odds with each other because they tend to force the design in different directions. Redundancy and derating of the design are effects of reliability, while ease of access is a concern of repairability.

Conceptual architecture characteristics were examined to reduce the vagueness associated with this stage of the conceptual design. These three areas will be of value in relating numerical types of design features with the intent of the design. Presently work is being conducted as to how the design information should be represented in the computer.

After the architecture and the context of the design are defined, the conceptual design phase is complete. Now it is desirable to move to the preliminary design stage. This phase of the design could also be classified as concept checking. The design is formally sized and checked to see if it meets the performance constraints specified at the beginning of the design problem. If the design does not meet the constraints, the concept is discarded. If more than one design concept passes the preliminary stage, the most efficient will be selected for the final design. The design chosen minimizes a certain undesirable aspect, or maximizes a desired performance criteria.

Once the design has been checked and the performance criteria have been met a final design will be presented. The final design stage can be defined as a conversion process, where the insights gained from the conceptual and preliminary phases, are converted to a user understandable form. These forms could be blue prints, tables, or production planing schemes.

Reviewing the types of knowledge needed in each of the design phases a conclusion can be drawn as to which types of computer reasoning will be of value, to a comprehensive design system. An example of how these three design stages can be rep esented in a computer are shown in figure 4 on the following page.

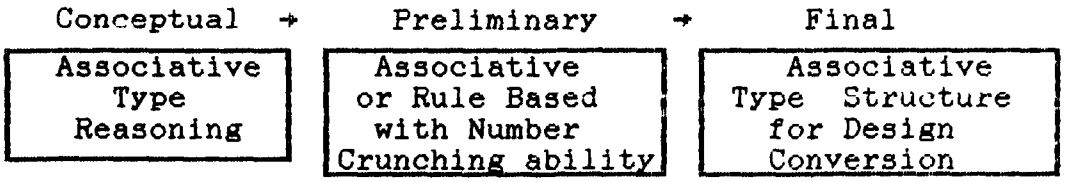

Figure 4: The three phases of design and the corresponding computer reasoning suggested for each phase.

Associative reasoning is a computer technique that can link all kinds of information related to a topic. Currently research is being conducted on this topic by Dr. Y.H. Pao, of Case Western University.

IV. Conclusions:

Expert systems exhibit promise as a valuable reasoning tool, but to a lesser extent than the associative procedures. The difficulty with expert systems occurs when a large number of rules are required to describe a knowledge base. The number of rules necessary for the joining case study was large by expert system standards. Attempting to represent the entire comprehensive design system with rules alone would demand a phenomenal number of rules. Program execution time becomes one problem with inordinately large rule bases. Another major problem is the amount of time needed to debug a large rule base.

Design can be characterized as an iterative process moving from a very abstract level to a higher degree of detail. The need for this iterative approach can not be overemphasized, modest quantities of elementary sizing information must be sprinkled into the design in order to promote continued development.

The type of knowledge needed for the comprehensive design system has been defined, providing a means for the computer to assist in the design process. The following is a summary of this knowledge process.

1. User interface: The interface is envisioned as a vehicle to link the user to the computer. If the computer program needs additional information this phase queries the user about his or her intent.

2. Experience: The experience knowledge base is used to relate present design context with past designs. Information retained concerning these past designs would include performance ratings, design architecture and links to vendor catalogues.

3. Force Flow - Functionality Expert: Force Flow is a study of how external loads are transferred from one location in the design space to another. Functionality applies the general principles of dynamics, kinematics, gear sizing and mechanism design.

4. Reliability - Repairability Expert: Redundancy and derating of the design are effects of reliability, while ease of access is a concern of repairability.

5. Domain Experts: Codes and standards are an important aspect of this knowledge base and should include GD&T ASME and the ANSI codes. These standards must be available to the computer user at any point in the design process.

6. Manufacturing Expert: This would include information from all the manufacturing disciplines including casting, forging, rolling, machining and assembling procedures.

7. Materials Expert: This expert could be a large data base of material properties available to the user. Several data bases are presently offered commercially.

8. Design Fundamentals Expert: Design Fundamentals would be a large library of computer programs capable of performing various engineering calculations. These might include FEM analysis, a systems modeling program and other useful programs including optimization and elementary sizing routines.

9. Detailing Expert: A detailing expert can transform design information from the preliminary and conceptual stages into blue prints, process and inspection plans.

These knowledge bases could be linked as illustrated in figure 5.

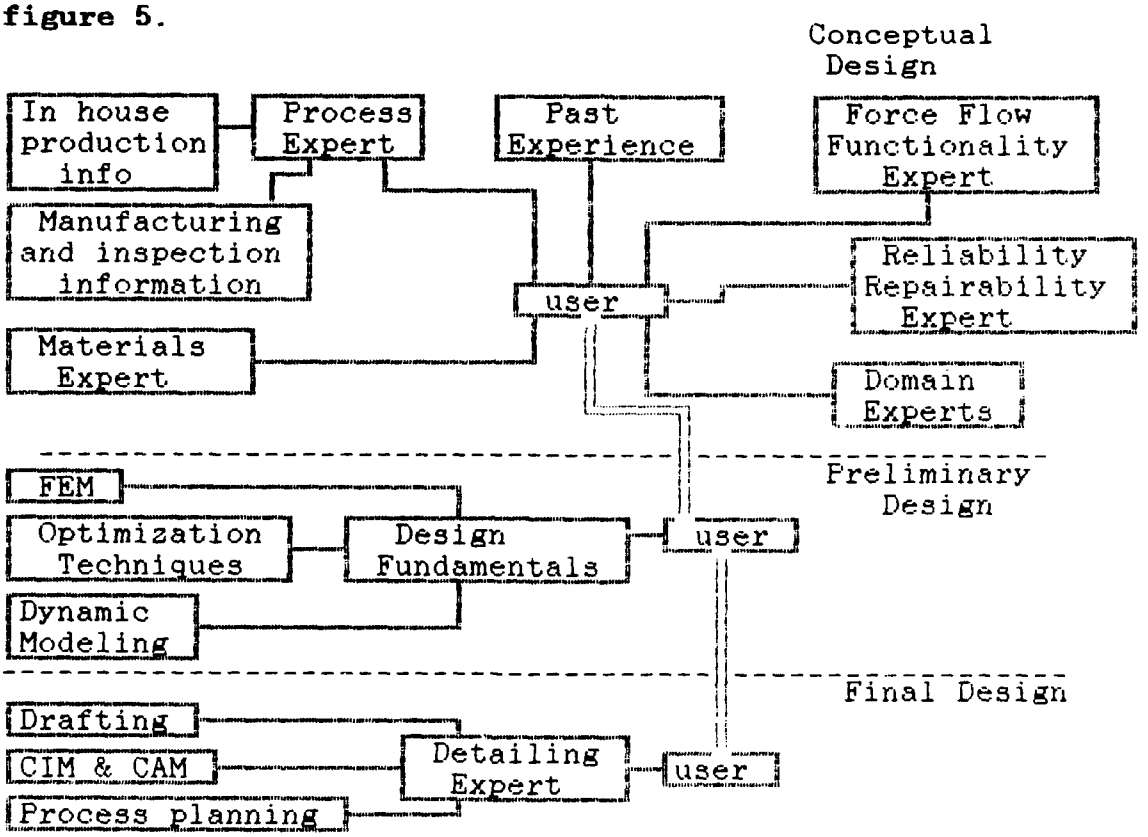

Figure 5: Possible knowledge structure for a comprehensive computer aided design system.

The biggest benefit of a comprehensive design package, is immediate feedback on the choices being made concerning the designed product. The computer also allows for the designs to be processed at a faster pace, hopefully producing cheaper and more reliable products.

V. Suggestions for further research:

With the programing technique of associativity, much can be accomplished toward the solution of the comprehensive computer aided design system. Certain immediate goals for the associative network would be in the domain of codes and standards. A system could be set up to search the domain literature to find certain codes related to a design context. Another area of interest would be in the conceptual design stage. A knowledge base could be implemented to develop a design, based on the topics of repairability vs. reliability.

References:

1. American Society for Testing and Materials ASTM Standards of Fasteners First Edition Philadelphia Pa. 1978

2. Blake, Alexander Design of Mechanical Joints, New York and Basel, Marcel Dekker Inc, 1985.

3. Davis, A.C. The science and practice of welding Volume 2 8th edition Cambridge University Press New York London 1984 Page 118.

4. Hart, Anna Knowledge Acquisition for expert Systems McGraw-Hill Book Company New York 1986

5. Levine, R. A Comprehensive Guide to AI and Expert Systems McGraw-Hill Book Company New York 1986

6. Linclon, B. Mechanical Fastening of plastics an Engineering Handbook Marcel Dekker Inc. New York and Basel 1984

7. Mackenzie, L.B. The Welding Encyclopedia 13th Edition Mcgraw-Hill Publishing Co. Inc. 1951 page 361-364

8. Parmley, Standard Handbook of Fastening and Joining McGraw-Hill book Company New York 1977

9. Priest, H. Malcolm American Welding Society The practical Design of Welded Steel Structures New York 1943 Pages 19-25

10. Reichenecker, W.J. and Heuschkel, J. Nasa Contributions to Metals Joining prepared under contract by Westinghouse Electric Corp. Office of Technology Utilization 1967

11. Shigley, Joseph E. Mechanical Engineering Design 4th edition McGraw-Hill Book Company 1983

12. Fastening joining and Assembly Reference Issue Machine Design November 19, 1987

APPENDIX MAY BE OBTAINED FROM

UNIVERSAL ENERGY SYSTEMS, INC.

OR FROM THE AUTHOR

1988 USAF-UES SUMMER FACULTY RESEARCH PROGRAM/
GRADUATE STUDENT RESEARCH PROGRAM

Sponsored by the
AIR FORCE OFFICE OF SCIENTIFIC RESEARCH
Conducted by the
Universal Energy Systems, Inc.
FINAL REPORT

THE STUDY OF TRIMETHYLSILYLPOLYPHOSPHATE (PPSE) AS A DEHYDRATING AGENT FOR POLYMERIZATIONS AND MODEL COMPOUND PREPERATIONS OF N-PHENYLBENZIMIDAZOLES

Prepared by:	Ronald C. Tomlinson
Academic Rank:	Graduate Student
Department and University:	Department of Chemistry Wright State University
Research Location:	Materials Laboratory, Nonmetallic Materials Division, Polymer Branch, Wright Paterson Air Force Base, Dayton, Ohio
USAF Researcher:	Bruce A. Reinhardt
Date:	8-31-88
Contract No:	F49620-88-C-0053

THE STUDY OF TRIMETHYLSILYLPOLYPHOSPHATE (PPSE) AS A DEHYDRATING AGENT FOR POLYMERIZATIONS AND MODEL COMPOUND PREPERATIONS OF N-PHENYLBENZIMIDAZOLES

by
Ronald C. Tomlinson

ABSTRACT

The dehydrating agent Trimethylsilylpolyphosphate (PPSE) was employed in a one step synthesis of N-Phenylbenzimidazoles. Model compounds produced from this agent are 2,2'-(1,3-phenlyene)bis (1-phenylbenzimidazole) and 2,2'-(1,4-(2,5-didecyloxybenzene)) bis(1-phenylbenzimidazole) from a TBOC derivative of N-Phenyl-1,2-phenylenediamine and the corresponding dicarboxylic acid in near quantitative yields.

I. INTRODUCTION:

Polybenzimidazoles are known to be remarkably stable polymers that retain their stiffness and toughness at elevated temperatures. Many are resistant to acids and bases and are not prone to oxidation [1]. These properties are of interest in composite materials because the polymers are light weight and have superior properties than most metals. The polymers and model compounds may have third order nonlinear optical properties (NLO) and are evaluated for this trait.

The Polymer Branch of the Materials Laboratory at Wright Paterson Air Force Base is particularly interested in the synthesis and physical properties of polybenzimidazoles and many other polymers. A data base of the structure versus properties relationships are a primary concern.

My master's thesis and research interests are in the organic synthesis of novel monomers which will lead to new 1-substituted polybenzimidazoles. As a graduate student of Dr. James J. Kane at Wright State University at Dayton, Ohio, whose research group works toward the goals of the Polymer Branch at WPAFB, my background was well suited for this project.

II. OBJECTIVES OF THE RESEARCH EFFORT:

My summer assignment was the study of trimethylsilyl polyphosphate (PPSE) as a dehydrating agent for the synthesis of polybenzimidazoles and model compounds. This project was two fold, first finding the optimum conditions for the synthesis of model compounds and then to use these conditions for the polymerization reactions. The primary goal was to find the optimum conditions for the synthesis of the model compounds:
2,2'-(1,3-phenylene)bis(1-phenylbenzimidazole) (1) and

2,2'-(1,4-(2,5-didecyloxybenzene)) bis(1-phenyl-benzimidazole) (2). These were produced from a diamine or TBOC derivative of the diamine and the corresponding dicarboxylic acid. Time did not permit any polymerization reactions but the TBOC derivative of a tetraamine monomer was produced. Future goals involve a model compound made from this tetraamine monomer and benzoic acid and polymerizations with the dicarboxylic acids used in the synthesis of (1) and (2) as well as other diacids.

III. RESULTS AND DISCUSION:

Polybenzimidazoles are conventionally made in two steps. The first is the formation of a polyamide from a substituted tetraamine and a aromatic diacid halide. This is followed by a cyclization step which is preformed either in polyphosphoric acid or thermally to produce the polybenzimidazole as shown in figure 1.

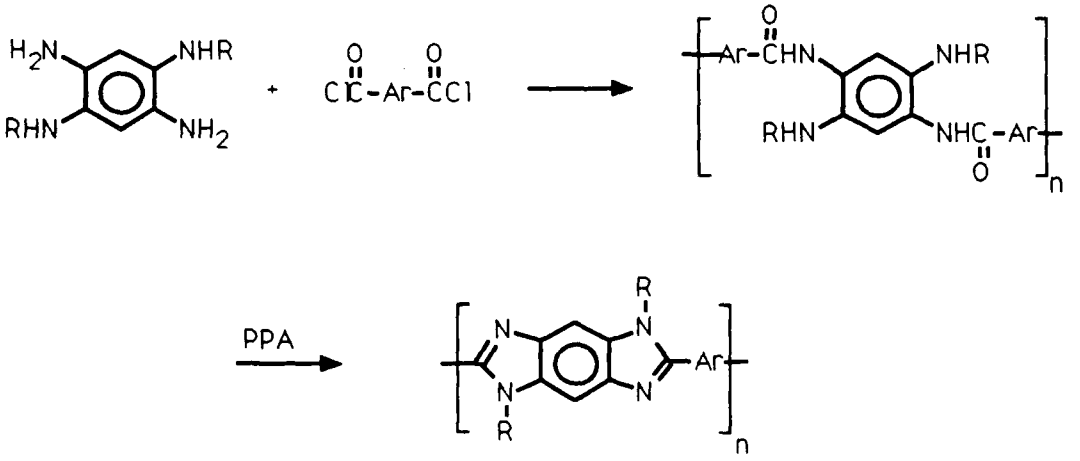

FIGURE 1

However, this condensation method usually results in low molecular weight materials which could arise from a number of possibilities[1]. A one step synthesis may improve the polymers produced from such a process.

Yamamoto and Watanabe [2] used PPSE in dichloroethane to synthesize 2-methyl substituted benzimidazole, benzthiazole and benzoxazole in 63, 93 and 68% yields respectively. They also determined three active forms of PPSE which are illustrated in figure 2. Structure I was found to be the major form in xylene. While structure II was found in the greatest percent in dichloroethane or

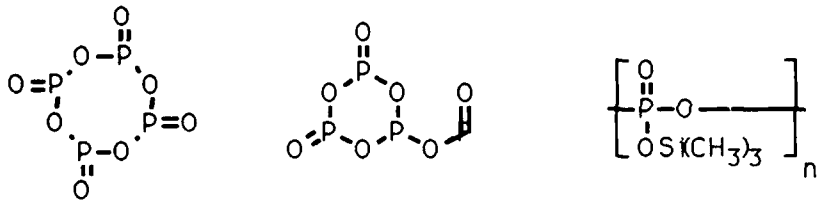

I II

TMS groups are omitted from I and II for clarity

FIGURE 2

dichloromethane and structure III is the predominate form without a solvent. Based on the yields obtained by Yamamoto and Watanabe with PPSE in dichloroethane the branched form, structure II is the most active dehydrating agent. In 1984 Alzpurua and Palomo [3] reported difficulty in repeating the synthesis of the 2-substituted benzoxazole by the method that Yamamoto and Watanabe reported. However, they found if the reaction was carried out in1,2-dichloro-benzene very high yields were obtained. From this work and work presently unpublished at the Polymer Branch, it was thought that PPSE may prove to be a valuable dehydrating agent in one step polymerizations reactions.

The optimum conditions for a polymerization reaction were determined from the model compound synthesis. The PPSE was made insitu from P_4O_{10} and hexamethlydisiloxane in 1,2-dichlorobenzene at 160°C. Figure 3 shows the reaction with N-Phenyl-1,2-phenlyene-diamine and isophthalic acid which gave an 82% yield of 2,2'-(1,3-phenlyene)bis(1-benzimidazole) (1). Attempts to improve

the yield by first heating the reactants and PPSE to 130°C for 1 hour and then increasing the temperature to 160°C for 4 hours failed.

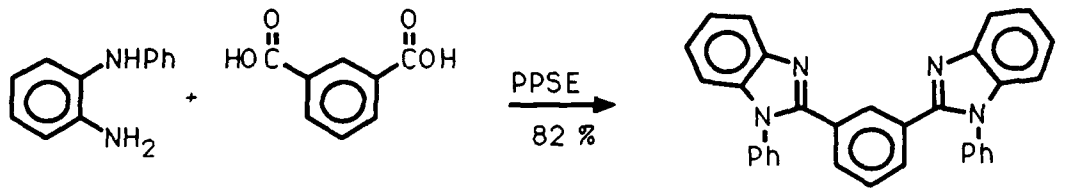

(1)

FIGURE 3

It was thought that decomposition of the diamine was the cause of a lower yield than what was desired. To combat this problem a protecting group for the amine was used. It's been shown that di-tert-butyldicarbonate (TBOC) is a good protecting group for Phenols and amino acids and when cleaved produces the free amine, CO_2 and propene [4-6]. The reaction was carried out under a nitrogen atmosphere at room temperature with recrystallized diamine to produce the TBOC derivative of N-phenyl-1,2-phenylenediamine (3) in a 90% yield and is shown in figure 4.

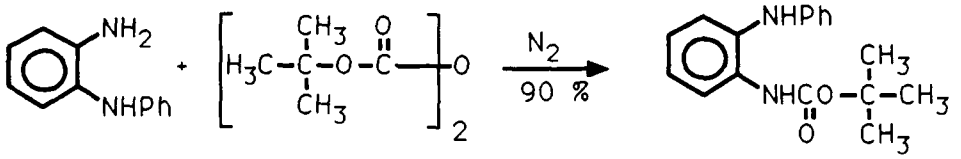

(3)

FIGURE 4

When the TBOC derivative of N-phenyl-1,2-phenylenediamine (3) and isophthalic acid were reacted in PPSE in 1,2-dichlorobenzene at 165°C a 92% yield of the model compound (3) was obtained. This reaction is shown in Figure 5 and is considered the optimum conditions.

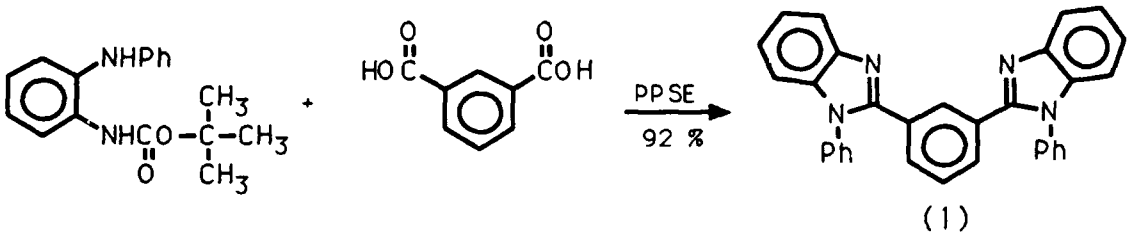

(1)

FIGURE 5

To aid in the solubility of the acid in dichlorobenzene and hopefully increase the molecular weight of a polymer the the model compound 2,2'-(1,4-(2,5-didecyloxbenzene))bis(1-phenyl-benzimidazole) (2) was synthesized. The reaction was preformed the same as for the model compound (1) except 2,5-didecyloxybenzene-1,4-dicarboxylic acid was used and this is illustrated in figure 6.

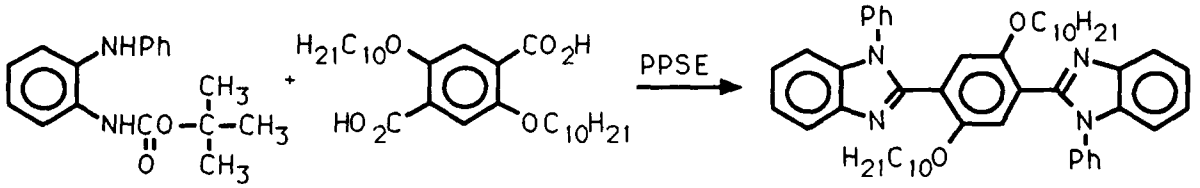

(2)

FIGURE 6

The tetraamine that will be used in future polymerization reactions is 2,2-bis(3-amino-4-anilinophenyl)hexafluoropropane. This was made in a four step synthesis starting from bisphenol AF as described by Lau [7]. The TBOC derivative of 2,2-bis(3-amino-4-anilinophenyl)hexafluoropropane (4) was formed similarly to that of N-phenyl-1,2-phenylenediamine and is shown in figure 7.

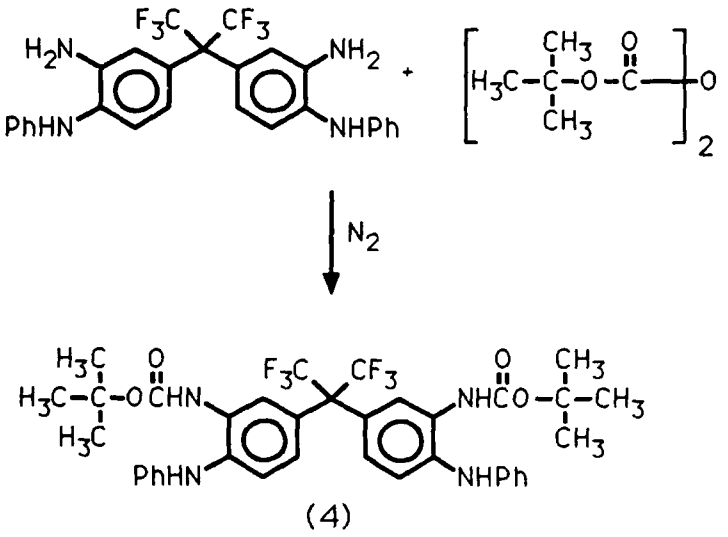

(4)

FIGURE 7

IV. EXPERIMENTAL:

The starting materials were obtained from Aldrich Chemical Company, Inc. or Daychem labs and were used as sold except where noted. The 2,2-Bis(3-amino-4-anilinophenyl)hexafluoropropane was produced from a four step synthesis as described by K. S. Lau [7]. FTIR spectra were obtained from a Nicolet 5DX , HNMR spectra were produced on a Varin EM-360, mass spectrum and analysis were preformed by the analytical branch of the Materials Laboratory at WPAFB. Melting were ran on a Laboratory Devices Mel-Temp apparatus and were uncorrected.

TBOC Derivative of N-Phenyl-1,2-phenylenediamine (3)

To 7.65 g, 0.042 mol of N-Phenyl-1,2-phenylenediamine (recrystallized from heptane) in 100 mL of diethylether was added 11.93 g, 0.042 mol of di-tert-butyldicarbonate under nitrogen at room temperature. A white precipitate formed after 0.5 hr. The reaction was allowed to stir at room temperature for 18 hr at which time no starting material could be observed by TLC (CH_2Cl_2/alumina). The white crystalline material was filtered and

washed with 50 mL of diethylether to give 10.78 g, 0.038 mol, 90.4% yield mp 177-181°C of (3). FTIR (KBr) cm^{-1}, 3373.7, 3304.3 NH stretch; 2980.2 aromatic CH stretch; 1701.3 C-O stretch; 1595-1446 C-C stretch; 1151.6 C-O-C stretch. MS $^{m}/_{e}$ 284 (M^{+}), 228, 211, 184, 169, 77, 65, 57(100%), 51, 42. Analysis calculated for $C_{17}H_{20}N_2O_2$: C, 71.79; H, 7.09; N, 9.86. Found: C, 71.57; H, 7.00; N, 9.48.

DiTOBC derivative of
2,2-Bis(3-amino-4-anilinophenyl)hexafluoropropane(4)

To 0.50 g, 0.97 mmol of 2,2-Bis (3-amino-4-anilinophenyl) hexafluoropropane in 10 mL of diethylether was added 0.42 g,1.94mmol of di-tert-butyldicarbonate in 5 mL of diethylether under nitrogen at room temper-ature. After 24 hr 0.2 eq. 0.05 g of additional di-tert-butyl-dicarbonate was added as a solid. The reaction was monitored by TLC ($CHCl_3$/alumina) and after 72 hr the solution was filtered and concentrated under high vacuum to give 0.68 g of a crude white crystalline material. Recrystallization from cyclohexane resulted in 0.44 g, mol 62%, yield mp 110-112°C of (4). FTIR (KBr) cm^{-1}, 3395.0-3367.9 NH stretch, 2980.2-2932 aromatic CH stretch, 1701.3 C-O, 1595.2-1496.9 C-C, 1250 C-O-C, 1159 CF_3. HNMR ($CDCl_3$) 1.5,18 H d CH_3; 6.2, 2 H bs NH; 6.6-7.5, 16H m aromatic; 7.7 2H bs NH. MS m/e 716 M+, 616, 516, 447, 182, 57 (100%), 44, 41. Analysis calculated for $C_{37}H_{38}F_6N_4O_4$: C, 61.99; H, 5.35; N, 7.82. Found: C, 62.16; H, 5.61; N, 7.59.

Model compound:
2,2'-(1,3-phenlyene)bis(1-phenylbenzimidazole) (1)
Procedure A:

PPSE was made as follows: 2.00 g of P_2O_5 was added to 10 mL of 1,2-Dichlorobenzene and 5 mL of hexamethyldisiloxane under nitrogen. This mixture was heated to 160°C resulting in a clear solution. To the cooled PPSE solution was added 0.42 g, 2.53 mmol of isophthalic acid followed by 1.11 g, 6.02 mmol of N-Phenyl-1,2-

phenylenediamine (recrystallized from heptane and sublimed) as solids. This mixture was rapidly heated to 160°C and maintained there for 4 hr. The resulting dark blue solution was poured into 100 mL of methanol and evaporated to dryness overnight. 200 mL of a 10% $NaHCO_3$ solution was added slowly which produced a violet solid. This was treated with charcoal and recrystallized from ethanol and water to give 0.95 g, 2.06 mmol, 82.3% yield of a light pink crystals mp 247-252°C of (1).

Procedure B:

The PPSE was made as in procedure A. To the cooled PPSE solution was added 0.37 g, 2.23 mmol of isophthalic acid followed by 1.50 g, 5.28 mmol of the TBOC derivative of N-Phenyl-1,2-phenylenediamine (3) as solids. The reaction was slowly heated to 165°C and maintained there for 4 hr. The reaction mixture was poured into 200 mL of a 10% $NaHCO_3$ solution. This was extracted with 3, 75 mL portions of CH_2Cl_2. The combined organics were washed with 3,100 mL portions of 10% $NaHCO_3$. The 1,2-dichlorobenzene and CH_2Cl_2 were evaporate overnight to produce dirty white crystals. Recrystallization from 1-propanol gave 0.95 g, 2.06 mmol, 92.4% yield of cream colored crystals mp 246-250°C of (1). FTIR (KBr) cm^{-1}, 3049.7 aromatic CH stretch; 1595.2-1454.4 C-C and C-N ring stretch. HNMR (CF_3O_2D) ppm 7.3-8.2 m. MS $^m/_e$ M^+462(100%), 385, 231, 167, 139, 77, 51. Analysis: calculated for $C_{32}H_{22}N_4$: C, 83.09; H, 4.79; N, 12.11. Found: C, 82.59; H, 5.07; N, 11.72.

Model compound:

2,2'-(1,4-(2,5-didecyloxybenzene))bis(1-phenylbenzimidazole) (2)

PPSE was made as in procedure A of the above. To the cooled PPSE solution was added 1.05 g, 2.23 mmol of 2,5-didecyloxybenzene-1,4-dicarboxylic acid followed by 1.51 g, 5.28 mmol of the TBOC derivative of N-Phenyl-1,2-phenylenediamine (3) as solids. The reaction was heated to 175°C and maintained there for 24 hr under nitrogen. The resulting dark blue-green solution was

poured into 200 mL of a 10% $NaHCO_3$ solution and was extracted with 3, 75 mL portions of CH_2Cl_2. The combined organics were washed with 3, 100mL portions of a 10% $NaCO_3$ solution. The dichlorobenzene and CH_2Cl_2 were evaporate overnight to produce a red oil. This was purified by column chromatography using silica gel and $CHCl_3$ to produce an amber oil. Trituration in n-pentane resulted in 1 g, 1.42 mmol, 64.7 %, mp 91-93°C of (2). FTIR (KBr) cm^{-1}, 2924.3 aliphatic CH, 1595.2-1419.7 C-C, 1095 C-O-C. HNMR ($CHCl_3$) ppm, 0.9-1.6 38H m, 3.3-3.6 4H bt, 6.9-7.5 18H m, 7.6-8.0 2H m. MS $M/_e$, 774 M+, 661, 647(100%), 507, 493, 477, 387, 299, 260, 245, 219, 195, 145, 99, 77, 57.

V. Spectra of Compounds (1-4):

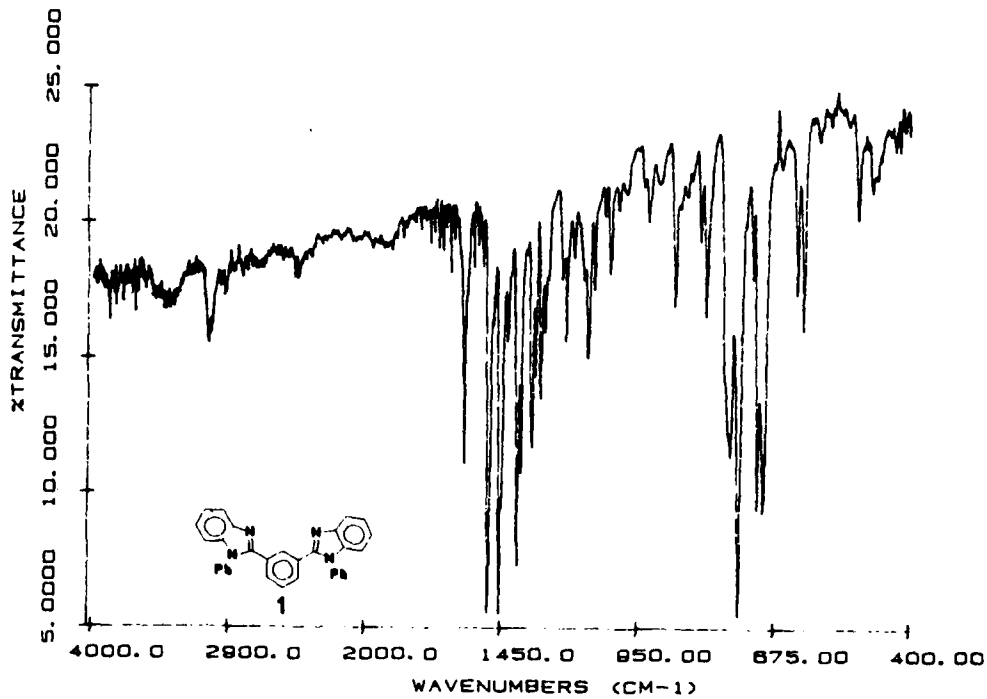
%TRANSMITTANCE
5.0000
10.000
15.000
20.000
25.000
4000.0
2900.0
2000.0
1450.0
950.00
675.00
400.00
WAVENUMBERS (CM-1)
1

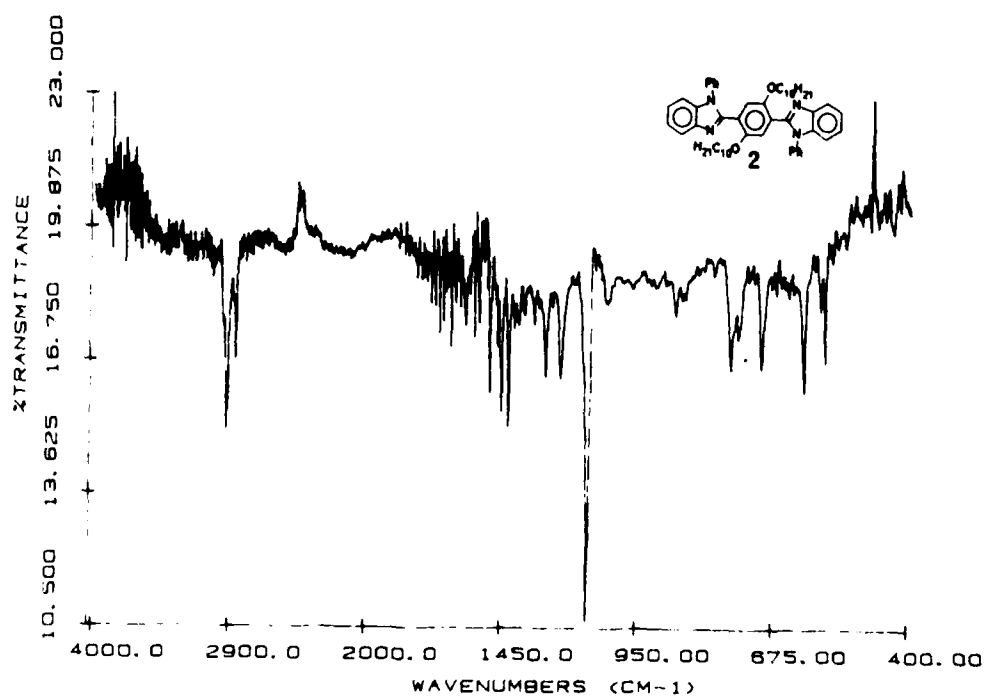
%TRANSMITTANCE
10.500
13.625
16.750
19.875
23.000
4000.0
2900.0
2000.0
1450.0
950.00
675.00
400.00
WAVENUMBERS (CM-1)
2

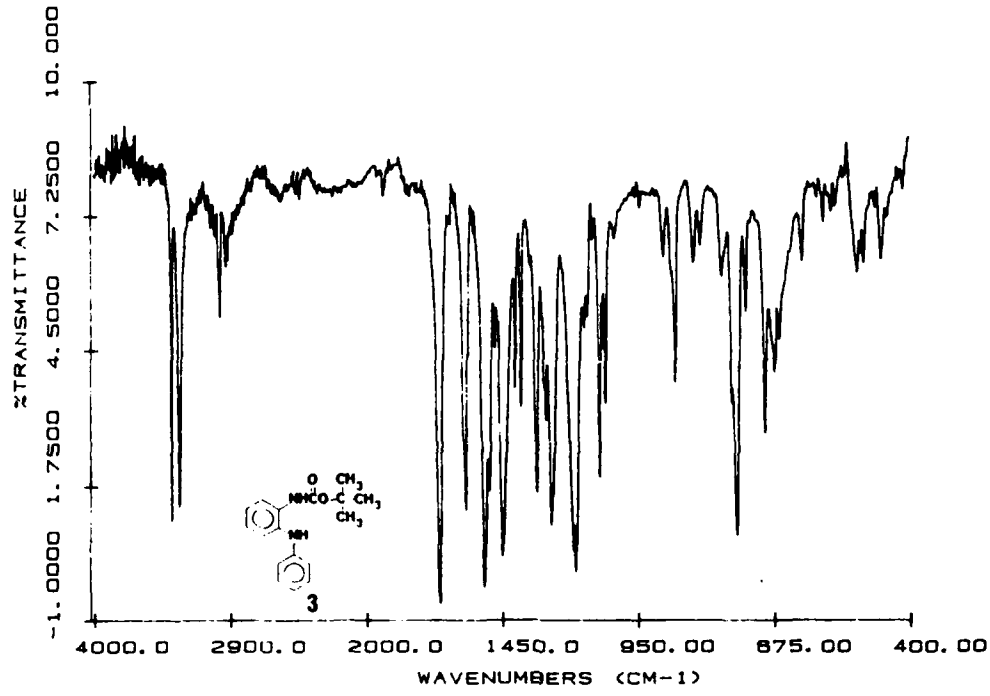
%TRANSMITTANCE
10.000
7.2500
4.5000
1.7500
-1.0000
4000.0
2900.0
2000.0
1450.0
950.00
875.00
400.00
WAVENUMBERS (CM-1)
3

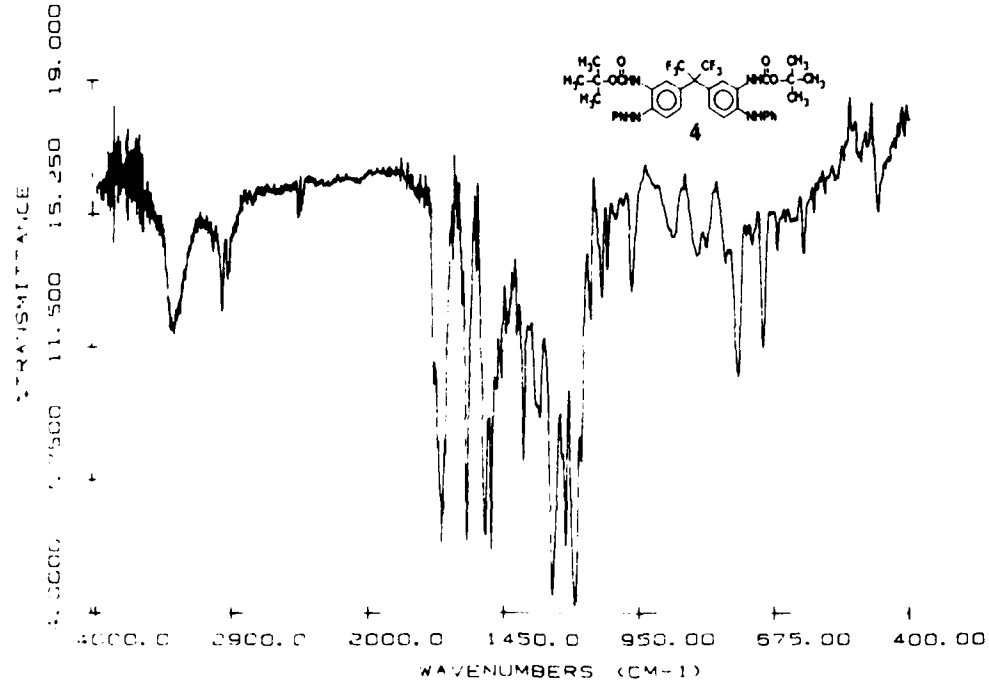
19.000
15.250
11.500
2900.0
2000.0
1450.0
950.00
875.00
400.00
WAVENUMBERS (CM-1)
4

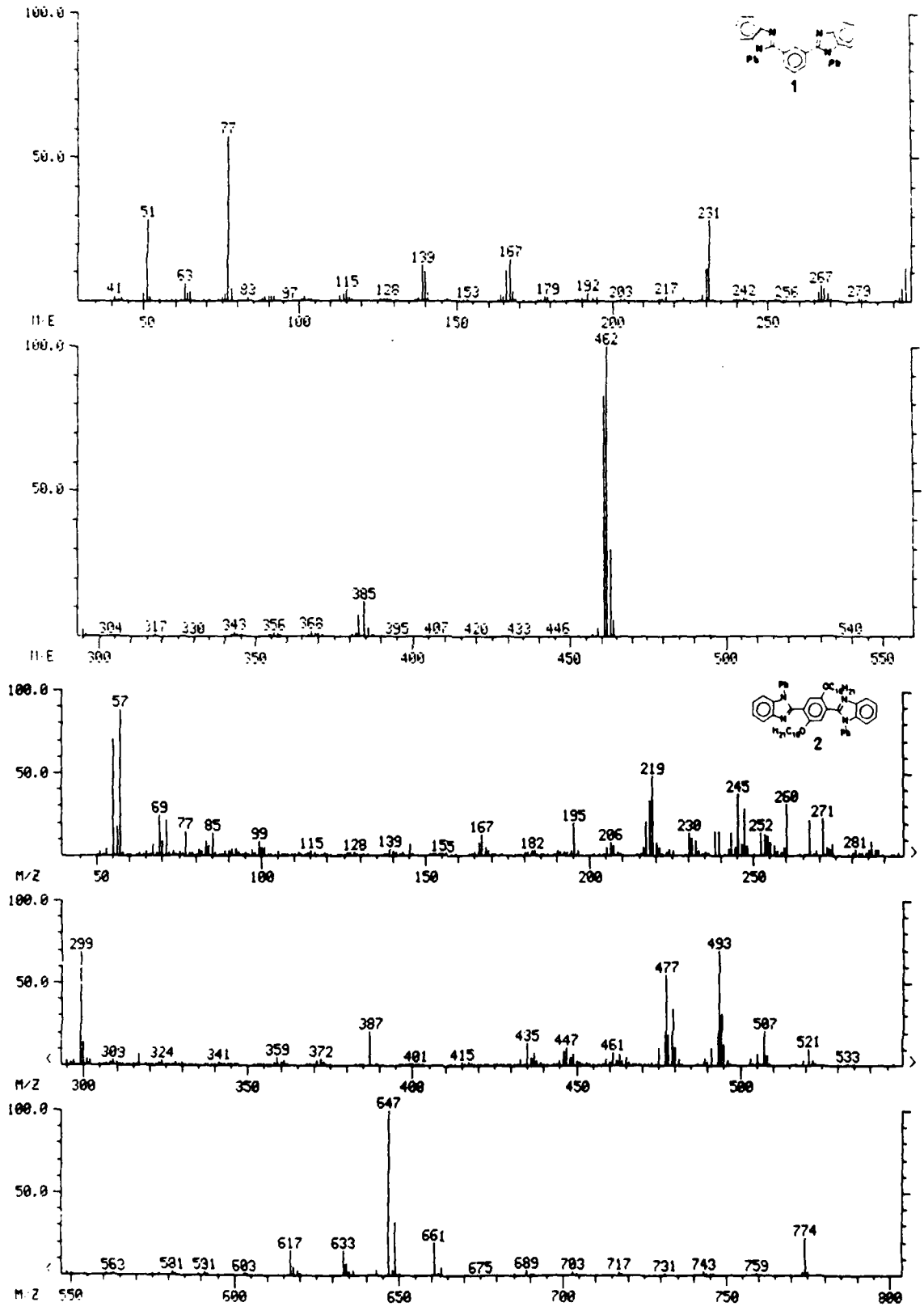
100.0
50.0
M/E
1
77
51
231
139
167
41
63
83
97
115
128
153
179
192
203
217
242
256
267
279
50
100
150
200
250
462
385
304
317
330
343
356
368
395
407
420
433
446
540
300
350
400
450
500
550
2
57
69
77
85
99
115
128
139
155
167
182
195
206
219
230
245
252
260
271
281
M/Z
299
303
324
341
359
372
387
401
415
435
447
461
477
493
507
521
533
563
581
591
603
617
633
647
661
675
689
703
717
731
743
759
774
550
600
650
700
750
800

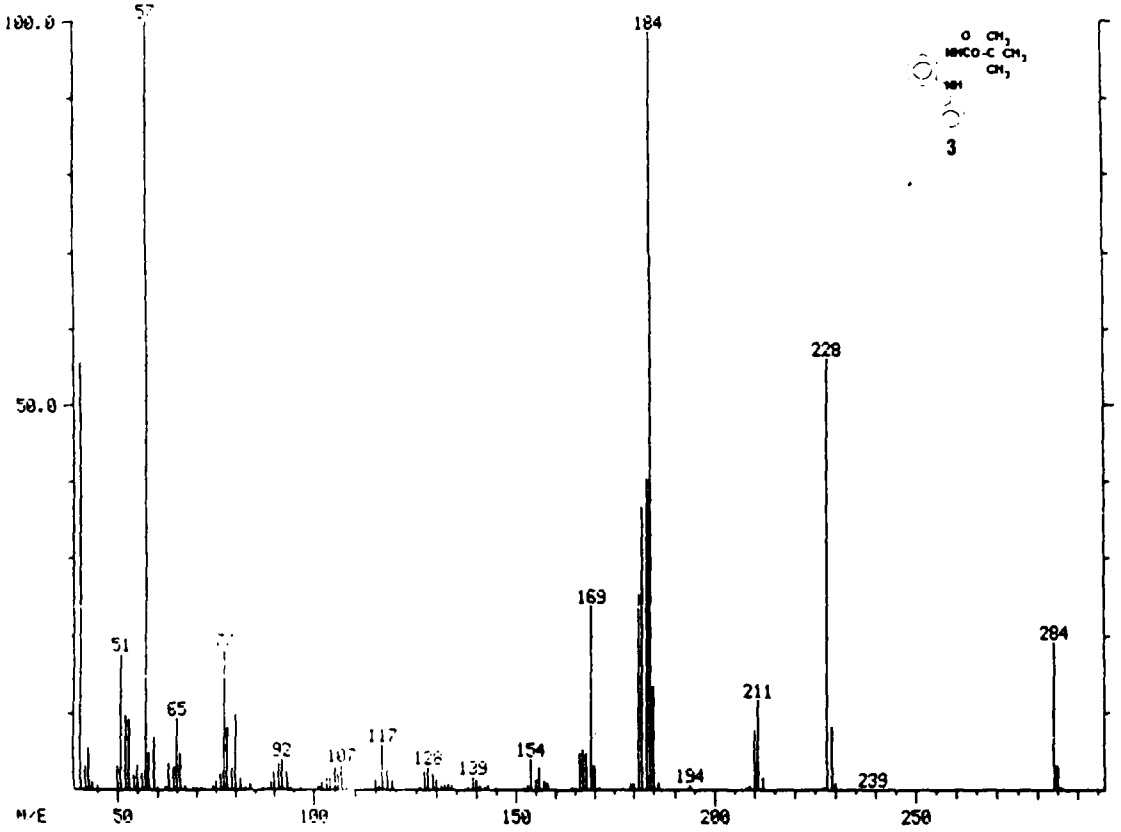
100.0
50.0
M/E
57
184
228
169
284
211
51
65
77
92
107
117
126
139
154
194
239
50
100
150
200
250
3

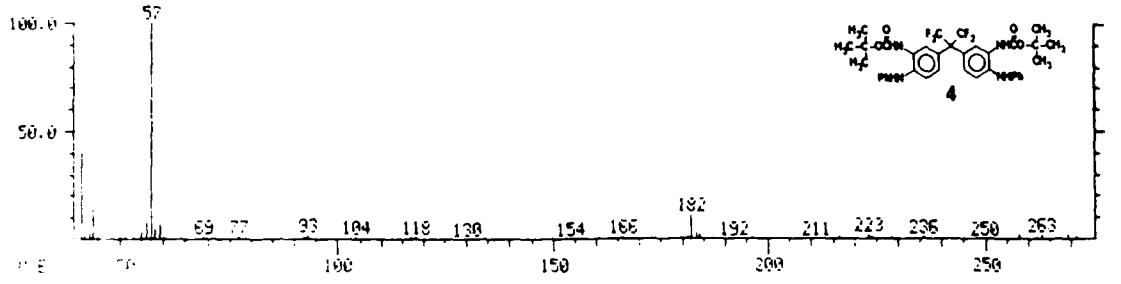
100.0
50.0
57
182
69
77
93
104
118
130
154
166
192
211
223
236
250
263
100
150
200
250
4

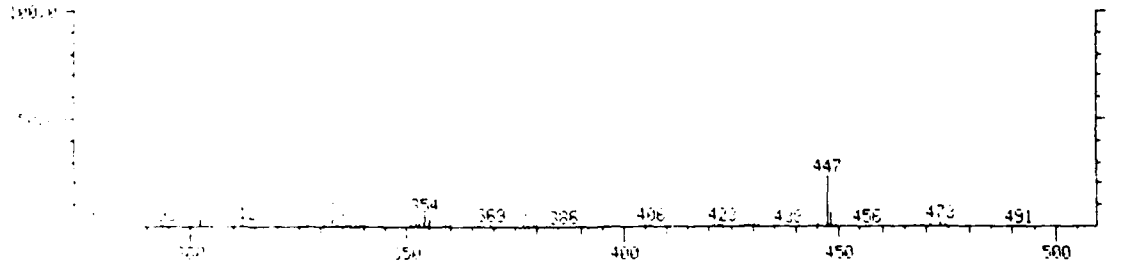
447
354
363
386
408
420
456
473
491
400
450
500

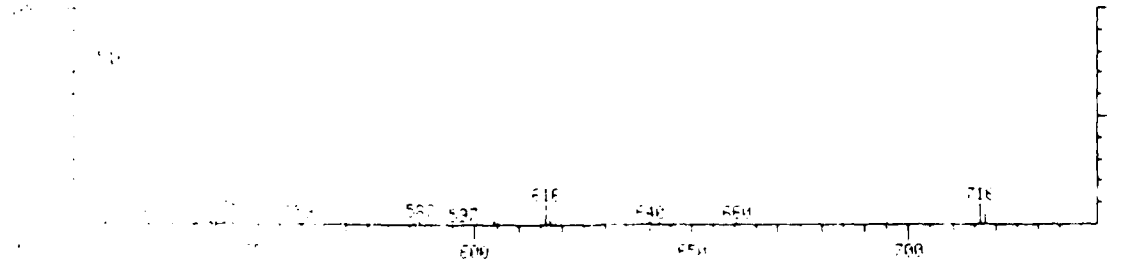
716
716
700

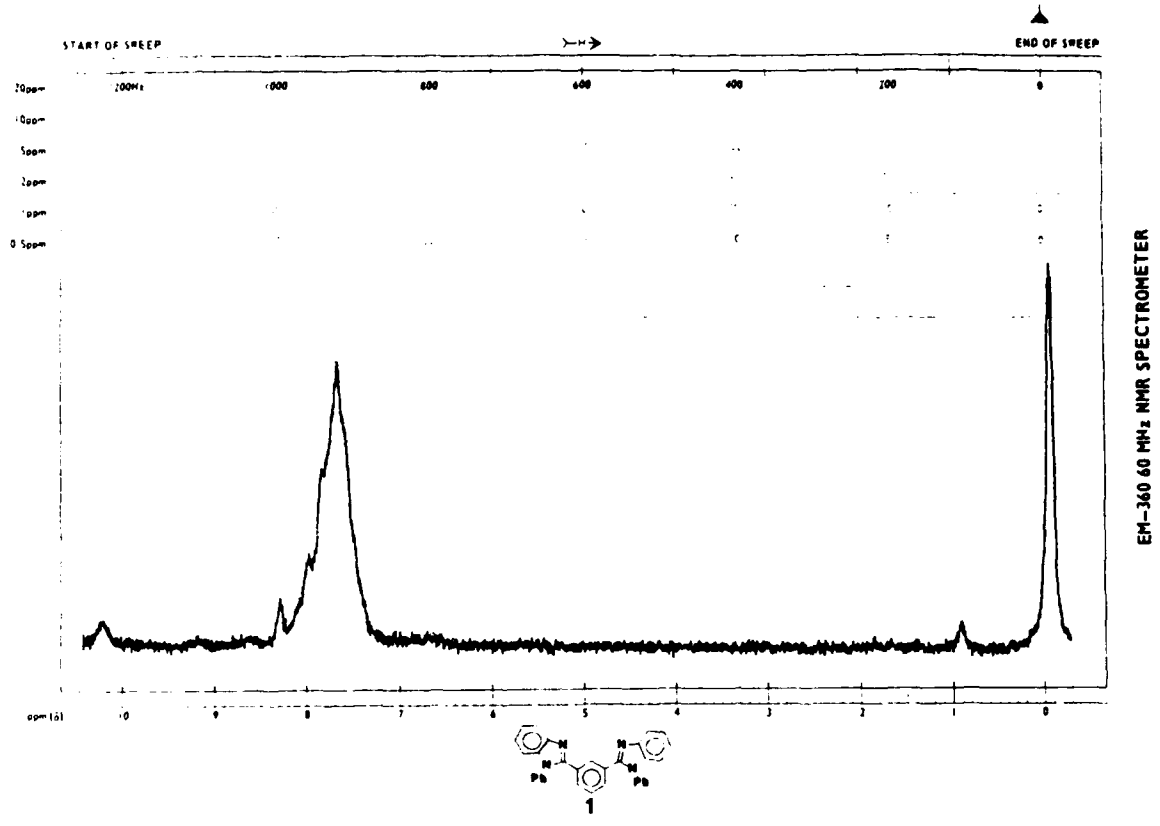
START OF SWEEP
END OF SWEEP
EM-360 60 MHz NMR SPECTROMETER

1

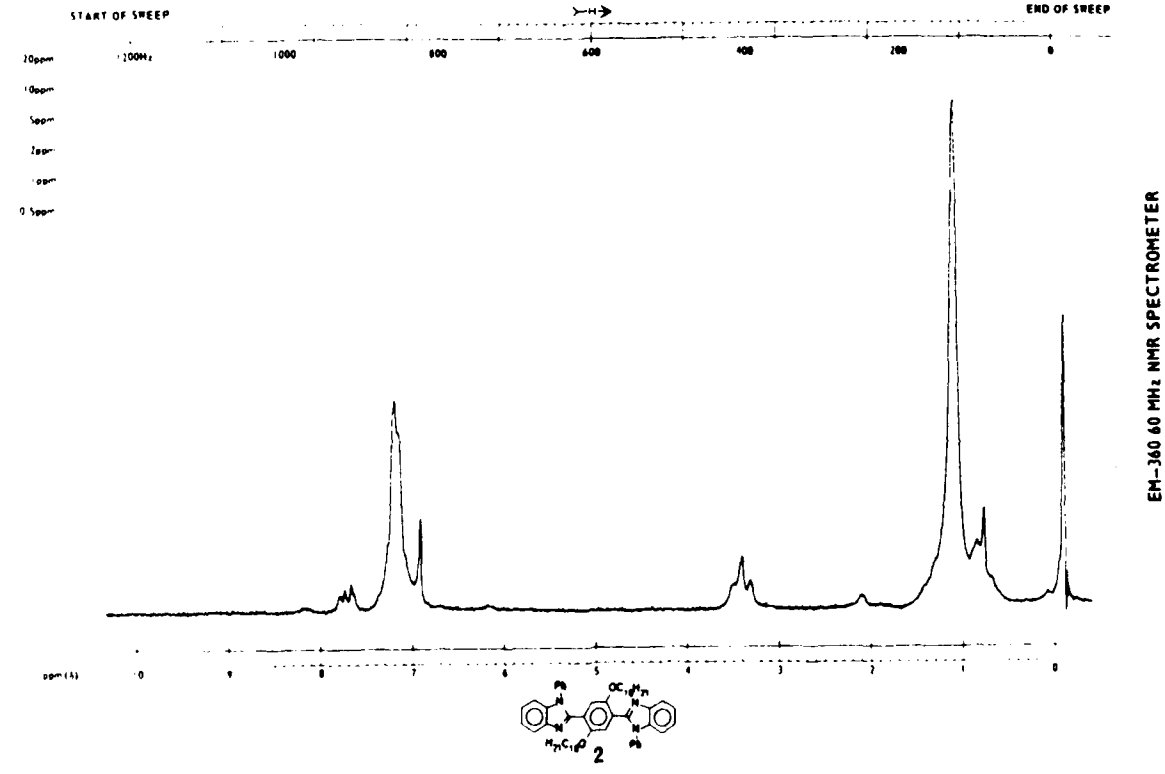
START OF SWEEP
END OF SWEEP
EM-360 60 MHz NMR SPECTROMETER

2

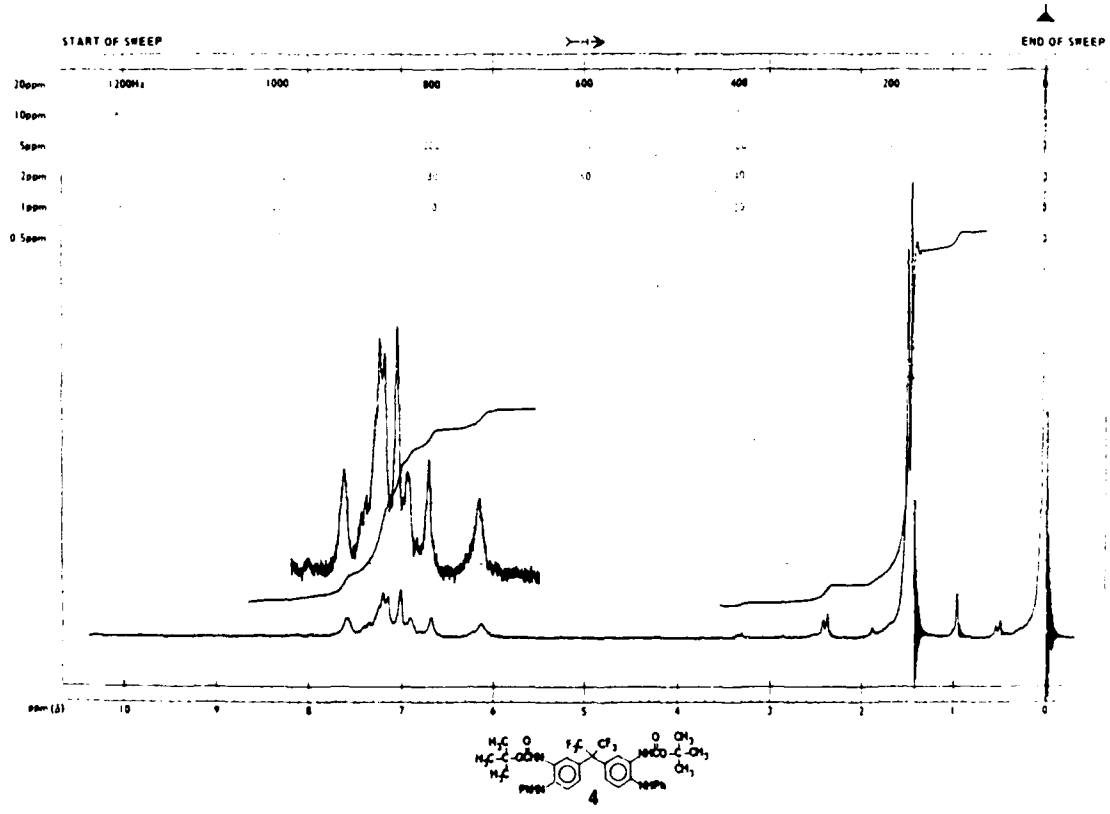

4

VI. RECOMENDATIONS

The high yield obtained for the synthesis of model compound (1) indicate that PPSE is a promising dehydrating agent and should be studied further. Future work at Wright State University will be to explore the reagent in polymerization reactions using this work as a guide. The TBOC derivative of the tetraamine (4) will be used extensively with various acids. Another avenue for study is the TBOC protecting group. This may prove as a valuable method for storing air sensitive tetraamines and should be explored in depth.

VII. ACKNOWLEDGMENTS

I would like to thank Bruce A. Reinhardt and Dr. James J. Kane whose guidance and expertise made this work possible. The wonderful people of the Reinhardt group: Gibby Dillard, Marilyn Unroe, Mark Prazak and Lt. Cady Coelman who made my summer stay very special.

I wish to thank the Air Force Systems Command of the Air force Scientific Research, Universial Energy Systems Inc. and the Polymer Branch of the Materials Laboratory for sponsorship of this research.

REFERENCES

1. Vogle, H. and Marvel, C. S., J. Polymer Sci., 50, 511 (1961).
2. Yamamoto, K. and Watanabe, H., Chem. Lett., 1225 (1982).
3. Alzpurua, J. M. and Palomo, C., Bull. Soc. Chim. Fr., 142 (1984).
4. Frechet, J. M. J., Eichler, E., Ito, H. and Willson, C. G., Polymer, 24, 995 (1983).
5. Pope, B. M., Yamamoto, Y. and Tarbell, D. S., Org. Syn., (1973).
6. Pope, B. M., Yamamoto, Y. and Tarbell, D. S., Org. Syn., 57, 45 (1977).
7. Lau, K. S. Y., Landis, A. L., Kelleghan, W. J. and Beard, C. D., J. Poly. Sci.Poly. Chem. Ed., 20, 2381 (1982).

MS. DEBORAH VEZIE

FINAL REPORT NUMBER 67

NO REPORT SUBMITTED

1988 USAF-UES SUMMER FACULTY RESEARCH PROGRAM

GRADUATE STUDENT RESEARCH PROGRAM

Sponsored by the

AIR FORCE OFFICE OF SCIENTIFIC RESEARCH

Conducted by

UNIVERSAL ENERGY SYSTEMS, INC.

FINAL REPORT

Effect of Various Metals on the Thermal Degradation of a Chlorotrifluorethylene Based Fluid

Prepared By:	Vijay K. Gupta and Oden L. Warren
Academic Rank:	Professor and Graduate Student
Department and University:	Chemistry Department Central State University / Iowa State Univ. Wilberforce, OH 45384 Ames, IA 50010
Research Location:	Materials Laboratory (AFWAL/MLBT) Wright-Patterson AFB, OH 45433
USAF Researcher:	Dr. Kent J. Eisentraut
Date:	31 August 1988
Contract No.	F49620-88-C-0053

SAME REPORT AS
PROF. VIJAY GUPTA
MATERIALS LABORATORY # 102